Technische Universität München

Department Chemie

Institute for Advanced Study

Structural Studies of *N*-methylated Cyclopeptides and of the Small Heat Shock Protein Hsp26 from *S. cerevisiae*

Johannes Gerhard Beck

Vollständiger Abdruck der von der Fakultät für Chemie der Technischen Universität München zur Erlangung des akademischen Grades eines

Doktors der Naturwissenschaften

genehmigten Dissertation.

Vorsitzender:	Univ.-Prof. Dr. Bernd Reif
Prüfer der Dissertation:	1. Univ.-Prof. Dr. Horst Kessler
	2. Univ.-Prof. Dr. Iris Antes

Die Dissertation wurde am 27.02.2012 bei der Technischen Universität München eingereicht und durch die Fakultät für Chemie am 04.04.2012 angenommen.

To Miriam and Lilli.

The work presented in this thesis was prepared from March 2007 until February 2012 in the group of Prof. Dr. Horst Kessler at the Department of Chemistry of the Technische Universität München, Germany.

Acknowledgments

I would like to thank my supervisor Prof. Horst Kessler for giving me the opportunity to join his group, for the excellent research facilities, and for the high personal and academic freedom.

There are a lot of other people I would also like to thank:

- Stephan Lagleder, Franz Hagn, Udaya Kiran Marelli, and Oliver Demmer for sharing some nice years and *espressi* in our common office. Thank you, Uday and Stephan for critically reading my thesis and for all your constructive comments.
- Stephan Lagleder for the nice trips to the EUROMAR in Gothenburg and Florence.
- Anders Friberg for the many relaxing walks and coffees on the weekends in Schwabing.
- Florian Opperer, Lucas Doedens, Carles Mas-Moruno, Jayanta Chatterjee, Burkhardt Laufer, and Stefanie Neubauer for the synthesis of all the highly interesting *N*-methylated cyclic peptides I studied within this thesis.
- Franz Hagn, Stephan Lagleder, Sandra Groscurth, and Sylvain Tourel for showing me how to use all different sorts of biochemistry lab equipment.
- Oliver Demmer and Andreas Frank for their introduction to MD simulations in GROMACS.
- Andreas Frank, Jayanta Chatterjee, and Peter Kaden for interesting discussions about peptide structure and flexibility.
- Rainer Haeßner and Gerd Gemmecker for continuous maintenance of NMR spectrometers, for the fast and flexible help in case of rare serious problems with our network and for the help with and discussions about NMR pulse sequences.
- Titus Franzmann and Prof. Johannes Buchner for their continuous inspiration and motivation to continue working on Hsp26.
- Prof. Burkhard Luy, Manoj Nimbalkar, Franz Hagn, Andreas Enthart and Andreas Frank for practical help on the NMR spectrometers.
- Prof. Michael Sattler, Prof. Bernd Reif, Prof. Steffen Glaser and Prof. Burkhard Luy for continuous teaching of all aspects of NMR theory in ‘the NMR seminar’.

- The whole Sattler group, especially Gülden Demiraslan and Peijian Zou for organizing the biochemistry lab.
- My students Lisa Girschick, Evelyn Bender and Christopher Bayer for their support in studying Hsp26.
- Martha Fill, Sabrina Nietsch and Evelyn Bruckmaier for their support in all administration matters.
- All other group members for a wonderful time inside and outside the lab.
- Anders Friberg, Stephan Lagleder, the *Dancing Dingo* and many other people for the great time at EUROMAR 2009.

I am deeply grateful to my family, especially to my wife Miriam for her endless support and to Lilli for being there.

Parts of this thesis have been published:

Mas-Moruno, C.; Beck, J. G.; Doedens, L.; Frank, A. O.; Marinelli, L.; Cosconati, S.; Novellino, E.; Kessler, H.; Increasing αvβ3 Selectivity of the Anti-Angiogenic Drug Cilengitide by *N*-Methylation, *Angewandte Chemie International Edition* **2011**, 50, 9496-500.

Chatterjee, J.; Laufer, B.; Beck, J. G.; Helyes, Z.; Pintér, E.; Szolcsányi, J.; Horvath, A.; Mandl, J.; Reubi, J. C.; Keri, G.; Kessler, H.; *N*-Methylated sst_2 Selective Somatostatin Cyclic Peptide Analogue as Potent Candidate for Treating Neurogenic Inflammation, *ACS Medicinal Chemistry Letters* **2011**, 2, 509-14.

Doedens, L.*; Opperer, F.*; Cai, M.*; Beck, J. G.*; Dedek, M.; Palmer, E.; Hruby, V. J.; Kessler, H.; Multiple N-methylation of MT-II backbone Amide Bonds leads to Melanocortin Receptor Subtype hMC1R Selectivity: Pharmacological and Conformational Studies, *Journal of the American Chemical Society* **2010**, 132, 8115-28.
*: joint first authorship

Book chapter:

Beck, J. G.; Frank, A. O.; Kessler, H.; *NMR of Peptides*, in NMR of Biomolecules: Towards Mechanistic Systems Biology, Eds. Bertini, I., McGreevy, K., Parigi, G.; WILEY-VCH Verlag GmbH & Co. KGaA, Weinheim **2012**.

Previous publications:

Schwefel, D.; Maierhofer, C.; Beck, J. G.; Seeberger, S.; Diederichs, K.; Möller, H. M.; Welte, W.; Wittmann, V.; Structural Basis of Multivalent Binding to Wheat Germ Agglutinin, *Journal of the American Chemical Society* **2010**, 132, 8704-19.

Beck, J. G.; Mathieu, D.; Loudet, C.; Buchoux, S.; Dufourc, E. J.; Plant sterols in "rafts": a better way to regulate membrane thermal shocks, *FASEB Journal* **2007**, 21, 1714-23.

Contents

Abbreviations and Symbols

1D	one-dimesional
2D	two-dimensional
2QF	double-quantum filtered
3D	three-dimensional
3QF	triple-quantum filtered
Å	Ångstrøm
ACTH	adrenal cortical stimulating hormone
B_0	static magnetic field strength
bFGF	basic fibroblast growth factor
bp	basepair
Caco-2	a continuous line of heterogeneous human epithelial colorectal adenocarcinoma cells
cAMP	cyclic adenosine monophosphate
CATH	a semi-automatic, hierarchical classification of protein domains
CD	circular dichroism
CGRP	calcitonin gene-related peptide
COLOC	correlation by long-range coupling
COSY	correlation spectroscopy
CPD	composite-pulse decoupling
CSA	cyclosporin A
CVFF	consistent valence force field
CXCR4	C-X-C chemokine receptor type 4
Da	Dalton
DDD	distance driven dynamics
DG	distance geometry
DIPSI	decoupling in the presence of scalar interaction
DISCO	differences and sums of traces within COSY spectra
DISGEO	a distance geometry algorithm
DMSO	dimethyl sulfoxide
DNA	deoxyribonucleic acid
EASY	efficient adiabatic symmetrized
EC_{50}	half maximal effective concentration
ECM	extracellular matrix
E. coli	*Escherichia coli* (the host organism for the majority of work with recombinant DNA)
E.COSY	exclusive correlation spectroscopy
EDTA	ethylenediaminetetraacetic acid
EMBED	a distance geometry algorithm for modeling structures
et-NOESY	exchange-transferred NOESY
FDA	U.S. Food and Drug Administration
FPLC	fast protein liquid chromatography
fs	femtosecond
GDP	guanosine diphosphate
GH	growth-hormone
GI	gastrointestinal tract
GPCR	G protein-coupled receptor
G Protein	guanine nucleotide-binding protein

GRK	G protein-coupled receptor kinase
GROMACS	groningen machine for chemical simulations
GTP	guanosine triphosphate
γ	gyromagnetic ratio
HEK293	human embryonic kidney 293
HEPES	2-[4-(2-hydroxyethyl)piperazin-1-yl]ethanesulfonic acid
HETLOC	ω_1-filtered-TOCSY without heteronuclear decoupling
HMBC	heteronuclear multiple-bond correlation
hMC1R	human melanocortin receptor subtype 1
HMQC	heteronuclear multiple-quantum correlation
HPLC	high performance liquid chromatography
HSDD	hypoactive sexual desire disorder
Hsp26	a small heat shock protein from *S. cerevisiae*
HSQC	heteronuclear single-quantum correlation
Hz	Hertz
IC_{50}	half maximal inhibitory concentration
INEPT	insensitive nuclei enhanced by polarization transfer
IPTG	isopropyl β-D-1-thiogalactopyranoside
J coupling	scalar coupling
JS	jump-symmetrized
k_{ex}	exchange rate
LB	lysogeny broth
MALDI	matrix-assisted laser desorption/ionization
MAP	mitogen-activated protein
MD	molcular dynamics
MIDAS	metal ion-dependent adhesion site
MLEV	Malcolm Levitt's CPD sequence - a decoupling scheme
mM	millimolar
mS	millisiemens
MSH	melanocyte stimulating hormone
MT-II	Melanotan II
Ni-NTA	Ni^{2+}-nitilotriacetic acid
NMR	nuclear magnetic resonance
NOE	nuclear Overhauser enhancement
ns	nanosecond
nm	nanometer
OD	optical density
PAMPA	parallel artificial membrane permeation assay
PASTA	protein assignment by threshold accepting
PCR	polymerase chain reaction
PDE	phosphodiesterase
PDMS	poly(dimethylsiloxane)
P.E.COSY	Primitive E.COSY
Pfu	*Pyrococcus furiosus*
PH-PDMAA	dimethylacrylamide copolymer
PI3K	phosphatidylinositol 3-kinases
PKA	protein kinase A
PLC-β	phospholipase C β
POMC	proopiomelanocortin
ppm	parts-per-million

ps	picosecond
RCSB PDB	protein data bank of the research collaboratory for structural bioinformatics
RDC	residual dipolar coupling
RMSD	root-mean-square deviation
ROE	rotating-frame Overhauser effect
ROESY	rotating-frame Overhauser effect spectroscopy
sc+	+ synclinal
sc-	- synclinal
S. cerevisiae	*Saccharomyces cerevisiae*, bakers yeast
SCOP	structural classification of proteins
SDL	specificity determining loop
SDS-PAGE	sodium dodecyl sulfate polyacrylamide gel electrophoresis
SETTLE	an algorithm to constrain water in MD simulation
SHAKE	a time integration algorithm for MD simulation
sHsp	small heat shock protein
SOB	super optimal broth
SPC	simple point charge
SRIF	somatotropin release inhibitory factor (= somatostatin)
sst_2	somatostatin receptor subtype 2
T4	enterobacteria phage T4
TALOS	torsion angle likelihood obtained from shift and sequence similarity
TAE	Tris-acetate-EDTA
Taq	*Thermus aquaticus*
Tris	2-amino-2-hydroxymethyl-propane-1,3-diol
TOCSY	total correlation spectroscopy
TOF	time of flight
TROSY	transverse relaxation optimized spectroscopy
UV/Vis	ultraviolet-visible
VEGF	vascular endothelial growth factor
WATERGATE	water suppression by gradient-tailored excitation
X-rays	electromagnetic radiation, wavelength of 0.01 – 10 nm
µM	micromolar
µs	microsecond
σ	cross relaxation rate
τ_c	rotational correlation time
Φ, Ψ	backbone dihedral angles
χ	side-chain dihedral angles
ω	larmor frequency

1 Introduction

Since many decades, drug development is inspired by lead structures that are derived from secondary metabolites like nonribosomal peptides, terpenoids, sterols, alkaloids, natural phenols, and polyketides that were isolated from a huge variety of different biological sources. The structures of secondary metabolites evolved under selection pressure for interacting with biosynthetic enzymes and target proteins as these are their key interaction partners. While this evolutionary aspect does clearly indicate a high probability for biological activity of secondary metabolites, the preferred receptor binding capability of organic compounds with naturally occurring scaffolds was also demonstrated experimentally.[1] This supported a concept of privileged structures that are more likely to interact with proteins, than other organic molecules. The observation of a strongly restricted number of protein folds further underlines the plausibility of this concept. Only 1393 or 1233 unique folds were identified by structural classification of proteins according to the SCOP database[2] and the CATH database[3], respectively. As no more folds were described in the last three years according to RCSB PDB[4] statistics, the number of protein folds is smaller than suggested by the underlying diverse protein sequences. Following the concept of key and lock developed by Emil Fischer in 1894,[5, 6] the conformational space covered by proteins provides only a delimited number of locks and the structural space covered by secondary metabolites provides many of the useful keys. The huge screening efforts undertaken by some big pharmaceutical companies within the last decade might have yielded a smaller number of interesting new drugs or lead structures than possible, as the preferred regions of chemical space provided by secondary metabolites (keys) on the one hand, and protein folds on the other hand (locks), were not considered carefully enough.

In recent years, researchers became more and more interested in protein-protein interactions. Such interactions transmit external signals into cells and throughout the cytosol to the nucleus and other compartments, which makes them important for regulating all kinds of processes within cells, tissues, organs and throughout whole organisms. The most obvious inhibitors for distinct protein-protein interactions do not consist in secondary metabolites but in peptides that are often derived from interacting proteins, such as Enfuvirtide[a][7], Cilengitide[b][8, 9], or Eptifibatide[c][10].

---

[a] Enfuvirtide is an HIV fusion inhibitor that is built up of amino acid residues 643–678 of HIV-1_{LAI} gp160.
[b] Cilengitide is an anti-cancer drug that inhibits angiogenesis. It was derived from the RGD motive found in many natural integrin binding proteins.
[c] Eptifibatide is an antiplatelet drug that was derived from barbourin, a protein found in snake venom that contains the KGD motive.

Although peptides do often not follow Lipinski's[11] and Veber's[12] rules for the evaluation of druglikeness, they have general advantages with respect to other drugs. Among these are a generally high activity and specificity, a low tendency for drug-drug-interactions and for tissue accumulation as well as a low toxicity.

However, the name *peptide* originates from the greek term πεπτος (*peptos*) meaning *digestible*. Low stability of peptides with respect to hydrolysis is indeed an important drawback for the application of peptides as drugs. The low oral bioavailability and an increased risk for immunogenic effects makes the development of peptides as therapeutics even more challenging. As the production of larger peptides like Enfuvirtide (36 amino acid residues) by solid-phase peptide synthesis is rather expensive, economic factors also delimit the utilization of peptides as drugs.

Numerous methods for improving peptides with respect to their applicability as drugs were developed. The inclusion of D-amino acid residues leads to increased stability with respect to proteases. Exchange of all residues by the corresponding D-amino acid residue, reversal of the peptide sequence and the combined application of both techniques yields inverso, retro[13] and retro-inverso[14-18] peptides, respectively. "Shifting" of amino acid side-chains by one position from the α carbon to the amide nitrogen atoms results in highly *N*-methylated glycin oligomers, so called peptoids. These possess less hydrogen bond donors than the according peptides and usually more favorable bioavailability profiles.[19,20] Additionally, peptide groups may be substituted by ester, sulfonamide, thioamide, sulfoxide, ethenylene, reduced amide, azapeptide and many other groups. The introduction of such peptide bond mimetics is accompanied by severe steric and electronic effects that do not only affect the close surrounding of the peptide bond, but also have pronounced effects on the overall peptide conformation. The sulfonamide group, for example, has a preferred dihedral angle of +/- 90°, which is exactly between *cis* (0°) and *trans* (180°) of peptide bonds. Therefore, activity and selectivity profiles are often biased strongly when peptide bond mimetics are introduced.

Cyclic (*N*-methylated) peptides containing D-amino acid residues do often possess distinct preferred conformations, that are in case of high receptor affinity usually also conserved in the receptor bound state. As discussed in more detail in chapter 4, such peptides are also very likely to overcome the problem of low oral bioavailability that provides the biggest limitation for a more widespread development of peptide therapeutics.

In recent years, the market for synthetic therapeutic peptides rose from € 5.3 billion in 2003 to € 8 billion in 2005.[21] According to a recent study the number of peptide drugs entering clinical trials grew from 0.3 peptides per year in the 1960s to 16.8 per year between 2000 and 2008.[22] In 2009, 75 therapeutic peptides had entered the European, American and / or Japanese market.[21] At least four (Glatiramer acetate, leuprolide acetate, goserelin acetate and octreotide acetate) have reached sales of $ 1 billion.[22]

The recent success of peptide drugs also inspired the research presented in the following chapters. The structures and dynamics of highly potent and receptor subtype selective *N*-methylated cyclic peptides targeting distinct subtypes of melanocortin receptors, somatostatin receptors and integrins are presented in chapter 2.2, chapter 2.3, and chapter 3, respectively. The determination of highly Caco-2[d,][23] permeable *N*-methylated cyclohexapeptide scaffolds, that may serve as structural templates for designing orally bioavailable peptide drugs is presented in chapter 4.

In chapter 5, the rational design, resonance assignment and CD spectroscopic investigation of a monomeric deletion protein of the small heat-shock protein Hsp26 from *S. cerevisiae* is presented. As the investigation of Hsp26 is rather different from the conformational analysis of peptides presented in all other chapters, an introduction to this project is given at the beginning of chapter 5.

[d] The term 'Caco-2' refers to a continuous line of heterogeneous human epithelial colorectal adenocarcinoma cells.

Chapter 1.1 and subchapters thereof are adapted in part from Beck, J. G.; Frank, A. O.; Kessler, H.; *NMR of Peptides*, in NMR of Biomolecules: Towards Mechanistic Systems Biology, Eds. Bertini, I., McGreevy, K., Parigi, G.; WILEY-VCH, Weinheim **2012**.

1.1 Structure and Dynamics of Peptides

Linear peptides are often flexible in solution and the underlying conformational exchange is usually fast on the timescale of chemical shifts for both, backbone and side-chain conformers. In this respect, peptides differ remarkably with respect to most proteins. While only 30 % of eukaryotic proteins are completely or partially disordered,[24] naturally occurring linear peptides with typical lengths of 5-40 residues do usually not adopt distinct backbone conformations in their natural (aqueous) environments. The flexibility of linear peptides also complicates the determination of their preferred bioactive conformations. These can be very different from any preferred solution conformation and every attempt to determine such conformations in another environment than their receptor is likely to yield functionally irrelevant structures.

The crystallization of many peptides is hindered by their high flexibility (exceptions are peptides with high Pro content). Moreover, small molecules have a relatively large surface and their conformation therefore more strongly depends on the environment (solvent, crystal, receptor binding). X-ray crystallography, which is the most used method for the determination of protein structures, is therefore less relevant for peptide structures. NMR spectroscopy has proven to be the most important technique for the investigation of the conformation and flexibility of peptides.

Chemically synthesized peptides are usually obtained with natural isotope abundance of ^{1}H, ^{13}C, and ^{15}N. Synthesis with high enrichment of ^{13}C and ^{15}N is expensive and usually avoided for peptides. However, fast tumbling and a small number of resonances lead to well-resolved NMR signals with little overlap, especially in constrained peptides. Therefore, sophisticated three-dimensional NMR experiments as used for ^{13}C- and ^{15}N-enriched proteins are rarely used for peptides.

Accordingly, one set of signals is observed in NMR spectra of linear peptides reflecting all the different fast exchanging states. Many structure investigation protocols are aimed at finding a single conformation that fulfills all the spectroscopically derived conformational restraints. These protocols fail to produce ensembles of conformations that reflect the peptides flexibility, as each single conformation is forced to fulfill all experimental restraints within the structure calculation process.

As the number of different populated states of a flexible linear peptide can be very high and may even exceed the number of experimentally derived restraints, an

extensive and precise description of its conformers and their populations may be very difficult to obtain. Due to the fact that only in the binding process a flexible peptide will adopt its bound conformation, a detailed description of the “preferred conformation” in solution as the bioactive conformation is useless or incorrect.

1.1.1 Cyclopeptide Conformations by NMR Spectroscopy

When peptides are cyclized, their conformational space is strongly reduced. Furthermore, backbones of cyclopeptides with chain lengths of up to six amino acid residues are often found to populate a distinct preferred conformation, at least in part of the cycle. Preferred backbone conformation is usually accompanied by preferred side-chain conformations (χ_1 dihedral angle). This shows that individual side-chain conformations may be stabilized when a strongly preferred backbone and neighboring residues provide a suitable environment. A precise description of their backbone structure and of their (side-chain-)conformer populations is often possible by combining NMR spectroscopy, distance geometry calculations and extensive MD simulations in explicit solvent. Even if few fast exchanging conformers are present, the identification of the conformers and their relative populations is possible if the averaging is carefully taken into account.[25]

1.1.2 Resonance Assignment

Peptide resonances are assigned in a three step process. Groups of scalar coupled protons are first identified from 2D TOCSY and 2D COSY spectra and assigned to distinct amino acid types according to their chemical shifts and constitutions (identification of amino acids). In a second step, the amino acid types are assigned to the peptide sequence using heteronuclear $^{1}J_{CH}$, $^{2}J_{CH}$ and $^{3}J_{CH}$ correlations from HSQC and HMBC spectra (sequential assignment). In the last step, stereospecific assignments of diastereotopic methylene protons and methyl groups are established, which are mostly based on homo- and heteronuclear ^{3}J coupling constants. Complete assignments of ^{13}C and ^{1}H resonances of peptides should be achieved via through-bond homo- and heteronuclear correlation experiments and not by spatial correlation experiments like ROESY, in order to avoid bias by mixing assignment and determination of stereostructure. The risk for misassignment of spin systems from NOEs is especially high for peptides that contain multiple similar residues. NOEs should therefore only be used for the determination of the conformation, not for assignments (constitution and diastereotopy).

Following this three-step process, protons are first grouped into spin systems in such a way that every single proton is assigned to a specific spin system (identified from COSY and TOCSY spectra) if at least one other proton of the same system is no more than three bonds apart. J_{HH} couplings across the peptide bond are usually not observed. Accordingly, protons from different amino acids are always assigned to different spin systems. The aromatic amino acids, as well as several others (Arg, Asn, Gln, and Met), consist of more than one spin system due to the fact that at least one of the protons within these residues is more than three bonds apart from all other protons. Several proton spin systems, such as AMXY in aromatic amino acids (or in Asn and Asp), occur in several amino acids and their identifications do not give rise to an immediate assignment to a distinct amino acid. However, heteronuclear long-range information to ^{13}C and from there to more distal spin systems, as obtained from HMBC, can connect spin systems. This is demonstrated in the example HMBC spectrum of Figure 1.1 for a Trp and a His residue.

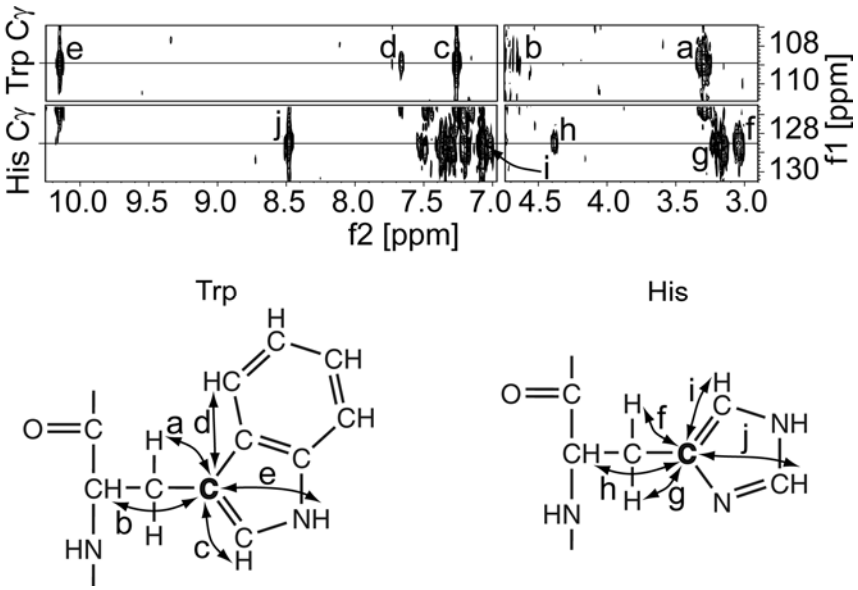

Figure 1.1: Example HMBC experiment: Signals connect distal spin systems in the His and Trp side-chains of MT-II via correlations to C^{γ} with the core spin system (H^{N}, H^{α}, $H^{\beta`}$, $H^{\beta``}$). The small letters a-j in the spectra designate correlations between distinct protons and C^{γ}, as given in the chemical structures of both amino acid residues. Note that the γ carbon of Trp is strongly high-field shifted.

When a peptide contains multiple identical residues and if intraresidual scalar couplings are the only couplings considered, the unambiguous assignment of all spin systems is prevented. Heteronuclear ^{2}J and ^{3}J correlations from the carbonyl carbon to the amide, α and β protons in the same amino acid and to the amide and a proton

of the adjacent amino acid yield the required sequence information[26] that is commonly obtained from HMBC spectra[27] (Figure 1.2).

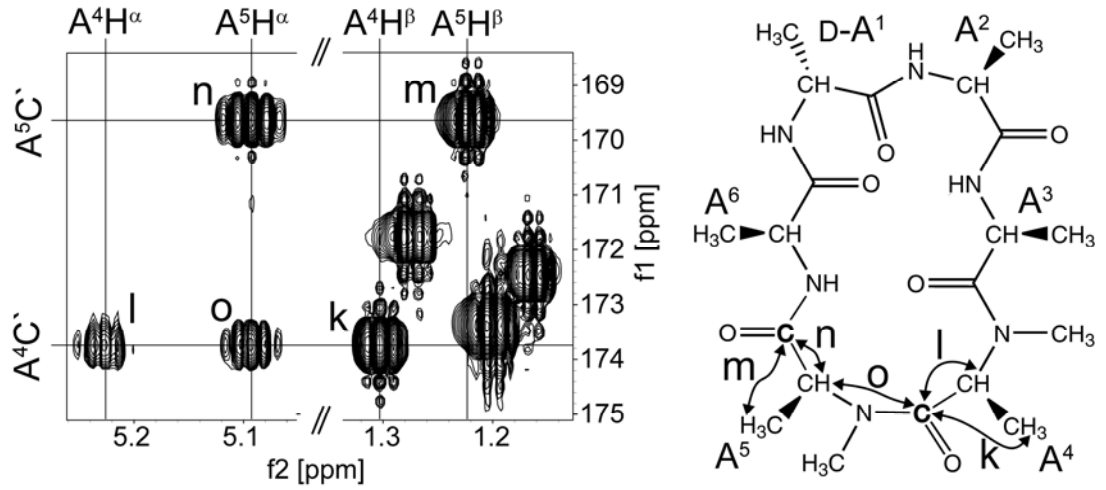

Figure 1.2: Sequential assignment as derived from an example HMBC spectrum of the cyclohexylalanine peptide cyclo(-D-Ala-Ala-Ala-MeAla-MeAla-Ala-). The small letters (k-o) in the spectrum (left) correspond to the accordingly labeled correlations in the chemical structure (right). The $^{13}C'$ resonances were first assigned to the individual spin systems via the intraresidual HMBC cross-peaks k, l and m, n, respectively. The sequential assignment was derived from the interresidual HMBC cross-peak (indicated as o) that links the spin systems in the given order.

Diastereotopic assignments of methylene protons are usually obtained by evaluating homo- and heteronuclear ^3J coupling constants from the protons of interest to neighboring hydrogen and carbon atoms as shown in Figure 1.3 for the example of the β protons in non-β-branched L- and D-amino acid residues. Another procedure for the assignment of diastereotopic protons or groups (by NOE or ROE, alone or in combination with J couplings) is most often used for proteins. However, it is believed that this cannot be used for peptides, because the number of NOEs (or ROEs) for peptides is usually much smaller and the system is underdetermined. ROEs should be reserved for stereostructure determination only. Experimentally derived restraints can be referred directly to distinct diastereotopic protons or methyl groups if the according assignments are available. In peptide structure investigations that are performed without diastereotopic assignments, restraints have to be referred to pseudoatoms (with large size), which generally decreases the precision and accuracy of structure calculations.

For the assignment of β protons, the populations of the three staggered χ_1 rotamers *sc-*, *sc+* and *trans* must be taken into account as the $^3J_{H\alpha\text{-}H\beta}$ and $^3J_{C'\text{-}H\beta}$ coupling constants used for stereospecific assignments depend on the populations of the χ_1

rotamers (Figure 1.3).[28] If only the *sc*- rotamer is populated in L-amino acid residues, $^3J_{H\alpha\text{-}H\beta proR}$ is large (12-14 Hz), while the other coupling constants are small (2–4 Hz for $^3J_{H\alpha\text{-}H\beta proS}$ and 1–2 Hz for the two $^3J_{C'\text{-}H\beta}$ coupling constants). If only the *trans* rotamer is populated, $^3J_{H\alpha\text{-}H\beta proS}$ and $^3J_{C'\text{-}H\beta proR}$ are large (12-14 Hz and 7-9 Hz, respectively), whereas $^3J_{H\alpha\text{-}H\beta proR}$ and $^3J_{C'\text{-}H\beta proS}$ are small, (2–4 Hz and 1–2 Hz, respectively). A high population of the *sc*+ rotamer is rarely observed in L-amino acid residues due to the close contact of the sterically demanding side-chain with the carbonyl and the amide group of the backbone. In the case of exclusive population of the *sc*+ rotamer, only $^3J_{C'\text{-}H\beta proS}$ is large (7–9 Hz), while the other coupling constants are small (2-4 Hz for the two $^3J_{H\alpha\text{-}H\beta}$ coupling constants and 1–2 Hz for $^3J_{C'\text{-}H\beta proR}$). For D-amino acid residues, similar characteristic patterns of homo- and heteronuclear $^3J_{H\alpha\text{-}H\beta}$ and $^3J_{C'\text{-}H\beta}$ are observed for the individual rotamer states (Figure 1.3).

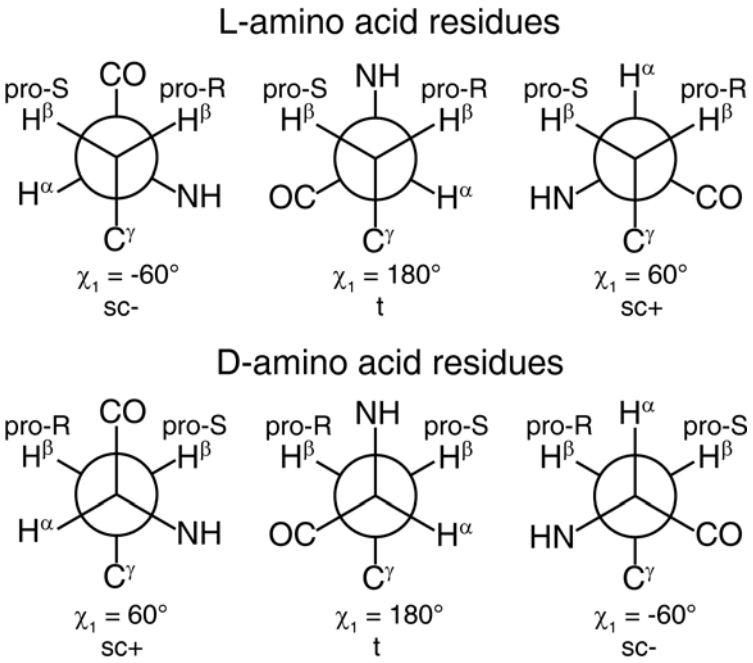

Figure 1.3: Diastereotopic assignments of *β*-hydrogen atoms. A: χ_1 rotamers and the according $^3J_{H\alpha\text{-}H\beta}$ and $^3J_{C'\text{-}H\beta}$ coupling constants of L- and D-amino acid residues as considered in the assignment process. The prochirality of the β protons is inverted for residues Asn, Asp, Cys, His, Met and Ser as for these residues, the priority of the more distal parts of the side-chains is higher than the priority of the peptide backbone.

In non-β-branched amino acid residues, $^3J_{H\alpha\text{-}H\beta proR}$, $^3J_{H\alpha\text{-}H\beta proS}$, $^3J_{C'\text{-}H\beta proR}$, and $^3J_{C'\text{-}H\beta proS}$ coupling constants depend on the populations of the *sc*-, *t* and *sc*+ rotamers ($p_{sc\text{-}}$, p_t and p_{sc+}) and on the coupling constants $^3J_{sc}$ and ^3J_t, which indicate whether the underlying nuclei are in *synclinal* or *trans* orientation with respect to each other, as shown in equations 1.1–1.4.[29]

$$^3J_{H\alpha-H\beta proR} = p_{sc-}\,^3J_t + p_t\,^3J_{sc} + p_{sc+}\,^3J_{sc} \qquad (1.1)$$

$$^3J_{H\alpha-H\beta proS} = p_{sc-}\,^3J_{sc} + p_t\,^3J_t + p_{sc+}\,^3J_{sc} \qquad (1.2)$$

$$^3J_{C`-H\beta proR} = p_{sc-}\,^3J_{sc} + p_t\,^3J_t + p_{sc+}\,^3J_{sc} \qquad (1.3)$$

$$^3J_{C`-H\beta proS} = p_{sc-}\,^3J_{sc} + p_t\,^3J_{sc} + p_{sc+}\,^3J_t \qquad (1.4)$$

Typical values for homonuclear (heteronuclear) $^3J_{sc}$ and ^3J_t in equations 1.1–1.4 are 2.6 Hz (1.4 Hz) and 13.6 Hz (8.5 Hz), respectively. If a set of four $^3J_{H\alpha\text{-}H\beta}$ and $^3J_{C'\text{-}H\beta}$ coupling constants was determined, the diastereotopic assignment is derived by solving the system of equations 1.1–1.4. The χ_1 rotamer populations are automatically obtained along with the diastereospecific assignments. Coupling constants are usually obtained from E.COSY, by quantitative J correlation, by forming differences and sums of traces within COSY spectra (DISCO), from phase-sensitive HMBC spectra and from ω_1-filtered TOCSY experiments (HETLOC). These techniques are described below in chapter 1.1.4.

1.1.3 Extraction of Precise Distances from ROESY Spectra

ROESY[30] and NOESY cross-peak intensities depend on transversal (σ_{xy}, equation 1.5) or longitudinal (σ_z, equation 1.6) cross relaxation rates, respectively. Proton distances may therefore in principal be derived from ROESY or NOESY experiments (Figure 1.4).

$$\sigma_{xy} = u_2 - u_0 = \frac{\gamma^4 h^2 \tau_c}{4\pi^2 10 r^6}\left(\frac{3}{1+4\varpi^2\tau_c^2} + 2\right) \qquad (1.5)$$

$$\sigma_z = W_2 - W_0 = \frac{\gamma^4 h^2 \tau_c}{4\pi^2 10 r^6}\left(\frac{6}{1+4\varpi^2\tau_c^2} - 1\right) \qquad (1.6)$$

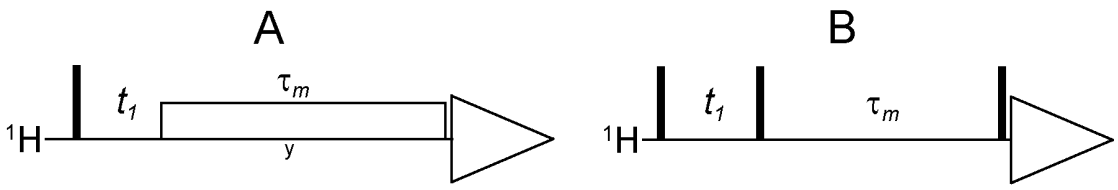

Figure 1.4: Basic 2D ROESY (A) and 2D NOESY (B) pulse sequences.

The bracketed terms of equations 1.5 and 1.6 show in which way the sign of σ_z and σ_{xy} depends on τ_c. σ_z is positive for very small molecules with a low molecular correlation time τ_c. Its sign changes when $\tau_c \approx 1.12\ \omega^{-1}$ and remains negative when $\tau_c > 1.12\ \omega^{-1}$. In contrast, σ_{xy} is always positive and nearly independent of τ_c. The molecular correlation times of peptides under common experimental conditions are often close to ω^{-1} and NOESY cross-peaks are very small or invisible. Because the ROE does not change its sign, ROESY spectra are generally preferred in peptide NMR studies, especially for small peptides with molecular weights equal to or lower than 1-2 kDa.

It is obvious from equation 1.5 that σ_{xy} depends on the inverse sixth power of the distance (r^{-6}) of two interacting protons. This suggests that the distance r_{ij} between protons i and j is easily obtained from ROESY spectra if a reference intensity (I_{ref}), and the corresponding reference distance (r_{ref}, e.g. between geminal protons (1.78 Å) or between aromatic protons) are available (equation 1.7).

$$r_{ij} = r_{ref} \cdot \sqrt[6]{\frac{I_{ref}}{I_{ij}}} \qquad (1.7)$$

However, this simple relation between peak intensity is valid only under certain limitations. Spin diffusion, spin-lock resonance offset effects and magnetization transfer by other mechanisms than transversal cross relaxation may affect cross-peak intensities strongly or even give rise to “false” cross-peaks. In order to derive precise distances, the following points should be considered carefully.

Initial rate approximation: The ROESY mixing time should be kept ≤ 150 ms to guarantee for an almost linear increase of the cross-peak intensities throughout the mixing time. On the other hand, weak cross-peaks may vanish when too small mixing times are applied and mixing times should thus be kept above 50 ms.

Offset effects: During ROESY spin-lock, the B_1 field (γB_1) has to be strong enough to lock even spins with pronounced offsets (Ω) efficiently. The effective angle of the spin-lock axis with respect to the z-axis (θ) is given in equation 1.8.

$$\theta = \arctan\left(\frac{\gamma B_1}{\Omega}\right) \qquad (1.8)$$

The offset dependent intensity loss (k_{ij}) of a cross-peak between two protons i and j depends on the angles of the spin-lock axis θ_i and θ_j with respect to the z-axis. If $\tau_c \approx \omega_0^{-1}$, k_{ij} is given by equation 1.9[31] and compensated cross-peak intensities I^{oc} are obtained by dividing the original cross-peak intensities I_{ij} and I_{ref} by k_{ij} (equation 1.10).

$$k_{ij} = \sin\theta_i \sin\theta_j \qquad (1.9)$$

$$I_{ij}^{oc} = \frac{I_{ij}}{k_{ij}} \qquad (1.10)$$

If k_{ij} is significantly smaller than 1, offset compensated distances r^{oc} are obtained from offset compensated cross-peak intensities I^{oc} (equation 1.11).

$$r_{ij}^{oc} = r_{ref} \sqrt{\frac{I_{ref}^{oc}}{I_{ij}^{oc}}} \qquad (1.11)$$

TOCSY artifacts are inseparably connected to ROESY experiments.[32] TOCSY artifacts appear in ROESY spectra if magnetization transfer via homonuclear J couplings is not fully suppressed. This is the case along the diagonal and antidiagonal, where the strongest TOCSY cross-peaks are observed in conventional ROESY spectra. While a weak B_1 field decreases TOCSY artifacts, it increases undesired offset effects. Optimization of a ROESY experiment for suppressing either TOCSY artifacts or offset effects will thus go along with an increase of the respective other undesired effect.

TOCSY artifacts may originate from one or multiple subsequent J transfers between two protons within the same spin system (Figure 1.5 B) or from subsequent cross relaxation and J transfer steps (Figure 1.5 C).

Cross-peaks originating from sole J transfer are of opposite sign with respect to the originate ROESY cross-peaks and thus identified easily. If cross-peaks result from a mixture of cross relaxation and J transfer between the two underlying nuclei, their sign may be either negative or positive, depending on the relative strength of both transfers (Figure 1.5 B). In case of a significant but not quantifiable contribution of J transfer, such cross-peaks may not be used for calculating distances. Therefore, special care has to be taken when reference intensities (equations 1.7 and 1.11) are derived from cross-peaks between geminal protons (Figure 1.5 B). Misinterpreting

such reference cross-peaks as exclusively “ROE” will bias any other distance information derived from the according spectrum.

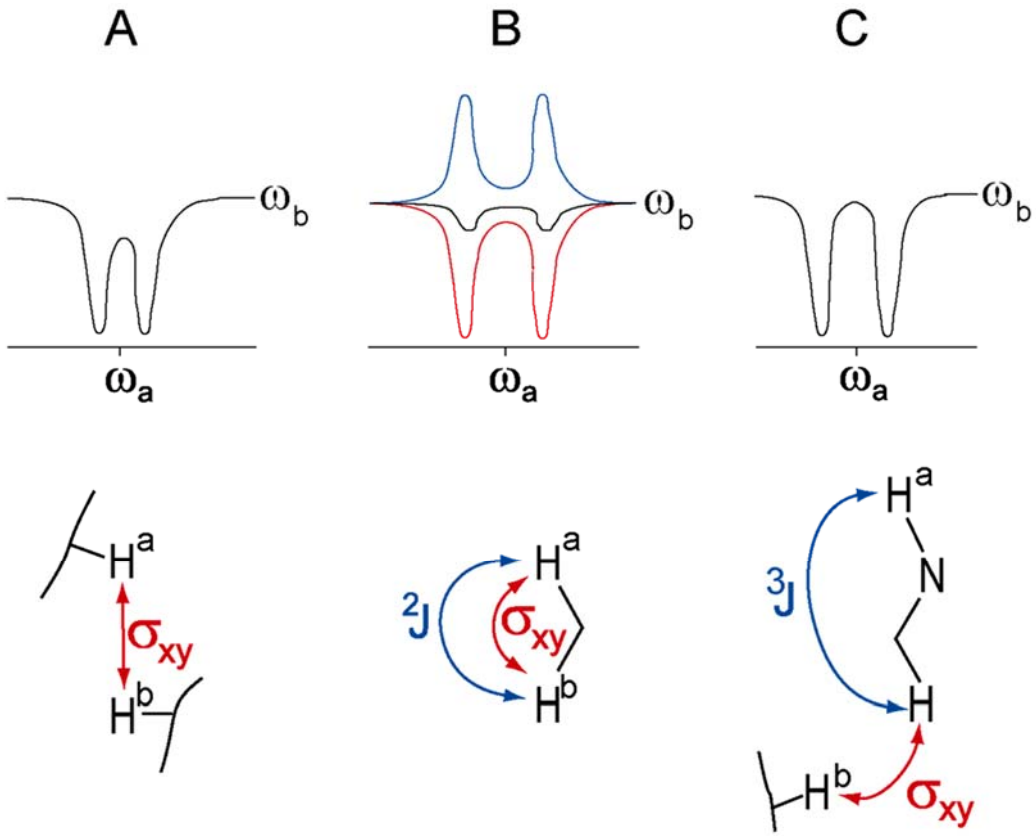

Figure 1.5: 2D ROESY spectra slices (black doublets, top) for three spin pairs Ha, Hb in three different geometries. A: Ideal cross-peak resulting from transversal cross relaxation (red arrow) exclusively. B: Cross-peak (black slice) of geminal protons that originates from a mixture of J transfer (blue slice and arrow) and transversal cross relaxation (red slice and arrow). C: Cross-peak between protons that are coupled by subsequent cross relaxation (red arrow) and J transfer (blue arrow) via a relayed spin.

The subsequent transfer via J coupling and cross relaxation or vice versa from one spin via a second spin to a third spin leads to cross-peaks that have the same sign as cross-peaks that originate from pure cross relaxation (Figure 1.5 C). Such cross-peaks may indicate close proximity of distant spins and thus, distance restraints derived from such cross-peaks may be incorrect. If spins are locked by continuous irradiation at a single frequency, TOCSY artifacts occur when the scalar coupled nuclei have similar chemical shifts or are disposed symmetrically from the transmitter frequency.

Overall, precise distances may be obtained from ROESY cross-peak intensities, when spin diffusion is small, offset effects are compensated for correctly and J-coupling effects are considered. Eliminating such effects allows for the calculation of even more exact distances from ROESY cross-peaks. Splitting the spin-lock in two

off-resonance mixing periods that are symmetrically placed above and below the proton resonances (JS-ROESY)[33] as well as sweeping the frequency of the spin-lock field through the spectrum[34] have proven successful in reducing undesirable offset effects and J transfer. JS-ROESY was recently optimized with adiabatic pulses in order to simplify the laborious setup.[35]

However, conventional ROESY and compensated ROESY experiments with mixing times of 100 - 150 ms have proven successful for the determination of inter proton distances in cyclic peptides with errors of about +/- 10 %. Furthermore, JS-ROESY experiments such as the recently published EASY-ROESY[35] will likely further improve the quality of distance information obtained in the structure investigation of peptides, especially with respect to J-coupling artifacts.

1.1.4 Extraction of Dihedral Angles from ^{3}J Couplings

^{3}J scalar coupling constants are often considered in the investigation of peptide structures as they are strictly related to dihedral angles by the Karplus-equation (equation 1.12).[28]

$$^3J = A\cos^2(\Phi`) + B\cos(\Phi`) + C \qquad (1.12)$$

In equation 1.12, $\Phi`$ is the dihedral angle. A, B and C are empirically derived parameters that depend on the coupled nuclei and their environment. These parameters have been calculated for the homo- and heteronuclear coupling constants of many nuclei in virtually all environments relevant to peptide structural investigation.

In NMR spectra of most peptides, narrow lines and low signal overlap enable the extraction of coupling constants from various multiplet patterns. In favorable cases, coupling constants can be read directly from multiplets in 1D ^{1}H NMR spectra. This, however, is restricted in many peptides to $^3J_{HN\text{-}H\alpha}$ coupling constants which are obtained from the amide proton resonance doublet splittings. The measurement of couplings between other nuclei (i.e. $^3J_{H\alpha\text{-}H\beta}$) is impeded by couplings to other protons that lead to complex multiplet structures. COSY cross-peaks, for example, show a characteristic multiplet pattern with antiphase splitting by the active coupling and in-phase splittings by couplings to other protons. Overlap usually leads to partial or full cancellation of individual lines, which renders the direct extraction of coupling constants from COSY cross-peaks impossible. A reduction of the number of multiplet

lines in COSY multiplets can suppress this overlap and allow for the extraction of numerous coupling constants. This is most commonly achieved by exclusive correlation spectroscopy (E.COSY)[36,37], by P.E.COSY[38], or by forming the differences or the sums of cross signals in COSY (DISCO)[39-41].

E.COSY spectra (Figure 1.6 A) are usually detected by the addition of 2QF-COSY spectra and 3QF-COSY spectra within one 2D experiment by consecutive double- and triple-quantum filtering, which is achieved by appropriate phase cycling. The sign of half of otherwise identical 2QF- and 3QF-multiplet components is inverted. When 2QF spectra and 3QF spectra are added, these components cancel to zero intensity and the simplification of the crosspeak multiplets is achieved. It is important to note that the 3QF component is less sensitive than the 2QF component and is therefore detected with a higher number of scans to compensate for the intrinsic intensity difference of these two components. 4QF is rarely considered in E.COSY spectra as the 4QF-COSY is even less sensitive than the 3QF-COSY and leads to increased measurement times. The potential problem of reading splittings as coupling constants that are too large from antiphase signals and too small from in-phase signals of partially overlapping peaks[42] is solved by E.COSY if J couplings are read as in-phase splittings of multiplet components that are separated in both dimensions (see Figure 1.6 A for the extraction of Hα-Hβ couplings).

The DISCO technique is based on cross-sections that are extracted from COSY spectra, usually from 2QF-COSY spectra. These are extracted along the direct dimension from crosspeaks in such a way that the multiplet splittings are obtained at the highest possible intensity. Similar to the underlying crosspeaks, each cross-section will be split in anti-phase by the active coupling that gave rise to the respective crosspeak and in-phase by the inactive couplings to all other coupled nuclei. If two appropriate slices are added, a simplified multiplet with beneficial properties can be obtained (Figure 1.6 B). The number of multiplet lines is reduced to half the number within the original slices, with antiphase splittings that are equal to the sum of the antiphase splittings in the two original slices, whereas in-phase splittings are conserved. Differences between slices can also be obtained that are similar to their sums, with the exception that the anti-phase splitting is equal to the difference of those of the original slices. Errors may arise from incorrect scaling of the cross-sections in such a way that half of the lines do not fully disappear. The extraction of $^3J_{H\alpha\text{-}H\beta'}$, $^3J_{H\alpha\text{-}H\beta''}$ and $^3J_{H\beta'\text{-}H\beta''}$ of Asp in a fourfold *N*-methylated analog of the alpha-melanocyte stimulating hormone (α-MSH)[43] is demonstrated in

Figure 1.6 B based on f2 traces of four crosspeaks in a 2QF-COSY spectrum. While DISCO is not used very often any more, it is still very useful for small peptides.

E.COSY and DISCO proved to be useful for the determination of homonuclear scalar coupling constants in many peptide studies. For a discussion of other techniques such as P.E.COSY,[38] the reader can refer to an earlier review article.[42]

Heteronuclear ^2J and ^3J coupling constants have an importance similar to that of their homonuclear counterparts in NMR studies of peptides. Numerous techniques for the determination of these coupling constants have therefore been developed. Nevertheless, their determination is usually more complicated than the determination of homonuclear coupling constants.

In the direct dimension, peaks in phase-sensitive HMBC spectra are split in anti-phase by the underlying active $^2J_{CH}$ or $^3J_{CH}$ couplings. Because of this, these heteronuclear couplings can, in principle, be determined from HMBC spectra. During the delay Δ of the HMBC experiment (Figure 1.6 C), transversal proton magnetization evolves under the coupling to ^{13}C, under homonuclear proton couplings, and at a proton specific offset. The homonuclear couplings and the proton-specific offset lead to signal distortions that overlap with the $^3J_{CH}$ couplings to be determined. For this reason, it is impossible to read $^3J_{CH}$ couplings directly by eye from HMBC multiplets. The Titman-Keeler method[44] provides a way for the extraction of these heteronuclear coupling constants from HMBC multiplets by fitting each HMBC multiplet with an appropriate reference multiplet from a reference spectrum (Figure 1.6 C). Reference multiplets must have the same distortions from evolution under homonuclear couplings and offset. Therefore, reference spectra like TOCSY or HSQC must be detected with an additional delay Δ and with the same transmitter frequency as the HMBC spectrum to be fit. The long range J_{CH} coupling constant is obtained as one of two parameters to be optimized in the fitting procedure. Fitting requires two identical reference multiplets that are shifted by trial couplings, subtracted from each other and adapted to the intensity of the HMBC multiplet. Overlays of a slice taken from an HMBC C'-Hβ crosspeak with slices that were calculated from a reference spectrum with different trial $J_{C'\text{-}H\beta}$ coupling constants are shown in Figure 1.6 C.

The ω_1-filtered TOCSY experiment (HETLOC)[45-47] which is also routinely used for measuring heteronuclear ^2J and ^3J coupling constants, differs from a conventional TOCSY experiment in a filter, which only allows ^{13}C or ^{15}N bound protons to enter t_1. Crosspeaks are observed between protons that belong to the same spin system, just as in a normal TOCSY experiment. Since no pulses are applied to the heteronuclei

from the beginning of t_1, the spin state of each heteronucleus is identical during t_1 and t_2. Therefore, only connected transitions contribute to the crosspeaks and multiplet patterns are of E.COSY type. The splitting of an H^N-H^α crosspeak in a ^{15}N-HETLOC spectrum[48] is shown in Figure 1.6 D. In the direct dimension, the splitting corresponds to the small heteronuclear multiple bond coupling constant of interest ($^3J_{HN\text{-}H\alpha}$). In the indirect dimension, the signal is split by the huge single bond coupling constant. The large splitting in the latter separates the two lines and allows for reading the small multiple bond coupling constant in the direct dimension even if linewidths are large. Only long range couplings to heteronuclei with directly bound protons can be determined from ω_1-filtered TOCSY experiments.

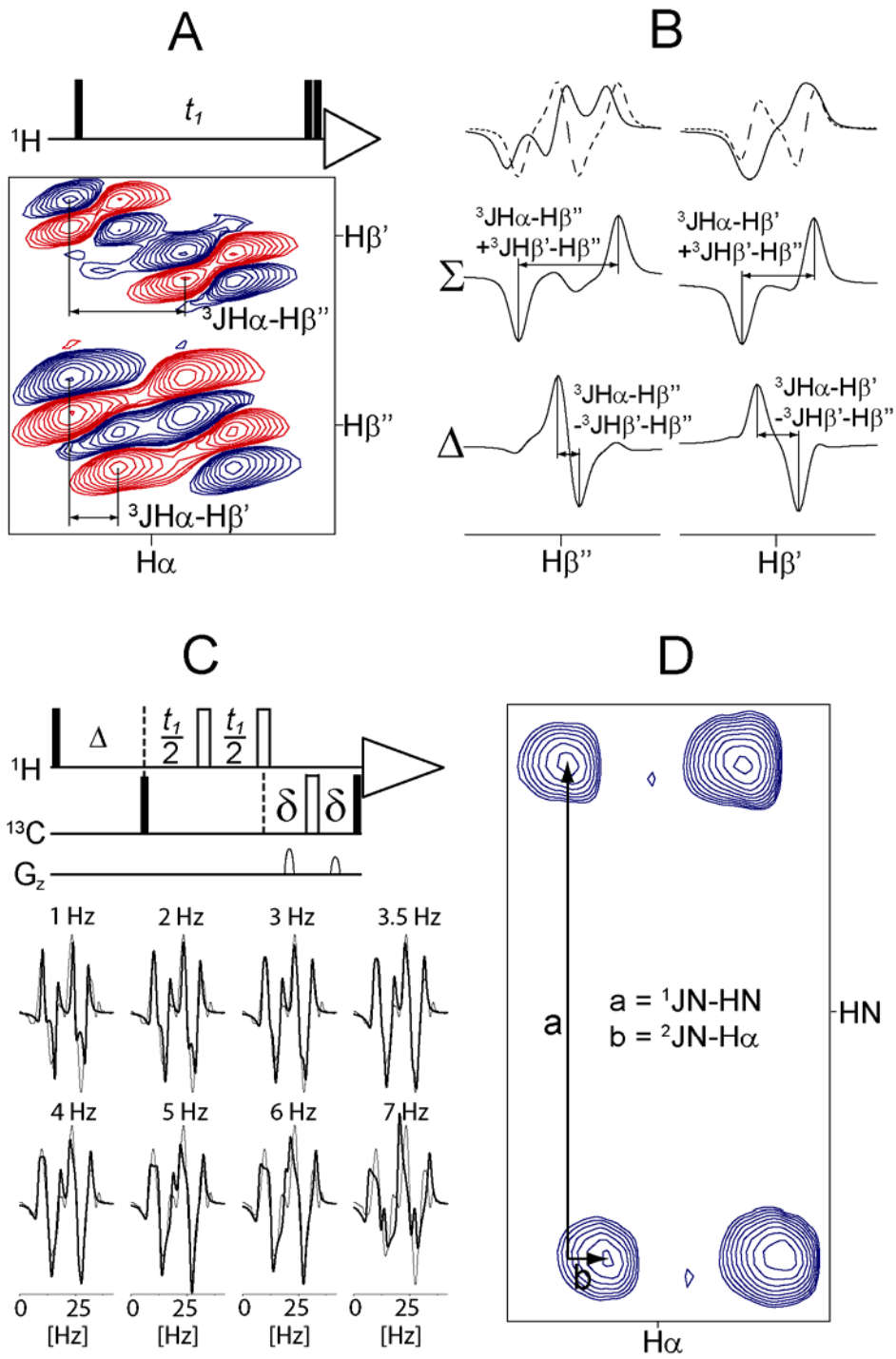

Figure 1.6: A: nQF-COSY pulse sequence. Appropriate phase cycling can provide sums of i. e. 2QF and 3QF-COSY, resulting in characteristic E.COSY multiplet patterns as shown below for a *N*-methylated Trp residue within (Ac-Nle-cyclo(5β→10ε)(Asp^5-MeHis^6-D-Phe^7-MeArg^8-MeTrp^9-MeLys^{10})-NH_2). Couplings are preferably read from appropriately chosen in-phase splittings, as demonstrated in the example experiment here, not from antiphase splittings which would result in an overestimation of the couplings. B: DISCO procedure for determining Asp_5 $^3J_{H\alpha-H\beta}$ couplings in the same peptide using the following cross sections of four 2QF-COSY crosspeaks: Left, solid line: $H^{\beta'}$(f1)-$H^{\beta''}$(f2), dashed line: H^{α}(f1)-$H^{\beta''}$(f2); right, solid line: $H^{\beta''}$(f1)-$H^{\beta'}$(f2), dashed line H^{α}(f1)-$H^{\beta'}$(f2)). Cross sections were extracted along the direct dimension. Sums and differences of J couplings that are read from antiphase splittings in the sums (Σ) and differences (Δ) of these traces are given below. C: Phase sensitive HMBC with gradient pulses. Multiplets like the H^{β}-C' (thin line) superimposed with reference spectra using

different trial coupling constants of 1-7 Hz (bold line) clearly suggest a coupling constant of 3-4 Hz in the example shown here. D: Part of a Gly H^N(f1)-H^α(f2) crosspeak from a ^{15}N-HETLOC spectrum of cyclo(-D-MeAla-Ala-Ala-Ala-Gly-MeAla-). The $^2J_{N\text{-}H\alpha}$ coupling is obtained as offset in the direct dimension (b) of 2 multiplet components that are split by the strong $^1J_{N\text{-}H}$ coupling in the direct dimension (a).

Numerous other methods for determining homo- and heteronuclear ^{2}J and ^{3}J coupling constants and modifications to the methods described above have been published. It is important to emphasize that especially quantitative J correlation experiments[49-51] frequently used in protein NMR studies may be similarly useful for the investigation of peptides.

1.1.5 Relative Orientations from Residual Dipolar Couplings

Angles between bond vectors and an external reference coordinate system are easily measured using residual dipolar couplings (RDCs). RDC derived relative orientations of bond vectors located at remote ends of a large molecule can be used as long range restraints for structure determination. Therefore, in the last few years, RDCs have become a popular source of structural information, especially in the case of large biomolecules, which complements short range restraints derived from NOEs and ^{3}J couplings.

As dipolar couplings average to zero in traditional isotropic solution state samples, their measurement requires special sample preparations. RDCs are obtained from NMR spectra of partially aligned samples in which the isotropic tumbling is systematically affected by an appropriate alignment medium. Spectra detected from appropriate samples possess linewidths that are very similar to the corresponding isotropic solution state samples. RDCs typically range from 0.05 % - 1 % of the underlying dipolar couplings.

Although residual dipolar couplings (RDCs) are routinely used for the investigation of protein structures, they have rarely been used in peptide NMR studies. Stretched cross linked poly(dimethylsiloxane) (PDMS) gels[52-54], dimethylacrylamide copolymer (PH-PDMAA) gels[55], polystyrene gels[54] and liquid crystalline phases[56,57] were used for studying peptides with RDCs.

According to Kummerlöwe *et al.*[58] the abundance of newly described, well suited alignment media for the investigation of small molecules will increase the popularity of RDCs in peptide conformational studies. The consideration of larger numbers of RDCs measured in different alignment media will further make a more detailed investigation of dynamic processes possible.

1.1.6 Distance Geometry and Molecular Dynamics Calculations

(Cyclo)peptide structures are usually derived in a two step process that consists in initial distance geometry (DG) and subsequent molecular dynamics (MD) calculations. DG ensures extensive sampling of the conformational space and provides ROE derived[59] structural models. These are used as starting conformations for the subsequent MD refinement, which is based on a force field that reflects all the inherent interactions among the atoms of the peptide and the solvent (electrostatic interactions, van der Waals interactions and hydrogen bonds).

Distance geometry calculations are themselves subdivided into three steps.[60] In a first step, holonomic matrices are generated that contain pair-wise upper and lower distance limits. The distance limits within these matrices are derived from rotations around all the rotatable bonds within the peptide under investigation (geometrical limits) and from experimentally derived information like ROEs. The latter substitute the geometrical limits in the holonomic matrices whenever the experimentally derived information is more restrictive. In a second step called metrization, randomly chosen distances from the pair-wise upper and lower distance limits of all peptide atoms are stored in a metric matrix. Finally, these distances are converted into a complex geometry where the matrix based distance space is projected into the three-dimensional Cartesian coordinate space in an operation called embedding. Programs like DISGEO automatically perform these steps so the user must only define a small number of output-relevant parameters, making DG a very comfortable tool.[61]

As DG screens the conformational space of a peptide much faster than force field based methods, high performing computational resources are not required. However, peptide structures calculated by DG lack accuracy due to the disregard of energy terms and need to be refined by force field driven methods like MD simulations. Extended MD simulations in explicit solvent may further give insight into dynamic processes that are fast on the time scale of NMR chemical shifts like flips of χ dihedral angles within side-chains.

1.1.7 Conformational Averaging of ROEs and J couplings

It was shown above that even for molecules with a well defined conformation, the determination of precise distances and dihedral angles is complicated by problems like J transfer within the ROESY mixing time (Figure 1.5) and the ambiguity of the Karplus-equation (equation 1.12). The conformational flexibility of a peptide makes its structure determination process even more difficult.

This flexibility is described by variations of the Φ, Ψ, and χ dihedral angles and by *cis* peptide bond isomers that occur in tertiary peptide bonds preceeding proline or other *N*-alkylated residues. As Φ, Ψ, and χ dynamics is usually fast on the timescale of NMR chemical shifts, only one set of NMR signals is observed that reflects the equilibrium of different fast exchanging conformations. Only *cis-trans* isomerization of peptide bonds is slow enough to yield distinct isomer-specific sets of NMR signals (Figure 1.7).

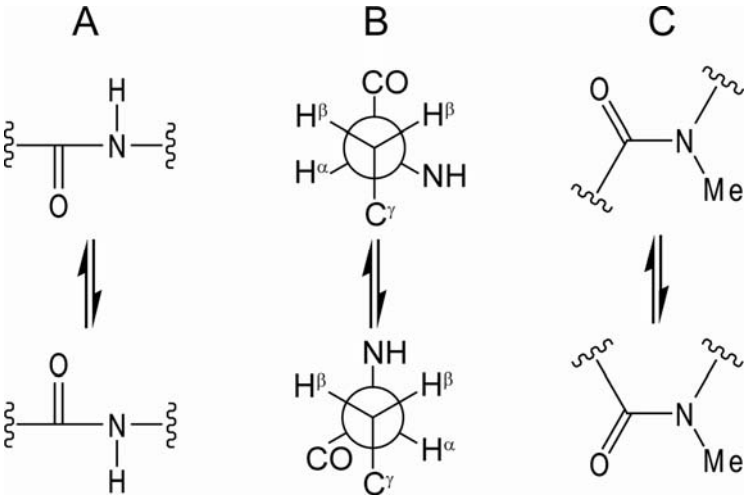

Figure 1.7: Flexibility of peptides. Typical dynamic processes like the reorientation of peptide bonds (A) and of side-chains (B) are fast on the timescale of NMR chemical shifts, whereas cis and trans isomers of peptide bonds (C) undergo slow exchange.

In equilibria of fast exchanging conformations, inter-proton distances may be strongly time-dependent. This is reflected in ROESY cross-peak intensities that may be used for structure calculations. Due to the r^{-6} dependence of the ROE, fast exchange between a low populated state p(1) with a short inter-proton distance $r_{ij}(1)$, and a high populated state p(2) with a long inter-proton distance $r_{ij}(2)$ leads to large ROESY cross-peaks which reflect almost exclusively the short inter-proton distance, $r_{ij}(1)$ (Figure 1.8 A). Distance restraints derived from such ROESY cross-peaks will be too short. The distribution of distances from D-MeTrp $H^{\delta 1}$ to MeLys $H^{\gamma`}$ and MeLys $H^{\gamma``}$ in cyclo(-MeAla-Tyr-D-MeTrp-MeLys-Val-MePhe-) as observed in a 50 ns MD trajectory is shown for illustration (Figure 1.8 B).

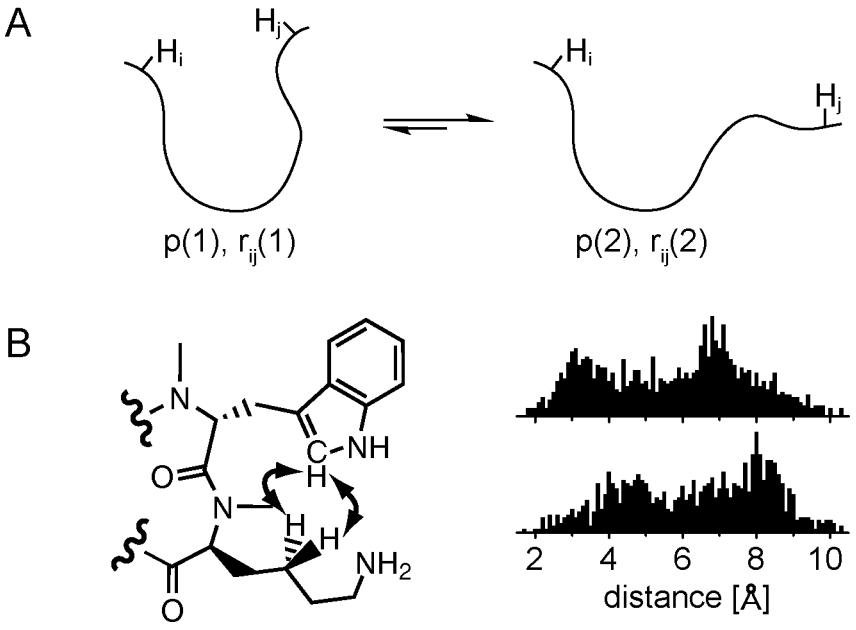

Figure 1.8: A: Two different conformations that exchange fast on the chemical shift timescale. A low populated (p(1) = 20%) first conformation with a small inter-proton distance of $r_{ij}(1)$ = 2 Å and a high populated second conformation (p(2) = 80%) with a large inter-proton distance of $r_{ij}(2)$ = 6 Å are expected to give rise to a ROESY cross-peak with an intensity that corresponds to an apparent distance of 2.6 Å. B: Two neighbored *N*-methylated residues D-Trp and Lys. Their side-chain dynamics in 3-*N*Me-(D-Trp[8],Lys[9],Phe[11])-seglitide is reflected by the distributions of the distances D-MeTrp $H^{\delta 1}$ to MeLys H^{γ} and D-MeTrp $H^{\delta 1}$ to MeLys H^{γ} within a 50 ns MD simulation. The ROESY cross-peak intensities of both interactions correspond to distances of 2.8 to 3.6 Å.

Fast exchange is also often reflected by ^3J coupling constants, which complicates their use as conformational restraints. Only in preferable situations, coupling constants suggest a single strongly preferred dihedral angle, (e.g. a Val χ_1 dihedral angle of 180° (+/- 15°) if $^3J_{H\alpha\text{-}H\beta}$ exceeds 12 Hz) which can then be used as a restraint that forces a single conformer to fulfill the J coupling.

Whenever ROEs and coupling constants can only be fulfilled by equilibria of the underlying rotamers, their applicability as restraints is limited to structure calculation techniques that consider averaging.

1.1.8 Importance of Solution Conformations

Preferred conformations of peptides are often studied in solvents like water, aqueous buffers or DMSO. The relevance of such solution conformations for biological systems, however, depends on their similarity with the conformations that are present in the receptor bound states.

Most of the peptide structures presented in the following chapters are restrained by cyclization and *N*-methylation, which leads to distinct preferred conformations.

Receptor binding of these peptides should not lead to siginficant structural changes of their backbones. In contrast, linear peptides are usually flexible in solution and any preferred solution conformation is likely to undergo a pronounced conformational adaptation while binding to a receptor. While biologically relevant structures of many restrained cyclopeptides were successfully determined in the absence of any receptor, more sophisticated methods are needed for studying the receptor bound state of flexible linear peptides. These include exchange transferred NOESY (et-NOESY)[62,63], saturation transfer difference NMR spectroscopy (STD-NMR)[64], intermolecular NOESY and X-ray crystallography.

2 Highly *N*-methylated Cyclic Peptides Targeting distinct Melanocortin and Somatostatin Receptor Subtypes

The project described in chapter 2.2 was a collaboration with my former colleagues Lucas Doedens and Florian Opperer, who synthesized the cyclic peptides under investigation. Matt Dedek and Erin Palmer, coworkers of Prof. Minying Cai and Prof. Victor Hruby at the University of Arizona, Tucson, measured affinities and activities.

The project described in chapter 2.3 was a collaboration with my former colleagues Jayanta Chatterjee and Burkhardt Laufer, who synthesized the cyclic peptides under investigation. Prof. Zsuzsanna Helyes, Erika Pintér and Prof. János Szolcsányi from University of Pécs, Hungary, as well as Aniko Horvath and Prof. Jozsef Mandl from Semmelweis University, Hungary, handled animals. Prof. Jean C. Reubi from the University of Bern, Switzerland, contributed somatostatin receptor autoradiography results. Prof. György Kéri from Semmelweis University, Hungary, conceived animal experiments.

Motivation

The importance of G protein-coupled receptors (GPCRs) is demonstrated impressively by the fact that about 40 % of drugs on the market target this class of receptors. According to a recent study, two out of three novel peptide candidates that entered clinical study between 1980 and 2008 were targeting GPCRs.[22] Many drugs that target GPCRs are not selective for distinct receptors. The antipsychotics olanzapine and clozapine, for example, act on twelve different GPCRs, leading to side effects like weight gain and cognitive deficits.[65] The design of new drugs targeting this class of receptors is due to the limited number of GPCR structures still based on the stepwise empirical optimization of known ligands. The three-dimensional structures of a potent and selective agonist of melanocortin receptor subtype 1 (chapter 2.2) and of a potent and selective agonist of somatostatin receptor subtype 2 (chapter 2.3) provide valuable insight into the pharmacophores that are required in order to selectively address these receptor subtypes.

2.1 G Protein-Coupled Receptors

The G protein-coupled receptors (GPCRs) are the largest of the numerous families of membrane bound receptors and important regulators of all kinds of physiological processes. Overall, about 800 GPCRs are encoded in the human genome, of which 460 were suggested to be olfactory and 340 to be non-olfactory receptors.[66] Currently, the physiological function of a large fraction of these receptors is not known, which are therefore referred to as orphan receptors.[67] However, the function of more and more non-olfactory orphan receptors is investigated due to their high potential as targets for pharmacological intervention.

Sequence alignment of the GPCR superfamily demonstrated a lack of overall homology.[68,69] Instead, six subgroups of GPCRs were identified, the well known families A, B, C, D, E and F.[69] However, classification depends on the applied criteria and the group of GPCRs that are considered. Five human GPCR families were identified based on phylogenetic criteria; the rhodopsin (i), adhesion (ii), frizzled/taste (iii), glutamate (iv), and the secretin family (v) (GRAFS classify-cation).[66,70]

GPCRs are built up of an N-terminal extracellular segment, seven transmembrane helices, three exoloops, three to four cytoloops and a C-terminal intracellular segment.[71] The N-terminus is the most diverse segment and varies from 10 to 600 residues,[67] whereas the seven TM helices share higher similarity. The highest similarity is observed within the regions that interact with guanine nucleotide binding proteins (G proteins).[72] These are located at the cytosolic ends of the TM helices three to six (TM3 – TM6). In contrast to helices in soluble proteins, the 7 TM helices of GPCRs are hydrophobic and contain proline residues that can kink the helices and thus alter the receptor structure.[71]

The first high resolution structure of a protein that possesses the characteristic seven trans membrane helix pattern of GPCRs was derived for the light driven proton pump bacteriorhodopsin.[73,74] Since then, a number of GPCR structures were determined; including Rhodopsin[75-78] and Opsin[79,80], β_2 adrenoceptor (β_2AR)[81-87], β_1 adrenoceptor (β_1AR)[88,89], A_{2A} adenosine receptor (A_{2A}AR)[90], CXCR4 chemokine receptor[91], and D3 dopamine receptor[92]. As some GPCR structures were solved in different states (with and without ligand bound), molecular models describing typical structural changes associated with the binding of agonists, inverse agonists and antagonists, are evolving. Just before the publication of the human adenosine A_{2A} receptor with the bound ligand ZM241385 by Jaakola *et al.*,[90] a competition between molecular

modeling research groups demonstrated that it is even today very difficult to predict the position of GPCR ligands within GPCR models with an accuracy that is sufficient for the rational design of GPCR ligands.[93]

While the external signals that are sensed by different GPCRs are very heterogeneous and consist in photons, ions, small organic molecules, peptides or even huge proteins, the subsequent intracellular signaling pathways are conserved. Heterotrimeric G proteins function as switches that link GPCR activation to intracellular signaling cascades. Inactive heterotrimeric G protein consists of three subunits (Gα, Gβ, Gγ) and GDP. Upon GPCR activation, G protein is bound, which leads to exchange of GDP by GTP, a process that goes in hand with a destabilization of the GPCR-G protein complex and thus leads to the dissociation of the G protein into Gα-GTP and Gβγ.

Each G protein belongs to one of four main families; $G\alpha_s$, $G\alpha_i$, $G\alpha_q$ and $G\alpha_{12}$[94] and the subsequent signaling pathways are depending on the G protein involved. While $G\alpha_s$-GTP activates adenyly cyclase and cyclic adenosine monophosphate (cAMP) activates Protein Kinase A (PKA) which modulates the activity of numerous proteins by phosphorylation of Serine and Threonine residues, $G\beta\gamma_s$ is inactive. The G_i pathway and the other G pathways differ strongly from the G_s pathway. $G\alpha_i$-GTP, for example, inhibits adenylate cyclase and the corresponding βγ subunit ($G\beta\gamma_i$) couples to a number of effector molecules leading to the activation of MAP kinases, and the regulation of PLC-β, K^+ channels, adenyly cyclase and phosphatidyl inositol-3-kinase (PI3K).

GPCR signaling is also inhibited by various physiological mechanisms. These include phosphorylation of GPCRs by G protein receptor kinases (GRKs)[95] subsequent arrestin[96,97] binding and receptor internalization[98], hydrolysis of Gα bound GTP, hydrolysis of cAMP by Phosphodiesterases (PDEs)[99] as well as dephosphorylation by Phosphatases competing with PKA.

Different agonists of a distinct GPCR may induce different active states and many ligands bind to numerous different GPCRs. Signaling induced by a ligand may be mediated by different G proteins. Moreover, crosstalk between signaling pathways, and a huge variety of the different proteins involved in signaling and its inhibition (21 Gα, 6 Gβ and 12 Gγ subunits[100], 7 originary GRKs[101], and 11 phospho-diesterase isoenzyme families[102]) show that GPCR signaling is far from being understood in all details.

For the current thesis, the melanocortin and somatostatin system are of special interest, as cyclic peptides were studied that target human melanocortin receptor

subtype 1 (hMC1R) and somatostatin receptor subtype 2 (sst_2), two GPCRs of high medical relevance.

2.2 Melanocortins, their Receptors, and Melanocortin Analogs

The melanocortins consist in a group of hormonal peptides that are derived from different but sequentially similar parts of the 31 kDa preprohormone proopiomelanocortin (POMC).[103,104] As the G protein-coupled melanocortin receptors (hMC1R, hMC2R, hMC3R, hMC4R, and hMC5R) transmit the binding of extracellular melanocortin into cells, they are important mediators for the various physiological functions that are controlled by the POMC system.[105] Skin and hair coloration,[106-108] inflammation[109] and immunomodulation,[110] steroid production and release,[111,112] cardiovascular functions,[113,114] energy homeostasis,[115] feeding behavior,[116-118] penile erection, sexual behavior,[119-121] and many other functions are associated with only one or two of the five melanocortin receptor subtypes. As most melanocortins (Figure 2.1) are rather unselective with respect to the different MCR subtypes, the search for highly selective and potent agonist and antagonist analogs is challenging.

The processing of POMC into different melanocortins,[122] the distribution of the different types of melanocortin receptors in the body,[123-129] their natural antagonists,[130,131] and MCR signaling,[105,115,132-136] were investigated intensively. For comprehensive introductions into the POMC system, the reader is referred to the literature.[106,115]

The melanocortins, namely, α-, β-, and γ-melanocyte stimulating hormone (α-, β-, and γ-MSH) and adrenal cortical stimulating hormone (ACTH) have a conserved Met-Glu-His-Phe-Arg-Trp-Gly heptapeptide sequence. The minimal sequence for MCR activity was shown to consist in the tetrapeptide His-Phe-Arg-Trp[137] (Figure 2.1).

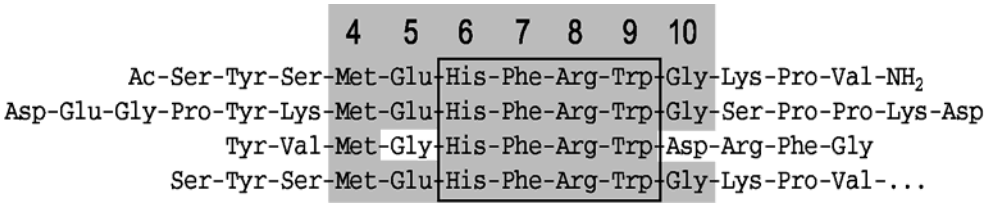

Figure 2.1: Sequences of α–MSH (top), β-MSH, γ-MSH, and ACTH (bottom). Only the first 13 of 39 ACTH residues are shown. The conserved heptapeptide sequence that corresponds to α–MSH_{4-10} is shaded gray. The smallest active sequence His^6-Phe^7-Arg^8-Trp^9 is also highlighted.

As no melanocortin receptor structure was published to date, most ligands binding to MCRs were discovered by the traditional approaches of medicinal chemistry and (high-throughput) screening. Recently some of the most interesting subtype specific MCR ligands that have been derived in the last decades were reviewed.[138,139] Hruby *et al*. draw great attention to the importance of the versatile different active states that are aquired by MCRs upon binding of different ligands.[139] Most importantly, the authors question whether non-peptidic ligands can activate MCRs in the same way as peptidic analogs.[139]

As reported already in 1980 by Sawyer *et al.*, the replacement of Met^4 and Phe^7 in α-MSH by norleucin (Nle) and D-Phe, respectively, yielded the more potent and stable [Nle^4, D-Phe7] α-MSH (NDP-α-MSH, MT-I, Melanotan I).[140] The super potent cyclic c[Cys^4, Cys^{10}]-α-MSH[141] and Ac-Nle-c[Asp^5, D-Phe^7, Lys^{10}]-α-MSH-(4-10)-NH_2[142,143] (MT-II, Melanotan II) were derived when the potential benefits of peptide cyclization had been recognized.[144,145] MT-II is very stable in vivo and can also cross the blood brain barrier. MT-I, MT-II, and bremelanotide (MT-II lacking amidation of the C-terminus) were used in a number of human clinical trials for pigmentation effects, erectile disfunction and female hypoactive sexual desire disorder (HSDD).[146-152] Modification of the aromatic ring in residue D-Phe^7 of MT-II was found to have a strong effect on activity and receptor subtype selectivity.[153] Since these early analogs were derived, a huge number of active peptides, cyclopeptides, and small organic molecules targeting MCRs were synthesized. As the physiological importance of hMC4R was described earlier than for hMC3R and hMC5R, the development of MSH analogs was focused on subtype 4 and even numerous hMC4R selective small organic molecules like THIQ[154] or MB243[155] were derived. However, within recent years, the association of MC3R with weight control[156-158], with erectile function and sexual behaviour[121] as well as with inflammatory responses and cardiovascular function[159] was described, whereas the MC5R was found to be involved in the regulation of exocrine gland function[160] and in the control of aggression.[161,162] This stimulated the development of potent and selective ligands targeting these melanocortin receptor subtypes.

MC4R selective and subnanomolar agonists with the disulfide scaffold Ac-cyclo(hCys-His-D-Phe-Arg-Trp-Cys])-NH_2[163] as well as similarly active and selective lactams cyclo(CO-CH_2-CH_2-CO-His-D-Phe-Arg-Trp-Dab)-NH_2 and cyclo(NH-CH_2-CH_2-CO-His-D-Phe-Arg-Trp-Glu)-NH_2)[164] and linear peptidic MC4R selective agonists[165,166] were reported.

[D-Trp] γ-MSH[167] and cyclo(Nle-Arg-D-Phe-Arg-Trp-Glu)-NH_2[168] are potent hMC3R selective agonists, while cyclo(CO-2,3-pyrazine-CO-D-Phe-Arg-Trp-Lys)-NH_2 was

found to be a potent hMC3R selective partial agonist.[169] Another selective agonist of the same receptor subtype was derived by replacement of His^6 in MT-II by 4-Amino-1,2,4,5-tetrahydro-2-benzazepin-3-one (Aba).[170]

The cyclic peptides Ac-Nle-cyclo(Asp-Oic-D-4,4'-Bip-Pip-Trp-Lys)-NH_2 (Oic: octa-hydro-indole-2-COOH, 4,4'-Bip: 4,4'-biphenylalanine, Pip: pipecolic acid)[171], and Ac-Nle-cyclo(Asp–His6-D-Nal(2')–Pip–Trp–Lys)–NH_2[172] are potent and highly selective hMC5R agonists, whereas similar potency and hMC5R selectivity was found for the antagonists Ac-cyclo(Cys-Glu-His-D-Phe-Arg-Trp-D-Cys)-Pro-Pro-Lys-Asp-NH_2[173], cyclo(CO-*cis*-CH=CH-CO-His-D-Nal(2')-Arg-Trp-Lys)-NH_2[174] but also for some small organic molecules.[175,176]

Many cyclic melanocortin analogs identified so far contain a cyclic core with more than six residues or/and a flexible sidechain-sidechain (e.g. Lys-Asp) linkage. Substitutions of single residues can lead to significant alterations of their conformation (and rearrange their pharmacophores). As a consequence, a reliable prediction of the receptor subtype selectivity of newly derived melanocortin analogs is very difficult and only possible if three-dimensional structures of new analogs are compared with three-dimensional structures of receptor subtype selective analogs.

2.2.1 Unselective MT-II and Selective 4-*N*Me-(His^6,Arg^8,Trp^9,Lys^{10})-MT-II

Ac-Nle^4-cyclo(Asp^5-His^6-D-Phe^7-Arg^8-Trp^9-Lys^{10})-NH_2 (MT-II) is a multipotent but unselective α-MSH derived agonist of human melanocortin receptor (hMCR) subtypes 1, 3, 4 and 5. A complete library of 31 MT-II analogs with one to five *N*-methylated peptide bonds (Figure 2.2) was synthesized by Lucas Doedens and Florian Opperer. The synthesis was performed according to the procedure originally described by Miller and Scanlan[177] which has been optimized by Biron *et al*. and which is compatible with all commonly used amino acids.[178]

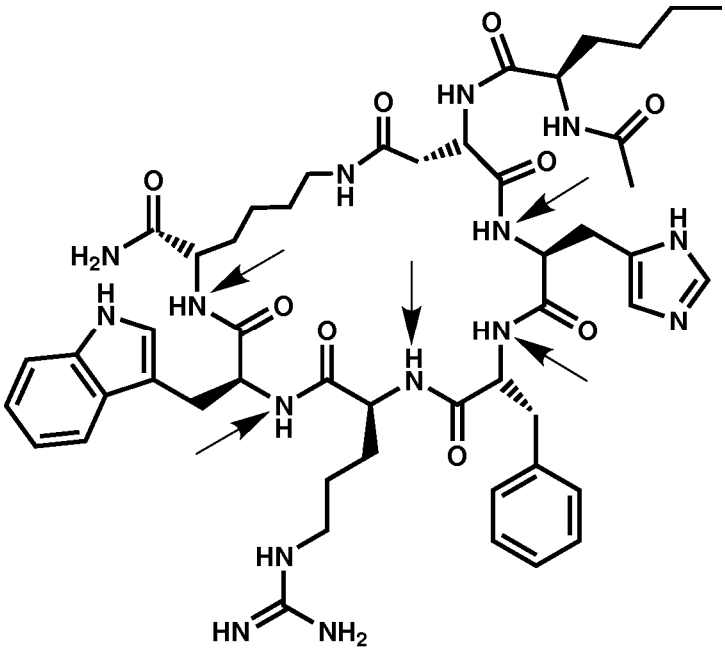

Figure 2.2: Chemical structure of MT-II. The five *N*-methylation sites that were considered for the design of a library of all $2^5 - 1 = 31$ analogs are indicated.

HEK293 cells that were stably expressing the hMC1R, hMC3R, hMC4R, and hMC5R were used for quantification of the activity for receptor binding and receptor activation. The binding activity of the 31 *N*-methylated peptides and MT-II was derived from replacement of the well established competitive ligand [^{125}I]-[Nle^4,D-Phe^7]-α-MSH (^{125}I-NDP-α-MSH). Receptor activation was measured using adenylate cyclase assays.

3-*N*Me-(His^6,Arg^8,Trp^9)-MT-II and 4-*N*Me-(His^6,Arg^8,Trp^9,Lys^{10})-MT-II were identified as potent and selective agonists of hMC1R (Table 2.1). Additional affinities and

activities for MT-II and the other 29 *N*-methylated analogs are given in the original publication.[43]

Table 2.1: Binding and cAMP assays of *N*-methylated MT-II analogs. IC_{50} = concentration of peptide at 50 % specific binding. EC_{50} = Effective concentration of peptide that was able to generate 50% maximal intracellular cAMP accumulation. NB = 0% of ^{125}I-NDP-α-MSH displacement observed at 10 µM. NA = 0% cAMP accumulation observed at 10 µM.

compound	hMC1R		hMC3R		hMC4R		hMC5R	
	IC_{50} [nm]	EC_{50} [nm]	IC_{50} [nm]	EC_{50} [nm]	IC_{50} [nm]	EC_{50} [nm]	IC_{50} [nm]	EC_{50} [nm]
3-*N*Me-(His^6,Arg^8,Trp^9)-MT-II	57	40	NB	NA	NB	NA	NB	NA
4-*N*Me-(His^6,Arg^8,Trp^9, Lys^{10})-MT-II	14	13	2200	NA	NB	NA	NB	NA

2.2.2 Structure of 4-*N*Me-(His^6,Arg^8,Trp^9,Lys^{10})-MT-II

The conformation of the highly potent and selective 4-*N*Me-(His^4,Arg^6,Trp^7, Arg^8)-MT-II (Figure 2.4, page 36) was investigated by NMR spectroscopy, restrained distance geometry calculations (DG), restrained 150 ps MD simulation in explicit water (rMD) and by unrestrained 30 ns MD simulation in explicit water (MD). Based on NMR assignments (Table 2.2) and other NMR data (ROEs, homo- and heteronuclear scalar coupling constants, H^N temperature gradients) and on restrained and unrestrained molecular dynamics a distinct and preferred structure could be derived for the peptide backbone. The amide bridged side-chains of the residues Asp^5 and *N*Me-Lys^{10} that are also part of the cyclic core were found to be flexible.

The resulting good agreement between measured and calculated distances clearly indicates a preferred backbone conformation of the structure obtained from the restrained MD simulation (Table A.1).[179]

In a very extended (30 ns) unrestrained MD simulation in explicit water this structure proved to be stable except for slight changes of four backbone dihedral angles in the range of 20° to 40° (Table 2.3).

Table 2.2: Resonance assignment of 4-*N*Me-(His[6],Arg[8],Trp[9],Lys[10])-MT-II in sodium acetate-d4 buffer (50 mM), pH 4.5, 298 K. Chemical shifts are referenced on sodium 3-(trimethylsilyl)propionate-2,2,3,3-d4 (^{1}H at 0.000 ppm).

	H^N (H^{NMe})	H^α	H^β	H^γ	H^δ	H^ε	H^ζ	others
Nle[4]	8.166	4.231	1.653 1.701	1.281	1.320	0.893	-	H^{Acetyl}: 2.062
Asp[5]	8.328	5.183	proR: 2.271 proS: 2.521	-	-	-	-	
***N*Me-His[6]**	(3.115)	5.392	proR: 3.272 proS: 3.063	-	2: 7.084	1: 8.563	-	
D-**Phe[7]**	7.657	4.668	proR: 2.901 proS: 2.661	-	7.152	7.327	7.320	
***N*Me-Arg[8]**	(1.559)	5.164	proR: 1.245 proS: 1.518	1.168 1.255	3.084	7.144	-	
***N*Me-Trp[9]**	(2.695)	6.021	proR: 3.287 proS: 3.216	-	1: 7.249	1: 10.180 3: 7.639	2: 7. 535 3: 7.150	η2: 7.321-
***N*Me-Lys[10]**	(2.774)	5.238	1.914	1.146 1.291	1.470 1.594	3.046 3.530	8.174	H^{Amide}: 7.145, 7.575

Table 2.3: Φ and Ψ dihedral angles of the average structure from the restrained MD (rMD) and from the trajectory of the unrestrained MD (MD).

	Φ_{rMD} [°]	Φ_{MD} [°]	ψ_{rMD} [°]	ψ_{MD} [°]
Nle[4]	-101	-75.5 +/- 39.6	109	29.4 +/- 82.5
Asp[5]	71	-89.7 +/- 32.7	144	112.7 +/- 16.9
***N*Me-His[6]**	-98	-102.4 +/- 15.7	78	117.4 +/- 19.2
D-**Phe[7]**	96	75.0 +/- 18.8	-126	-116.0 +/- 10.1
***N*Me-Arg[8]**	-135	-122.9 +/- 8.0	80	83.2 +/- 9.9
***N*Me-Trp[9]**	-120	-136.6 +/- 14.0	63	96.0 +/- 12.7
***N*Me-Lys[10]**	-114	-120.7 +/- 9.9	0	83.0 +/- 63.4

Indicators for the reliability of the structure shown in Figure 2.4 can be seen in the predominantly parallel orientation of CO(i) to $C^\alpha H^\alpha$(i+1) bond vectors[180] and in an overall high dispersion of backbone chemical shifts (H^α: 4.231 to 6.021 ppm (Figure 2.3), H^{Me}: 1.559 to 3.115 ppm). A comparative attempt to discuss the spectral data of non-*N*-methylated MT-II by one single preferred conformation failed. There was considerable backbone dynamics as indicated by a high heterogeneity of the best 30 out of 50 MT-II conformers obtained from DG calculations (RMSD of the backbone carbon and nitrogen atoms of 1.26 Å). Moreover, a low dispersion of chemical shifts (H^α: 4.198 to 4.644 ppm (Figure 2.3), H^N: 7.871 to 8.541 ppm), a lack of strong differentiation of all seven backbone H^N temperature gradients (-8.61 to -5.24 ppb/K) and of amide proton exchange rates as estimated by ROESY exchange peaks, as well as a smaller preference of distinct side-chain conformations was

observed. Altogether, these indicators suggest a more flexible peptide backbone of MT-II as compared to 4-*N*Me-(His^6,Arg^8,Trp^9,Lys^{10})-MT-II.

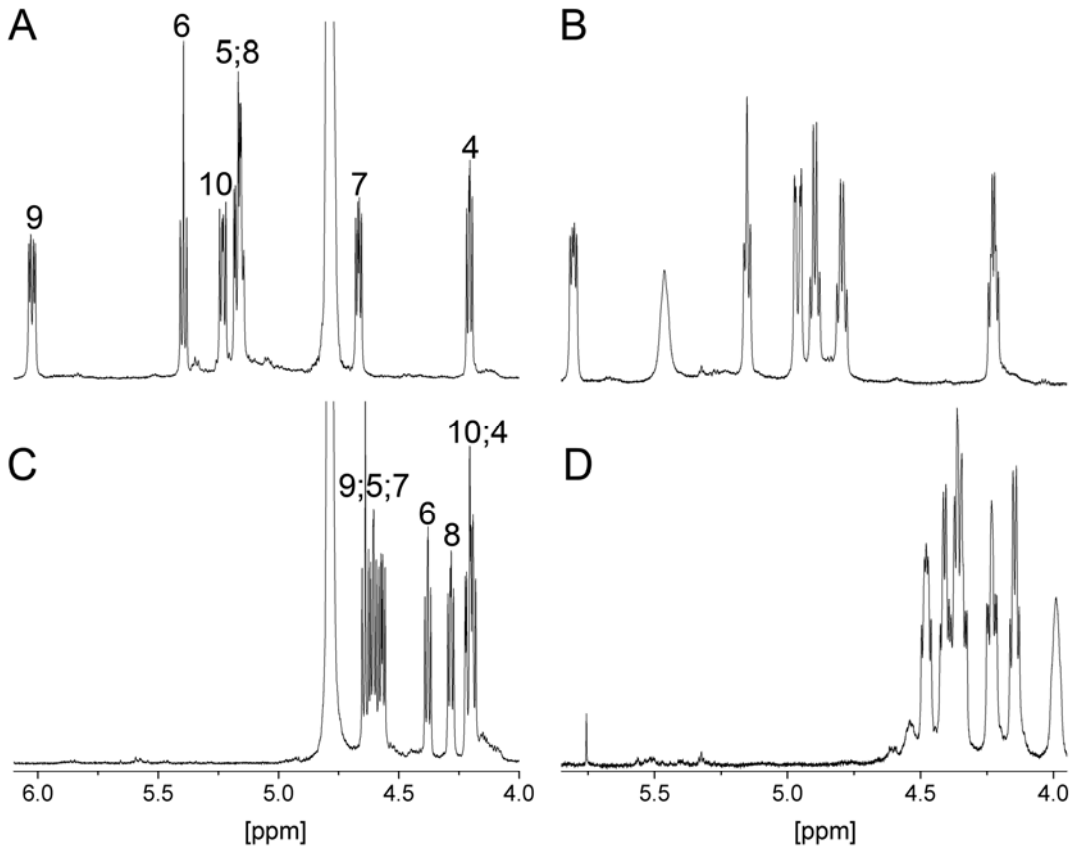

Figure 2.3: H^{α} regions of ^1H NMR spectra of 4-*N*Me-(His^6,Arg^8,Trp^9,Lys^{10})-MT-II (A and B) and MT-II (C and D). Spectra A and C were detected in 50 mM sodium acetate-d_4 D_2O buffer (pH 4.5), B and D were detected in DMSO-d_6. The numbers refer to H^{α} atoms of the respective residues in the α-MSH sequence.

The conformation of 4-*N*Me-(His^6,Arg^8,Trp^9,Lys^{10})-MT-II is shown in Figure 2.4. The ROE pattern demonstrates that all peptide bonds are *trans* configurated. As most of the amide bonds are *N*-methylated, turn-structures are not only defined by intramolecular hydrogen bonds.[181] Steric effects and dipole orientation such as the parallel orientation of CO(i) to $C^{\alpha}H^{\alpha}$(i+1) bond vectors[180] seem to contribute most strongly to the conformation of smaller *N*-methylated cyclic peptides.

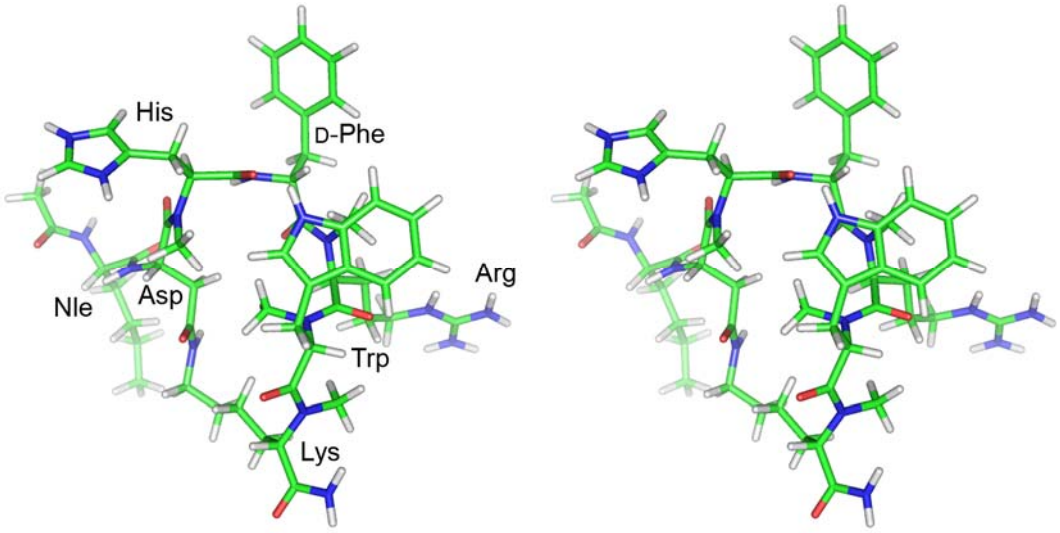

Figure 2.4: Stereoview of the solution structure of 4-*N*Me-(His[6],Arg[8],Trp[9],Lys[10])-MT-II as determined by NMR spectroscopy and MD calculations.

According to the *N*Me-His[6] backbone dihedral angles (Φ=-98°, Ψ=78°) the structure obtained from restrained MD simulation possesses an inverted γ-turn[181] centered at *N*Me-His[6]. A distance of 3.4 Å between the Asp[5] carbonyl oxygen and the D-Phe[7] amide nitrogen, a hydrogen bond angle of 141° and a moderately negative temperature gradient of D-Phe[7] H^N (-5.92 ppb/K in the aqueous buffer, -5.55 ppb/K in DMSO) indicate that the hydrogen bond within this inverted γ-turn is rather weak and protection from the solvent is incomplete. According to the minimal requirement for β-turns,[182] which consists in a distance of less than 7 Å between C^{α}_{i} and C^{α}_{i+3}, the inverted γ-turn is located within a β-turn ranging from Asp[5] to *N*Me-Arg[8] (C^{α}-C^{α} distance: 6.4 Å). A distance of 7.6 Å between the α-carbon atoms of *N*Me-His[6] and *N*Me-Trp[9] almost fulfills the criterion for a second overlapping *β*-turn, which is close to type II' *β*-turn geometry, as D-Phe[7] Φ, D-Phe[7] Ψ, *N*Me-Arg[8] Φ, and *N*Me-Arg[8] Ψ possess dihedral angles of 96°, -126°, -135° and 80°, respectively. The overlapping turns result in a virtually complete helical twist (*α*-turn) that extends from residues Asp[5] to *N*Me-Trp[9]. Hydrophobic clustering of the *N*Me-Trp[9] *N*-methyl group with the Asp[5] H^{β}, *N*Me-Arg[8] H^{α}, *N*Me-Lys[10] H^{γ} atoms and the *N*Me-His[6] *N*-methyl group (indicated by the presence of ROESY cross-peaks between the *N*Me-Trp[9] methyl protons and the Asp[5] H^{β}, *N*Me-Arg[8] H^{α}, *N*Me-Lys[10] H^{γ}, *N*Me-His[6] *N*-methyl protons) seems to stabilize this helical twist. Within the unrestrained 30 ns MD simulation starting from the structure of the restrained MD, slight changes occurred in a few backbone dihedral angles as compared to the average structure from the restrained MD simulation. Asp[5] Ψ, *N*Me-His[6] Ψ, D-Phe[7] Φ and *N*Me-Trp[9] Ψ were

most affected and changed from 144° to 113°, 78° to 117°, 96° to 75° and 63° to 96°, respectively (Table 2.3). The RMSD between the atoms of the peptide backbone from Asp^5 to *N*Me-Lys^{10} of structures obtained from the unrestrained and restrained MD simulation is 1.0 Å. According to the *N*Me-His^6 backbone dihedral angles (Φ = -102°, Ψ = 117°) the inverted γ-turn is less pronounced in the structure obtained from unrestrained MD simulation. Upper bounds of some distance restraints within the cyclic core structure (Asp^5H^{β} - D-Phe^7H^N; Asp^5H^{β} - *N*Me-His^6H^{Me}; D-Phe^7H^N - *N*Me-Arg^8H^{α}; *N*Me-Arg^8H^{α} - *N*Me-$Lys^{10}H^{Me}$; *N*Me-Trp^9H^{Me} - *N*Me-$Lys^{10}H^{\alpha}$) were violated during the unrestrained MD simulation. This can be traced back directly to the aforementioned changes in backbone dihedral angles. As illustrated in more detail in the sections describing the side-chain dynamics and structure calculations, it seems that the changes in the backbone dihedral angles were caused by artificial strains in the amide linked Asp^5 and *N*Me-Lys^{10} side-chains. These were introduced within the DG calculation as our structure calculation protocol did not take conformational averaging explicitly into account. Accordingly, the conformer obtained from restrained MD seems to be the best structural model for the peptide backbone and we focused the analysis of side-chain conformation on this structure.

In consideration of the high binding affinity to hMC1R (IC_{50}=14 nm) and the strong restriction that cyclization and fourfold *N*-methylation pose on conformational changes within the backbone of 4-*N*Me-(His^6,Arg^8,Trp^9,Lys^{10})-MT-II, we think that its backbone conformation in aqueous solution is very close to the conformation present in the receptor bound state.

The conformation of the peptide backbone also offers an explanation for the strong interference of D-Phe^7 *N*-methylation with hMCR affinity, as *N*-methylation goes in hand with an increased spatial requirement and increased hydrophobicity in comparison to the replaced amide proton. If D-Phe^7 is *N*-methylated, these hydrophobic and steric effects would prohibit the formation of the backbone conformation present in 4-*N*Me-(His^6,Arg^8,Trp^9,Lys^{10})-MT-II, as close proximity between the Asp^5 carbonyl oxygen and the D-Phe^7 *N*-methyl group is disfavored. Hence, the *N*Me-D-Phe^7 substitution would not simply displace a hydrogen bond donor, but also lead to an altered conformation of the peptide backbone, which would affect the presentation of the pharmacophore and prevent interaction of the aromatic ring with the 3rd and the 6th transmembrane binding domains aromatic groups.

2.2.3 Dynamics of 4-*N*Me-(His^6,Arg^8,Trp^9,Lys^{10})-MT-II

Investigation of side-chain conformation about the χ_1 angle requires a careful analysis of homo- and heteronuclear J-couplings as well as the consideration of NOE distances in stereospecifically assigned β protons. Extended MD simulations of a solution structure in explicit solvent can further clarify which structural flips of side-chain dihedral angles are correlated.

The sums of the $^3J_{H\alpha\text{-}H\beta}$ coupling constants of the individual amino acid side-chains are in the order of 15 Hz, which excludes higher populations of the χ_1=60° conformation (*sc*+) for the L amino acid residues, and of the χ_1=-60° conformation (*sc*-) for the D-Phe^7 residue (Table 2.4). A strong difference between the two $^3J_{H\alpha\text{-}H\beta}$ coupling constants together with a sum of both of about 15 Hz indicate however a preferred (χ_1=-60°) conformation for Asp^5 ($^3J_{H\alpha\text{-}H\beta proS}$ = 10.7 Hz) and *N*Me-Trp^9 ($^3J_{H\alpha\text{-}H\beta proR}$ = 11.1 Hz), whereas *N*Me-His^6 and *N*Me-Arg^8 with identical $^3J_{H\alpha\text{-}H\beta proR}$ and $^3J_{H\alpha\text{-}H\beta proS}$ coupling constants populate the (χ_1=-60°) and (χ_1=180°) conformations. For D-Phe^7 the difference of the $^3J_{H\alpha\text{-}H\beta}$ coupling constants is small indicating a less pronounced preference of the χ_1=60° over the χ_1=180° rotamer. For *N*Me-Lys^{10} the $^3J_{H\alpha\text{-}H\beta}$ coupling constants indicate populations of 70 to 30 % for the χ_1=-60° and χ_1=180° rotamers or vice versa. It is not clear, which of both is higher populated as the chemical shifts of the two β protons are degenerated. The *N*Me-Lys^{10} H^ζ signal is split by two similar $^3J_{H\alpha\text{-}H\beta}$ coupling constants that indicate an equilibrium of different rotamers for the χ_4 dihedral angle of *N*Me-Lys^{10}. Overall, the dynamics of the χ_1 and χ_4 diehedral angles of the *N*Me-Lys^{10} clearly shows that no distinct preferred conformation should be suggested for the lactam bridged side-chains.

Table 2.4: $^3J_{H\alpha\text{-}H\beta}$ coupling constants as experimentally determined from E.COSY. The according χ_1 populations were derived by linear combination of $^3J_{H\alpha\text{-}H\beta}$(ap) = 12 Hz, $^3J_{H\alpha\text{-}H\beta}$(ga) = 3.5 Hz.

	$^3J_{H\alpha\text{-}H\beta}$ [Hz]		p(χ_1 = -60°) [%]	p(χ_1 = 180°) [%]	p(χ_1 = 60°) [%]
	H^α-H^β proR	H^α-H^β proS			
Nle[4]	8.2; 6.2		84		16
Asp[5]	3.8	10.7	74	11	15
***N*Me-His**[6]	7.9	7.9	48	48	4
D-Phe[7]	5.3	9.2	14	25	61
***N*Me-Arg**[8]	7.0	7.0	40	40	20
***N*Me-Trp**[9]	11.1	4.7	78	19	3
***N*Me-Lys**[10]	9.5, 6 Hz		100		0

Dynamics of the side-chains that are not involved in cyclization were further investigated by 30 ns molecular dynamics simulations in explicit water (Figure 2.5). For analyzing the side-chain dynamics based on the structure obtained from the rMD calculation, position restraints were applied on the carbon and nitrogen atoms of the peptide backbone from Asp[5] C^α to *N*Me-Lys[10] C^α. Analysis of the MD simulation performed with such position restraints revealed that all χ_1 populations except of the χ_1 populations of *N*Me-Arg[8] and of *N*Me-Lys[10] were well consistent with the $^3J_{H\alpha\text{-}H\beta}$ coupling constants (Table 2.4, Figure 2.5). The strong preference of χ_1=-60° for Asp[5] and for *N*Me-Trp[9] as well as the evenly populated χ_1=-60° and χ_1=180° rotamers for Nle[4] and *N*Me-His[6] are indicated by $^3J_{H\alpha\text{-}H\beta}$ coupling constants and well reproduced by the MD simulation. For D-Phe[7], the preference of the χ_1=60° rotamer with respect to the χ_1=180° rotamer, that is indicated by the $^3J_{H\alpha\text{-}H\beta}$ coupling constants, is not reflected by the MD trajectory, which suggests similar populations of the two rotamers.

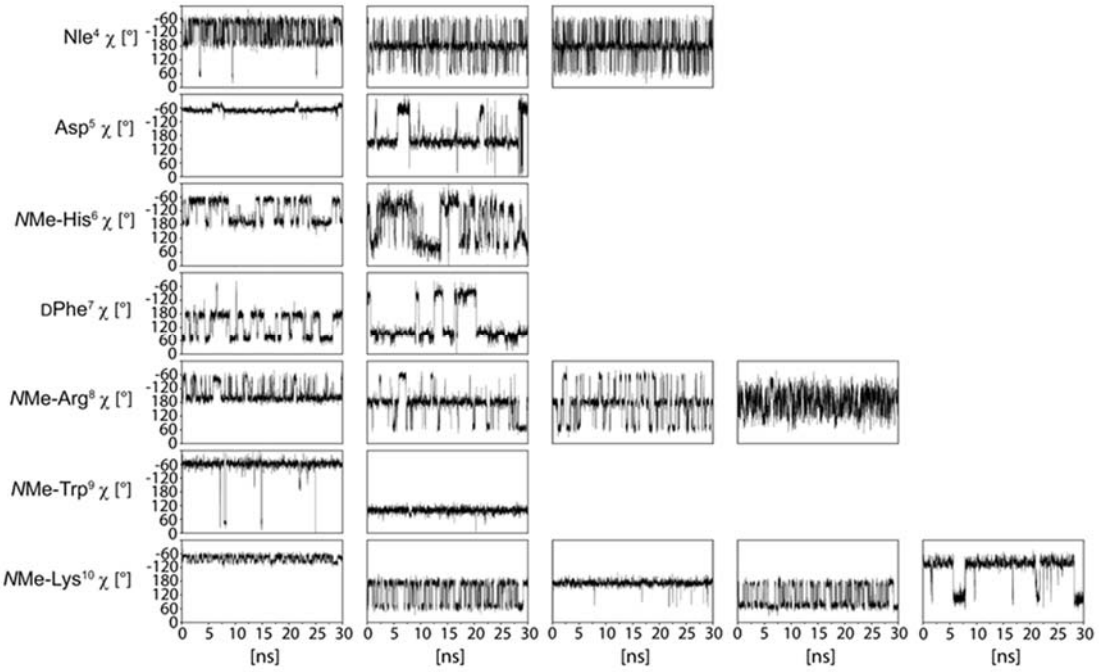

Figure 2.5: χ dihedral angles as observed during the unrestrained 30 ns MD simulation. The column number (from the left to the right) corresponds to the χ dihedral angle positions within the side-chains.

As indicated by the MD simulation, by the ROEs and by the upfield or downfield chemical shifts, hydrophobic clustering is crucial for the different side-chain conformations of 4-*N*Me-(His^6,Arg^8,Trp^9,Lys^{10})-MT-II in aqueous solution. Stacking of the *N*Me-His^6 and D-Phe^7 side-chains, that was also reported in other structural investigations of α-MSH analogs is well observed within the MD trajectory (when *N*Me-His^6 $\chi_1 \approx 180°$ and D-Phe^7 $\chi_1 \approx 60°$). Hydrophobic contacts between the D-Phe^7 and *N*Me-Arg^8 side-chains that agree with strong upfield shifts of the *N*Me-Arg^8 β and γ protons are also observed within the MD trajectory (when D-Phe^7 $\chi_1 \approx 180°$). The clustering of the *N*Me-Trp^9 indolyl ring with the *N*-methyl group of *N*Me-Arg^8, which is observed in Figure 2.4, is confirmed by ROE contacts between methyl protons and all indolyl protons as well as by a strongly upfield shifted H^{Me} resonance at 1.559 ppm. ROEs between the *N*Me-His^6 methyl protons and the *N*Me-Trp^9 δ1 and ε1 protons as well as between D-Phe^7 H^{α} and *N*Me-Trp^9 $H^{\varepsilon 1}$ are well consistent with the orientation of the indolyl ring given in Figure 2.4. An additional ROE between the *N*Me-His^6 methyl protons and the *N*Me-Trp^9 ε_3 proton indicates another orientation of the indolyl group that was not sampled during 30 ns unrestrained MD simulation. In this orientation the indolyl group also seems to stack on top of the *N*Me-Arg^8 *N*-methyl group as shown in Figure 2.4 but with the six membered ring of the indolyl group pointing to the left and the five membered ring pointing to the right.

A dispersion of chemical shifts of 4-*N*Me-(His^{6},Arg^{8},Trp^{9},Lys^{10})-MT-II in DMSO-d6 (H^{α}: 4.245 to 5.824 ppm (Figure 2.3), H^{Me}: 1.893 to 3.058 ppm), which is similar to the dispersion in the aqueous buffer (H^{α}: 4.231 to 6.021 ppm (Figure 2.3), H^{Me}: 1.559 to 3.115 ppm), indicates that hydrophobic interactions observed in aqueous buffer are also present in the slightly more hydrophobic DMSO. This suggests that such hydrophobic interactions might also be present in hMC1R bound state. In addition it is often found that stronger conformational preference which is accompanied by stronger biological activity indicates a closer similarity to the bioactive conformation.

2.3 Somatostatin, its Receptors, and Somatostatin Analogs

Somatostatin (somatotropin release inhibitory factor, SRIF) was first isolated by Vale *et al.* in 1972 from ovine hypothalamus and described as a factor inhibiting growth-hormone (GH) secretion.[183] Two forms are found in the human body, somatostatin-14 and somatostatin-28, that consist of 14 and 28 amino acid residues, respectively (Figure 2.6). Both forms possess a cyclododecapeptide substructure that is established via an intramolecular disulfide bond. Their various physiological functions[184] are mediated by similar high-affinity binding to five different subtypes of the seven trans-membrane G protein-coupled human somatostatin receptors,[185] $sst_{1\text{-}5}$. Receptor interaction inhibits the secretion of a number of different hormones[186] like GH, insulin, glucagon, gastrin and cholecytokinin. Despite of high research efforts, it is only partially understood how the various diseases that are affected by somatostatin (e. g. cancers, neuroendocrine tumors, GI abnormalities)[184,187-192] are linked to the individual receptor subtypes and the presence of more than one sst receptor subtype seems to be necessary in order to induce some of the various different somatostatin effects.

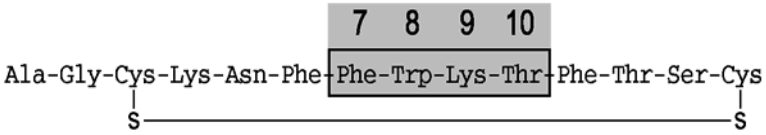

Figure 2.6: Sequence of somatostatin-14 (SRIF-14). In somatostation-28 (SRIF-28), additional 14 *N*-terminal residues Ser-Ala-Asn-Ser-Asn-Pro-Ala-Met-Ala-Pro-Arg-Glu-Arg-Lys are present. The essential amino acid sequence Phe^7-Trp^8-Lys^9-Thr^{10} that is conserved in many analogs is shaded gray.

Many potent and selective somatostatin analogs were derived within the last decades.[193] Improved potency and selectivity, increased serum stability and oral bioavailability were obtained[194] by reducing the overall length of the peptide chain,[195,196] by introducing D-Trp^8 in place of Trp^8,[197,198] by reducing the cyclopeptides ring size,[199-201] and by head-to-tail cyclization[144,201]. Additionally, potent small organic compounds targeting somatostatin receptors were derived.[202-204]

A number of cyclic somatostatin analogs are applied as therapeutics.[205,206] D-Phe-cyclo(Cys-Phe-D-Trp-Lys-Thr-Cys)-Thr(ol) (Octreotide)[206], D-βNal-cyclo(Cys-Phe-D-Trp-Lys-Val-Cys)-Thr-NH_2 (Lanreotide)[207], and D-Phe-cyclo(Cys-Tyr-D-Trp-Lys-Val-Cys)-Thr-NH_2 (Vapreotide)[208] are used for the treatment of carcinoid syndromes such as acromegaly but also for managing oesophageal variceal bleeding. More

details about the application of these and similar analogs in therapies and diagnostics as well as about their application in past and current clinical trials is given in the literature.[193,206,209-212]

The structures of many somatostatin analogs were studied by NMR spectroscopy,[213] which also resulted in consensus structures for sst_1 selective analogs, sst_2 agonists, sst_2 antagonists, and sst_4 agonists.[214-217]

2.3.1 Somatostatin and Neurogenic Inflammation

Somatostatin also plays an important role in the peripheral nervous system. It exerts the downregulation of nociception and of neurogenic components of inflammatory processes[218,219] that are important in the pathology of several inflammatory diseases like rheumatoid arthritis, allergic contact dermatitis, psoriasis, asthma, and inflammatory bowel diseases. These effects (and the bad pharmacodynamic profile of somatostatin itself) inspired the development of somatostatin analogs as anti-inflammatory and analgesic drugs. The release of calcitonin gene-related peptide (CGRP) from sensory fibers of isolated rat tracheae and acute neurogenic plasma protein extravasation in the rat paw are two processes that are associated with neurogenic inflammation and accessible from according *in vitro* and *in vivo* testing.

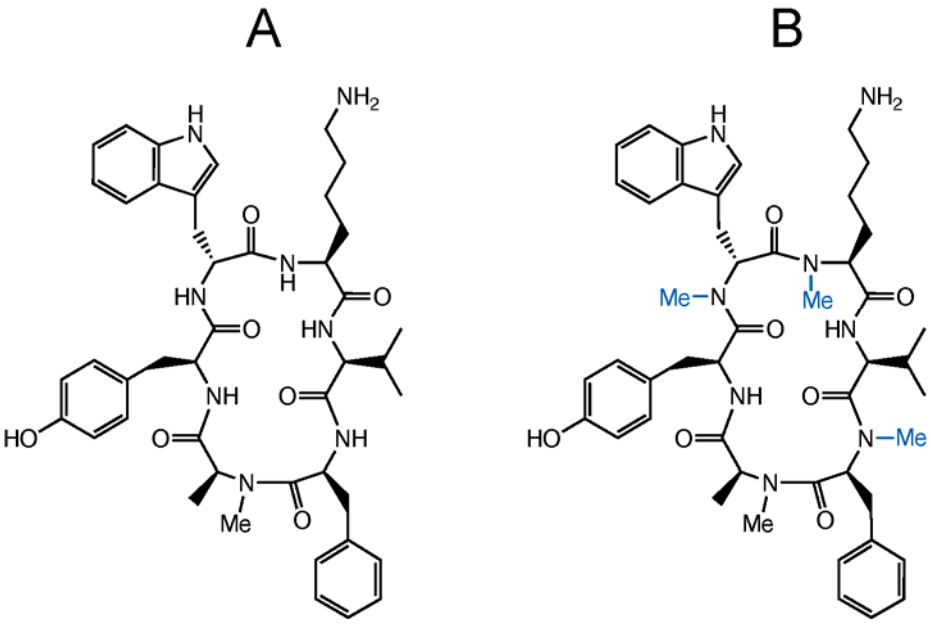

Figure 2.7: cyclo(*N*MeAla^6-Tyr^7-D-Trp^8-Lys^9-Val^{10}-Phe^{11}) (seglitide),[220] (A); cyclo(*N*MeAla^6-Tyr^7-*N*MeD-Trp^8-*N*MeLys^9-Val^{10}-*N*MePhe^{11}), (3-*N*Me-(D-Trp^8,Lys^9,Phe^{11})-seglitide),[221] with additional *N*-methyl groups highlighted in blue (B).

cyclo(*N*MeAla^6-Tyr^7-D-Trp^8-Lys^9-Val^{10}-Phe^{11}) (seglitide, Figure 2.7 A) was first described by Veber *et al.* as a highly potent drug candidate for the treatment of diabetes.[220] However, different effects were found for the new *N*-methylated seglitide derivative with three additional *N*-methyl groups (cyclo(*N*MeAla^6-Tyr^7-*N*MeD-Trp^8-*N*MeLys^9-Val^{10}-*N*MePhe^{11}), 3-*N*Me-(D-Trp^8, Lys^9, Phe^{11})-seglitide, Figure 2.7 B). It inhibits both, CGRP release from sensory fibers of isolated rat tracheae and acute neurogenic plasma protein extravasation in the rat paw. 3-*N*Me-(D-Trp^8,Lys^9,Phe^{11})-seglitide was therefore identified as an interesting analgesic drug candidate.[221] For more details about the results of *in vivo* and *in vitro* biological tests, the reader is referred to the original publication.[221]

Additionally, all six seglitide analogs that possessed only one or two of the *N*-methyl groups at D-Trp^8, Lys^9 and Phe^{11} were synthesized and tested. These and seglitide itself did show much weaker or no such (*in vivo* and *in vitro*) inhibitory effects, although their sst receptor affinity was shown to be significantly higher.[221] This finding was highly interesting, and motivated the investigation of the three-dimensional structure of 3-*N*Me-(D-Trp^8,Lys^9,Phe^{11})-seglitide, that is reported in the following sections.

2.3.2 Structure of 3-*N*Me-(D-Trp^8,Lys^9,Phe^{11})-seglitide

The solution conformation was determined employing extensive 2D NMR studies and extended MD (molecular dynamics) simulations. The conformation of 3-*N*Me-(D-Trp^8,Lys^9,Phe^{11})-seglitide is shown in Figure 2.8. A very strong ROE between *N*Me-Phe^{11} H$^\alpha$ and *N*Me-Ala^6 H$^\alpha$ clearly demonstrates that the peptide bond between *N*Me-Phe^{11} and *N*Me-Ala^6 is in *cis*-conformation. No further ROEs were observed between other α-protons of neighboring residues, which indicate that all other peptide bonds are in trans-conformation (Table B.1). Although most of the amide bonds are *N*-methylated, two β-turns about *N*Me-D-Trp^8, *N*Me-Lys^9 and *N*Me-Phe^{11}, *N*Me-Ala^6 exhibit a characteristic intramolecular hydrogen bond pattern via the two H^N atoms.

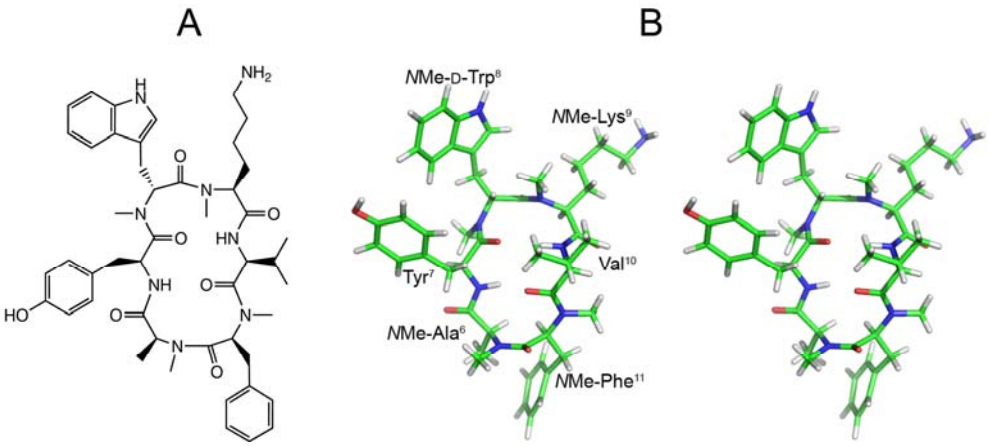

Figure 2.8: A: The structural formula of 3-*N*Me-(D-Trp[8],Lys[9],Phe[11])-seglitide. B: Stereoview of the solution structure of 3-*N*Me-(D-Trp[8],Lys[9],Phe[11])-seglitide as determined by NMR spectroscopy and MD calculations. The conformation shown here was extracted by cluster analysis as the most representative frame of the MD calculation.

According to the backbone dihedral angles of *N*Me-D-Trp[8] (Φ=92°, Ψ=-99°) and *N*Me-Lys[9] (Φ=-119°, Ψ=5°) the structure obtained from restrained MD simulation possesses a β-turn (type II') centered at these two residues.[201] A distance of 2.2 Å between the Val[10] amide proton and the Tyr[7] carbonyl oxygen, a hydrogen bond angle of 129° and a weakly negative temperature gradient of Val[10] H^N (-0.3 ppb/K in DMSO) indicate that the hydrogen bond within this turn is rather strong. A second β-turn (type VIa) possesses dihedral angles of *N*Me-Phe[11] (Φ=-44°, Ψ=122°) and *N*Me-Ala[6] (Φ=-119°, Ψ=77°) and a *cis* configuration of the peptide bond between *N*Me-Phe[11] and *N*Me-Ala[6]. A distance of 1.8 Å between the Tyr[7] amide proton and the Val[10] carbonyl oxygen, a hydrogen bond angle of 151° and a weakly negative temperature gradient of Tyr[7] H^N (-1.3 ppb/K in DMSO) indicate that the hydrogen bond within this β-turn is even stronger than the hydrogen bond of the type II' β-turn. The Tyr[7] H^N-Val[10] O' and Val[10] H^N- Tyr[7] O' hydrogen bonds orient the Tyr[7] and Val[10] residues in a geometry that is usually found for individual hydrogen bonded residues in neighbored antiparallel β-strands. The backbone dihedral angles of Tyr[7] (Φ = -116°, Ψ = 110°) and Val[10] (Φ = -163°, Ψ = 102°) confirm the similarity to this secondary structure element, as they are close to the corresponding backbone dihedral angles in parallel and antiparallel β-sheets.

Table 2.5: Resonance assignment of 3-*N*Me-(D-Trp[8],Lys[9],Phe[11])-seglitide in DMSO-d6 at 298 K. Chemical shifts are referenced on DMSO (^{1}H at 2.520 ppm).

	H^N (H^{NMe})	H^α	H^β	H^γ	H^δ	H^ε	H^ζ	H^η
***N*Me-Ala[6]**	(2.404)	4.772	0.228					
Tyr[7]	8.359	4.928	2.681 2.805		6.949	6.698		9.273
***N*Me-D-Trp[8]**	(2.886)	5.188	proR: 3.184 proS: 2.915		1: 7.136	1: 10.960 3: 7.449	2: 7.410 3: 7.105	2: 7.144
***N*Me-Lys[9]**	(2.506)	4.873	1.153 1.848	0.669 0.872	1.405	2.705	7.683	
Val[10]	6.995	4.891	2.142	proR:0.833 proS:0.774				
***N*Me-Phe[11]**	(3.210)	5.295	3.080 3.140		7.254	7.315	7.258	

Besides hydrogen bonding, hydrophobic clustering of the Val[10] γ-methyl groups with the *N*Me-Lys[9] *N*-methyl group and of the *N*Me-Ala[6] β-methyl group to the π-surface of the neighbored *N*Me-Phe[11] phenyl ring seem to stabilize the peptide backbone conformation (Figure 2.8). These hydrophobic contacts are indicated by Val[10] H^γ-*N*Me-Lys[9] H^{Me} ROEs and by *N*Me-Ala[6] H^β-*N*Me-Phe[11] $H^{\delta/\varepsilon}$ ROEs as well as by a strongly highfield shifted *N*Me-Ala[6] H^β resonance.

The high spatial requirements of the four *N*-methyl groups and the two strong hydrogen bonds between the Tyr[7] and Val[10] residues indicate that the backbone of 3-*N*Me-(D-Trp[8],Lys[9],Phe[11])-seglitide should be in a well defined and rather inflexible conformation, as observed during the extended MD simulation. This suggests that its backbone conformation in solution can sustain in the receptor bound state. Even weak conformational changes of the backbone during the binding process might be thermodynamically highly disfavored and lead to the comparably weak affinity to sst_2 (no perfect match between cyclopeptide structure and the sst_2 receptor), as compared to other less constrained analogs that might adapt to the sst_2 binding pocket more easily.

Table 2.6: Average Φ and Ψ dihedral angles and their standard deviations as extracted from the MD trajectory.

	Φ_{MD} [°]	Ψ_{MD} [°]
***N*Me-Ala^{6}**	-122.8 +/- 6.6	67.9 +/- 21.5
Tyr^{7}	-132.7 +/- 19.2	114.9 +/- 13.1
***N*Me-D-Trp^{8}**	81.1 +/- 11.4	-107.2 +/- 8.1
***N*Me-Lys^{9}**	-111.6 +/- 12.0	0.8 +/- 22.1
Val^{10}	-117.4 +/- 18.3	120.8 +/- 14.0
***N*Me-Phe^{11}**	-44.7 +/- 24.7	115.6 +/- 9.4

The conformation occupied by 3-*N*Me-(D-Trp^{8},Lys^{9},Phe^{11})-seglitide, that possesses a single *cis* peptide bond, is also found in a highly Caco-2[23] permeable scaffold. As described in more detail in chapter 4, the right *N*-methylation pattern has to be present on this scaffold, in order to achieve high Caco-2 permeability for cyclo-(a-A-A-A-A-A) peptides. Among all the different *N*-methylated seglitides that were tested *in vitro* and *in vivo*,[221] only 3-*N*Me-(D-Trp^{8},Lys^{9},Phe^{11})-seglitide possesses an *N*-methylation pattern that is favoring high oral bioavailability for cyclic hexapeptides with a single *cis* peptide bond.

2.3.3 Dynamics of 3-*N*Me-(D-Trp^{8},Lys^{9},Phe^{11})-seglitide

Investigation of side-chain conformation about the χ_1 angle requires a careful analysis of homo- and heteronuclear J couplings as well as the consideration of NOE distances in stereospecifically assigned β protons.[222] Extended MD simulations of a solution structure in explicit solvent can further clarify which structural flips of side-chain dihedral angles are correlated.

Table 2.7: $^{3}J_{H\alpha\text{-}H\beta}$ Coupling Constants and the according χ_1 populations, as derived by assuming the following coupling constants: $^{3}J_{H\alpha\text{-}H\beta}$(ap) = 12 Hz, $^{3}J_{H\alpha\text{-}H\beta}$(ga) = 3.5 Hz.

	$^{3}J_{H\alpha\text{-}H\beta}$ [Hz]		$p_{(\chi1 = -60°)}$ [%]	$p_{(\chi1 = 180°)}$ [%]	$p_{(\chi1 = 60°)}$ [%]
	H^{α}-H^{β} proR	H^{α}-H^{β} proS			
Tyr^{7}	4.5, 7.1		54		46
***N*Me-D-Trp^{8}**	10.5	5.8	0	78	22
***N*Me-Lys^{9}**	11.0, 4.7		100		0
Val^{10}	4.0		94	6	0
***N*Me-Phe^{11}**	5.8, 10.6		100		0

The sums of the $^3J_{H\alpha-H\beta}$ coupling constants of the residues *N*Me-D-Trp[8], *N*Me-Lys[9] and *N*Me-Phe[11] exceed 15 Hz, which excludes higher populations of the χ_1 = 60° conformation (*sc*+) for the *N*Me-D-Trp[8] residue, and of the χ_1 = -60° conformation (*sc*-) for the *N*Me-Lys[9] and *N*Me-Phe[11] residues (Table 2.7). The sum of the Tyr[7] $^3J_{H\alpha-H\beta}$ coupling constants (12.6 Hz) is significantly smaller and indicates a considerable population of the χ_1=60° rotamer, that is for steric reasons usually disfavored in L-amino acid residues. A small $^3J_{H\alpha-H\beta}$ coupling constant of 4.0 Hz excludes the Val[10] χ_1=180° rotamer (with antiperiplanar orientation of H^α and H^β) from being populated significantly. A strong difference between the two $^3J_{H\alpha-H\beta}$ coupling constants together with a sum of both of more than 15 Hz indicate a preferred (χ_1=180°) conformation for *N*Me-D-Trp[8] ($^3J_{H\alpha-H\beta proR}$ = 10.5 Hz), whereas signal overlap or a poor signal to noise ratio precluded similar unambiguous stereospecific assignments and a similar detailed analysis of χ_1 populations of the other non β-branched residues. Consideration of the intraresidual Val[10] H^N-H^{Me} and H^α-H^{Me} ROEs together with the small $^3J_{H\alpha-H\beta}$ coupling constant (4.0 Hz) and the large $^3J_{HN-H\alpha}$ constant (9.3 Hz) clearly demonstrated a very strong preference of χ_1 = -60° for this residue.

The qualitative analysis of strong sidechain-sidechain ROEs from *N*Me-D-Trp[8] $H^{\delta1}$ to both *N*Me-Lys[9] H^γ protons and the strong highfield shift of one of the β protons (1.153 ppm) and the two γ protons (0.669 ppm, 0.872 ppm) of *N*Me-Lys[9], (Table 2.5) further suggest the close proximity of these *N*Me-Lys[9] protons to the surface of the indolyl ring system. Despite of the apparent close proximity of these side-chains, the MD trajectory suggests some flexibility for the χ_1 and χ_2 dihedral angles of both residues. However, as clustering of these side-chains was successfully correlated with sst receptor activity for other analogs,[223] the close contact of these side-chains has to be assumed also for the sst_2 bound state of 3-*N*Me-(D-Trp[8],Lys[9],Phe[11])-seglitide.

Overall, the $^3J_{H\alpha-H\beta}$ coupling constants agree well with χ_1 rotamer populations that were observed in the MD simulation (Figure 2.9).

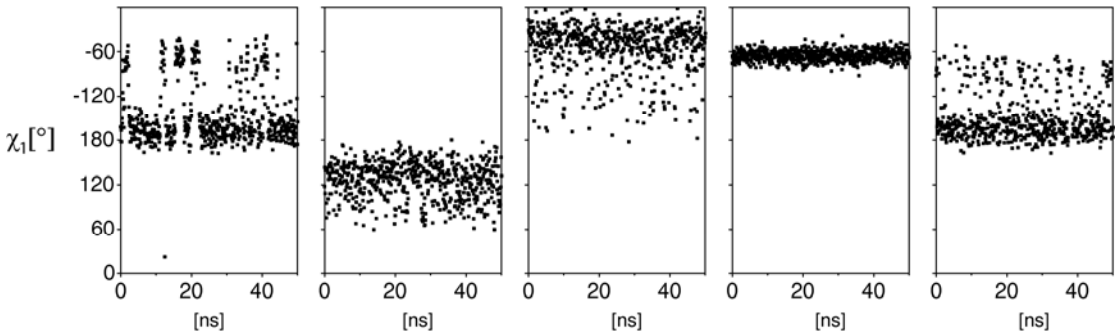

Figure 2.9: χ_1 dihedral angles as observed during 50 ns MD simulation from residue Tyr^7 on the left in sequential order to residue *N*-Me-Phe^{11} on the right.

3 Di-*N*-methylated Analogs of *c*(RGDfV) Targeting Integrin Subtype αvβ3 Selectively

This project was a collaboration with my former colleagues Carles Mas-Moruno, Lucas Doedens and Andreas Frank, who synthesized the cyclic peptides under investigation and performed solid-phase binding assays as well as preliminary NMR studies. Molecular docking was contributed by Prof. Luciana Marinelli, Prof. Ettore Novellino and Sandro Cosconati from the Università di Napoli "Federico II", Italy.

Motivation

The anti-angiogenic drug Cilengitide [*c*(RGDf*N*MeV)] is an unselective inhibitor for αvβ3, αvβ5, and α5β1 integrin subtypes. Integrin subtype selective Cilengitide analogs will help to better understand the importance of the individual integrin subtypes in angiogenesis and possibly reduce side effects. Within the current project, the αvβ3 specific analog *c*(RG*N*MeDf*N*MeV) was derived by introducing two *N*-methyl groups on the *c*(RGDfV) template. Conformational analysis and docking studies yielded a better understanding of the structural properties that are critical for discrimination between αvβ3 and αvβ5 integrins.

Chapter 3 and subchapters thereof are adapted in part from Mas-Moruno, C.; Beck, J. G.; Doedens, L.; Frank, A. O.; Marinelli, L.; Cosconati, S.; Novellino, E.; Kessler, H.; Increasing αvβ3 Selectivity of the Anti-Angiogenic Drug Cilengitide by *N*-Methylation, *Angewandte Chemie International Edition* **2011**, 50, 9496-500.

3.1 Cilengitide and Integrins

The drug Cilengitide, *c*(RGDf*N*MeV), is a cyclic RGD pentapeptide (R = arginine, D = aspartic acid, G = glycine) that is currently in clinical phase III for the treatment of brain tumors and in phase II for other cancer types.[224,225] The antitumoral properties of this peptide are based on its antagonistic activity for pro-angiogenic integrins, such as αvβ3, αvβ5, or α5β1. However, the specific roles of these integrin subtypes in angiogenesis and cancer are not yet clear and fully understood. In the following, di-*N*-methylated analogs of the stem peptide *c*(RGDfV) are presented, which retain an αvβ3-binding activity in the nanomolar range but have lost most of the activity for integrins αvβ5 and/or α5β1. Highly active and selective peptides for αvβ3 are important tools to study the specific role of this integrin in angiogenesis and cancer.

Integrins are heterodimeric receptors that govern cell–cell and cell–extracellular matrix (ECM) interactions, and play crucial roles in a plethora of cellular functions.[226] The fact that many integrins are involved in pathological processes, such as tumor angiogenesis, has stimulated their study as therapeutic targets.[227-230] A number of integrin receptors recognize and bind the tripeptide sequence RGD, which is a prominent cell adhesion motif present in ECM proteins.[231,232] Mimicking this tripeptide sequence with RGD-peptides or peptidomimetics is hence a promising approach to target integrins involved in angiogenesis and to develop anti-cancer agents.[9,224,225,228,233,234]

It is known that αvβ3 and αvβ5 are involved in two different angiogenic pathways.[235] Whereas angiogenesis induced by basic fibroblast growth factor (bFGF) or tumor necrosis factor α depends on αvβ3, angiogenesis triggered by vascular endothelial growth factor (VEGF) or transforming growth factor-α is αvβ5-dependent. These two integrins are also described to be important mediators in the regulation of hypoxia in glioblastomas.[236] However, mice lacking either αv or β3 and β5 integrins showed extensive angiogenesis.[237,238] These intriguing results were a matter of debate and challenged our understanding about the role of these two integrins in angiogenesis.[239-241] The integrin α5β1 is also highly expressed in angiogenic vasculature by several angiogenic stimuli, such as bFGF but not by VEGF.[242,243] Since αvβ3, αvβ5 and α5β1 have partially overlapping ligand affinities,[232] it is plausible that α5β1 might substitute the pro-angiogenic activity of the other integrins. Paradoxically, another recent study showed that low concentrations of Cilengitide stimulates VEGF-mediated angiogenesis.[244] Although the doses used in this study are far lower than therapeutic concentrations[245,246] and hence such a “pro-

angiogenic" effect is not likely to be observed in the clinical studies, it becomes evident that a better understanding of anti-angiogenic agents is necessary.[244]

3.2 Activity of di-*N*-methylated *c*(RGDfV) Analogs

It was already shown in the preceeding chapter 2 but also in previous publications that *N*-methylation can increase the selectivity towards specific receptor sub-types.[247-253] Selectivity is often caused by the induction of conformational constraints in the peptide backbone, which lead to preferred single conformers that are essential for biological activity.[43,247,253] This suggested that further *N*-methylation of Cilengitide could result in enhanced selectivity profiles. For this reason a library containing all the di-*N*-methylated analogs of *c*(RGDfV) (Figure 3.1) was designed and synthesized.

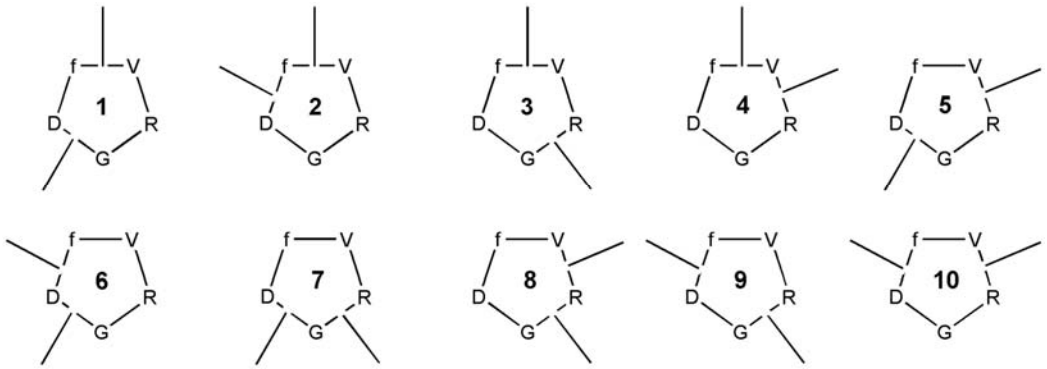

Figure 3.1: Schematic representation of the library of di-*N*-methylated analogs of *c*(RGDfV).

The impact of the extra *N*-methylation on Cilengitide in terms of integrin binding activity and selectivity was evaluated using an ELISA-type solid-phase binding assay for the pro-angiogenic integrins αvβ3, αvβ5, and α5β1 as well as for the platelet receptor αIIbβ3 (Table 3.1).

The analogs in which Val was non-methylated (**5**–**10**) showed a dramatic decrease in αvβ3-binding activity, regardless of the position of the *N*-methylated residues. This effect was particularly observed for peptides **9** and **10**, in which the antagonistic activity for the vitronectin receptor was totally lost. In contrast, when Val was *N*-methylated, the resulting analogs (**1**–**4**) displayed low nanomolar activity for the αvβ3 integrin receptor. These results indicate that *N*MeVal is a crucial residue to retain the activity for this receptor, probably by inducing a preferred bioactive αvβ3-binding conformation.[9,254]

Table 3.1: The di-*N*-methylated analogs of Cilengitide and their binding affinity (IC_{50} in nM) towards αvβ3, αvβ5, α5β1 and αIIbβ3.

		αvβ3	αvβ5	α5β1	αIIbβ3	αvβ5/ αvβ3	α5β1/ αvβ3
Cilengitide	*c*(RGDf***N*MeV**)	0.65 (±0.07)	11.7 (±1.5)	13.2 (±0.6)	815 (±60)	18	20
1	*c*(RG***N*MeD**f***N*MeV**)	5.9 (±2.5)	>3000	270 (±95)	>1000	>500	46
2	*c*(RGD***N*Mef*N*MeV**)	36.2 (±8.1)	>10000	>2000	>10000	>250	55
3	*c*(R***N*MeG**Df***N*MeV**)	13.2 (±1.8)	313 (±122)	>1000	>2000	24	>75
4	*c*(***N*MeR**GDf***N*MeV**)	1.9 (±0.3)	40.9 (±3.2)	39.5 (±1.3)	>1000	22	21
5	*c*(***N*MeR**G***N*MeD**fV)	142 (±33)	>10000	>2000	>10000	>70	>14
6	*c*(RG***N*MeD*N*Mef**V)	173 (±12)	>10000	>5000	>10000	>58	>29
7	*c*(R***N*MeG*N*MeD**fV)	965 (±96)	>10000	>1000	>10000	-	-
8	*c*(***N*MeR*N*MeG**DfV)	>1000	>10000	>10000	>2000	-	-
9	*c*(R***N*MeG**D***N*Mef**V)	>10000	>10000	>10000	>2000	-	-
10	*c*(***N*MeR**GD***N*Mef**V)	>10000	>10000	>10000	>10000	-	-

Analogs **9** and **10**, which are totally inactive, are both *N*-methylated at D-Phe. It could be hypothesized that this biological effect was due to the loss of a hydrogen-bond donor at this position;[255] however, peptide **2**, which also has a *N*Me-D-Phe unit, exhibits a remarkable nanomolar antagonistic activity. The effect of *N*Me at the Arg residue is also interesting. In a previous study, a peptide with a single *N*-methylation of this residue showed an IC_{50} of 5.5 nm.[9] Herein, the presence of *N*MeArg is found in peptides with activities ranging from superpotent (1.9 nm, **4**), moderate (142 nm, **5**), low (>1000 nm, **8**) and very low (>10000 nm, **10**). These data clearly indicate that the biological activity of these peptides more strongly depends on their overall conformation rather than on the local effects of a single *N*-methylation.[256-258] Noteworthy, most members of the library are inactive for the integrins αvβ5 and α5β1. If we focus on peptides **1** to **4** (highly active for αvβ3) only **4** shows nanomolar activity for these receptors, with selectivity ratios very similar to Cilengitide. In contrast, in peptides **1** and **2** the activity for αvβ5 is strongly or fully suppressed, with selectivity ratios much higher than those found for Cilengitide (>500-fold for **1** and >250-fold for **2**). Compound **3** does not show an improved selectivity towards αvβ5 but towards α5β1. For all these compounds the selectivity of Cilengitide against αIIbβ3 was either maintained or improved. A strong reduction in binding activity for αvβ5 and α5β1 was also observed for analogs **5**–**10**. However, these peptides are of lower biological interest due to their low (or absent) affinity for αvβ3.

3.3 Structures of Selected di-*N*-methylated *c*(RGDfV) Analogs

To rationalize these findings and to explain the obtained selectivities in a better way, three peptides were chosen for structural studies: peptide **1**, a selective ligand that shows nanomolar activity for αvβ3 and low activity for αvβ5; peptide **4**, which is active for both receptors in the nanomolar range and therefore not selective; and peptide **10**, totally inactive for all integrins. Based on NMR spectroscopic assignments (Table 3.2), ROEs, homo- and heteronuclear scalar coupling constants, H^N temperature gradients, and on distance geometry calculations, distinct preferred structures could be derived for the three peptide backbones (Figure 3.2).

Table 3.2: Resonance assignment of **1**, **4**, and **10** in DMSO-d6 at 300 K. Chemical shifts are referenced on DMSO (^{1}H at 2.520 ppm).

1	H^N (H^{Me})	H^α	H^β	H^γ	H^δ	H^ε	H^ζ
Arg[1]	8.345	3.539	1.96	1.467	3.11	7.558	
Gly[2]	7.593	3.592 / 4.148					
***N*Me-Asp**[3]	(2.834)	4.638	2.398 / 2.920				
D-**Phe**[4]	8.07	5.011	proR: 3.092 proS: 2.764		7.189	7.243	7.173
***N*Me-Val**[5]	(2.859)	4.327	2.056	proR: 0.867 proS: 0.540			

4	H^N (H^{Me})	H^α	H^β	H^γ	H^δ	H^ε	H^ζ
***N*Me-Arg**[1]	(2.603)	4.732	1.689 / 2.069	1.350 / 1.475	3.160	7.610	
Gly[2]	8.256	3.395 / 3.740					
Asp[3]	8.670	4.661	proR: 2.822 proS: 2.452				
D-**Phe**[4]	7.459	4.990	proR: 2.917 proS: 2.852		7.183	7.253	7.200
***N*Me-Val**[5]	(2.749)	4.854	2.121	proR: 0.731 proS: 0.342			

10	H^N (H^{Me})	H^α	H^β	H^γ	H^δ	H^ε	H^ζ
***N*Me-Arg**[1]	(3.227)	3.707	1.838 / 2.022	1.401 / 1.582	3.145	7.591	
Gly[2]	8.334	3.331 / 4.099					
Asp[3]	7.217	4.879	proR: 2.723 proS: 2.295				
***N*Me**-D-**Phe**[4]	(2.667)	5.502	2.944 / 3.199		7.222	7.273	7.211
Val[5]	6.805	4.751	2.015	proR: 0.683 proS: 0.912			

The structures of **1**, **4**, and **10** possess pronounced differences. In peptide **1**, all peptide bonds are in *trans* configuration and all peptide bond planes, except of the Gly^2-*N*Me-Asp^3 peptide bond are oriented almost perpendicular to the plane of the

peptide ring (Figure 3.2). Characteristic dihedral angles for complete β- and γ-turns are missing. The C-O bond vectors of Arg[1], *N*Me-Asp[3] and D-Phe[4] are aligned parallel with respect to C^{α}-H^{α} bond vectors of the respective subsequent residues. Antiparallel orientations of these dipolar bonds is crucial for stabilizing peptide conformations.[180] Two similar ROEs between *N*Me-Asp[3] H^{Me} and both Gly[2] α protons (Table C.1) clearly support the Gly[2]-*N*Me-Asp[3] peptide bond to be in plane with the peptide ring. Extended 50 ns MD simulation in explicit DMSO further indicated significant flexibility of the Gly residue and the adjacent peptide bonds.

According to the backbone dihedral angles of *N*Me-Val[5] (Φ=-121.5°, Ψ=87.1°), *N*Me-Arg[1] (Φ=-114.5°, Ψ=164.2°) and an intermediary *cis* configured peptide bond, peptide **4** possesses a β-turn of type VIb along these residues (Figure 3.2). A strongly negative temperature gradient of Gly[2] H^N (-5.04 ppb/K in DMSO) indicates that the turn is not stabilized by a hydrogen bond. Asp[3] is located in position i+1 of an inverted γ-turn. Asp[3] Φ=-90.4° and Asp[3] Ψ=90.9° suggest a weak hydrogen bond between Gly[2] O' and D-Phe[4] H^N, that is also supported by protection of D-Phe[4] H^N from the solvent (δ = 7.459 ppm; $\Delta\delta/\Delta T$ = -2.34 ppb/K). The C-O bond vectors of *N*Me-Arg[1], Gly[2], Asp[3] and D-Phe[4] are aligned parallel with respect to C^{α}-H^{α} bond vectors of the respective subsequent residue. Extended 50 ns MD simulation in explicit DMSO indicated significant flexibility of the *N*Me-Arg[1]-Gly[2] and the Asp[3]-D-Phe[4] substructures.

A γ-turn centered at *N*Me-D-Phe[4] (Φ = 79.8°, Ψ = -95.1°) with a characteristic strong hydrogen bond between Asp[3] O' and Val[5] H^N (δ = 6.805 ppm; $\Delta\delta/\Delta T$ = 0.53 ppb/K) is found in peptide **10** (Figure 3.2). No further β- and γ-turns are present. The C-O bond vectors of Gly[2], Asp[3] and *N*Me-D-Phe[4] are aligned parallel with respect to C^{α}-H^{α} bond vectors of the respective subsequent residue. Extended 50 ns MD simulation in explicit DMSO indicated significant flexibility of the Arg[1]-Gly[2] substructures.

Further, molecular-docking studies of these peptides were attained into the αvβ3 X-ray structure[254] as well as in newly constructed αvβ5 homology models. Docking of **1** on αvβ3 showed that this peptide is able to interact with this receptor similarly to Cilengitide (Figure 3.3 a). Nevertheless, note that the substitution of the Asp residue in Cilengitide with *N*MeAsp in **1** does affect to a certain extent the binding mode to αvβ3. In particular, this modification causes the loss of a hydrogen bond with (β3)-D216 CO but more importantly an evident relocation of the lower part of the peptide occurs (Figure 3.3 b). This result explains why **1** has approximately tenfold lower affinity to αvβ3 than Cilengitide (5.9 nm and 0.65 nm, respectively).

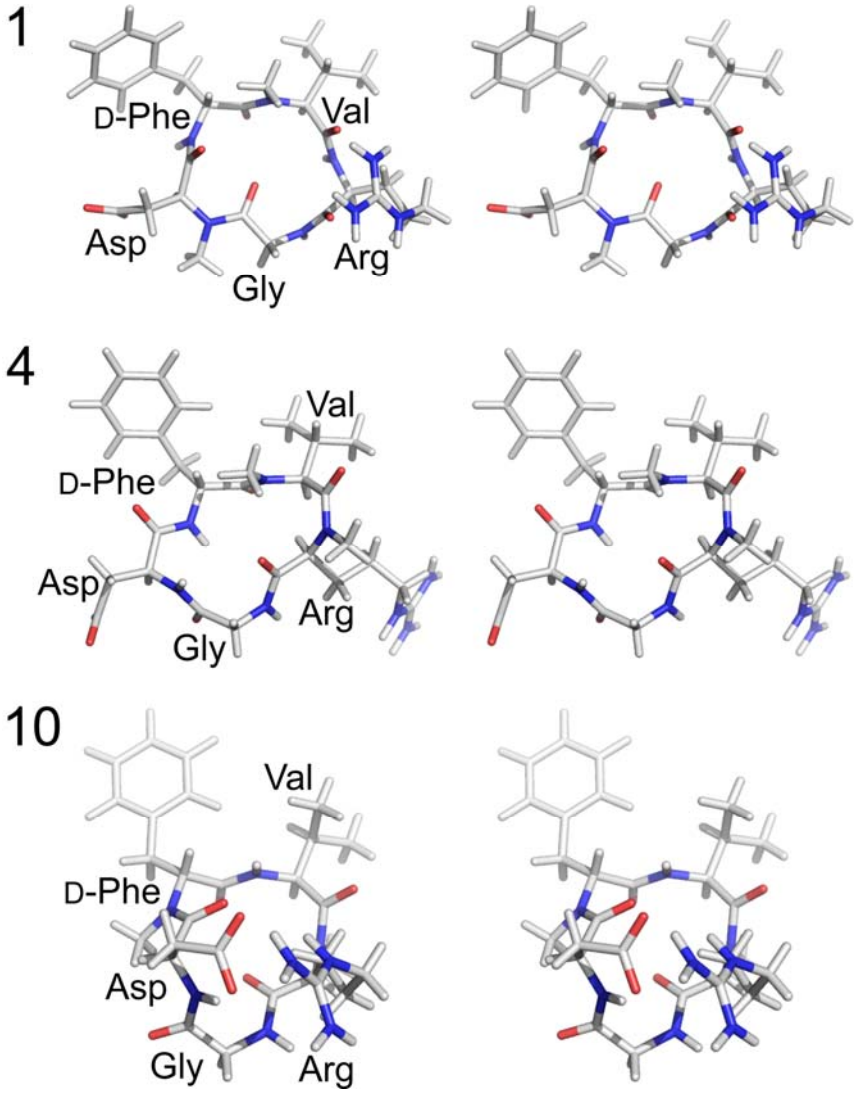

Figure 3.2: Stereoviews of peptides **1**, **4**, and **10**.

For docking to the αvβ5 receptor, 100 αvβ5 homology models, differing in the specificity determining loop (SDL) conformation, were generated. Prior to docking calculations, all 100 models were tested for their capability to host the unselective Cilengitide and only those able to bind were further considered for docking of **1**, **4**, and **10**. As predicted, in these models Cilengitide assumed a binding pose similar to the experimentally determined bound state in αvβ3.[254]

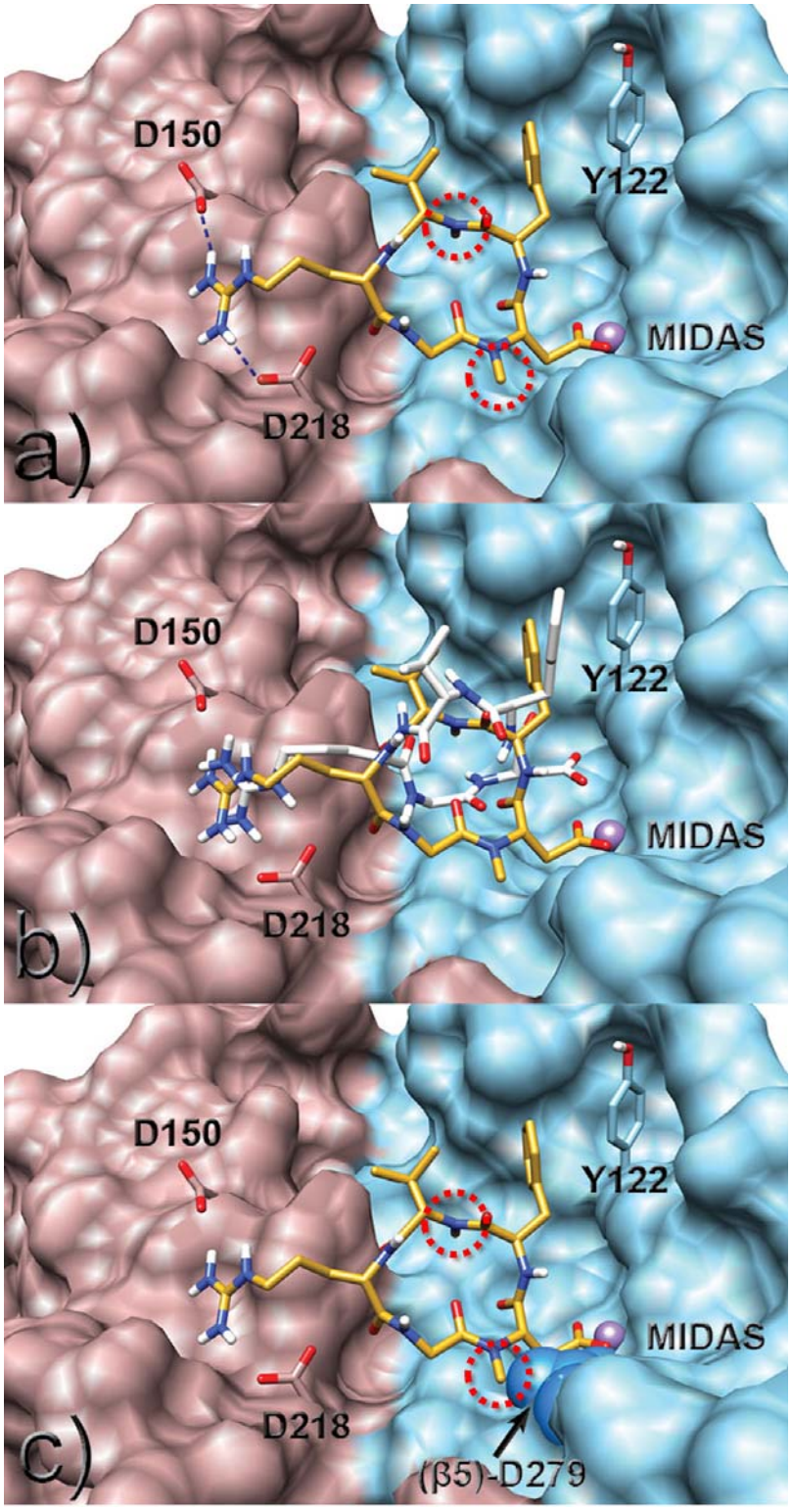

Figure 3.3: (a) Structure of **1** (yellow) docked in the αvβ3 integrin binding pocket. The αv and β3 subunits are represented by the pink and cyan surfaces, respectively. In both subunits the amino acid side-chains important for the ligand binding are represented as sticks. The metal ion in the MIDAS region is represented by a magenta sphere. For comparison reasons, the X-ray structure of Cilengitide (white sticks) (b) as well as the (β5)-D279 residue (blue spheres) (c) are represented. Red circles highlight *N*-methyl groups in a) and c).

Interestingly, analysis of the multiple docking simulations performed on the αvβ5 selected models demonstrated that in the case of **1**, a well-defined binding mode could not be easily identified. The ligand Asp *N*-methylation causes a pronounced effect on the binding to αvβ5. In an attempt to rationalize such a behavior, the predicted **1**/αvβ3 complex was superimposed to the modeled αvβ5 receptor structure. As represented in Figure 3.3 c), it is clear that the (β3)-A252/(β5)-D279 mutation results in a remarkable restriction of the available space. The methyl group of the *N*MeAsp would be hardly adapted in the same binding fashion as in the **1**/αvβ3 complex. This, in turn, seems to strongly affect the RGD binding to αvβ5.

Docking studies were also helpful in suggesting why the *N*-methylation of the Arg residue (**4**) is ineffective in producing the αvβ3/αvβ5 selectivity (Table 3.1). In fact, such a modification, while inducing a different peptide conformation with respect to Cilengitide, does not influence the binding of **4** which is still assured by the conserved RGD sequence (Figure 3.4).

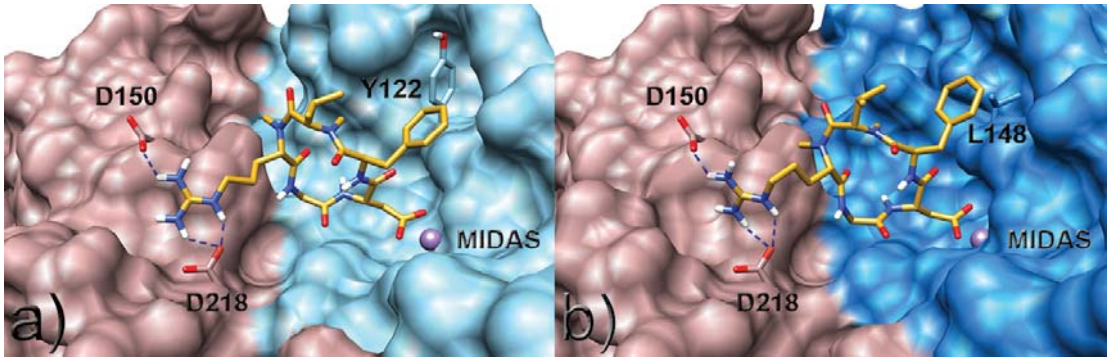

Figure 3.4: Structure of **4** (orange) docked in the αvβ3 (a) and αvβ5 (b) integrins. The αv, β3 and β5 subunits are represented by pink, cyan and blue surfaces, respectively. In both subunits the amino acid side-chains important for the ligand binding are represented as sticks. The metal ion in the MIDAS region is represented by a magenta sphere.

Conversely, docking of **10** revealed that this peptide is unable to efficiently bind to the metal-ion-dependent adhesion site (MIDAS) and the αv subunit β propeller at the same time. Indeed, a comparison between the NMR solution structure of **10** and the X-ray bound conformation of Cilengitide showed that the double methylation of Arg and D-Phe residues (**10**) induces marked differences in distance between the Arg and Asp C^{α} atoms (5.0 Å and 6.4 Å for **10** and Cilengitide, respectively) as well as in the orientation of the C^{α}-C^{β} bond vectors of the same residues. Both features are well known to be critical for integrin binding and selectivity.[224,259,260] Hence, unlike in **1** and **4**, the double *N*-methylation in **10** seems to induce a non-productive peptide conformation that prevents binding to αvβ3 and αvβ5 integrins.

In conclusion, it was demonstrated that double *N*-methylation of the *c*(RGDfV) peptide backbone allows for fine tuning of the peptide's biological activity by inducing preferred bioactive conformations. Certain members of the library of di-*N*-methylated *c*(RGDfV) retained nanomolar affinity for αvβ3 but were totally inactive for the integrin subtypes αvβ5 and α5β1, thus improving the selectivity of Cilengitide. Compounds displaying such selectivity profiles represent new promising tools to study the role of closely related integrins in essential biological processes.

4 Orally Bioavailable Peptides

This project was a collaboration with my former and current colleagues Jayanta Chatterjee, Burkhardt Laufer and Stefanie Neubauer, who synthesized the peptides under investigation. Marelli Udaya Kiran and Andreas Frank verified structures and performed initial NMR analysis.

Motivation

The widespread development of peptides as therapeutics is delimited by insufficient oral bioavailability of most peptides. Only few possess surprisingly high oral bioavailability and the reasons for this exceptional behavior are not well understood. Analyzing unique structural properties that are found in permeable peptides can help to rationalize the oral bioavailability of peptides in terms of structural models.

4.1 Introduction

Oral bioavailability is still one of the most appreciated properties of drugs. Empirical rules such as Lipinski's "rule of five" or Veber's rules consider parameters such as the number of rotatable bonds and hydrophobic patch size in order to filter out drug candidates that are suggested not to be absorbed into the bloodstream upon oral administration.[11,12] However, as described by Zhang and Wilkinson in 2007,[261] 20 % of all FDA-approved oral drugs did not agree with all "rule of 5" criteria and only 70 % of the drugs that fulfilled these criteria had been approved for oral use.[e] Accordingly, neither compliance with simple criteria like "the rule of 5" does guarantee for oral bioavailability, nor does their violation very reliably predict insufficient oral bioavailability.

However, as suggested by "the rule of 5" most peptides are not (or almost not) orally bioavailable. On the other hand, a number of peptides are surprisingly well absorbed within the gastrointestinal (GI) tract. Amanitins[262], phalloidin[12], antamanide[12], cyclosporine A[263,264], some cyclic hexa- and octapeptidic somatostatin analogs[194,205,265], microcystin LR[266], a cyclic agonist of melanocortin receptor subtype 4[267], and some triple and fourfold *N*-methylated stereoisomers of cyclo(-Leu-Leu-Leu-Leu-Pro-Tyr-)[268] possess significant oral bioavailability and/or intestinal permeability. In spite of an oral bioavailability of only 0.1 %[269], the vasopressin analog desmopressin[270] is (also) used orally. Moreover several *N*-alkylated cyclopeptides and depsipeptides lead to different kinds of intoxications upon oral administration. This suggests that many other *N*-alkylated cyclopeptides are absorbed into the bloodstream, although scientific publications describing explicitly the oral bioavailability of such compounds are very rare.

Although among peptides, oral bioavailability is preferably found for cyclic and *N*-methylated analogs,[271] the structural features that are responsible for the oral bioavailability of peptides are not well understood. The rational design of peptide drugs that possess sufficient oral bioavailability is therefore still a daunting task. A clearer understanding of the structural properties that make some peptides cross the GI tract into the bloodstream would promote the development of peptides as drugs. As in peptides, Φ, Ψ, and χ dihedrals can adopt many different angles, structural properties favoring oral bioavailability can only be identified in three-dimensional structures.

[e] Based on FDA-approved drugs in 2007

The different mechanisms that seem to operate in the absorption of the structurally heterogeneous orally bioavailable peptides introduce a further level of complexity to delineate the absorption of orally bioavailable peptides in the GI tract in terms of structural properties. The most important mechanisms for the absorption of drugs in the intestine include passive diffusion through enterocytes (transcellular pathway), passive paracellular diffusion (paracellular pathway), endo-/exocytosis, uptake via the dipeptide carrier, and the release from enterocytes back into the lumen by p-glycoprotein.[272] While internal hydrogen bond formation clearly suggests membrane permeation (transcellular pathway) for the most lipophilic peptides, e.g. *N*-methylated cyclo(-Leu-Leu-Leu-Leu-Pro-Tyr-)[268], there seems to be another route involved for the transport of peptides that possess multiple polar side-chains, like α-amanitin.[262]

The extensive study of intestinal bioavailability of a library of 54 differentially *N*-methylated cyclic (-a-A-A-A-A-A-) peptides showed that multiple *N*-methylation could dramatically improve intestinal permeability of hydrophilic cyclic peptides. Although the exact transport route of these peptides was not fully characterized, the data however, suggested a facilitated diffusion.[273]

The permeation of Caco-2[f] monolayers indicated a variable pattern of oral bioavailability of cyclic (-a-A-A-A-A-A-) peptides, depending upon the site and number of *N*-methylation. The highest Caco-2 permeation was observed for eight peptides that possessed either two or four *N*-methyl groups (Figure 4.1, B-D). Caco-2 permeation of these peptides was similar to testosterone ($P_{app} > 1 \times 10^{-5}$ cm/s) or even higher (testosterone: a marker of transcellular permeability). On the contrary, the vast majority of the other 46 peptides possessed much lower Caco-2 permeability, similar to or even less than mannitol ($P_{app} < 1 \times 10^{-6}$ cm/s), a marker for paracellular permeability.

[f] The term 'Caco-2' refers to a continuous line of heterogeneous human epithelial colorectal adenocarcinoma cells.

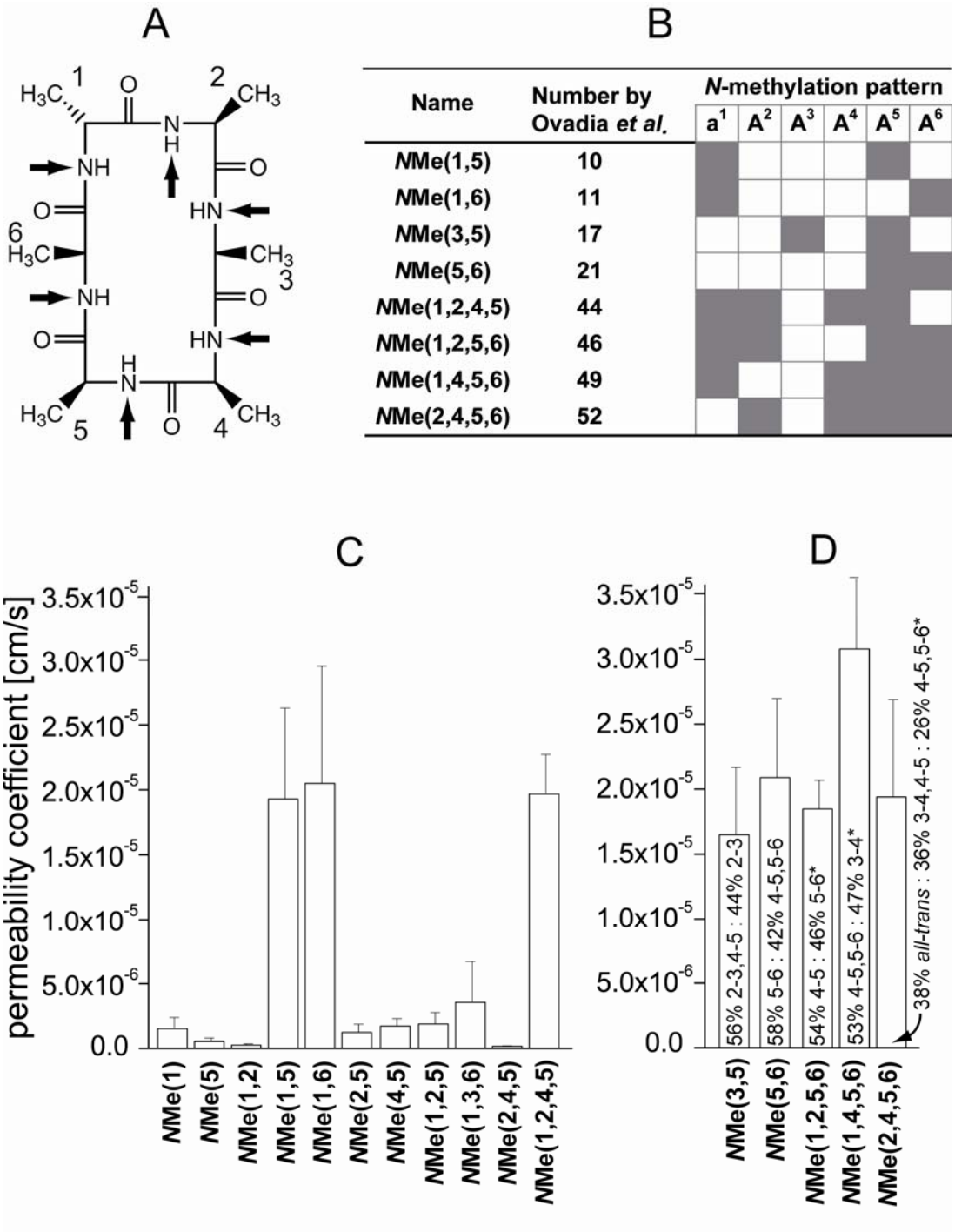

Figure 4.1: (A) *N*-methylated cyclic (-a-A-A-A-A-A-) peptides described by Ovadia *et al*.[273] (B) *N*-methylation pattern of eight peptides that possess highest Caco-2 permeability. (C) Caco-2 permeability coefficients of all conformationally homogeneous peptides and (D) heterogeneous peptides that are considered for structural analysis. The numbers in the bars denote the population of the conformers (%) and the sites of *cis* peptide bonds. *: Additional minor conformations were observed.

4.2 Lipophilicity and Permeation Pathway

In the $PAMPA_{lecithin}$ tests none of the better-performing permeable peptides crossed the artificial membane.[273] Moreover, the reversed phase HPLC revealed shorter retention times in contrast to testrosterone which eluted much slower. This observation did not correlate with Caco-2 permeation rates of the peptides (Figure 4.2). Similar to PAMPA tests, this suggested a considerably higher lipophilicity of testosterone, as compared to all the peptides. In spite of high Caco-2 permeation rates of these peptides (comparable to the permeability of testosterone), the transcellular diffusion mechanism must therefore be excluded. This clearly suggests that other mechanisms lead to the high Caco-2 permeation rates as opposed to the one suggested by White *et al.* for orally bioavailable *N*-methylated stereoisomers of cyclo(-Leu-Leu-Leu-Leu-Pro-Tyr-).[268]

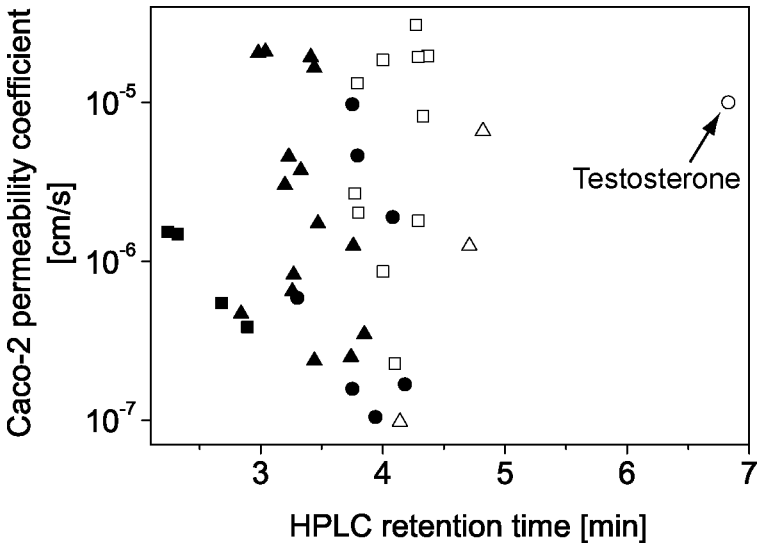

Figure 4.2: HPLC retention time and Caco-2 permeation of single (■), double (▲), triple (●), tetra (□), penta (Δ) *N*-methylated cyclo(-a-A-A-A-A-A-) peptides, and testosterone (○).

Based on the two-dimensional chemical structures of the highly-permeable peptides, almost no common structural property could be assigned besides the presence of either two or four *N*-methyl groups.[273] Therefore, a detailed conformational analysis was performed to identify the three-dimensional structural behavior, which leads to high Caco-2 permeability.

4.3 NMR Conformational Studies

For 43 out of 54 peptides, two or more sets of ^{1}H NMR signals indicated equilibria of two or more preferred *cis-trans* isomers with population of at least 5 %. Side-conformers (*cis-trans* isomer populations ≥ 5 %) were not only observed for weakly permeable peptides, but also for five of the eight highly permeable peptides (Figure 4.1 D). In addition to the highly Caco-2 permeable peptides, three-dimensional structures were also derived for conformationally homogeneous peptides (Figure 4.1 C), as for these peptides; the observed Caco-2 permeability could be analyzed based on a single preferred conformation. Among the eleven conformationally homogeneous peptides (Figure 4.1, C) and the five conformationally heterogeneous peptides under investigation (Figure 4.1, D), only *N*Me(1,6), *N*Me(1,5), and *N*Me(1,2,4,5) were found to possess both high permeability and conformational homogeniety. These peptides were considered as highly Caco-2 permeating structures (Figure 4.3) and served as templates for the analysis of other conformationally homogeneous or well permeable peptides, whereas for the other highly permeable peptides *N*Me(3,5), *N*Me(5,6), *N*Me(1,2,5,6), *N*Me(1,4,5,6) two preferred conformations and for *N*Me(2,4,5,6) even three preferred conformations had to be considered.

4.4 First highly Caco-2 permeable Template Structure

The first template structure is represented by the conformationally homogeneous peptide *N*Me(1,6). It possesses a typical all-*trans* cyclohexapeptide structure with two opposite β-turns of type II (Figure 4.3, top). *N*Me-Ala^{6} and *N*Me-D-Ala^{1} are located in positions i+1 and i+2 of one of these turns. A characteristic hydrogen bond is formed between the carbonyl oxygen atom of the ith residue of this turn (Ala^{5} O') and the amide proton of residue i+3 (Ala^{2} H^{N}). Ala^{3} and Ala^{4} are located in positions i+1 and i+2 of the opposite turn, that also possesses a characteristic hydrogen bond between the carbonyl oxygen atom of residue i of this turn (Ala^{2} O') and the amide proton of residue i+3 (Ala^{5} H^{N}). The amide protons of Ala^{2} (7.201 ppm, +0.5 ppb/K) and Ala^{5} (7.585 ppm, -1.7 ppb/K) are shifted towards higher fields and Ala^{2} H^{N} is very efficiently shielded from the solvent, which is well consistent with the hydrogen bonds described above.

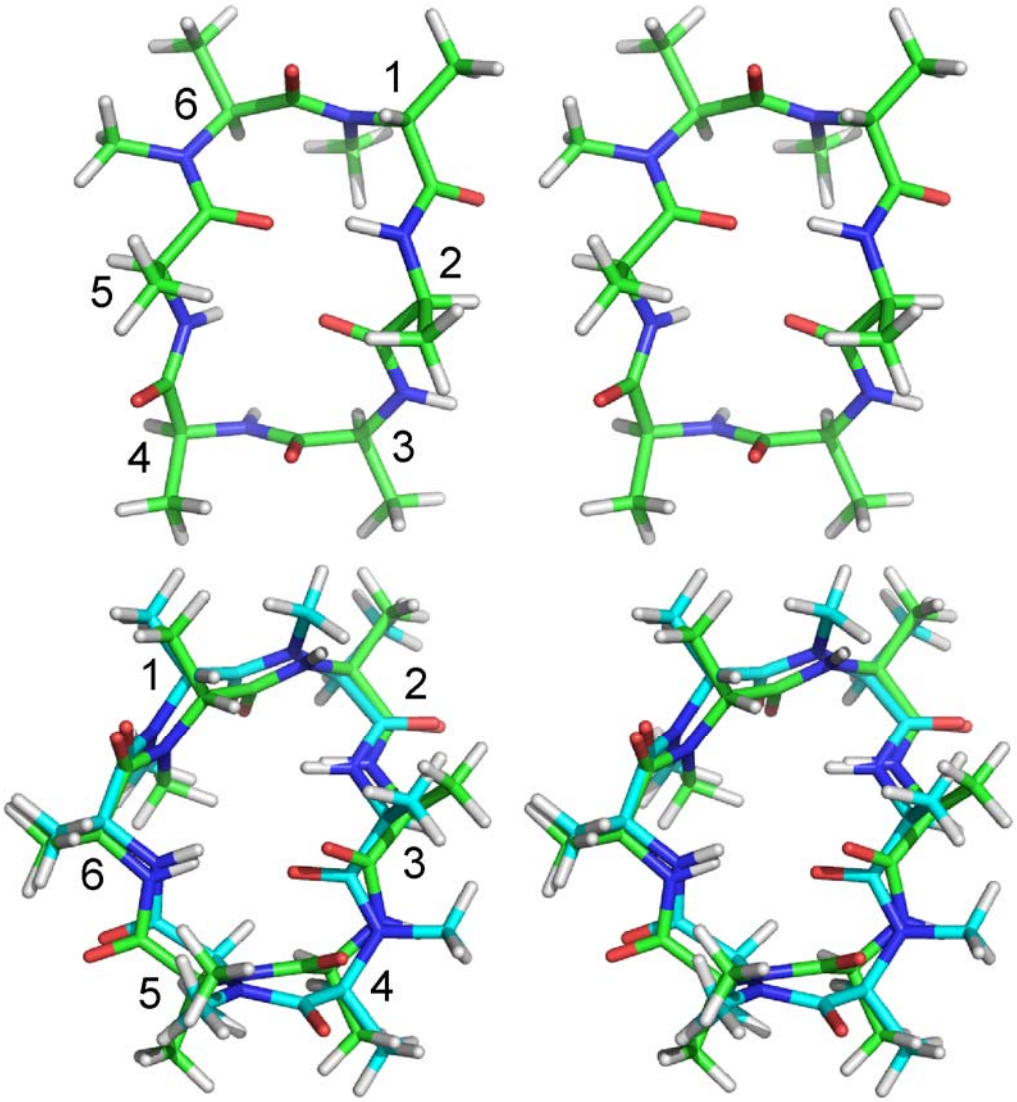

Figure 4.3: Stereostructures of conformationally homogeneous Caco-2 cell permeating cyclohexapeptides that are structural templates for high oral bioavailability. Top: *N*Me(1,6), bottom: overlay of *N*Me(1,5) and *N*Me(1,2,4,5).

The structure shown in top of Figure 4.3 also agrees with 10 intraresidual, 19 sequential interresidual, and 8 non-sequential interresidual ROEs (Appendix D, Table D.23). The Φ dihedral angles of the protonated amino acids also agree well with the according $^{3}J_{HN\text{-}H\alpha}$ coupling constants of 9.0 Hz (Ala^{2}), 4.2 Hz (Ala^{3}), 7.6 Hz (Ala^{4}), and 7.8 Hz (Ala^{5}).

Beside *N*Me(1,6), only four of all the peptides under investigation displayed an all-*trans* conformation. These peptides represent the weakly Caco-2 permeable peptides *N*Me(1), *N*Me(1,2), and *N*Me(1,3,6) along with one of three conformers populated by the highly Caco-2 permeable peptide *N*Me(2,4,5,6).

H^{N} and C^{β} chemical shifts, the temperature dependence of H^{N} chemical shifts and the $^{3}J_{HN\text{-}H\alpha}$ coupling constants in the four subsequent residues Ala^{3}-Ala^{6} of *N*Me(1,2) are very similar to the respective parameters in the four subsequent residues Ala^{2}-Ala^{5} of

*N*Me(1,6) (Figure 4.4). This suggests a high conformational similarity between the structures of *N*Me(1,2) and *N*Me(1,6), but with altered sequence positions of the Ala residues (Figure 4.4 A and B).

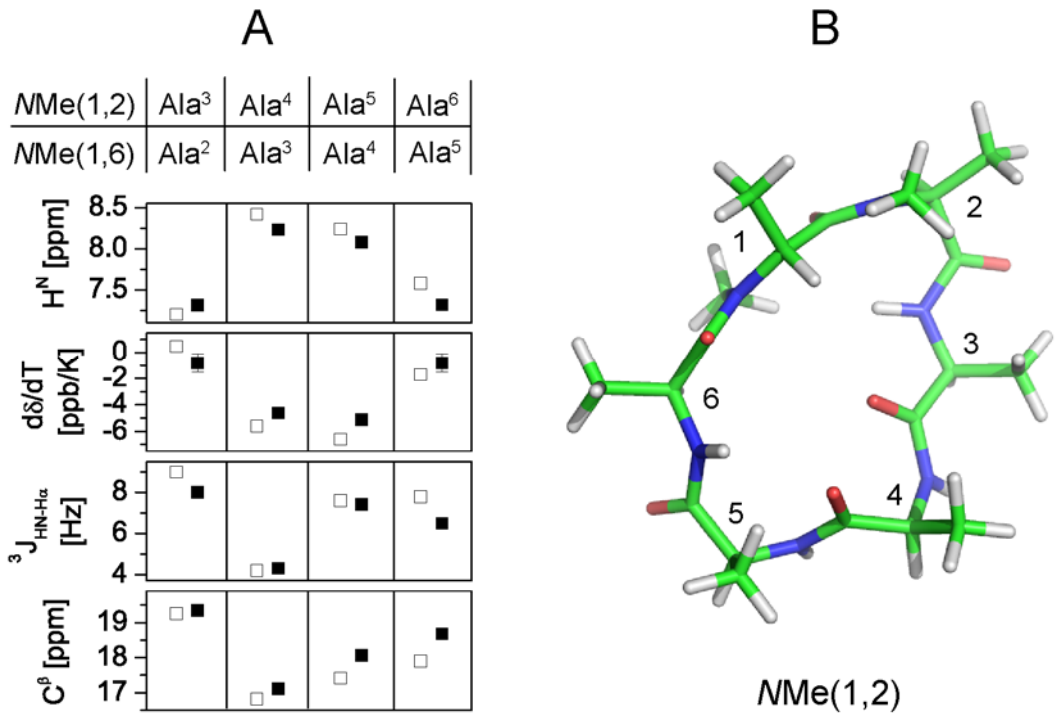

Figure 4.4: Comparison of H^N chemical shifts, their temperature dependence, $^3J_{HN\text{-}H\alpha}$ couplings, and C^β chemical shifts of the four subsequent non-*N*-methylated Ala residues in *N*Me(1,6) (□) and *N*Me(1,2) (■).

The structure calculated for *N*Me(1,2) (Figure 4.4 B) is similar to the one of *N*Me(1,6) shown in Figure 4.3 but there are also significant structural differences to *N*Me(1,6), that exceed a simple shift of the peptide sequence along the scaffold. The *N*-methyl group of the peptide bond linking the residues in positions i+1 and i+2 of the upper β-turn is pointing up, which indicates a β-turn of type I with *N*Me D-Ala^1 and *N*Me Ala^2 in positions i+1 and i+2, respectively. As the peptide bond linking the residues in position i (Ala^6) and i+1 (*N*Me-Ala^1) is rotated out of the peptide plane, this β-turn does not possess ideal geometry and the characteristic $O'_i - H^N_{i+3}$ peptide bond is not formed. The high field shift and low temperature dependence of Ala^3 H^N (7.316 ppm, -0.8 ± 0.7 ppb/K) are indicative for strong shileding from the solvent. Shielding from the solvent is achieved by the central orientation of Ala^3 H^N (see Figure 4.4 B), which is also supported by a strong ROE between Ala^3 H^N and *N*Me-Ala^1 H^α.

In the lower turn, which is centered at Ala^4 and Ala^5, Ala^5 H^N is pointing down, which indicates similarity to type II β-turn geometry. However, the close proximity of Ala^4 O' and Ala^6 H^N further indicates the presence of a γ-turn. It is not absolutely clear,

whether Ala^6 H^N is hydrogen bonded to Ala^4 O' or Ala^3 O'. However, strong shielding from the solvent is clearly indicated by a strong shift to higher field (7.320 ppm) and by its low temperature dependence (-0.8 ± 0.7 ppb/K). However, beside of the large number of distance restraints that are well satisfied by the structure shown in Figure 4.4, few distance restraints are violated significantly (Table D.21), which suggests some flexibility for *N*Me(1,2), especially along Ala^6. As described in Appendix D, even more flexibility was observed for the other all-*trans* peptides *N*Me(1) and *N*Me(1,3,6).

To conclude, the first structural template possesses an all-*trans* scaffold with β-turns of type II along the two *N*-methylated residues and along Ala^3-Ala^4. This structure is only found for *N*Me(1,6). In four other peptides all-*trans* conformers are found only with β-turns of other type in different sequence positions (*N*Me(1,2)), in fast exchange with other conformations (*N*Me(1) and *N*Me(1,3,6)), or in slow exchange with other conformations (*N*Me(2,4,5,6)). The observation of low Caco-2 permeability for *N*Me(1), *N*Me(1,2), and *N*Me(1,3,6), suggests that similar structures with β-turns of other type in different sequence positions are not orally bioavailable. The specific conformation of *N*Me(1,6) seems to be a key for high oral availability. Any alteration of the *N*-Me pattern disrupt its structure and suppress its Caco-2 permeability.

4.5 Second highly Caco-2 permeable Template Structure

The second Caco-2 permeable template is derived from the conformations of *N*Me(1,5) and *N*Me(1,2,4,5) (Figure 4.3). It possesses β-turns along D-Ala^1-Ala^2 and along Ala^4-Ala^5. A *cis* peptide bond between Ala^4 and Ala^5 leads to a characteristic type VI geometry for the latter β-turn. A key prerequisite for this conformation is the presence of Ala^5 *N*-methylation, as only this allows for the occurrence of the characteristic *cis* peptide bond. Accordingly, the least *N*-methylated structure that occupies this conformation is *N*Me(5) (Figure 4.5, top). Additional *N*-methylation of D-Ala^1, Ala^2, and Ala^4 does not significantly alter the conformation, as these amide protons are solvent exposed (Figure 4.5, second row from top). It should be emphasized here, that *N*-methylation of Ala^3 and Ala^4 which possess similarly solvent exposed amides in the first template structure (*N*Me(1,6), Figure 4.3 top) leads at least to a parital disruption of the *N*Me(1,6) structure. The structure of *N*Me(5) is also conserved in the triply *N*-methylated analogs *N*Me(1,2,5) and *N*Me(2,4,5) as well as for the tetra *N*-methylated analog *N*Me(1,2,4,5) as shown in Figure 4.5. As the conformation of this template seems to be highly preferred whenever Ala^3 and Ala^6

are not *N*-methylated, high cooperativity between the upper β-turn with the D-configured residue in position i+1 and the lower β-turn (type VI) has to be assumed.

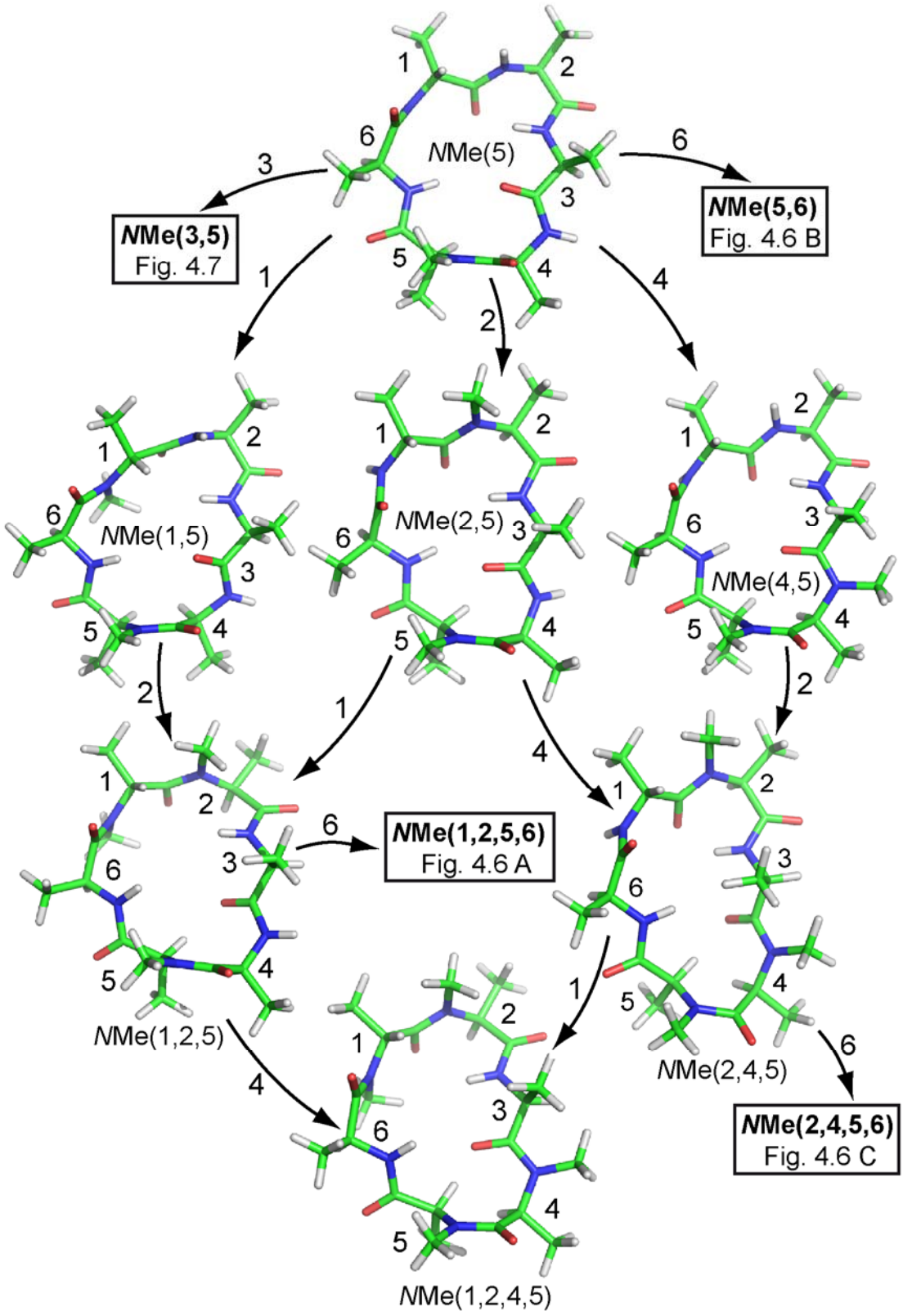

Figure 4.5: The structures of peptides *N*Me(5), *N*Me(1,5), *N*Me(2,5), *N*Me(4,5), *N*Me(1,2,5), *N*Me(2,4,5), and *N*Me(1,2,4,5) are very similar. Starting from *N*Me(5) as the parent peptide that possesses the characteristic *cis* peptide bond between residues Ala^4 and Ala^5, the other six peptides can be considered as higher *N*-methylated analogs. The numbers given on the arrows indicate the sequence position on which new *N*-methyl groups are attached.

As Ala^6 H^N is hydrogen bonded to Ala^3 O' in the structures with a single *cis* peptide bond between Ala^4 and Ala^5, *N*-methylation of Ala^6 strongly distorts the overall conformation of the peptide. *N*-methylation at Ala^6 of the conformationally homogeneous peptides *N*Me(5), *N*Me(1,2,5), and *N*Me(2,4,5), for example, leads to equilibria of two conformers (*N*Me(5,6), *N*Me(1,2,5,6)) or even three conformers (*N*Me(2,4,5,6)) (Figure 4.6).

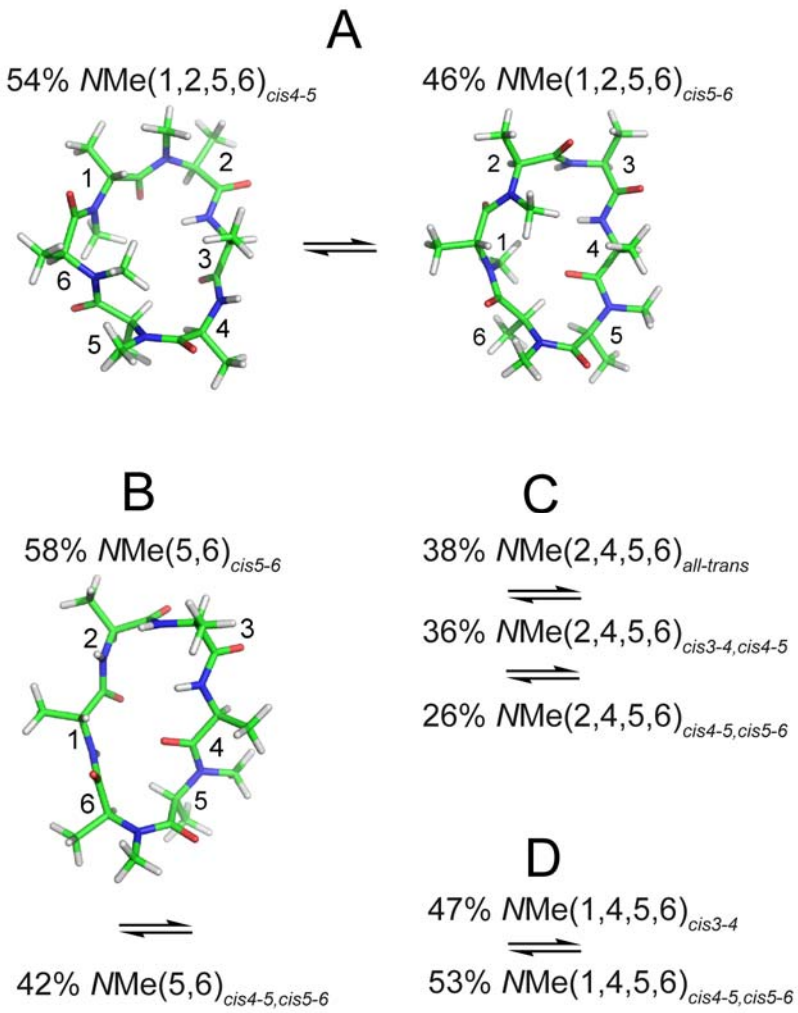

Figure 4.6: Structures and peptide bond configurations illustrating the effect of *N*-methylation at Ala^6 on peptides possessing the conformation of the second template structure. A) *N*Me(1,2,5,6), B) *N*Me(5,6), C) *N*Me(2,4,5,6) and D) *N*Me(1,4,5,6). Some conformers could not be derived due to lack of ROEs and the presence of artifacts resulting from exchange effects.

Only in *N*Me(1,2,5,6), the characteristic conformation with a single *cis* peptide bond between Ala^4 and Ala^5 is conserved but found in equilibrium with a second conformation that possesses a single *cis* peptide bond between Ala^5 and Ala^6. In respect of the *cis-trans* peptide bond pattern, the latter structure is also similar to one

*N*Me(5,6) conformer, which is found in equilibrium with a second conformer which possessing two subsequent *cis* peptide bonds between Ala^4 and Ala^6 (Figure 4.6). Two *N*Me(2,4,5,6) conformers also show two subsequent *cis* peptide bonds between Ala^4 and Ala^6, and between Ala^3 and Ala^5, respectively. In a third conformer, all peptide bonds are in *trans* configuration, which indicates similarity to the first template structure, rather than similarity to the second template structure. Although the conformation of *N*Me(1,4,5) was not investigated due to the presence of a side conformer with a population of 7 %, *N*Me(1,4,5) most likely represents same conformation that was found for very similar peptides like *N*Me(1,5) or *N*Me(1,2,4,5) (Figure 4.5). The skewing effect of Ala^6 *N*-methylation is again clearly demonstrated by the *cis*-*trans* pattern of the peptide bonds in *N*Me(1,4,5,6), which originates via the additional *N*-methylation of *N*Me(1,4,5) at Ala^6 (Figure 4.6).

Ala^3 *N*-methylation is not tolerated by the second template structure, as replacement of the H^N atom by a methyl group is not possible due to the spatially restricted orientation of this atom within the cyclopeptide ring. Accordingly, *N*Me(3,5) does not occupy the conformation that is characteristic for the second template structure, despite of the Ala^5 *N*-methyl group. However, one of the two conformations occupied by *N*Me(3,5) possesses a single *cis* peptide bond between Ala^2 and Ala^3 instead, which results in a conformation that is very similar to the second template but with β-turns that are shifted by two sequence positions along the scaffold, such that the upper (lower) turn is centered at Ala^5 and Ala^6 (Ala^2 and Ala^3). Resemblance of the structures is also confirmed by a high similarity of chemical shifts and temperature gradients of H^N chemical shifts within the Ala^2-Ala^6 substructure of *N*Me(1,5) and the $_D$-Ala^6-Ala^4 substructure of *N*Me(3,5) (see Table D.17 in Appendix D). The *N*Me(3,5) conformation with a single *cis* peptide bond between Ala^2 and Ala^3 is thus very similar to *N*Me(1,5) but possesses altered configuration of Ala^1 and Ala^3, as indicated in Figure 4.7.

A similar shift of the peptide sequence along the scaffold with a single *cis* peptide bond was also observed for one of the two conformers found for the peptide with the highest Caco-2 permeability (NMe(1,4,5,6)$_{cis(3\text{-}4)}$). In this conformer, the sequence is only shifted by one position along the scaffold, which results in a structure with a *cis* peptide bond between Ala^3 and Ala^4 (positions i+1 and i+2 of the lower β-turn). Accordingly, Ala^6 and $_D$-Ala^1 are found in positions i+1 and i+2 of the upper β-turn (Figure 4.7). For this conformer, $^3J_{HN\text{-}H\alpha}$ coupling constants, temperature gradients of H^N chemical shifts, and chemical shifts indicate high structural similarity to NMe(1,2,5,6)$_{cis(4\text{-}5)}$ (Figure 4.6 A and Table D.18).

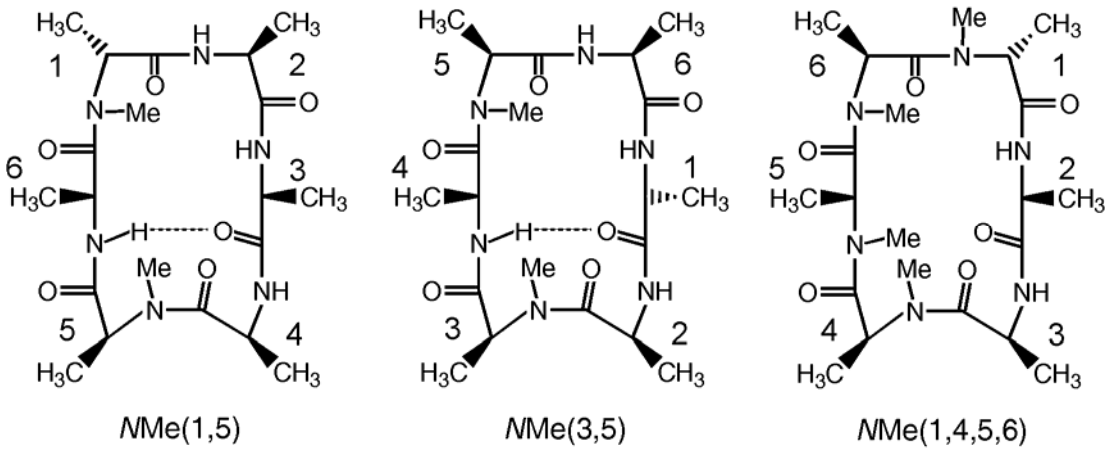

Figure 4.7: Illustration of the similarity between the structure of *N*Me(1,5), the structure of *N*Me(3,5) with a single Ala^2-Ala^3 *cis* peptide bond, and with the structure of *N*Me(1,4,5,6) with a single Ala^3-Ala^4 cis peptide bond. Three-dimesnsional coordinates were not derived for *N*Me(3,5) and *N*Me(1,4,5,6) due to artifacts from exchange in the ROESY spectrum and lack of ROEs. Strong ROEs between the H^{α} nuclei of the residues in positions i+1 and i+2 of the lower turn support our models.

For the seven very similar structures shown in Figure 4.5, variable Caco-2 permeability was observed. Only *N*Me(1,5) and *N*Me(1,2,4,5) permeate Caco-2 cells efficiently. It is obvious that although *N*-methylation at many different positions is tolerated without significant structural alterations, distinct *N*-methylation patterns are required in order to obtain high Caco-2 permeability.

The observed low permeability of the four peptides shown in Figure 4.5 that do not possess Ala^1 *N*-methyl groups on the one hand, and the high permeation of *N*Me(1,5) and *N*Me(1,2,4,5), on the other hand, show that Ala^1 *N*-methylation is essential for Caco-2 permeability of the second template structure. The importance of Ala^1 *N*-methylation for Caco-2 permeation is also supported by the high permeability of *N*Me(3,5) and *N*Me(1,4,5,6), which exhibit conformations that possess altered sequence positions on the otherwise identical single *cis* peptide scaffold. As illustrated in Figure 4.7, the *N*-methylated residue Ala^5 and Ala^6 occupy the i+1st position of the upper β-turn in *N*Me(3,5) (*N*Me(1,4,5,6)), a position that is usually occupied by D-Ala^1. It is further important to note that the conformer of *N*Me(5,6), that displays the characteristic single *cis* peptide bond scaffold, does not contain an *N*-methyl group on Ala^2 (which is in i+1st position of the upper β-turn). However, in contrast to the hydrogen atom in the i+1st position of the upper β-turn, which is solvent exposed in all the structures shown in Figure 4.5, it points up from the peptide plane and is therefore shielded from the solvent (see on the left of Figure 4.6). This may allow for the high Caco-2 permability of *N*Me(5,6) although the

N-methylation that was described above as crucial for high Caco-2 permeability, is not present.

In contrast to the high impact of Ala^1 *N*-methylation on Caco-2 permeability of the peptides, there is no significant influence of *N*-methylation at Ala^2 and Ala^4 as suggested by the low Caco-2 permeability conformationally of the conformationally homogeneous peptides *N*Me(5), *N*Me(2,5), *N*Me(4,5) and *N*Me(2,4,5). The limited contribution of *N*-methylation at Ala^2 and Ala^4 on Caco-2 permeation is further supported by similar (high) Caco-2 permeation rates of *N*Me(1,5) and *N*Me(1,2,4,5). However, the low permebility of *N*Me(1,2,5) in contrast to the high permeability of *N*Me(1,5) and *N*Me(1,2,4,5) is surprising.

Overall, our analysis suggests the following key characteristics for Caco-2 permeability of cyclic (-a-A-A-A-A-A-) peptides exhibiting the second template structure: a) one β-turn of type VI with an *N*-methylated *cis* peptide bond between the residues that occupy positions i+1 and i+2, b) an *N*-methylated residue in position i+1 of the opposed β-turn or shielding of the according amide hydrogen atom from the solvent, c) D- and L- configuration of the residues found in position i+1, i+2 and i+3 of the upper turn do not seem to be very important for Caco-2 permeability.

4.6 Striking Similarity with Orally Bioavailable Peptides

Three-dimensional structures of some orally bioavailable peptides are similar to structures of highly Caco-2 permeable cyclic(-a-A-A-A-A-A-) peptides presented above. In the structure of Cyclosporin A (CSA) published by Loosli *et al.*[274] and in the refined structure published by Klages *et al.*[52] either β-turns at the ends of the CSA β-strands are similar to turns in cyclic (-a-A-A-A-A-A-) peptides that belong to the second template structure. The upper turn which is centered at D-Ala^1 and Ala^2 in the highly Caco-2 permeating and conformationally homogeneous peptides *N*Me(1,5) and *N*Me(1,2,4,5) (Figure 4.3, bottom) is similar to the upper turn of CSA with *N*Me-Gly^3 and *N*Me-Leu^4 in positions i+1 and i+2, respectively (Figure 4.8, A). Please note, that the glycine contains no assymetric carbon and can therefore easily occupy the position of a D-configured residue. Additionally, the opposite type VI β-turn centered at Ala^4 and Ala^5 in *N*Me(1,5) and *N*Me(1,2,4,5) is similar to the second turn of CSA with *N*Me-Leu^9 and *N*Me-Leu^{10} in positions i+1 and i+2, respectively (Figure 4.8, B).

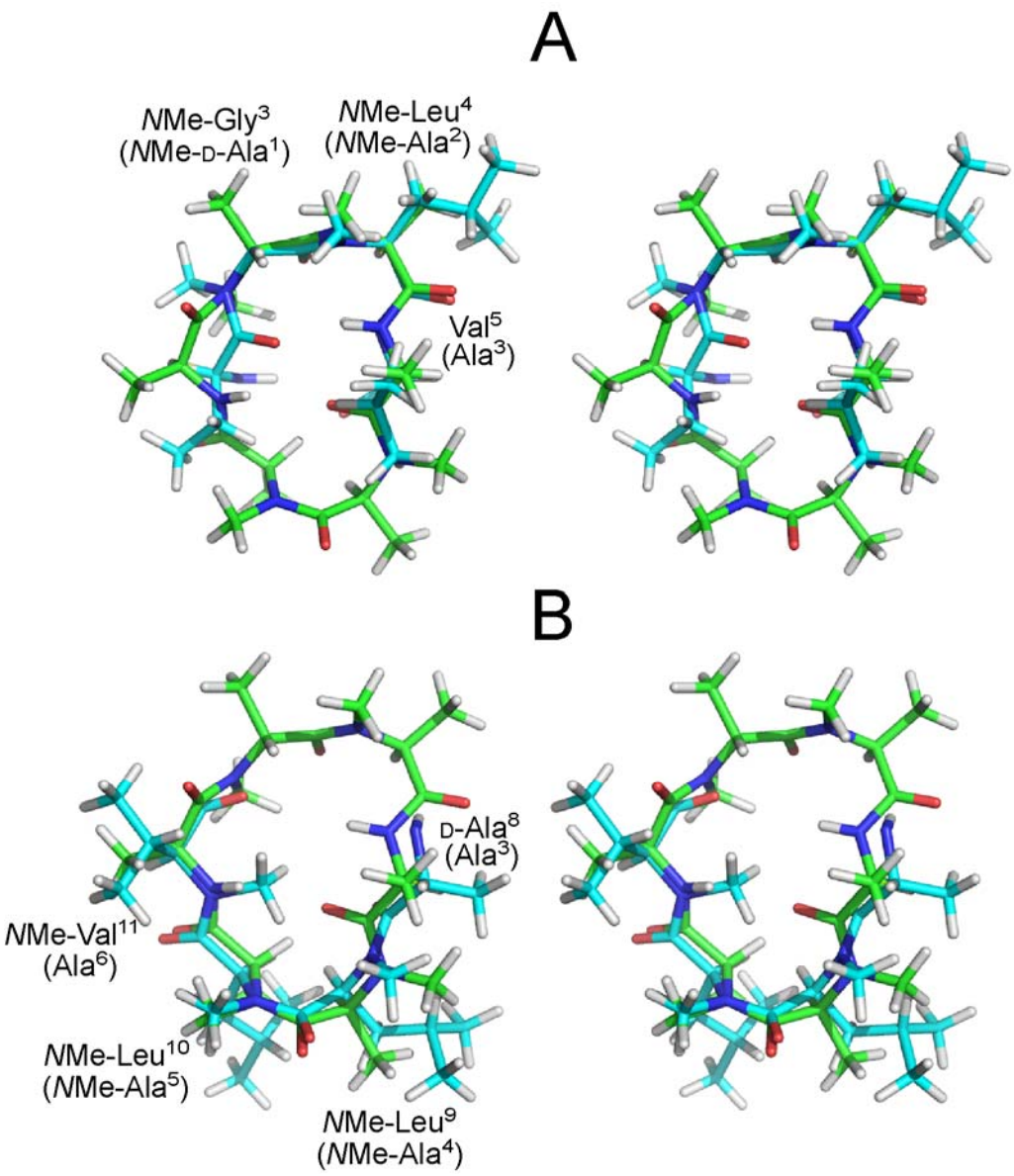

Figure 4.8: Fit of the type I β-turn of CSA (A) and the type VI β-turn of CSA (B) with the according turns of the highly Caco-2 permeable peptide *N*Me(1,2,4,5). In panels A and B only the relevant residues of CSA are shown (cyan) together with the according residues of *N*Me(1,2,4,5) (green, labels in brackets).

The similarity of *N*Me(1,2,4,5) with the orally bioavailable somatostatin analog cyclo(-Pro-Phe-*N*Me-D-Trp-*N*Me-Lys-Thr-*N*Me-Phe-)[194] is even more striking, as its *N*-methylation pattern is identical to the pattern in *N*Me(1,2,4,5) considering the proline (teritiary amide bond) of the somatostatin analog as an *N*-methylated residue (Figure 4.9, A). Additionally, a D-amino acid residue is found in position i+1 of the upper turn in *N*Me(1,2,4,5) and in cyclo(-Pro-Phe-*N*Me-D-Trp-*N*Me-Lys-Thr-*N*Me-Phe-).

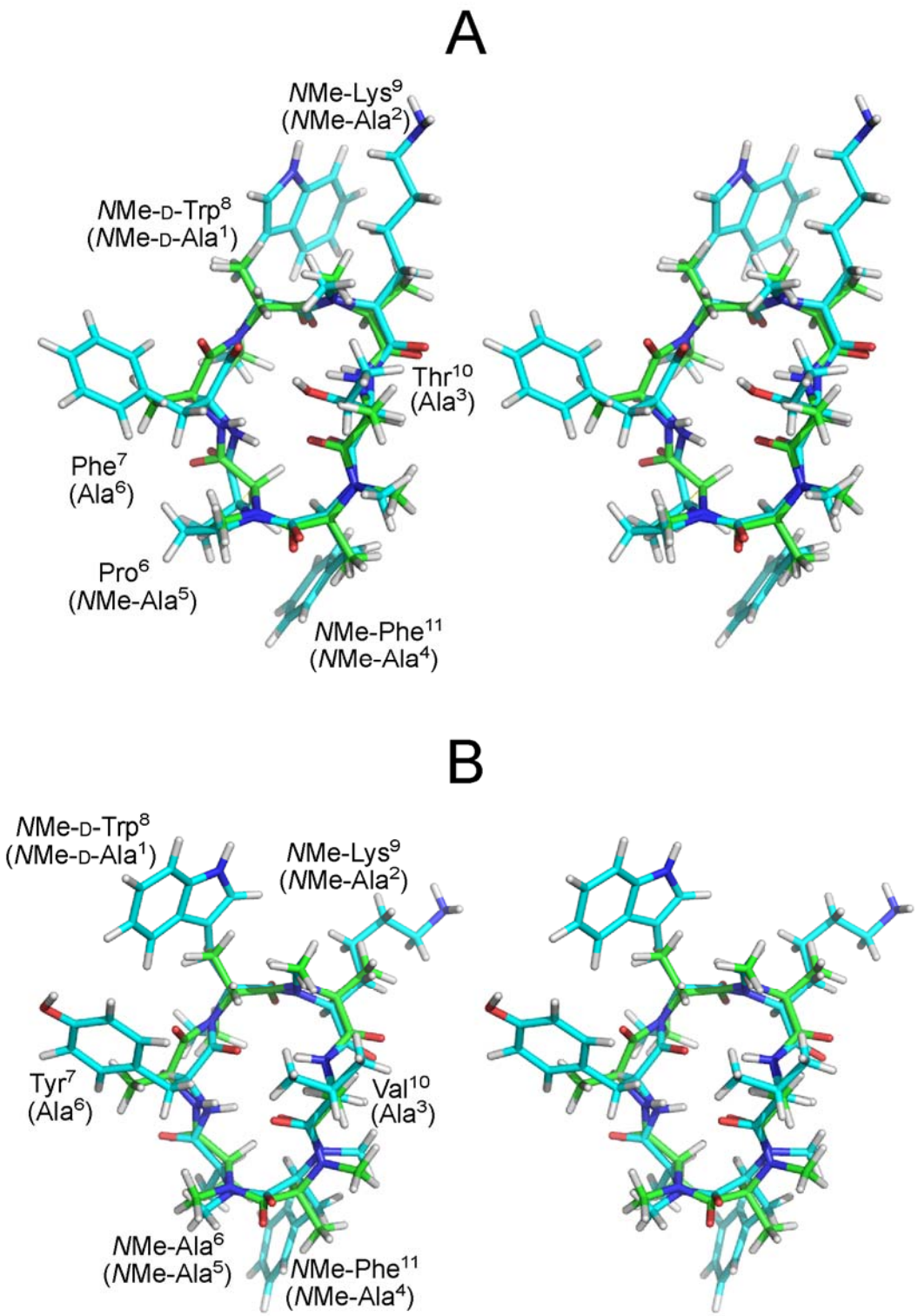

Figure 4.9: Fit of the cyclo(-Pro-Phe-*N*Me-D-Trp-*N*Me-Lys-Thr-*N*Me-Phe-) (A) and 3-*N*Me-(D-Trp^{8},Lys^{9},Phe^{11})-seglitide (B) on the *N*Me(1,2,4,5) solution structures (RMSD(C^{α}): 0.58 Å (A), 0.64 Å (B)). Somatostatin analogs and *N*Me(1,2,4,5) are shown in white and green color, respectively. Bracketed labels refer to *N*Me(1,2,4,5).

3-*N*Me-(D-Trp^{8},Lys^{9},Phe^{11})-seglitide, another somatostatin analog that was described in chapter 2.3, possesses a surprisingly high activity in vivo after intraperitoneal

injection, as compared to the other seglitide analogs with less *N*-methyl groups but higher sst receptor affinity.[221] Among all the *N*-methylated analogs that were tested, only this analog depicted the *N*-methylation pattern and conformation of the highly Caco-2 permeable cyclic peptide *N*Me(1,2,4,5) (Figure 4.9, B). The high in vivo activity of this peptide might be attributed to its improved 'druglike' distribution in rats, as compared to the less *N*-methylated analogs that were investigated in the same study.[221]

4.7 Conclusion

In conclusion, the extensive conformational studies of the cyclic (-a-A-A-A-A-A-) peptides shed light on the structural requirements that convey permeability to these peptides. It was shown here that solvent shielding of the amide bonds is not the sole factor to impart permeability to the cyclic peptides. Apparently, conformational homogeneity on the timescale of peptide *cis-trans* isomerization does not always guarantee permeability to these peptides and that conformational heterogeneity does not necessarily suppress permeability. On the contrary, the overall structural pattern of the peptides presented here as the template structures governs the permeability property. Employing the cyclic (-a-A-A-A-A-A-) peptides the contribution of the backbone conformation towards permeability of these peptides was evaluated, and any side-chain contribution was minimized. Given the significance of the backbone conformation of the peptide as a crucial factor regulating Caco-2 permeation, alanine residues of permeable cyclic (-a-A-A-A-A-A-) peptides may be substituted by pharmacophores to obtain enhanced intestinal permeability of bioactive peptides. A first indication that it is possible to transform the Ala-peptides into biologically functional derivatives with good permeability is presented by Cyclosporin A and the *N*-methylated somatostatin peptide as shown above. Ongoing research efforts by my colleagues Marelli Udaya Kiran and Florian Rechenmacher are directed at the incorporation of bioactive sequences into highly permeable cyclic (-a-A-A-A-A-A-) peptides to convey oral bioavailability. If the procedure presented here holds equally good for other systems, a long-standing problem in medicinal chemistry of peptides would be solved.

5 Hsp26 from *S. cerevisiae*

This project was a collaboration with Titus Franzmann and Professor Johannes Buchner from the chair in Biotechnology of the Technische Universität München.

Motivation

The capability to sense stress conditions and to react appropriately are critical for cells and organisms to endure hard times. The molecular chaperone Hsp26 helps baker's yeast (*S. cerevisiae*) to sustain heat stress conditions by stabilizing substrate proteins in states that are capable to refold into wt protein when heat stress conditions are over. A thermosensor/thermoswitch unit seems to induce critical temperature dependent conformational changes in Hsp26, that are independent of any covalent modifcation like phosphorylation. The characterization of the thermoswitch unit at atomic resolution would provide interesting insight into this unique property of Hsp26.

5.1 Introduction

Over the past years the elucidation of the molecular details underlying the folding diseases has sparked interest in protein folding and protein misfolding. Consequently, research concerning molecular chaperones enjoys great popularity as these represent the largest group of proteins assisting protein folding[275-278]. Beside of the Hsp60, Hsp70, Hsp90 and Hsp100 chaperone systems the small heat shock proteins (sHsps), which form the core of this project, represent one family of molecular chaperones.

sHsps are involved in numerous diseases like cataract,[279] ischemic and reperfusion injury as caused by stroke and heart attack,[280] neuronal disorders like Alzheimer`s disease,[281] non-small-cell lung carcinoma,[282] rheumatoid arthritis,[283] Charcot-Marie-Tooth disease,[284,285] axonal distal hereditary motor neuropathy,[285,286] or an inherited, adult onset, desmin-related myopathy[287]. The fact that most of these illnesses are also associated with misfold or precipitated protein suggests that folding diseases might be caused in many cases by malfunction of chaperones. To better understand the functional mechanism of sHsps and to find out how this mechanism is affected by defective mutations, structural models are required that describe the function of sHsps in atomic detail.

In spite of structural differences between the numerous members of the widespread[288] sHsp family, there are several features most small heat-shock proteins have in common. These include a low molecular weight of 12-43 kDa, a conserved α-crystallin domain of 80-100 residues, the capability to form large oligomers, a dynamic quaternary structure, induction by stress conditions and suppression of protein aggregation as molecular chaperones. The structural organization, consisting of an N- and a C-terminal region flanking the α-crystallin domain, is also conserved.[288] These common properties of different sHsps suggest further similarities in the mechanism to prevent proteins from irreversible aggregation during cellular stress.

Unfortunately, the fact that sHsps form oligomers of high molecular weight compromises their NMR spectroscopic investigation, as NMR spectroscopic structure investigations are limited to proteins with molecular weights of about 100 kDa with the NMR spectroscopic techniques developed so far.

The small heat-shock protein Hsp26 from *S. cerevisiae* was chosen for this project due to the availability of a well characterized dimer model protein ($Hsp26_{30-195}$)[289] that in contrast to wild-type Hsp26 (which forms large 24mers) seemed to be well

suited for NMR spectroscopic structural studies. Due to the high similarity between the different sHsps the investigation of Hsp26 appeared promising to yield information about general features of the sHsp`s chaperone mechanism. Moreover, the Hsp26 24mer was shown to undergo conformational changes upon heat activation,[289,290] which indicated the presence of a thermosensor/thermoswitch domain. Heat induced conformational changes seem to occur mainly in the middle domain (MD) of Hsp26, which in contrast to the other domains shows only low sequence homology. Due to the lack of similar sequences among protein structures described in the literature[g] it was impossible to construct a useful homology model for the MD.

Figure 5.1: Organization of protein domains in Hsp26. The N-terminal domain (NTD), the middle domain (MD), the α-crystallin domain, and the C-terminal extension (CTE) are supposed to be formed by residues 1-29, 30-90, 91-195 and 196-214, respectively. A tryptophane residue in position 72 (W) is indicated.

5.2 Dimeric Hsp26 Deletion Protein $Hsp26_{30\text{-}195}$

Circular dichroism spectroscopy, fluorescence quenching and fluorescence resonance energy transfer (FRET) experiments indicate analog temperature dependent conformational changes in the Hsp26 24mer and in the $Hsp26_{30\text{-}195}$ dimer. According to fluorescence measurements, these conformational changes occur with the same rate constants in both proteins.[289]

5.2.1 Expression and Purification

$Hsp26_{30\text{-}195}$ was expressed from *E. coli* BL21 (DE3) cells transformed with a pET28b+ vector containing the $Hsp26_{\Delta N30\text{-}195C}$ gene inserted via Nco1 and Not1 restriction sites. After protein expression in Lysogeny broth (LB) medium or isotope enriched M9 minimal medium for producing non-isotope labeled or $^{13}C/^{15}N$ labeled protein, respectively, cells were lysed using a Basic Z cell disrupter. Purification of the protein by fast protein liquid chromatography (FPLC) included the application of the lysate to a Q-Sepharose anion exchange and a Resource S cation exchange column and

[g] The structure databaseses covered by the HHpred interactive server for protein homology detection and structure prediction (Max Planck Institute for Developmental Biology) were considered.

yielded 15 mg $Hsp26_{30\text{-}195}$ per liter of cell culture. The buffers used for FPLC contained 20 mM HEPES, pH 8 (buffer A) with additional 1 M NaCl (buffer B). Experimental details are described in chapter 6.2.14.

In the initial purification step, the application of a 150 ml linear gradient of 0-50 % buffer B for elution of the lysate from 24 ml *Q-Sepharose fast flow* resin, yielded fractions (labels 1 - 7 in Figure 5.2 B) that were pooled for the final Resource S purification step at NaCl concentrations of 120 mM – 220 mM NaCl. In the final purification step, the application of a 60 ml linear gradient of 0 - 100 % buffer B for elution from a 6 ml Resource S column yielded the major protein fraction (labels 1', and 2' in Figure 5.2 D) at 230 mM - 340 mM NaCl.[h]

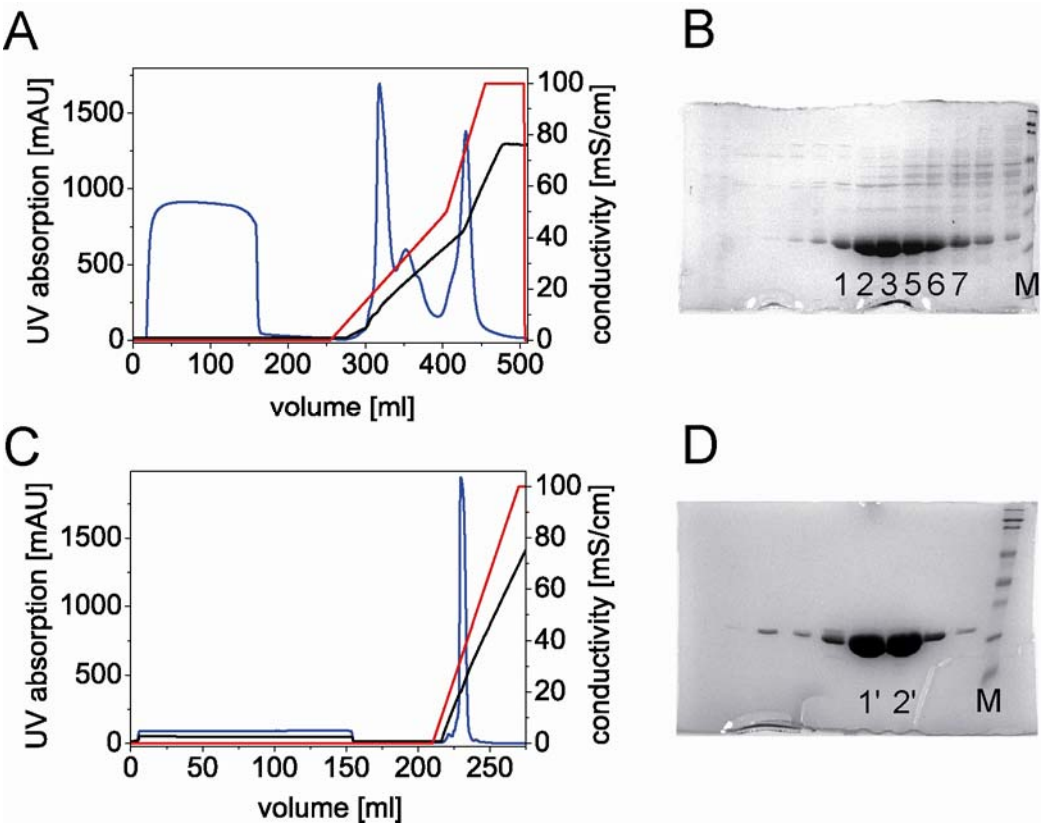

Figure 5.2: Purification of $Hsp26_{30\text{-}195}$ by FPLC. A) Chromatogram of the initial Q-Sepharose purification step. B) SDS-PAGE of Q-Sepharose fractions: The fractions 1 - 7 were collected at 312 - 333 ml (corresponding to 12 – 22 % buffer B) and pooled. C) FPLC chromatogram of the final Resource S (6 ml) purification step. D) SDS-PAGE of Resource S fractions. The fractions 1', and 2' were collected at 228 - 234 ml (corresponding to 23 - 34 % buffer B). The UV absorption at 280 nm is shown in blue color (mAU scale on the left), the conductivity is shown in black (mS/cm scale on the right) and the percentage of buffer B injected into the column (min. 0 %, max. 100 %) is shown in red color. In B) and D), M indicates protein marker (SERVA prestained SDS-PAGE protein marker 6.5 - 200 KDa, liquid mix) with bands at 6.5, 14.4, 21, 29, 45, 67, 116, and 200 kDa.

[h] NaCl concentrations were calculated from the conductivity of the eluate.

5 mM EDTA, which had been described as an additional component of buffers A and B for similar purification strategies interfered with the binding of $Hsp26_{30-195}$ to Q-Sepharose. The equilibration of the Q-Sepharose column with buffer A to a conductivity ≤ 1.5 mS/cm and the quantitative removal of medium from the cells before lysis as well as a sufficient dilution of the lysate with buffer A were also found to be critical for reproducible and quantitative binding of $Hsp26_{30-195}$ to the Q-Sepharose stationary phase.

The solution of $Hsp26_{30-195}$ that was obtained from Resource S column was dialyzed twice against 2 L of 10 mM NaP_i, 1 mM EDTA, pH 7.5. Protein samples that were not immediately used for further studies were split to aliquots of 500 µl – 1 ml, frozen in liquid nitrogen and stored at -80 °C.

5.2.2 NMR Spectroscopy of $Hsp26_{30-195}$

The NMR spectroscopic study of the structural properties underlying the thermoswitch of $Hsp26_{30-195}$ was complicated by strongly broadenend and imhomogeneous peaks in the ^{1}H-^{15}N heteronuclear single-quantum coherence (^{1}H-^{15}N HSQC) spectra. Although elevated temperatures (318 K) were found to improve the spectral quality, the number of signals was far lower than expected from the number of amide protons. Signal intensities of the individual peaks still differed strongly and many peaks displayed shoulders or side-signals. No substantial improvement of the spectra could be achieved despite of substantial efforts to optimize the experimental conditions that included the addition of 200 mM, 400 mM, and 800 mM glycin, the variation of the pH (4.7 – 9.2) as well as the application of transverse relaxation optimized (TROSY)[291] ^{1}H-^{15}N HSQC spectra. Standard and TROSY ^{1}H-^{15}N HSQC spectra of $Hsp26_{30-195}$ are shown in Figure 5.3.

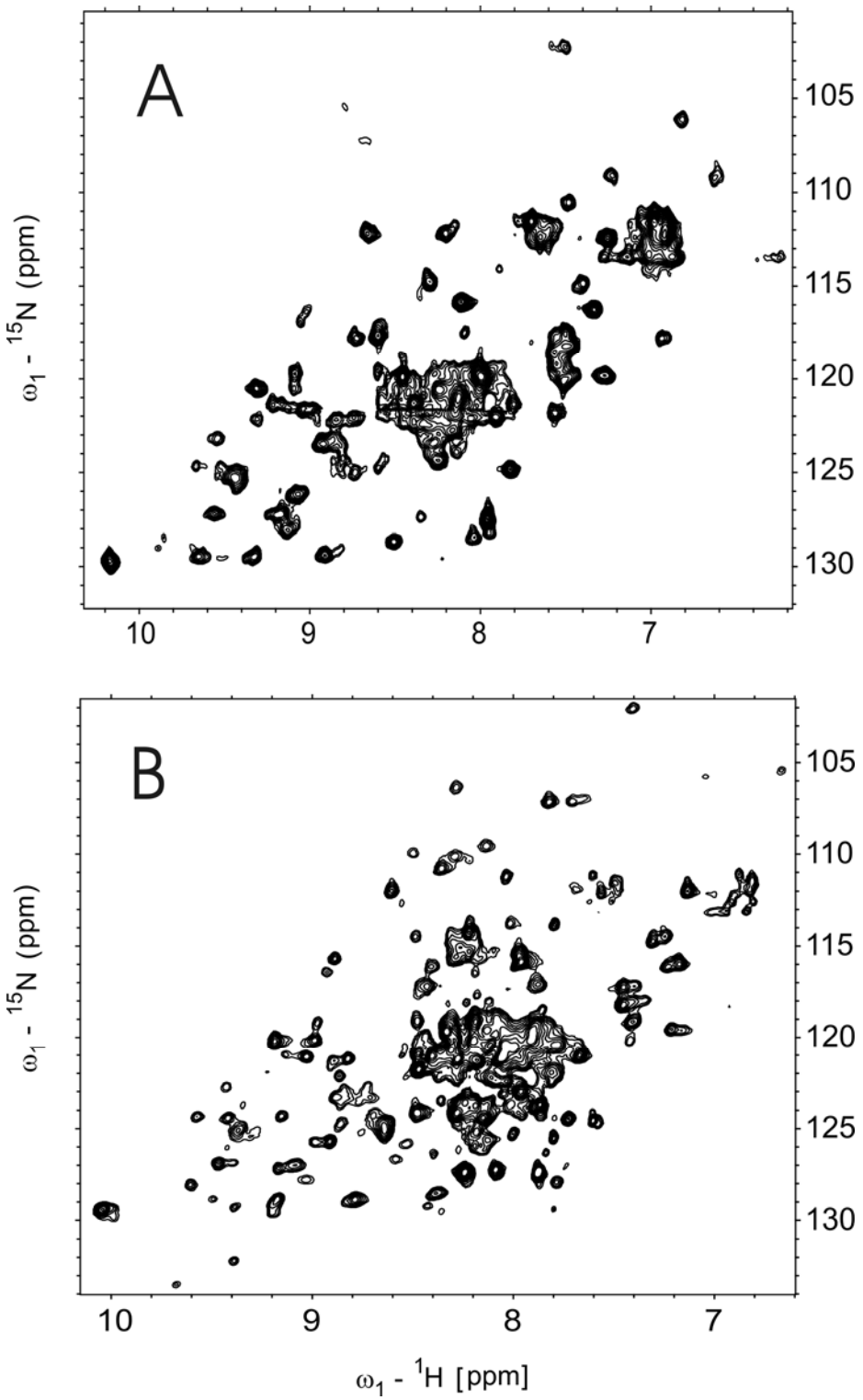

Figure 5.3: A: 600 MHz ^{15}N-HSQC spectrum of 1,55 mM [^{15}N] Hsp26$_{30-195}$, 10 mM phosphate and 1 mM EDTA at pH 7.5 in $H_2O/^2H_2O$ (90/10) detected at 45°C. B: 900 MHz TROSY[291] ^{15}N-HSQC spectrum of 1,0 mM [^{13}C,^{15}N] Hsp26$_{30-195}$ (60% deuterated), 10 mM phosphate and 1 mM EDTA at pH 7.5 in $H_2O/^2H_2O$ (90/10) detected at 45°C.

5.3 Monomeric Hsp26 Deletion Protein Hsp26$_{30\text{-}195(\Delta 137\text{-}153)}$

As only a small fraction of the Hsp26 resonances could be assigned from triple resonance spectra of Hsp26$_{30\text{-}195}$, a significant improvement of the spectral quality had to be achieved. In this respect, the design of a monomeric Hsp26$_{30\text{-}195}$ deletion protein seemed promising, as a reduction of the molecular weight from 37 kDa (dimer) to 18 kDa (monomer) was expected to strongly improve the quality of the NMR spectra.

5.3.1 Design of Hsp26$_{30\text{-}195(\Delta 137\text{-}153)}$

Many high resolution structures of sHsps display one characteristic extended loop per α-crystallin domain monomer which is located between two adjacent β-strands. A part of this loop forms a β-strand that partitions in a β-sheet of the respective α-crystallin dimerization partner domain which leads to intersubunit composite β-sheets (Figure 5.4).

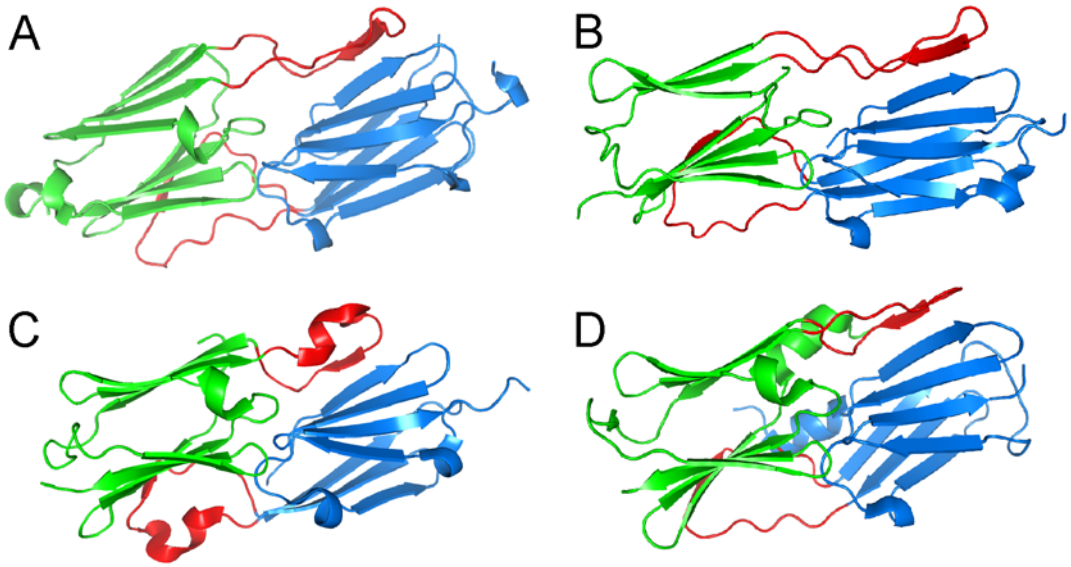

Figure 5.4: α-crystallin domain dimers of sHsps. A) sHsp16.5 from *Methanococcus janaschii*[292] B) sHsp16.9 from *wheat*[293] C) XAC1151 from *Xanthomonas axonopodis pv. citri*[294] D) StHsp14.0 from *Sulfolobus tokodaii*[295]. Monomers are shown in blue and green, respectively. The loops contributing to intersubunit composite β-sheets are highlighted in red color.

The deletion of the amino acid residues forming the according loop in Hsp26 was considered as a key step towards monomeric Hsp26 deletion protein that comprises MD and α-crystallin domain. As structure homology is usually higher than sequence

homology, structural modeling was preferred over sequence alignment for determining these residues. A homology model of the Hsp26 α-crystallin domain was derived from the structure of *wheat* Hsp16.9[293] using the HHpred interactive server for protein homology detection and structure prediction, which is part of the bioinformatics toolkit of the Department of Protein Evolution at the Max Planck Institute for Developmental Biology.[296,297] The loop predicted by the homology model of the Hsp26 α-crystallin domain consisted in residues 137 – 153 (Figure 5.5).

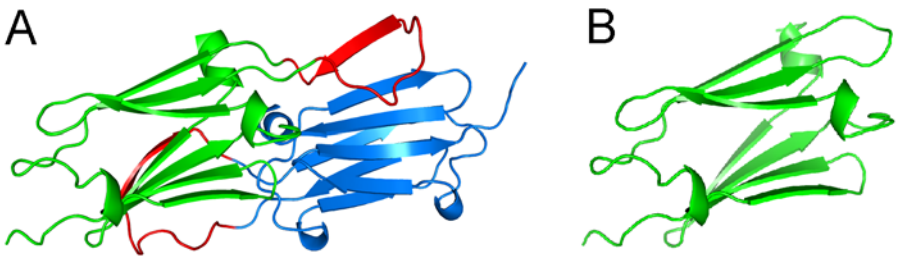

Figure 5.5: A: Homolgy model of the Hsp26 α-crystallin domain dimer as derived from the structure of *wheat* Hsp16.9.[293] The loop (residues 137 - 153) that is suggested to be involved in dimerization via β-strand exchange is highlighted in red. B: Structural model of monomeric Hsp26 α-crystallin domain as obtained by removal of residues 137 – 153 from the homology model using the program SYBYL.

5.3.2 Deletion of the Bases Encoding Residues 137-153 by PCR

A plasmid for expressing $Hsp26_{30\text{-}195(\Delta 137\text{-}153)}$ in *E. coli* BL21 (DE3) was derived directly from the pET28b+ - $Hsp26_{\Delta N30\text{-}195C}$ template using polymerase chain reaction (PCR). Primers consisted in the 27 nucleotides encoding residues S154 - T162 and in the reverse complement of the 30 nucleotides encoding residues N127 - P136. The pET28b+ - $Hsp26_{30\text{-}195(\Delta 137\text{-}153)}$ plasmid was obtained by a final blunt end cyclization step (see chapters 6.2.3-6.2.6 for primer sequences and further experimental details).

5.3.3 Expression and Purification

$Hsp26_{30\text{-}195(\Delta 137\text{-}153)}$ was expressed in *E. coli* BL21 (DE3) cells transformed with a pET28b+ vector containing the $Hsp26_{\Delta N30\text{-}195C(\Delta 137\text{-}153)}$ gene inserted via Nco1 and Not1 restriction sites. After protein expression in Lysogeny broth (LB) medium or isotope enriched M9 minimal medium for producing non-isotope labeled or $^{13}C/^{15}N$ labeled protein, respectively, cells were lysed using a Basic Z cell disrupter. Purification of the protein by FPLC included the application of the lysate to a

Q-Sepharose anion exchange and a Resource S cation exchange column and yielded 10 mg $Hsp26_{30\text{-}195(\Delta 137\text{-}153)}$ per liter of cell culture. The buffers used for FPLC contained 20 mM HEPES, pH 8 (buffer A) with additional 1 M NaCl (buffer B). Experimental details are given in chapter 6.2.15.

In the initial purification step, the application of a 150 ml linear gradient of 0-50 % buffer B for elution of the lysate from 24 ml *Q-Sepharose fast flow* resin, yielded fractions with NaCl concentrations of 80 mM – 200 mM NaCl (labels 1 - 6 in Figure 5.6 B) that were pooled for further purification. In the final purification step, the application of a 60 ml linear gradient of 0 - 100 % buffer B for elution from a 6 ml Resource S column yielded the major protein fraction (labels 1', 2', and 3' in Figure 5.6 D) at NaCl concentrations of 120 mM - 280 mM.[i] As $Hsp26_{30\text{-}195(\Delta 137\text{-}153)}$ eluted from the Resource S column at low NaCl concentration, strong dilution of the pooled fractions obtained from the first purification step (with buffer A) was critical for reliable binding of the protein to the second column.

[i] NaCl concentrations were calculated from the conductivity of the eluate.

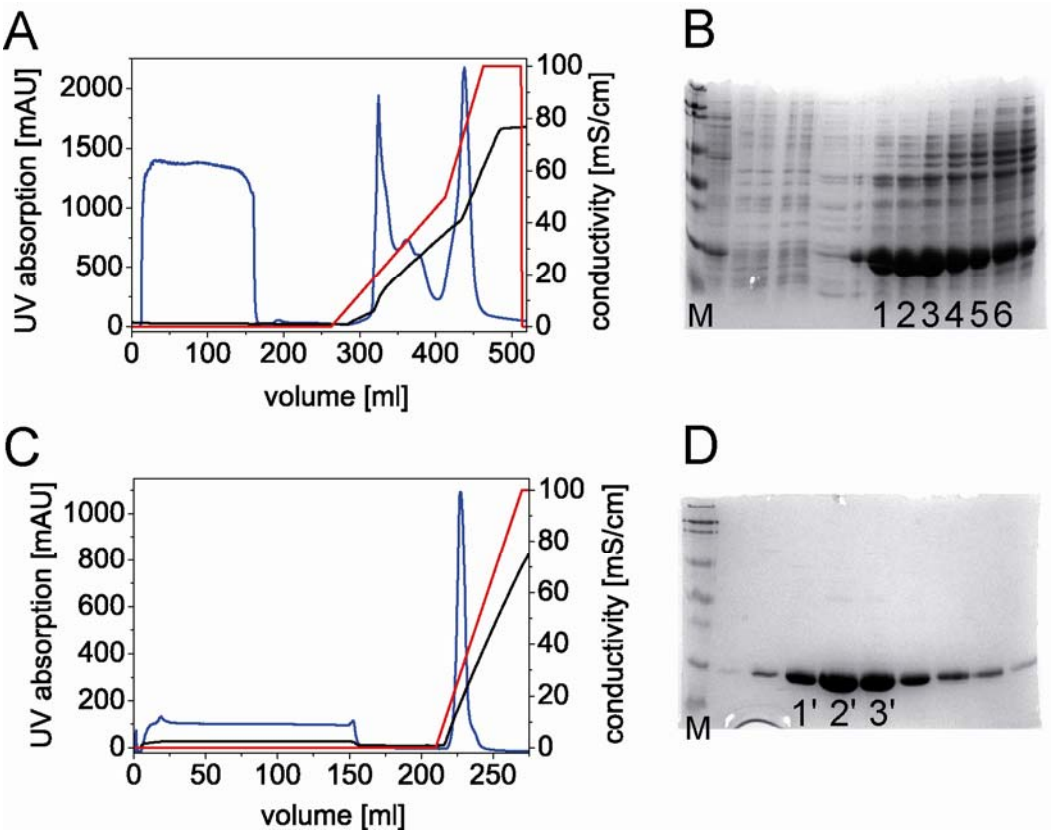

Figure 5.6: Purification of $Hsp26_{30\text{-}195(\Delta 137\text{-}153)}$ by FPLC. A) Chromatogram of the initial Q-Sepharose purification step. B) SDS-PAGE of Q-Sepharose fractions: Fractions 1, 2, 3, 4, 5, and 6 were collected at 320 - 338 ml (58 - 76 ml after start of the gradient) and pooled C) FPLC chromatogram of the final 6 ml Resource S purification step. D) SDS-PAGE of Resource S fractions. Fractions 1', 2', and 3' were collected at 222 - 231 ml (12 - 21 ml after start of the gradient). The UV absorption at 280 nm is shown in blue color (mAU scale on the left), the conductivity is shown in black (mS/cm scale on the right) and the percentage of buffer B injected into the column (min. 0 %, max. 100 %) is shown in red color. In B) and D), M indicates protein marker (SERVA prestained SDS-PAGE protein marker 6.5 - 200 KDa, liquid mix) with bands at 6.5, 14.4, 21, 29, 45, 67, 116, and 200 kDa.

5 mM EDTA, which had been described as an additional component of buffers A and B for similar purification strategies interfered with the binding of $Hsp26_{30\text{-}195(\Delta 137\text{-}153)}$ to Q-Sepharose. Furthermore, the equilibration of the Q-Sepharose column with buffer A to a conductivity ≤ 1.5 mS/cm and the quantitative removal of medium from the cells before lysis as well as a sufficient dilution of the lysate with buffer A were found to be critical for reproducible and quantitative binding of $Hsp26_{30\text{-}195(\Delta 137\text{-}153)}$ to Q-Sepharose.

$Hsp26_{30\text{-}195(\Delta 137\text{-}153)}$ was dialyzed twice against 2 L of 10 mM NaP_i, 1 mM EDTA, pH 7.5. Protein samples that were not immediately used for further studies were split to aliquots of 0.5 – 1 ml, frozen in liquid nitrogen and stored at -80 °C.

The molecular m/z ratio found for fully ^{15}N labeled protein by MALDI-TOF mass spectrometry was 16714. This agrees very well with the theoretical average

molecular mass of 16716 Da for the $[M+H]^+$ ion of quantitatively ^{15}N labeled $Hsp26_{30\text{-}195(\Delta 137\text{-}153)}$.

5.3.4 NMR Spectroscopy

In contrast to $Hsp26_{30\text{-}195}$, ^1H-^{15}N heteronuclear single-quantum coherence (HSQC) spectra of ^{15}N-labeled $Hsp26_{30\text{-}195(\Delta 137\text{-}153)}$ possessed uniform peak shape and the reduced line width compared to the initial construct clearly indicated monomeric protein (Figure 5.7). Ultracentrifugation experiments performed by Titus Franzmann at the chair in Biotechnology of the TU München indicated a molecular mass of 16.3 kDa which is in good agreement with the theoretical average molecular mass value of 16513 Da for a monomer at natural abundance of isotopes.

The good dispersion of the ^1H-^{15}N HSQC signals indicates a high β-sheet content, whereas a fraction of signals are clustered in the center of the spectrum clearly indicates that some parts of the protein are unfolded. An enlargement of this region in the spectrum is shown in the top left corner of Figure 5.7.

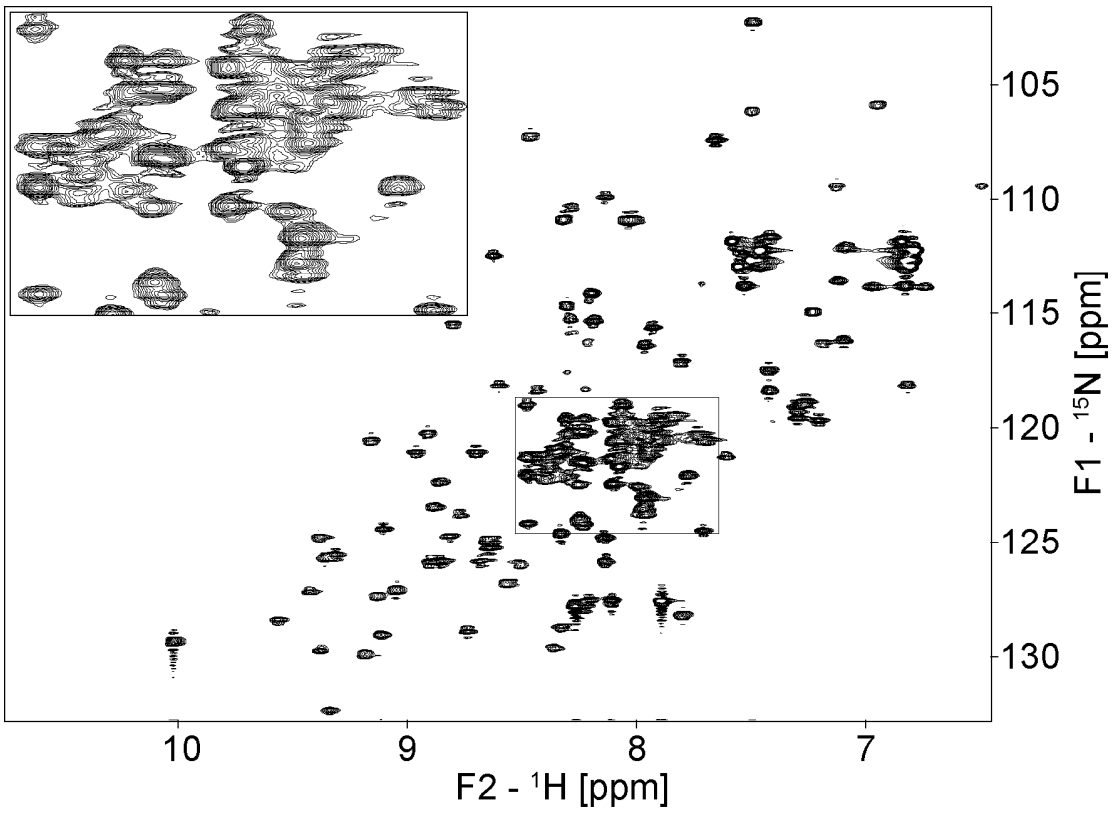

Figure 5.7: ^1H-^{15}N HSQC spectrum of ^{15}N-labeled $Hsp26_{30\text{-}195(\Delta 137\text{-}153)}$ (1.0 mM) detected at 298 K and pH 7.5 in 10 mM NaP_i, 1 mM EDTA, 90 % H_2O / 10 % D_2O at 600 MHz. Overlapping signals in the center of the spectrum are highlighted in the top left corner.

Assignments of $^{1}H^{N}$, $^{1}H^{\alpha}$, $^{13}C^{\alpha}$, $^{13}C^{\beta}$, $^{13}C'$, and ^{15}N nuclei were obtained using a strategy that combines chemical shift data from a set of different 3D triple-resonance experiments.[298,299] The resonance assignment is given in Appendix E.

Torsion angle likelihood obtained from shift and sequence similarity (TALOS) was used for estimating the secondary structure of $Hsp26_{30\text{-}195(\Delta137\text{-}153)}$. The seven β-sheets of the Hsp26 α-crystallin domain homology model are well supported by TALOS predictions (indicated as 'β' in Figure 5.8 A). The presence of a largely undistorted α-crystallin domain in $Hsp26_{30\text{-}195(\Delta137\text{-}153)}$ is further confirmed by mapping of the β-sheets suggested by TALOS (red) onto the Hsp26 α-crystallin model derived by homology modeling (Figure 5.8 B). TALOS predictions also suggest a lack of α-helical substructure throughout the protein and a largely unfolded MD. Therefore, the structure of the MD, which is the interesting thermosensor/ thermoswitch domain, could not be studied in the monomeric deletion protein $Hsp26_{30\text{-}195(\Delta137\text{-}153)}$.

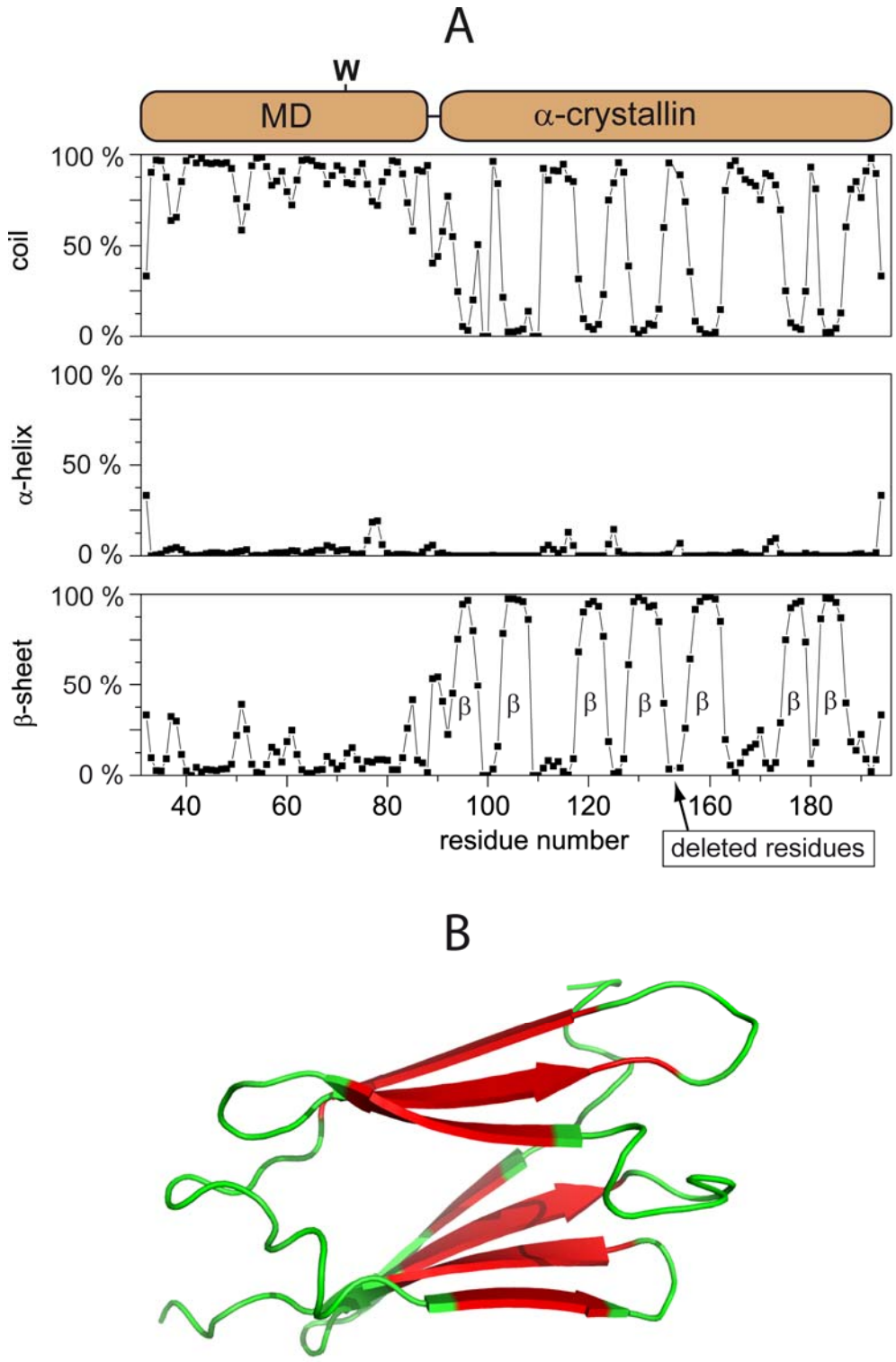

Figure 5.8: A) Secondary structure predicted by TALOS for $Hsp26_{30\text{-}195(\Delta 137\text{-}153)}$. A scheme of the middle domain (MD), and the α-crystallin domain are shown above. The only tryptophane residue (W72) found in this Hsp26 deletion protein is indicated. B) β-strands as predicted by TALOS (red) mapped onto the Hsp26 structural model derived from *wheat* sHsp16.9.

6 Summary

The present thesis covers a broad field of scientific research ranging from NMR spectroscopic conformational studies of potent bioactive and highly Caco-2 permeable *N*-methylated cyclic peptides to protein design by molecular modeling, molecular cloning, protein expression in *E. coli* and purification by ion exchange fast protein liquid chromatography (FPLC).

In chapter 2, the structures of potent agonists at distinct subtypes of the G protein-coupled melanocortin and somatostatin receptors were described. The α-MSH analog 4-*N*Me-(His^6,Arg^8,Trp^9,Lys^{10})-MT-II (chapter 2.2) possesses a turn conformation along Asp^5-Trp^9, that leads to a unique orientation of the His^6, D-Phe^7, Arg^8 and Trp^9 side-chains (Figure 2.4). Due to the high flexibility of non-*N*-methylated MT-II, this peptide could not be described by a single preferred conformation. While 4-*N*Me-(His^6,Arg^8,Trp^9,Lys^{10})-MT-II is a highly potent and selective agonist at human melanocortin receptor subtype 1 (hMC1R), MT-II itself is a potent but unselective agonist at hMC1R, hMC3R, hMC4R, and hMC5R. The conformation of 4-*N*Me-(His^6,Arg^8,Trp^9,Lys^{10})-MT-II seems to match the hMC1R binding site, whereas MT-II appears to be sufficiently flexible to adapt to the binding sites of four different hMCR subtypes.
The conformation of 3-*N*Me-(D-Trp^8,Lys^9,Phe^{11})-seglitide (chapter 2.3) was found to be similar to the conformation of seglitide (cyclo(*N*MeAla^6-Tyr^7-D-Trp^8-Lys^9-Val^{10}-Phe^{11})) with two β-turns of type II' and VIa centered at *N*Me-D-Trp^8-*N*MeLys^9 and Phe^{11}-*N*MeAla^6, respectively (Figure 2.8). The same conformation and *N*-methylation pattern was also found for one highly Caco-2 permeable cyclo(D-Ala-Ala$_5$) model peptide (see below and chapter 4), suggesting that the unexpectedly strong peripheral anti-inflammatory effect induced by 3-*N*Me-(D-Trp^8,Lys^9,Phe^{11})-seglitide might be due to an improved distribution of this peptide in the body as compared to less *N*-methylated analogs.

In chapter 3, the conformations of three double *N*-methylated analogs of *c*(RGDfV) were described (Figure 3.2). In *c*(RG*N*MeDf*N*MeV), all peptide bonds are in *trans* geometry. No intramolecular hydrogen bonds and no Φ and Ψ dihedral angles indicating characteristic β-turn or γ-turn geometries are present. In *c*(*N*MeRGDf*N*MeV) a type VIb β-turn with a *cis* peptide bond between valine and arginine is found along the *N*-methylated residues and an inverted γ-turn is centered at the aspartate residue. In *c*(*N*MeRG*N*MeDfV) all peptide bonds are in *trans*

geometry and a γ-turn centered at D-phenylalanine is present. The specific backbone conformation brings the side-chains of arginine and aspartate into close proximity. Docking studies that were pursued by Sandro Cosconati and Prof. Luciana Marinelli at the University of Naples, Italy, revealed structural models for the highly different activity and selectivity profiles of these three peptides at the avβ3 and avβ5 integrins.

The conformational studies of 16 *N*-methylated cyclo(-D-Ala-Ala_5-) peptides presented in chapter 4 give insight into structural properties (*N*-methylation, and β-turn pattern) that lead to high Caco-2 permeability. Two highly permeable template structures were identified (Figure 4.3). The first permeable template structure possesses two β-turns of type II along Ala^6-D-Ala^1 and along Ala^3-Ala^4 and is found for the peptide with *N*-methyl groups at Ala^6 and D-Ala^1, *N*Me(1,6). The second permeable template structure possesses two β-turns along D-Ala^1-Ala^2 (type I) and along Ala^4-Ala^5 (type VI). It is occupied by a number of cyclo(-D-Ala-Ala_5-) peptides with *N*-methylation at position five. *N*-methylation of this structure at position one seems to be important for Caco-2 permability, as among the peptides possessing this conformation, only the ones with *N*-methyl groups at position one were found to be highly permeable (*N*Me(1,5) and *N*Me(1,2,4,5)).

In chapter 5, studies are presented that were performed in order to characterize the unique thermosensor/thermoswitch domain of the small heat shock protein Hsp26 from *S. cerevisiae* by NMR spectroscopy at atomic resolution. As native Hsp26 forms 24mers, that are too large for common solution state NMR spectroscopic studies, deletion proteins were used. A dimeric deletion protein ($Hsp26_{30-195}$ that lacks C- and N-terminal residues) was expressed in *E. coli* using isotope enriched minimal media, purified by FPLC and studied by 2D and 3D NMR spectroscopy. As the quality of the spectra obtained from this dimeric deletion protein was insufficient, the monomeric deletion protein $Hsp26_{30-195(\Delta 137-153)}$ was designed using molecular modeling. Molecular cloning, protein expression in *E. coli* BL21 (DE3) and ion exchange fast protein liquid chromatography yielded pure $Hsp26_{30-195(\Delta 137-153)}$. Unfortunately, the domain hosting the thermosensor/thermoswitch was found to be unfolded in this monomeric deletion protein according to secondary structure predictions from TALOS.

7 Experimental Section

7.1 Materials and Methods - Peptide Projects

7.1.1 NMR Spectroscopy

NMR Spectroscopy of 4-*N*Me-(His^6,Arg^8,Trp^9,Lys^{10})-MT-II

DQF-COSY, E.COSY, TOCSY, ROESY, ^{13}C-HMBC and ^{13}C-HSQC spectra were recorded at 298 K on a Bruker DMX spectrometer operating at 600 MHz. A COLOC spectrum[26] was recorded at 298 K on a Bruker Avance III spectrometer operating at 600 MHz. A phase sensitive HMBC and a reference HSQC spectrum with offset and rf-amplitude-compensated BEBOP[300,301] and BIBOP pulses[302,303] were detected at 298 K on a Bruker Avance III spectrometer operating at 750 MHz.[304,305] Samples were prepared in 50 mM Sodium acetate-d4 buffer (pH 4.5, 10% D_2O, 0.05 % NaN_3) at concentrations of 12-38 mM in 5 mm NMR tubes. This low pH was chosen to keep hydrogen exchange induced line broadening small and to enhance comparability with numerous earlier structural studies on MCR effectors that were performed under the same conditions. Sodium 3 (trimethylsilyl)propionate 2,2,3,3 d4 (^{1}H at 0.000 ppm) was used as internal standard. Data were processed with Topspin 1.3 software from Bruker. The homo- and heteronuclear experiments 2QF-COSY, E.COSY, TOCSY, ROESY, and magnitude mode ^{13}C-HMBC were performed with a spectral width of 11 ppm for ^{1}H and 180 ppm for ^{13}C. Individual HSQC spectra covering aliphatic (^{13}C offset = 35 ppm, spectral width = 50 ppm) and aromatic ^{13}C resonances (^{13}C offset = 120 ppm, spectral width = 30 ppm) were detected. The phase sensitive HMBC spectrum and the reference HSQC spectrum were detected with a spectral width of 9 ppm for ^{1}H and 190 ppm for ^{13}C. A COLOC spectrum was detected with spectral widths of 9.5 ppm for ^{1}H and 190 ppm for ^{13}C. The increments in t1 and t2 were adjusted to the information extracted from the individual experiments, ranging from 384 to 2048 increments in t1 and from 4096 to 16384 complex data points in t2. Depending on the sample concentration and the individual experiments, 16 to 48 transients were averaged for each t1 value. A mixing time of 80 ms was used for TOCSY (spin-lock field: 6 kHz; mixing sequence MLEV-17). Water signal suppression was achieved by WATERGATE techniques.[306] The sequential assignment was obtained from heteronuclear J correlations that were extracted from HSQC and HMBC spectra. A compensated ROESY experiment, which was used for the extraction of inter proton distances, was performed with 150 ms mixing time and a spin-lock field of 4000 kHz.[31] The volume integrals of the individually assigned cross-peaks were compensated for offset effects and converted into distance

constraints using the isolated spin pair approximation.[307] In order to compensate for watergate solvent signal suppression artifacts, of any two cross-peaks representing an internuclear distance, the peak with the higher water resonance offset in the direct dimension was preferably considered for distance calculations. The ROESY cross-peak volumes were calibrated against the distance (1.78 Å) between the prochiral *N*Me-Lys10 H^{ε} protons. 18 intraresidual, 36 sequential interresidual and 9 non-sequential interresidual ROE derived distance restraints were used for structure calculations, with restraints between the lactam bridged residues Asp^5 and *N*Me-Lys^{10} counted as sequential.

$^3J_{HN\text{-}H\alpha}$ coupling constants were determined from 1D ^1H NMR spectra, $^3J_{H\alpha\text{-}H\beta}$ coupling constants from E.COSY and heteronuclear $^3J_{C\text{-}H}$ coupling constants from HMBC and reference HSQC spectra.[42,44,304,305]

NMR Spectroscopy of 3-*N*Me-(D-Trp^8,Lys^9,Phe^{11})-seglitide

E.COSY, TOCSY, ROESY, ^{13}C-HMBC, ^{13}C-HSQC and a phase sensitive HMBC with selective ^{13}C-pulses were recorded at 298 K on a Bruker Avance III spectrometer operating at 500 MHz. Samples were prepared in DMSO-d6 at concentrations of 10 mM in a 3 mm NMR tube. DMSO-d6 (^1H at 2.52 ppm) was used as internal standard. Data were processed with Topspin 1.3 software from Bruker. The homo- and heteronuclear experiments E.COSY, TOCSY, ROESY, and magnitude mode ^{13}C-HMBC were performed with a spectral width of 11 ppm for 1H and 195 ppm for ^{13}C. Individual phase sensitive HMBC spectra covering *N*-methyl and Val γ-methyl ^{13}C resonances (offset = 25 ppm, spectral width = 20 ppm) and backbone ^{13}C resonances (^{13}C offset = 172 ppm, spectral width = 8 ppm) were detected with a spectral width of 10 ppm for ^1H. The increments in t1 and t2 were adjusted to the information extracted from the individual experiments, ranging from 80 to 1433 increments in t1 and from 8192 to 32768 complex data points in t2. Depending on the individual experiments, 16 to 120 transients were averaged for each t1 value. A mixing time of 80 ms was used for TOCSY (spin-lock field: 6.2 kHz; mixing sequence MLEV-17). The sequential assignment was obtained from heteronuclear J correlations that were extracted from HSQC and HMBC spectra. A compensated ROESY experiment, which was used for the extraction of inter proton distances, was performed with 150 ms mixing time and a spin-lock field of 2.1 kHz.[31] The volume integrals of the individually assigned cross-peaks were converted into distance constraints using the isolated spin pair approximation.[307] The ROESY cross-peak

volumes were calibrated against the distance (2.81 Å) between the *N*Me D-Trp^{8} $H^{\varepsilon 1}$ and $H^{\zeta 2}$ protons. 10 intraresidual, 16 sequential interresidual and 7 non-sequential interresidual ROE derived distance restraints were used for structure calculations, with restraints between *N*Me-Ala^{6} and *N*Me-Phe^{11} counted as sequential.

$^{3}J_{HN\text{-}H\alpha}$ coupling constants were determined from 1D ^{1}H NMR spectra, $^{3}J_{H\alpha\text{-}H\beta}$ coupling constants from E.COSY and heteronuclear $^{3}J_{C'\text{-}H}$ coupling constants from phase sensitive HMBC spectra, using according reference signals.[42,44]

NMR Spectroscopy of Double *N*-methylated Cyclic (-R-G-D-f-V-) Peptides

1D ^{1}H NMR, E.COSY, TOCSY, ROESY, ^{13}C-HMBC, ^{13}C-HSQC, and ^{15}N-HETLOC were recorded at 300 K on a Bruker Avance III spectrometer operating at 500 MHz. Samples were prepared in DMSO-d6 at concentrations of 42 mM cyclo (-R-G-*N*MeD-f-*N*MeV-), 46 mM cyclo (-*N*MeR-G-D-*N*Mef-V-) and 80 mM cyclo (-*N*MeR-G-D-f-*N*MeV-) in 3 mm NMR tubes. DMSO-d6 (^{1}H at 2.52 ppm, ^{13}C at 40.45 ppm) was used as internal standard. Data were processed with Topspin 1.3 software from Bruker. The homo- and heteronuclear experiments E.COSY, TOCSY, HSQC, and magnitude mode ^{13}C-HMBC were recorded with a spectral width of 13 ppm for ^{1}H. HSQC and magnitude mode ^{13}C-HMBC were recorded with a spectral width of 160 ppm and 200 ppm for ^{13}C, respectively. ROESY spectra were recorded with spectral widths of 8.2 ppm (cyclo (-R-G-*N*MeD-f-*N*MeV-), cyclo (-*N*MeR-G-D-*N*Mef-V-)) and 10.8 ppm (cyclo (-*N*MeR-G-D-f-*N*MeV-)). ^{15}N filtered 2D TOCSY experiments (^{15}N-HETLOC)[45,46] were set up as described by Uhrín *et al.*[48] and recorded with spectral widths of 8.4 ppm (cyclo (-R-G-*N*MeD-f-*N*MeV-)) and 8.8 ppm (cyclo (-*N*MeR-G-D-*N*Mef-V-)) for ^{1}H. The increments in t1 and t2 were adjusted to the information extracted from the individual experiments, ranging from 192 to 2048 increments in t1 and from 1024 to 32768 complex data points in t2. Depending on the individual experiments, 8 to 72 transients were averaged for each t1 value. A mixing time of 80 ms was used for TOCSY (spin-lock field: 6.25 kHz; mixing sequence DIPSI2). The sequential assignments were obtained from heteronuclear J correlations that were extracted from HSQC and HMBC spectra. Compensated ROESY experiments, which were used for the extraction of inter proton distances, were performed with 100 ms mixing time and with spin-lock fields of 4 kHz.[31] The spin-lock was achieved using a train of 15° pulses. The volume integrals of the individually assigned cross-peaks were compensated for offset effects and converted into distance constraints using the isolated spin pair approximation.[307] The ROESY

cross-peak volumes were calibrated against the distance between the Val^5 H^{γ} protons (cyclo (-R-G-*N*MeD-f-*N*MeV-)), against the distance (2.41 Å) between the Val H^{α} and H^{β} protons (cyclo (-*N*MeR-G-D-*N*Mef-V-)) and against the distance (1.8 Å) between the Arg^1 H^{β} protons (cyclo (-*N*MeR-G-D-f-*N*MeV-)). For cyclo (-R-G-*N*MeD-f-*N*MeV-) the bounds obtained that way turned out to be too short and were thus stretched by 15 %; a procedure that was justified by significant overlap of the cross-peaks with edges of the diagonal peaks and by possible TOCSY transfer, which may have diminished the cross-peak volumes. 8 intraresidual, 10 sequential interresidual and 1 non-sequential interresidual ROE derived distance restraints were used for structure calculations of cyclo (-R-G-*N*MeD-f-*N*MeV-). Another 3 sequential interresidual and 1 non-sequential interresidual ROEs were used for MD trajectory analysis. 7 intraresidual, 12 sequential interresidual and 3 non-sequential interresidual ROE derived distance restraints were used for structure calculations of cyclo (-*N*MeR-G-D-f-*N*MeV-). 10 intraresidual, 7 sequential interresidual and 3 non-sequential interresidual ROE derived distance restraints were used for structure calculations of cyclo (-*N*MeR-G-D-*N*Mef-V-). Another 7 sequential interresidual ROEs were used for MD trajectory analysis. Restraints between residues 1 and 5 were counted as sequential.

$^3J_{HN\text{-}H\alpha}$ coupling constants were determined from 1D ^1H NMR spectra and $^3J_{H\alpha\text{-}H\beta}$ coupling constants from E.COSY. $^3J_{N\text{-}H\beta}$ coupling constants were obtained from ^{15}N-HETLOC spectra by reading the f2 splitting of (E.COSY type) H^N-H^{β} cross-peaks.

NMR Spectroscopy of *N*-methylated Cyclic (-a-A-A-A-A-A-) Peptides

1D ^1H NMR, TOCSY, ROESY, and ^{13}C-HMBC spectra were recorded at 300 K on a Bruker Avance III spectrometer operating at 500 MHz. Samples were prepared in DMSO-d6 at concentrations of 5-40 mM in 3 mm NMR tubes. DMSO-d6 (^1H at 2.52 ppm, ^{13}C at 40.45 ppm) was used as internal standard. Data were processed with Topspin 1.3 software from Bruker. The homo- and heteronuclear experiments were recorded with spectral widths that were just sufficient to display all resonances in the respective dimensions (^1H: 8 - 10 ppm; ^{13}C: 190 ppm). The increments in t1 and t2 were adjusted to the information extracted from the individual experiments, ranging from 256 to 1024 increments in t1 and from 4096 to 8192 complex data points in t2. Depending on the individual experiments, 8 to 48 transients were averaged for each t1 value. A mixing time of 80 ms was used for TOCSY (spin-lock field: 6.25 kHz; mixing sequence MLEV17). The sequential assignments were obtained from heteronuclear J correlations that were extracted from HMBC spectra.

Compensated ROESY experiments, which were used for the extraction of inter proton distances, were performed with 100 ms mixing time and with spin-lock fields of 4 kHz.[31] The spin-lock was achieved using a train of 15° pulses. The volume integrals of the individually assigned cross-peaks were compensated for offset effects and converted into distance constraints using the isolated spin pair approximation (see chapter 6.1.2).[307] For calibration against intraresidual H^{α} - H^{β} distances, one third of the average of the offset compensated intraresidual H^{α} - H^{β} crosspeak volumes was used as reference intensity in equation 1.11 (chapter 1.1.3). The average of the three distances between the α hydrogen atom and one of the three β hydrogen atoms in the sc+, sc- and trans rotamers (= 2.58 Å) was used as reference distance in equation 1.11 (chapter 1.1.3).

7.1.2 Distance Restraints

Distance restraints were derived in six steps:

1. Integration of cross-peaks in offset compensated ROESY spectra.
2. Dividing of their intensities by k_{ij} for offset compensation. k_{ij} is obtained by equations 1.8 and 1.9 that are given in the introduction (chapter 1.1.3).
3. Calculation of crude distances from offset compensated intensities based on reference peaks using equations 1.10 and 1.11 that are also given in the introduction (chapter 1.1.3).
4. Multiplication of the crude distances with $(n_i n_j)^{1/6}$, where n_i and n_j are the number of degenerated protons of resonances i and j (multiplicity correction).
5. Addition of 10% to the multiplicity corrected distances and subtraction of 10% from the multiplicity corrected distances to obtain upper and lower bounds, respectively.
6. Addition of 0.4 Å (0.8 Å) to the upper bounds of restraints between one (two) methyl groups (pseudoatom correction).

7.1.3 Distance Geometry Calculations

A home-written distance geometry program was used for metric matrix distance geometry calculations.[308] Beyond the geometric distance bounds (holonomic restraints) experimental distance restraints were placed in the final distance matrix whenever the latter were more restrictive. Upon random metrization, 50 template structures were embedded in four dimensions and partially minimized using

conjugate gradient minimization. The following distance bound driven dynamics (DDD) simulation[309] was carried out in two subsequent steps (100 ps at 500 K, 40 ps at 1 K). Holonomic and experimental distance constraints plus a chiral penalty function were used in the DDD simulation to generate violation energies and forces. For each four dimensional structure a distance matrix was derived that served for the computation of coordinates in three dimensions using the EMBED algorithm. Another conjugate gradient minimization step, DDD simulations (100 ps at 500 K, 60 ps at 1 K) and two more conjugate gradient minimization steps were carried out to optimize the structures under the influence of distance constraints and chiral penalty functions. Distance restraints involving methyl groups were referred to pseudoatoms in the structure calculation process. The coordinates of the pseudoatoms were calculated as arithmetic mean of the corresponding three methyl proton coordinates.

7.1.4 Restrained Molecular Dynamics Simulations

Restrained MD calculations (rMD) were carried out employing the module DISCOVER of the INSIGHT II 2001 program (Biosym/MSI Inc.) with the CVFF force field. The ROE restraints were included with a force constant of 10 kcal mol^{-1} $Å^{-2}$. The calculations were done with the explicit-image model of periodic boundary conditions. The best structure resulting from the DG calculation was placed in a cubic box of length 30 Å and soaked with water. After energy minimization using steepest descent and conjugate gradient, the system was heated gradually starting from 10 K and increasing to 50, 100, 150, 200, 250 and 300 K in 1 ps steps, each by direct scaling of velocities. The system was equilibrated for 50 ps with temperature bath coupling. Coordinates were saved every 100 fs for another 150 ps. The average structure of the 150 ps rMD calculation was subjected to energy minimization and further investigated by unrestrained MD simulations.

7.1.5 Unrestrained Molecular Dynamics (MD) Simulations

Unrestrained MD Simulations of 4-*N*Me-(His^6,Arg^8,Trp^9,Lys^{10})-MT-II

The GROMACS 4.0 software package (www.gromacs.org)[310-312] was used to perform unrestrained MD calculations. Visualization of the simulation trajectories was performed using the software packages VMD[313] and SYBYL 8.0.[314] The scripts g_cluster, g_dist and g_angle, that were used for analysis of the MD trajectory, were all packaged with GROMACS. The 53a6 united atom (CH, CH_2 and CH_3 groups

represented as a single atom) forcefield, one of the GROMOS96 force fields,[315] was used for the molecular dynamic simulations. Rigid SPC water which was constrained using SETTLE[316] served as water model. Solute bonds were constrained by the SHAKE algorithm[317] and temperature and pressure control was executed by Berendsen coupling.[318] Periodic boundary conditions were employed on a octahedral simulation box, which was built with a distance of 1.4 nm for the solute. Cut off distances of 1.4 nm for electrostatic and Lennard-Jones non-bonding interactions were applied. Simulation time steps were set to 2 fs. Upon addition of two acetate counter ions and soaking of the box with water, the system was equilibrated by an initial minimization and subsequent 50 ps MD simulations at 50, 100, 150, 200, 250 and 298 K using position restraints. Within the individual MD steps, the temperature was gradually increased, while the force constants of the position restraints were decreased exponentially from 250000 $KJmol^{-1}nm^{-2}$ at 50° K to 25° $KJmol^{-1}nm^{-2}$ at 250° K. At 298 K no position restraints were applied. For adjacent pressure equilibration a 100 ps MD simulation was performed at 298 K. The final 30 ns MD simulation was carried out at 298 K. Coordinates were saved every 10 ps. For the MD simulation with strict conservation of the peptide backbone obtained from the restrained MD simulation, position restraints of 250000 $KJmol^{-1}nm^{-2}$ were applied on all backbone carbon and nitrogen atoms between Asp^5 C^{α} and *N*Me-Lys^{10} C^{α}.

Unrestrained MD Simulations of 3-*N*Me-(D-Trp^8,Lys^9,Phe^{11})-seglitide

The GROMACS 4.0 software package (www.gromacs.org)[310-312] was used to perform unrestrained MD calculations. Visualization of the simulation trajectories was performed using the software packages VMD[313] and SYBYL. The scripts g_cluster, g_dist and g_angle, that were used for analysis of the MD trajectory, were all packaged with GROMACS. The 53a6 united atom (CH, CH2 and CH3 groups represented as a single atom) forcefield, one of the GROMOS96 force fields,[315] was used for the molecular dynamic simulations. Temperature and pressure control was executed by Berendsen coupling.[318] Periodic boundary conditions were employed on a octahedral simulation box, which was built with a distance of 2 nm for the solute, that consisted of more than 1200 DMSO molecules. Cut off distances of 1.4 nm for electrostatic and Lennard-Jones non-bonding interactions were applied. Simulation time steps were set to 2 fs. Upon soaking of the box with DMSO, the system was equilibrated by an initial minimization and subsequent 50 ps MD simulations at 50,

100, 150, 200, 250 and 298 K using position restraints. At every single temperature a temperature and a pressure equilibration was performed. Within the individual MD steps, the temperature was gradually increased, while the force constants of the position restraints were decreased exponentially from 250000 $KJmol^{-1}nm^{-2}$ at 50 K to 25 $KJmol^{-1}nm^{-2}$ at 250° K. At 298 K no position restraints were applied. The final 50 ns MD simulation was carried out at 298° K. Coordinates were saved every 10 ps. As the applied forcefield does not explicitly take the covalent contribution of the observed strong hydrogen bonds into account, we compensated for that by applying one single distance restraint between Tyr^7 H^N and Val^{10} H^N, during the MD simulation. This restraint was in well agreement with an experimentally derived ROE between these atoms. We further applied a dihedral angle restraint on Val^{10} χ_1 in order to keep this dihedral angle within the experimentally determined range.

Unrestrained MD Simulations and Energy Minimizations of Double *N*-methylated Cyclic (-R-G-D-f-V-) Peptides

The GROMACS 4.0 software package (www.gromacs.org)[310-312] was used to perform energy minimizations and unrestrained MD calculations. Visualization of the simulation trajectories was performed using the software packages VMD[313] and SYBYL. The scripts g_cluster, g_dist and g_angle, that were used for analysis of the MD trajectory, were all packaged with GROMACS. The 53a6 united atom (CH, CH_2 and CH_3 groups represented as a single atom) forcefield, one of the GROMOS96 force fields,[315] was used for the molecular dynamics simulations. Temperature and pressure control was executed by Berendsen coupling.[318] Periodic boundary conditions were employed on a octahedral simulation box, which was built with a distance of 2 nm for the solute, that consisted of more than 1200 DMSO molecules. Cut off distances of 1.4 nm for electrostatic and Lennard-Jones non-bonding interactions were applied. Simulation time steps were set to 2 fs.

Energy minimizations in explicit DMSO were performed after careful equilibration of the surrounding solvent, which was ensured by subsequent MD simulations at a series of different temperatures of 50, 100, 150, 200, 250, 300, 250, 200, 150, 100 and 50 K. At every step 20 ps temperature equilibration and 20 ps pressure equilibration were performed. Position restraints of 250000 $KJmol^{-1}nm^{-2}$ were employed on the peptide atoms at all these steps until the temperature was decreased back to 150 K. For the last two temperature steps at 100 K and 50 K, position restraints were reduced to 25000 $KJmol^{-1}nm^{-2}$ and 2500 $KJmol^{-1}nm^{-2}$,

respectively. The final steepest descent energy minimization was run without position restraints and stopped as soon as the biggest force was smaller than 100 $KJmol^{-1}nm^{-1}$.

Preparation for MD simulations was similar but slightly different: The system was equilibrated by an initial minimization and subsequent 50 ps MD simulations at 50, 100, 150, 200, 250 and 300 K using position restraints. At every single temperature a temperature and a pressure equilibration was performed. Within the individual MD steps, the temperature was gradually increased, while the force constants of the position restraints were decreased exponentially from 250000 $KJmol^{-1}nm^{-2}$ at 50 K to 25 $KJmol^{-1}nm^{-2}$ at 250°K. At 300 K no position restraints were applied. The final 50 ns (cyclo(-R-G-*N*MeD-f-*N*MeV-) and cyclo(-*N*MeR-G-D-f-*N*MeV-)) and 100 ns (cyclo(-*N*MeR-G-D-*N*Mef-V-)) MD simulations were carried out at 300 K. Coordinates were saved every 10 ps. For analyzing the quality of the MD runs, apparent inter-proton distances were back calculated (equation 7.1) from 1001 conformations that were extracted at intervals of 50 ps (cyclo(-R-G-*N*MeD-f-*N*MeV-) and cyclo(-*N*MeR-G-D-f-*N*MeV-)) and of 100 ps (cyclo(-*N*MeR-G-D-*N*Mef-V-)).

$$r_{app} = \left(\frac{1001}{\sum_{frame=0}^{1000} r_{frame}^{-6}} \right)^{1/6} \qquad (7.1)$$

r_{frame} was calculated for the frames of the trajectories for every single internuclear distance under consideration. A self written perl script was used for this purpose that extracted the coordinates from the frames, calculated the distances and performed r^{-6} based averaging of the individual distances resulting in r_{app} (equation 7.1).

Consistency between experimental and back calculated ROEs could be improved by adding few conformational constraints to the final MD simulations of cyclo(-R-G-*N*MeD-f-*N*MeV-) and cyclo(-*N*MeR-G-D-f-*N*MeV-). For cyclo(-R-G-*N*MeD-f-*N*MeV-), *N*Me-Asp^3 Ψ and D-Phe^4 Φ were restrained to 82° and 120°, respectively (D-Phe^4 $^3J_{HN\text{-}H\alpha}$ = 9.3 Hz). For cyclo(-*N*MeR-G-D-f-*N*MeV-), Gly^2 Ψ and Asp^3 Φ were restrained to -45° and -120°, respectively (Asp^3 $^3J_{HN\text{-}H\alpha}$ = 9.0 Hz). Additionally, a time averaged distance restraint was applied to keep *N*Me-Arg^1 C^α and D-Phe^4 H^N between 3.3 and 4.1 Å (the ROE between *N*Me-Arg^1 H^α and D-Phe^4 H^N suggests 3.15 to 3.84 Å).

7.2 Materials and Methods – Hsp26 Project

7.2.1 Chemicals and Enzymes

If not otherwise indicated in the text, chemicals were obtained from Merck or Sigma-Aldrich. DNA oligonucleotides were purchased from Biomers GmbH (Ulm, Germany). DNA sequencing was provided by SeqLab GmbH (Göttingen, Germany). Enzymes for cloning DNA were obtained from Promega (Madison, WI, USA), New England Biolabs (Ipswitch, MA, USA) and Agilent Technologies (Santa Clara, CA, USA). The *Wizard® SV Gel and PCR Clean-up System* (Promega Corporation, Madison, WI, USA) was used for purifying PCR product DNA from agarose gels and for removing restriction enzymes. Plasmid DNA was isolated from *E. coli* using *Wizard® Plus SV Minipreps* (Promega Corporation, Madison, WI, USA).

7.2.2 Buffer Solutions and Culture Media

Cation and anion exchange FPLC Buffers

Buffer A: 20 mM HEPES, pH 8
Buffer B: 20 mM HEPES, 1 M NaCl, pH 8
Initially, this buffer system was also used in slightly different composition containing additional 5 mM EDTA.

Ni-NTA FPLC Buffers

Puffer A: 300 mM KCl, 50 mM NaPi, 10 mM imidazole, pH 8
Puffer B: 300 mM KCl, 50 mM NaPi, 500 mM imidazole, pH 8

SOB^{++} Medium

A solution of 20 g tryptone, 5 g yeast extract, 0.5 g NaCl, and 0.186 g KCl in 1 liter H_2O was autoclaved. 10 ml of sterile 1 M $MgSO_4$ and 10 ml of sterile 1 M $MgCl_2$ were added just befor use.

TB Buffer

Upon addition of 10 ml HEPES (0.2 M, pH 6.7) and 30 ml $CaCl_2$ (0.1 M) to 50 ml KCl (1 M) and dilution with H_2O to a final volume of 200 ml, the pH was adjusted to 6.7 using KOH. 2.18 g $MnCl_2 \cdot 4H_2O$ were added and the solution was sterilized (0.2 µm cellulose acetate sterile syringe filter, VWR, Radnor, PA, USA).

10 x TAE buffer

48.4 g Tris base, 11.4 ml glacial acetic acid, and 2.92 g EDTA disodium salt were dissolved in 600 ml H_2O. The pH was adusted to 8.0 before additional H_2O was added to a final volume of 1 liter.

10 x DNA sample buffer

4 % (w/v) bromophenol blue, 50 % (v/v) glycerol.

LB medium

10 g/l tryptone, 5 g/l yeast extract, 5 g/l NaCl.

M9 minimal medium

100 ml M9 medium (10 x), 10 ml trace elements solution (100 x), 20 ml glucose solution (20 % w/v)*; 1 ml $MgSO_4$ (1 M), 0.3 ml $CaCl_2$ (1 M), 1 ml biotin solution (1 mg/ml), 1 ml thiamine solution (1 mg/ml), 1 ml kanamycin sulfate solution (35 mg/ml).

* with $^{2}H_7$,$^{13}C_6$ glucose, the amount per Liter medium was reduced to 1.5 - 2 g

M9 medium (10 x): 60 g/l Na_2HPO_4, 30 g/l KH_2PO_4, 5 g/l NaCl, 5 g/l $^{15}NH_4Cl$
Trace elements solution (100 x): 5 g/l EDTA, 0.83 g/l $FeCl_3 \cdot 6\ H_2O$, 84 mg/l $ZnCl_2$, 13 mg/l $CuCl_2 \cdot 2\ H_2O$, 10 mg/l $CoCl_2 \cdot 6\ H_2O$, 10 mg/l H_3BO_3, 1,6 mg/l $MnCl_2 \cdot 6\ H_2O$. After addition of the EDTA to slightly less than the final volume, pH was adusted to 7.5. Then, the remaining components were added and the volume was adjusted to 1 liter.

5 x SDS-PAGE loading buffer

10 % (w/v) SDS, 50 % (v/v) glycerol, 300 mM Tris/HCl (pH 6.8), 0.05 % (w/v) bromophenol blue, 5% (v/v) 2-mercaptoethanol.

4 x SDS-PAGE separating gel buffer

0.8 % SDS, 1.5 M Tris base (pH 8.8).

2 x SDS-PAGE loading gel buffer

0.4 % SDS, 0.25 M Tris/HCl (pH 6.8).

10 x SDS-PAGE running buffer

0.25 M Tris/HCl, 2M glycine, 1 % SDS (pH 8.8).

7.2.3 Vectors and DNA Oligonucleotides

The plasmid for expressing $Hsp26_{30\text{-}195}$ (pET28b+ - $Hsp26_{\Delta N30\text{-}195C}$) was obtained from the chair in Biotechnology. It was derived by Titus Franzmann via the Nco1/Not1 restriction sites of pET28b+ (Merck Biosciences GmbH, Schwalbach) using the DNA oligonucleotides 5' GAT CGC GGC CGC TTA CTT CTG AGG CTT CAA TTT TG 3', and 5' GAT CCC ATG GGG AGA GGC TAC GCA CCA AGA C 3' for amplification of the Hsp26 inserts.

The plasmid for expressing $Hsp26_{30\text{-}195(\Delta 137\text{-}153)}$ was derived from the plasmid pET28b+ - $Hsp26_{\Delta N30\text{-}195C}$. The oligonucleotides used for amplification of pET28b+ - $Hsp26_{\Delta N30\text{-}195C}$ DNA in order to delete the DNA encoding Hsp26 residues 137-153 is given in Table 6.1.

Table 6.1: Primers from 5' end (left) to 3' end (right).

forward	TCT GGT AAG TTC AAG AGA GTC ATC ACT
reverse	TGG AAT TTC ACC AGA AAC CAA AAT TTG GTT

The plasmid was obtained by cyclization due to intra-molecular blunt end ligation reaction (chapter 6.2.6).

7.2.4 Polymerase Chain Reaction

Polymerase chain reaction (PCR)[319,320] was applied for amplifying DNA. *Pfu* polymerase (Promega Corporation, Madison, WI, USA) including a proofreading function was applied in 50 µl batches for preparing DNA that was used in later cloning steps (Table 6.2). *Taq* polymerase was applied in 10 µl batches for analyzing whether inserts were properly included in plasmids (Table 6.2).

Table 6.2: Components of *Pfu* PCR reactions (left) and *Taq* PCR reactions (right).

5 µl	Pfu polymerase buffer (10x)	1 µl	Thermopol buffer (10x)
1.5 µl	100 mM dNTP mix	0.3 µl	100 mM dNTP mix
2 µl	10 µM primer A	0.3 µl	T7 Promotor primer *forward*
2 µl	10 µM primer B	0.3 µl	T7 Promotor primer *reverse*
0.5-1.5 µl	DNA template	0.5 µl	DNA template
36-37 µl	sterile ddH_2O	7.5 µl	sterile ddH_2O
1 µl	*Pfu* polymerase ('hot start')	0.1 µl	*Taq* polymerase

Temperature profile cycles applied for PCR reactions are shown in Table 6.3. *Pfu* polymerase was added after initial melting at 95°C ('hot start'), whereas *Taq* polymerase was added already before the initial heating step.

Table 6.3: Temperature profiles for PCR reactions.

1)	2 min at 95 °C	initial melting
2a)	30 s at 95 °C	melting at the beginning of each cycle
2b)	30-45 s at 50-70 °C[#]	annealing
2c)	1-15 min[‡] at 68 °C (*Pfu*) or 72 °C (*Taq*)	extension at the end of each cycle
3	10 min at 68 °C (*Pfu*) or 72 °C (*Taq*)	final extension
4	4 °C	storage

Steps 2a-c were repeated 20-30 times.

[#] Annealing temperatures were set 10 °C below the estimated melting temperature T_m of the primers.

[‡] Extension times were chosen such that the product DNA could well be synthesized based on synthesis rates of 500 bp/min (*Pfu*) and 2000 bp/min (*Taq*), respectively

Upon PCR, the non-mutated and methylated template plasmid was selectively digested by incubation of the PCR reaction with 1 µl (20U) of *DpnI* at 37 °C for 6-12 h.

7.2.5 Agarose Gel Electrophoresis

Agarose gels (0.7 – 1%) for analytical and preparative gel electrophoresis were made by dissolving 0.49 – 0.7 g agarose in 70 ml hot 1 x TAE buffer. 4 µl ethidiumbromide stock solution (1 % w/v) was added just before casting of the gel at about 60 °C. Typical samples consisted of 1 µl 10 x DNA sample buffer and 9 µl PCR product. The electrophoresis was performed in a BIO-RAD system controlled by a E702 microcomputer electrophoresis power supply under constant voltage of 60-90 V. DNA bands were identified by their fluorescence at 254 nm using a BIO-RAD gel documentation system.

7.2.6 Intra-Molecular Blunt End Ligation

1 µl T4 DNA ligase reaction buffer (10 x) (New England Biolabs, Ipswitch, MA, USA), 1 µl T4 DNA ligase (400 000 cohesive end units/ml, New England Biolabs, Ipswitch, MA, USA) and 1 µl T4 polynucleotide kinase (10 U/µl, Fermentas) were added to 7 µl of PCR product as extracted from an agaose gel upon preparative gel electrophoresis. The reaction was incubated over night at room temperature and 3 µl were transformed into competent *E. coli* XL1 blue cells.

7.2.7 *E. coli* Strains

Table 6.4: *E. coli* bacterial strains used.

E. coli	**genotype**	**reference / source**
BL21 (DE3)	*E. coli* B strain F^- *dcm ompT hsdS*(r_B^- m_B^-) *gal* λ(DE3)	[321] / Novagen
XL1 blue	recA1 endA1 gyrA96 thi-1 hsdR17 supE44 relA1 lac [F´ proAB lacIqZΔM15 Tn10 (Tetr)]	Novagen

7.2.8 Preparation of Chemically Competent Cells

3 ml LB medium were inoculated with appropriate *E. coli* cells and incubated overnight at 37°C. 500 ml SOB^{++} medium were inoculated with the overnight culture and incubated at 25°C until the OD at 600 nm had reached 0.5. The culture was cooled on ice (15 min) and centrifuged for 10 minutes (4°C, 6000 g, prechilled centrifugation tubes). The pellet was gently resuspended in 100 ml ice-cooled TB buffer, incubated on ice (15 min) and centrifuged for 10 minutes (4 °C, 6000 g, prechilled centrifugation tubes). After gently resuspending the pellet in 18.6 ml ice-cooled TB buffer, 1.4 ml DMSO were added and the suspension was kept on wet ice for another 15 minutes. The cell suspension was aliquoted at 500 µl per tube in prechilled Eppendorf tubes that were shock-frozen in liquid nitrogen and stored at -80°C.

7.2.9 Chemical Transformation of *E. coli*

The plasmid to be transformed and an aliquot of cells (Eppendorf tube) were put on ice until the cells were thawn. 1 µl of plasmid was added to the cells; both were mixed gently, put on ice for 10 minutes and subsequently exposed to 42°C in a heater for 60 seconds without shaking. After cooling on ice for 10 minutes, 700 ml LB

medium were added and the batch was shaken gently in a heater at 37 °C for 1 hour. After centrifugation (4000 g, 1 minute) the supernatant was removed, the cells resuspended in the remaining volume and then plated on agar plates containing appropriate antibiotics.

7.2.10 Storage of *E. coli*

BL21 (DE3) and XL1 blue *E. coli* cells containing plasmids were stored as glycerol stocks. These were prepared by pipetting 700 µl cell culture (OD ~ 0.6) into a cryo tube. 300 µl of glycerol (75 %) were added and carefully mixed with the cell culture. After incubation at 4 °C for one hour, the tube was shock-frozen in liquid nitrogen and stored at -80 °C.

7.2.11 Expression Analysis

In order to test for protein expression levels under different conditions (temperatures, induction times, media, ^{2}H, ^{13}C and ^{15}N isotope contents etc.), well defined amounts of cells were taken from different test cultures at defined timesteps for later analysis by SDS-PAGE. At each timestep, the OD was determined at 600 nm and the volume of the sample was adjusted such that its volume (in ml) multiplied by its OD was equal to one. Immediately upon volume adjustment, the sample was transferred into an Eppendorf tube and centrifuged for 5 minutes at full speed. After quantitative removal of the supernatant, 5 µl SDS-PAGE loading buffer (5 x) and 15 µl water were added, and the sample was heated for 5 minutes to 95°C before it was stored at room temperature for later analysis by SDS-PAGE.

7.2.12 SDS-PAGE

Sodium dodecylsulfate polyacrylamide gel electrophoresis (SDS-PAGE) was performed in SE 250 mini-vertical gel electrophoresis units (Hoefer). 0.625 ml acrylamide/bisacrylamide (37.5:1, 40 % w/v) (Serva, Heidelberg, Germany), 2.5 ml loading gel stock solution (2 x), 0.1 ml 10 % (w/v) SDS, and 1.775 ml H_2O were used to prepare 5 ml loading gel. 3.75 ml acrylamide/bisacrylamide (37.5:1, 40 % w/v), 2.5 ml separating gel stock solution (4 x), 0.2 ml 10 % (w/v) SDS, and 3.55 ml H_2O were used to prepare 10 ml separating gel. 65 µl ammoniumpersulfate (APS) solution

(10 %) and 4 µl N,N,N',N'-tetramethylethylendiamin (TEMED) were added directly before casting of loading and separating gels.
Samples were prepared by heating a mixture of 5 µl loading buffer (5 x) and 20 µl protein solution in Eppendorf tubes for 5 minutes to 95 °C.

7.2.13 Fast Protein Liquid Chromatography

ÄKTA FPLC device (Amersham Pharmacia Biotech; today GE Healthcare, Munich; Germany) including a UPC-900 control unit, a P-920 pump, a P-900 fraction collector, an INV-907 valve, a M-925 mixer, a 0.6 ml mixing chamber, a conductivity flow cell, and a Hg lamp.

Columns

Cation exchange	24 ml Q-Sepharose fast flow resin (GE Healthcare, Munich, Germany) self packed into a XK 16/20 column (GE Healthcare, Munich, Germany)
Anion exchange	6 ml Resource S column (GE Healthcare, Munich, Germany)
Desalting	HiPrep 26/10 Desalting (GE Healthcare, Munich, Germany)

7.2.14 Expression and Purification of $Hsp26_{30\text{-}195}$

$Hsp26_{30\text{-}195}$ was expressed from *E. coli* BL21 (DE3) cells that contained constructs of pET28b+ vectors with $Hsp26_{\Delta N30\text{-}195C}$ gene inserted via Nco1 and Not1 restriction sites. These cells were obtained from Titus Franzmann at the chair in Biotechnology of the Technische Universität München. The pET28b+$Hsp26_{\Delta N30\text{-}195C}$ construct was extracted once from these cells using *Wizard® Plus SV Minipreps* (Promega Corporation, Madison, WI, USA) and transformed before each expression into *E. coli* BL21 (DE3) cells that were plated on Agar plates containing Lysogeny broth (LB) medium supplemented with 35 µg/ml Kanamycin. The plates were incubated at 37 °C for 24 hours. Precultures containing 20 – 50 ml LB medium with 35 µg/ml Kanamycin were derived from individual colonies and shaken over night at 37 °C.
1 Liter LB medium supplemented with 35 µg/ml Kanamycin or 1 Liter isotope (^{13}C and ^{15}N) enriched minimal medium (M9) supplemented with 35 µg/ml Kanamycin were inoculated with 20 ml preculture and shaken at 37 °C until the OD had reached 0.7 - 0.9. Protein expression was induced by addition of 1 mM isopropyl-β-D-thiogalactopyranoside (IPTG). Expression was done for 3 – 5 h at 37 °C. After centrifugation (20 min, 6000 g, 4°C) the supernatant was decanted. The cell pellet was washed carefully for few seconds with 30 ml ice cold buffer A (20 mM HEPES,

pH 8) to remove remaining salts and then resuspended in 40 ml buffer A. The cells were lysed using a Basic Z cell disrupter (Constant Systems Ltd., Daventry, UK) at a pressure of 2.0 kbar. As soon as the first lysate left the disruption apparatus, 1 ml Protease-Inhbitors Mix B (Serva, Heidelberg, Germany) and ~ 1 mg DNAse I (Serva, Heidelberg, Germany) were added into the ice-cooled collecting flask. Non-lysed cells and all other insoluble contents were removed from the lysate by centrifugation (30 min, 50000 g, 8°C).

Purification of $Hsp26_{30\text{-}195}$ by fast protein liquid chromatography (FPLC) was performed at 4 °C. The supernatant was diluted with ice-cooled buffer A to a volume of 150 ml and applied to a Q-Sepharose anion exchange column (GE Healthcare, Munich, Germany) at a flow rate of 4 ml/min (column inner diameter of 16 mm, length of 12 cm). After washing with 100 ml buffer A at 4 ml/min, $Hsp26_{30\text{-}195}$ was eluted applying a linear NaCl gradient (0 – 0.5 M) with a volume of 150 ml at 4 ml/min. The eluate was separated into 3 ml fractions and analyzed by sodium dodecyl sulfate polyacrylamide gel electrophoresis (SDS-PAGE). 30 µl Protease-Inhbitors Mix B were added immediately upon elution to all fractions containing 30 – 270 mM NaCl.

The fractions containing $Hsp26_{30\text{-}195}$ according to SDS-PAGE were pooled, diluted to a final volume of 150 ml with buffer A (20 mM HEPES, pH 8) and applied to an equilibrated Resource S (6 ml) cation exchange column (GE Healthcare, Munich, Germany) at a flow rate of 2 ml/min. After washing with 60 ml buffer A at 2 ml/min, $Hsp26_{30\text{-}195}$ was eluted applying a linear NaCl gradient (0 – 1 M) with a volume of 60 ml at 2 ml/min. The eluate was separated into 3 ml fractions and analyzed by SDS-PAGE. Pure fractions were pooled and dialyzed twice against 2 L 10 mM NaP_i, 1 mM EDTA at 4 °C. The protein was further analyzed by MALDI-TOF mass spectrometry.

7.2.15 Expression and Purification of $Hsp26_{30\text{-}195(\Delta137\text{-}153)}$

The expression and purification of $Hsp26_{30\text{-}195(\Delta137\text{-}153)}$ were performed exactly as described for $Hsp26_{30\text{-}195}$.

7.2.16 Circular Dichroism Spectroscopy

CD spectroscopy was performed on a Jasco J-715 spectropolarimeter (Jasco, Groß-Umstadt, Germany) using 0.1 cm path-length quartz cuvettes (Helma AG, Müllheim, Germany). If not otherwise mentioned, spectra were recorded with 5 transients from 190 – 260 nm with a scanning speed of 50 nm/min, a bandwidth of 5 nm and a

response of 2 s. For thermal transitions, a heating speed of 60 K/h was used and the signals at 219 nm or 222 nm were followed.

7.2.17 UV/Vis Spectroscopy

UV/Vis spectroscopy was performed on a Cary-100 UV/Vis spectrophotometer (Varian, Palo Alto, CA, USA). The optical density of cell cultures was monitored at 600 nm in a BIO-RAD SmartSpec Plus spectrophotometer.

7.2.18 NMR Spectroscopy

A two-dimensional ^{1}H-^{15}N HSQC spectrum and a set of three-dimensional out-and-back triple-resonance[298,299,322] spectra including HNCO, HNCA, HN(CO)CA, HNCACB, HN(CO)CACB, and HN(CA)CO were recorded of $^{13}C/^{15}N$-labeled $Hsp26_{30\text{-}195(\Delta 137\text{-}153)}$ (1 mM in 10 mM NaP_i, 1 mM EDTA) at 298 K on a 600 MHz Avance III Bruker spectrometer equipped with a cryo TCI probe (^{1}H, ^{13}C, ^{15}N) with z-gradient. The coupling of $^{13}C^{\alpha}$, $^{13}C'$ and ^{1}H to ^{15}N during t1 was suppressed in the ^{1}H-^{15}N HSQC experiment by inversion of these resonances in the middle of t1 using ^{15}N hard pulses as well as two gauss cascade amplitude and phase modulated pulses (*Q3.1000*) with a length of 256 µs on $^{13}C^{\alpha}$ and $^{13}C'$. The t1 period of the ^{1}H-^{15}N HSQC was embedded in zz-filters.[323] Water suppression was achieved using WATERGATE[306] within the second INEPT step and by applying water flip-back pulses with a sinc amplitude modulation (*SINC1.1000*) and a length of 1 ms within the zz-filter elements. 8 transients with 1024 (256) complex data points were recorded in the direct (indirect) dimension and the data was processed in TOPSPIN 1.3 (Bruker BioSpin, Rheinstetten, Germany) to a matrix of 1024 x 1024 data points including linear prediction (*LPfr*) of 128 output points (*LPBIN*) based on 32 coefficients (*NCOEFF*) in the indirect dimension.

The experiments *hncogp3d*, *hncagp3d*, *hncocagp3d*, *hncacbgp3d*, *hncocacbgp3d*, and *hncacogp3d*, as delivered with TOPSPIN 2.1 were applied with gauss cascade amplitude and phase modulated pulses (*Q3.1000*) with a length of 256 µs for selective inversion and refocusing $^{13}C'$, $^{13}C^{\alpha}$, or $^{13}C^{\alpha/\beta}$. Gauss cascade amplitude and phase modulated pulses with a length of 400 µs were used for selective excitation of $^{13}C'$, $^{13}C^{\alpha}$, or $^{13}C^{\alpha/\beta}$ (*Q5.1000* and Q5tr.1000). Pulses with a sinc amplitude modulation (*SINC1.1000*) and a length of 1 ms were applied for aligning the water

magnetization along the +z axis before acquisition. More experimental details are given in Table 6.5.

Table 6.5: Experimental details for NMR spectra recorded of $Hsp26_{30\text{-}195(\Delta 137\text{-}153)}$.

Experiment	*Transients*	f1 (^{13}C)		f2 (^{15}N)		f3 (^{1}H)	
		Incr.	sw (min, max) [ppm]	Incr.	sw (min, max) [ppm]	Data points	sw (min, max) [ppm]
HNCO	8	96	163.8 - 182.2	50	97 - 137	1024	-1.3 - 10.7
HNCA	8	90	40.6 – 67.4	50	102 - 132	1024	-1.3 - 10.7
HN(CO)CA	8	90	40.6 – 67.3	50	102 - 132	1024	-1.3 - 10.7
HNCACB	16	110	6.2 - 68.8	50	102 - 132	1024	-1.3 - 10.7
HN(CO)CACB	16	110	6.2 - 68.8	50	102 - 132	1024	-1.3 - 10.7
HN(CA)CO	16	90	163.8 - 182.2	50	102 - 132	1024	-1.3 - 10.7

The spectra were processed in TOPSPIN 1.3 to 256, 128 and 1024 data points along f1, f2, and f3, respectively. 96 (48) data points (*LPBIN*) were predicted along f1 (f2) using 24 (12) coefficients (*NCOEFF*). Peaks were picked in Sparky 3.110 (T. D. Goddard and D. G. Kneller, University of California, San Francisco). The sequential assignment was established using Protein ASsignment by Threshold Accepting (PASTA).[324] Secondary structure was estimated using N, C^{α}, C^{β}, and C' chemical shifts in TALOS+.[325] Only confidence for β-strand higher than 0.8, as read from the file *predSS* was considered for color coding of the Hsp26 structural model shown in Figure 5.8 B.

Appendix A

Table A.1: Comparison between the experimentally derived distance restraints (d_{low}), (d_{upp}) and calculated (d_{rMD}) interproton distances of compound 4-*N*Me-(His^6,Arg^8,Trp^9,Lys^{10})-MT-II as obtained from restrained MD calculation. Violations of upper bounds (positive sign) and of lower bounds (negative sign) are given in the last column (d_{viol}).

interproton distance		d_{low} [Å]	d_{upp} [Å]	d_{MD} [Å]	d_{viol} [Å]
Asp^5 H^{β}_{proR}	Asp^5 H^{α}	2.32	2.84	2.629	
Asp^5 H^{β}_{proS}	Asp^5 H^{α}	2.58	3.15	3.050	
Asp^5 H^{α}	*N*Me-His^6 H^{Me}	2.08	3.19	2.758	
Asp^5 H^{β}_{proR}	*N*Me-His^6 H^{α}	4.13	5.05	4.635	
Asp^5 H^{β}_{proR}	*N*Me-His^6 H^{Me}	2.52	3.68	3.286	
Asp^5 H^{β}_{proS}	*N*Me-His^6 H^{α}	4.73	5.78	5.248	
Asp^5 H^{α}	*N*Me-His^6 H^{α}	4.15	5.07	4.608	
Asp^5 H^{β}_{proR}	D-Phe^7 H^{N}	3.15	3.85	3.520	
Asp^5 H^{β}_{proS}	D-Phe^7 H^{N}	3.43	4.19	4.100	
Asp^5 H^{β}_{proR}	*N*Me-Trp^9 H^{Me}	2.62	3.78	2.716	
Asp^5 H^{α}	*N*Me-Lys^{10} H^{ζ}	3.06	3.74	4.014	+0.27
Asp^5 H^{β}_{proR}	*N*Me-Lys^{10} H^{ζ}	2.77	3.38	3.054	
*N*Me-His^6 H^{Me}	*N*Me-His^6 H^{α}	3.21	4.43	3.913	
*N*Me-His^6 H^{α}	D-Phe^7 H^{N}	2.05	2.51	2.390	
*N*Me-His^6 H^{β}	D-Phe^7 H^{N}	3.71	5.23	4.326	
*N*Me-His^6 H^{Me}	D-Phe^7 H^{N}	3.4	4.64	4.334	
*N*Me-His^6 H^{α}	D-Phe^7 H^{α}	3.78	4.62	4.500	
*N*Me-His^6 H^{Me}	*N*Me-Trp^9 H^{Me}	3.24	4.97	3.689	
*N*Me-His^6 H^{Me}	*N*Me-Trp^9 $H^{\delta1}$	3.4	4.64	3.660	
D-Phe^7 H^{N}	D-Phe^7 H^{α}	2.53	3.09	3.053	
D-Phe^7 H^{β}	D-Phe^7 H^{N}	2.32	3.53	3.187	
D-Phe^7 H^{N}	*N*Me-Arg^8 H^{α}	3.77	4.61	4.748	+0.14
D-Phe^7 H^{α}	*N*Me-Arg^8 H^{Me}	2.11	3.22	2.679	
D-Phe^7 H^{β}	*N*Me-Arg^8 H^{β}	3.08	5.16	4.752	
D-Phe^7 H^{β}	*N*Me-Arg^8 H^{Me}	2.65	4.52	4.450	
D-Phe^7 H^{α}	*N*Me-Trp^9 $H^{\varepsilon1}$	4.37	5.34	4.472	
*N*Me-Arg^8 H^{Me}	*N*Me-Arg^8 H^{α}	3.17	4.39	3.872	
*N*Me-Arg^8 H^{α}	*N*Me-Trp^9 H^{Me}	2.08	3.18	2.779	
*N*Me-Arg^8 H^{β}	*N*Me-Trp^9 H^{α}	4.23	5.87	5.526	
*N*Me-Arg^8 H^{Me}	*N*Me-Trp^9 H^{α}	3.98	5.29	5.034	
*N*Me-Arg^8 H^{Me}	*N*Me-Trp^9 H^{Me}	3.34	5.06	4.816	
*N*Me-Arg^8 H^{α}	*N*Me-Trp^9 H^{α}	3.75	4.59	4.579	
*N*Me-Arg^8 H^{Me}	*N*Me-Trp^9 $H^{\delta1}$	3.3	4.53	4.760	+0.23
*N*Me-Arg^8 H^{Me}	*N*Me-Trp^9 $H^{\varepsilon1}$	3.27	4.5	4.184	
*N*Me-Arg^8 H^{Me}	*N*Me-Trp^9 $H^{\varepsilon3}$	3.63	4.9	4.359	
*N*Me-Arg^8 H^{Me}	*N*Me-Trp^9 $H^{\eta2}$	3.6	4.86	4.123	
*N*Me-Arg^8 H^{Me}	*N*Me-Trp^9 $H^{\zeta2}$	3.45	4.7	3.806	
*N*Me-Arg^8 H^{Me}	*N*Me-Trp^9 $H^{\zeta3}$	2.89	4.08	4.327	+0.25

interproton distance		d_{low} [Å]	d_{upp} [Å]	d_{MD} [Å]	d_{viol} [Å]
*N*Me-Arg^{8} H$^{\alpha}$	*N*Me-Lys^{10} H^{Me}	3.32	4.56	4.472	
*N*Me-Arg^{8} H$^{\beta}$	*N*Me-Lys^{10} H^{Me}	3.26	5.19	5.333	+0.14
*N*Me-Trp^{9} H^{Me}	*N*Me-Trp^{9} H$^{\alpha}$	3.15	4.37	3.905	
*N*Me-Trp^{9} H$^{\alpha}$	*N*Me-Lys^{10} H^{Me}	2.23	3.35	2.996	
*N*Me-Trp^{9} H^{Me}	*N*Me-Lys^{10} H$^{\alpha}$	3.56	4.83	4.889	+0.06
*N*Me-Trp^{9} H^{Me}	*N*Me-Lys^{10} H$^{\zeta}$	3.34	4.58	4.504	
*N*Me-Trp^{9} H^{Me}	*N*Me-Lys^{10} H$^{\delta}$	3.63	5.59	5.450	
*N*Me-Trp^{9} H^{Me}	*N*Me-Lys^{10} H$^{\gamma 1}$	2.85	4.04	3.964	
*N*Me-Trp^{9} H^{Me}	*N*Me-Lys^{10} H$^{\gamma 2}$	2.85	4.04	3.057	
*N*Me-Trp^{9} H$^{\alpha}$	*N*Me-Lys^{10} H$^{\alpha}$	3.78	4.62	4.620	
*N*Me-Trp^{9} H$^{\alpha}$	Amide^{11} H^{N}	3.95	5.52	5.457	
*N*Me-Lys^{10} H$^{\beta}$	*N*Me-Lys^{10} H^{Me}	2.31	4.14	3.617	
*N*Me-Lys^{10} H$^{\delta}$	*N*Me-Lys^{10} H$^{\alpha}$	2.57	3.84	4.258	+0.42
*N*Me-Lys^{10} H$^{\delta}$	*N*Me-Lys^{10} H$^{\zeta}$	2.83	4.16	3.447	
*N*Me-Lys^{10} H$^{\delta}$	*N*Me-Lys^{10} H$^{\beta}$	2.42	4.36	2.532	
*N*Me-Lys^{10} H$^{\delta 1}$	*N*Me-Lys^{10} H^{Me}	4.33	5.66	5.053	
*N*Me-Lys^{10} H$^{\delta 2}$	*N*Me-Lys^{10} H^{Me}	4.33	5.66	5.731	+0.07
*N*Me-Lys^{10} H$^{\varepsilon}$	*N*Me-Lys^{10} H$^{\gamma}$	2.99	5.06	3.218	
*N*Me-Lys^{10} H$^{\gamma}$	*N*Me-Lys^{10} H$^{\alpha}$	2.57	3.85	2.597	
*N*Me-Lys^{10} H$^{\gamma}$	*N*Me-Lys^{10} H$^{\zeta}$	2.88	4.22	3.798	
*N*Me-Lys^{10} H$^{\gamma}$	*N*Me-Lys^{10} H^{Me}	2.96	4.87	4.133	
*N*Me-Lys^{10} H^{Me}	*N*Me-Lys^{10} H$^{\alpha}$	3.22	4.44	3.897	
*N*Me-Lys^{10} H$^{\alpha}$	Amide^{11} H^{N}	2.87	4.21	3.349	
*N*Me-Lys^{10} H$^{\beta}$	Amide^{11} H^{N}	2.94	4.99	3.889	
*N*Me-Lys^{10} H^{Me}	Amide^{11} H^{N}	3.43	5.38	4.116	

Appendix B

Table B.1: Comparison between the experimentally derived distance restraints (d_{low}), (d_{upp}) and calculated (d_{MD}) interproton distances of 3-*N*Me-(D-Trp^{8},Lys^{9},Phe^{11})-seglitide as obtained from restrained MD calculation (r^{-6} averaged distance as backcalculated from the 50 ns MD trajectory). Violations of upper bounds (positive sign) and of lower bounds (negative sign) are given in the last column (d_{viol}).

interproton distance		d_{low} [Å]	d_{upp} [Å]	d_{MD} [Å]	d_{viol} [Å]
*N*Me-Ala^{6} H^{Me}	*N*Me-Ala^{6} H$^{\alpha}$	3.60	4.81	3.59	-0.01
*N*Me-Ala^{6} H^{Me}	*N*Me-Ala^{6} H$^{\beta}$	3.19	4.69	3.49	
*N*Me-Ala^{6} H$^{\alpha}$	Tyr^{7} H^{N}	2.18	2.66	2.32	
*N*Me-Ala^{6} H$^{\beta}$	Tyr^{7} H^{N}	4.11	5.42	4.28	
*N*Me-Ala^{6} H^{Me}	Tyr^{7} H^{N}	3.04	4.11	3.90	
*N*Me-Ala^{6} H^{Me}	Tyr^{7} H$^{\alpha}$	4.40	5.78	5.40	
*N*Me-Ala^{6} H$^{\alpha}$	*N*Me-D-Trp^{8} H^{Me}	4.50	5.90	5.37	
*N*Me-Ala^{6} H^{Me}	Val^{10} H$^{\gamma 2}$	4.27	6.02	6.33	+0.31
*N*Me-Ala^{6} H$^{\alpha}$	*N*Me-Phe^{11} H$^{\alpha}$	1.61	1.96	1.61	
*N*Me-Ala^{6} H^{Me}	*N*Me-Phe^{11} H$^{\alpha}$	4.61	6.03	4.26	-0.35
Tyr^{7} H^{N}	*N*Me-D-Trp^{8} H$^{\alpha}$	4.08	4.99	4.74	
Tyr^{7} H^{N}	*N*Me-D-Trp^{8} H^{Me}	3.89	5.15	4.18	
Tyr^{7} H$^{\alpha}$	*N*Me-D-Trp^{8} H^{Me}	2.28	3.18	2.45	
Tyr^{7} H^{N}	Val^{10} H^{N}	2.82	3.44	3.31	
Tyr^{7} H^{N}	Val^{10} H$^{\gamma 2}$	2.99	4.06	4.26	+0.20
Tyr^{7} H^{N}	*N*Me-Phe^{11} H^{Me}	5.01	6.52	5.11	
*N*Me-D-Trp^{8} H$^{\alpha}$	Val^{10} H^{N}	3.19	3.90	3.59	
*N*Me-D-Trp^{8} H$^{\alpha}$	Val^{10} H$^{\gamma 2}$	4.61	6.04	5.03	
Val^{10} H^{N}	Val^{10} H$^{\beta}$	3.28	4.01	3.64	
Val^{10} H$^{\alpha}$	Val^{10} H$^{\beta}$	2.06	2.52	2.35	
Val^{10} H^{N}	Val^{10} H$^{\gamma 1}$	3.39	4.55	3.65	
Val^{10} H$^{\alpha}$	Val^{10} H$^{\gamma 1}$	2.61	3.59	2.81	
Val^{10} H^{N}	Val^{10} H$^{\gamma 2}$	2.70	3.70	2.92	
Val^{10} H$^{\alpha}$	Val^{10} H$^{\gamma 2}$	3.53	4.72	3.70	
Val^{10} H^{N}	*N*Me-Phe^{11} H$^{\alpha}$	4.25	5.19	4.59	
Val^{10} H$^{\alpha}$	*N*Me-Phe^{11} H^{Me}	2.21	3.10	2.45	
Val^{10} H$^{\beta}$	*N*Me-Phe^{11} H^{Me}	2.38	3.31	3.59	+0.28
Val^{10} H$^{\gamma 2}$	*N*Me-Phe^{11} H^{Me}	4.43	6.21	5.47	
Val^{10} H$^{\gamma 1}$	*N*Me-Phe^{11} H^{Me}	4.43	6.22	4.96	
*N*Me-Phe^{11} H$^{\alpha}$	*N*Me-Phe^{11} H^{Me}	3.44	4.60	3.11	-0.33

Appendix C

Table C.1: Comparison between the experimentally derived distance restraints (d_{low}), (d_{upp}) and calculated (d_{DG}, d_{MD}) interproton distances of c(-R-G-*N*MeD-f-*N*MeV-) as obtained from distance geometry calculation and unrestrained MD calculation (r^{-6} averaged distance that were backcalculated from 1001 frames of the 50 ns MD trajectory). Violations of upper bounds (positive sign) and of lower bounds within the MD trajectory (negative sign) are also given (d_{viol}).

interproton distance		d_{low} [Å]	d_{upp} [Å]	d_{DG} [Å]	d_{MD} [Å]	d_{viol} [Å]	utilization(**)
Arg^1 H^N	Arg^1 H$^\alpha$	1.92	2.35	2.21	2.02		c
Arg^1 H$^\alpha$	Gly^2 H^N	2.55	3.12	2.27	3.44	+0.32(*)	c
Arg^1 H^N	*N*Me-Val^5 H$^\alpha$	1.85	2.26	2.06	2.09		c
Arg^1 H^N	*N*Me-Val^5 H$^{\gamma proR}$	2.96	4.01	3.56	3.53		c
Arg^1 H^N	*N*Me-Val^5 H^{Me}	3.44	4.60	4.66	4.97	+0.37	a
Gly^2 H^N	*N*Me-Asp^3 H^{Me}	3.09	4.18	4.34	3.79		c
Gly^2 H$^{\alpha'}$	*N*Me-Asp^3 H^{Me}	2.66	3.65	2.41	2.48	-0.18	a
Gly^2 H$^{\alpha''}$	*N*Me-Asp^3 H^{Me}	2.66	3.65	3.22	3.81	+0.16	a
Gly^2 H^N	*N*Me-Val^5 H$^\alpha$	3.46	4.23	4.90	4.49	+0.26	c
*N*Me-Asp^3 H$^\alpha$	*N*Me-Asp^3 H^{Me}	2.68	3.67	2.57	2.54	-0.12	c
D-Phe^4 H^N	Gly^2 H$^{\alpha'}$	3.74	4.57	5.64	4.95	+0.38	a
D-Phe^4 H^N	*N*Me-Asp^3 H$^\alpha$	2.13	2.60	2.01	2.24		c
D-Phe^4 H^N	*N*Me-Asp^3 H^{Me}	3.01	4.08	4.50	3.49		c
D-Phe^4 H^N	D-Phe^4 H$^\alpha$	2.88	3.08	2.83	2.86	-0.02	c
D-Phe^4 H^N	*N*Me-Val^5 H$^\alpha$	3.69	4.51	5.06	4.74	+0.23	c
D-Phe^4 H$^\alpha$	*N*Me-Val^5 H$^{\gamma proS}$	3.90	5.16	4.88	4.99		c
D-Phe^4 H$^\alpha$	*N*Me-Val^5 H^{Me}	2.18	3.07	2.29	2.41		c
*N*Me-Val^5 H$^{\gamma proR}$	Arg^1 H$^\alpha$	4.36	5.73	5.11	5.09		c
*N*Me-Val^5 H^{Me}	*N*Me-Val^5 H$^\beta$	2.24	3.14	2.75	2.76		c
*N*Me-Val^5 H$^\alpha$	*N*Me-Val^5 H$^{\gamma proR}$	2.54	3.51	2.75	2.98		c
*N*Me-Val^5 H$^\alpha$	*N*Me-Val^5 H$^{\gamma proS}$	2.62	3.60	2.62	2.76		c
*N*Me-Val^5 H^{Me}	*N*Me-Val^5 H$^{\gamma proS}$	3.22	4.74	3.68	3.97		c

(*) These strong upper bound violations seem to results from sequential magnetization transfer via J coupling and cross relaxation.

(**) Distance information used as restraints within the preceeding distance geometry calculation (c) and distance information used exclusively for the analysis (a) of the MD trajectory.

Table C.2: Comparison between the experimentally derived distance restraints (d_{low}), (d_{upp}) and calculated (d_{DG}, d_{MD}) interproton distances of compound c(-*N*MeR-G-D-f-*N*MeV-) as obtained from distance geometry calculation and unrestrained MD calculation (r^{-6} averaged distance that were back calculated from 1001 frames of the 50 ns MD trajectory), respectively. Violations of upper bounds (positive sign) and of lower bounds (negative sign) are also given (d_{viol}).

interproton distance		d_{low} [Å]	d_{upp} [Å]	d_{DG} [Å]	d_{MD} [Å]	d_{viol} [Å]	utilization(**)
*N*Me-Arg^{1} H$^{\alpha}$	*N*Me-Arg^{1} H^{Me}	3.53	4.72	3.33	3.59		c
*N*Me-Arg^{1} H^{Me}	*N*Me-Val^{5} H$^{\alpha}$	4.49	5.89	4.02	4.34	-0.15	c
Gly^{2} H^{N}	*N*Me-Arg^{1} H$^{\alpha}$	2.50	3.05	2.98	2.37	-0.13	c
Gly^{2} H^{N}	*N*Me-Arg^{1} H^{Me}	3.38	4.54	4.63	4.26		c
Asp^{3} H^{N}	Gly^{2} H^{N}	2.99	3.66	4.33	3.39		c
Asp^{3} H^{N}	Asp^{3} H$^{\alpha}$	2.42	2.96	2.88	2.81		c
Asp^{3} H^{N}	D-Phe^{4} H^{N}	2.95	3.61	3.28	2.78	-0.17	c
D-Phe^{4} H^{N}	*N*Me-Arg^{1} H$^{\alpha}$	3.15	3.85	3.48	4.26	+0.41	c
D-Phe^{4} H^{N}	Gly^{2} H^{N}	3.36	4.11	3.85	3.51		c
D-Phe^{4} H^{N}	Asp^{3} H$^{\alpha}$	1.98	2.42	2.55	2.49	+0.07	c
D-Phe^{4} H$^{\alpha}$	*N*Me-Val^{5} H^{Me}	2.18	3.07	2.25	2.42		c
*N*Me-Val^{5} H$^{\alpha}$	*N*Me-Arg^{1} H$^{\alpha}$	1.60	1.96	1.71	1.77		c
*N*Me-Val^{5} H$^{\gamma proR}$	*N*Me-Arg^{1} H$^{\alpha}$	3.85	5.10	4.18	4.11		c
*N*Me-Val^{5} H^{Me}	*N*Me-Arg^{1} H$^{\alpha}$	4.58	6.00	3.54	4.61		c
*N*Me-Val^{5} H^{Me}	Gly^{2} H^{N}	4.55	5.96	5.66	5.88		c
*N*Me-Val^{5} H^{Me}	D-Phe^{4} H^{N}	4.14	5.46	3.84	4.20		c
*N*Me-Val^{5} H$^{\gamma proS}$	D-Phe^{4} H$^{\alpha}$	3.13	4.22	4.30	4.89	+0.67	c
*N*Me-Val^{5} H^{Me}	*N*Me-Val^{5} H$^{\alpha}$	3.41	4.57	3.30	3.62		c
*N*Me-Val^{5} H^{Me}	*N*Me-Val^{5} H$^{\beta}$	2.35	3.27	3.22	2.88		c
*N*Me-Val^{5} H$^{\alpha}$	*N*Me-Val^{5} H$^{\gamma proS}$	2.23	3.13	2.84	2.87		c
*N*Me-Val^{5} H^{Me}	*N*Me-Val^{5} H$^{\gamma proS}$	2.80	4.23	3.83	4.06		c
*N*Me-Val^{5} H$^{\alpha}$	*N*Me-Val^{5} H$^{\gamma proR}$	2.14	3.02	2.62	2.96		c

(*) These strong upper bound violations seem to results from sequential magnetization transfer via J coupling and cross relaxation.

(**) Distance information used as restraints within the preceeding distance geometry calculation (c) and distance information used exclusively for the analysis (a) of the MD trajectory.

Table C.3: Comparison between the experimentally derived distance restraints (d_{low}), (d_{upp}) and calculated (d_{MD}) interproton distances of compound c(-*N*MeR-G-D-*N*Mef-V-) as obtained from unrestrained MD calculation (r^{-6} averaged distance that were calculated back from 2001 frames of the 100 ns MD trajectory). Violations of upper bounds (positive sign) and of lower bounds within the MD trajectory (negative sign) are also given (d_{viol}).

interproton distance		d_{low} [Å]	d_{upp} [Å]	d_{DG} [Å]	d_{MD} [Å]	d_{viol} [Å]	utilization(**)
*N*Me-Arg^1 H$^\alpha$	*N*Me-Arg^1 H^{Me}	2.45	3.4	2.51	2.50		c
*N*Me-Arg^1 H$^\alpha$	Gly^2 H^N	2.49	3.05	2.56	2.21	-0.28	a
*N*Me-Arg^1 H^{Me}	Gly^2 H^N	3.13	4.23	4.53	3.59		c
*N*Me-Arg^1 H$^\alpha$	Asp^3 H^N	4.11	5.03	4.78	5.63	+0.6	c
*N*Me-Arg^1 H$^\alpha$	Val^5 H$^{\gamma proS}$	5.45	7.06	5.82	6.64		a
*N*Me-Arg^1 H^{Me}	Val^5 H^N	4.5	8.00	4.52	4.73		c
*N*Me-Arg^1 H^{Me}	Val^5 H$^\alpha$	2.3	3.21	2.50	2.44		c
*N*Me-Arg^1 H^{Me}	Val^5 H$^{\gamma proS}$	4.74	6.6	4.05	5.09		a
*N*Me-Arg^1 H^{Me}	Val^5 H$^{\gamma proR}$	4.23	5.97	5.26	4.27		a
Gly^2 H^N	Asp^3 H^N	2.43	2.97	3.18	3.79	+0.82(*)	c
Gly^2 H^N	*N*Me-D-Phe^4 H^{Me}	3.8	5.04	6.11	5.71	+0.67	c
Gly^2 H^N	Val^5 H^N	4.49	5.49	6.00	5.34		c
Asp^3 H^N	Asp^3 H$^\alpha$	2.88	3.08	2.76	2.70	-0.18	c
Asp^3 H$^\alpha$	*N*Me-D-Phe^4 H^{Me}	2.34	3.26	2.38	2.41		c
*N*Me-D-Phe^4 H^{Me}	*N*Me-D-Phe^4 H$^\alpha$	3.5	4	3.26	3.57		c
*N*Me-D-Phe^4 H$^\alpha$	Val^5 H^N	2.06	2.52	2.21	2.10		c
*N*Me-D-Phe^4 H$^\alpha$	Val^5 H$^{\gamma proS}$	4.51	5.91	6.04	4.69		a
*N*Me-D-Phe^4 H$^\alpha$	Val^5 H$^{\gamma proR}$	4.5	5.9	4.57	5.76		a
*N*Me-D-Phe^4 H^{Me}	Val^5 H^N	3.9	5.16	4.49	4.90		c
*N*Me-D-Phe^4 H^{Me}	Val^5 H$^\alpha$	3.93	5.2	5.59	5.58	+0.38	a
Val^5 H^N	Val^5 H$^\alpha$	2.88	3.08	2.89	2.80	-0.08	c
Val^5 H^N	Val^5 H$^\beta$	3.13	3.83	3.16	2.49	-0.64(*)	c
Val^5 H^N	Val^5 H$^{\gamma proS}$	2.79	3.81	4.33	3.10		c
Val^5 H^N	Val^5 H$^{\gamma proR}$	3.65	4.86	2.97	3.82		c
Val^5 H$^\alpha$	Val^5 H$^\beta$	2.17	2.65	2.28	2.66	+0.01	c
Val^5 H$^\alpha$	Val^5 H$^{\gamma proS}$	3.59	4.78	2.61	2.99	-0.60	c
Val^5 H$^\alpha$	Val^5 H$^{\gamma proR}$	2.75	3.76	3.37	2.90		c

(*) These strong upper bound violations seem to results from sequential magnetization transfer via J coupling and cross relaxation.

(**) Distance information used as restraints within the preceeding distance geometry calculation (c) and distance information used exclusively for the analysis (a) of the MD trajectory.

Table C. 4: Temperature dependence of H^N chemical shifts, $^3J_{HN\text{-}H\alpha}$ coupling constants, $^3J_{H\alpha\text{-}H\beta}$ coupling constants and the according χ_1 populations in peptide **1**. The ranges given for the χ_1 populations were derived by assuming the following pairs of coupling constants: $^3J_{H\alpha\text{-}H\beta(ap)}$ = 12 Hz and $^3J_{H\alpha\text{-}H\beta(ga)}$ = 3.5 Hz as well as $^3J_{H\alpha\text{-}H\beta(ap)}$ = 13.6 Hz, $^3J_{H\alpha\text{-}H\beta(ga)}$ = 2.6 Hz.

	Δω/ΔT [ppb/K]	**$^3J_{HN\text{-}H\alpha}$ [Hz]**	**$^3J_{H\alpha\text{-}H\beta}$ [Hz]**	**$p_{(\chi1 = -60°)}$ [%]**	**$p_{(\chi1 = 180°)}$ [%]**	**$p_{(\chi1 = 60°)}$ [%]**
Arg[1]	-5.02	7.0	ca. 9 / ca. 6	90-94		6-10
Gly[2]	-4.16	7.2 / 2.8				
***N*Me-Asp**[3]			8.5 / 5.4	83-85		15-17
D-**Phe**[4]	-8.38	9.3	proR: 8.8 proS: 5.8	10-15	56-63	27-29
***N*Me-Val**[5]			11.2	0-22	78-90	0-22

Table C. 5: Temperature dependence of H^N chemical shifts, $^3J_{HN\text{-}H\alpha}$ coupling constants, $^3J_{H\alpha\text{-}H\beta}$ coupling constants and the according χ_1 populations in peptide **4**. The ranges given for the χ_1 populations were derived by assuming the following pairs of coupling constants: $^3J_{H\alpha\text{-}H\beta(ap)}$ = 12 Hz and $^3J_{H\alpha\text{-}H\beta(ga)}$ = 3.5 Hz as well as $^3J_{H\alpha\text{-}H\beta(ap)}$ = 13.6 Hz, $^3J_{H\alpha\text{-}H\beta(ga)}$ = 2.6 Hz.

	Δω/ΔT [ppb/K]	**$^3J_{HN\text{-}H\alpha}$ [Hz]**	**$^3J_{H\alpha\text{-}H\beta}$ [Hz]**	**$p_{(\chi1 = -60°)}$ [%]**	**$p_{(\chi1 = 180°)}$ [%]**	**$p_{(\chi1 = 60°)}$ [%]**
***N*Me-Arg**[1]			11.2 / 4.8	98-100		0-2
Gly[2]	-5.04	5.7 / 5.1				
Asp[3]	-4.93	9.0	proR: 8.4 proS: 5.7	26-28	53-58	16-19
D-**Phe**[4]	-2.34	8.2	proR: 8.2 pro: 5.3	24	51-55	21-25
***N*Me-Val**[5]			10.7	0-26	74-85	0-26

Table C. 6: Temperature dependence of H^N chemical shifts, $^3J_{HN\text{-}H\alpha}$ coupling constants, $^3J_{H\alpha\text{-}H\beta}$ coupling constants and the according χ_1 populations in peptide **10**. The ranges given for the χ_1 populations were derived by assuming the following pairs of coupling constants: $^3J_{H\alpha\text{-}H\beta(ap)}$ = 12 Hz and $^3J_{H\alpha\text{-}H\beta(ga)}$ = 3.5 Hz as well as $^3J_{H\alpha\text{-}H\beta(ap)}$ = 13.6 Hz, $^3J_{H\alpha\text{-}H\beta(ga)}$ = 2.6 Hz.

	Δω/ΔT [ppb/K]	**$^3J_{HN\text{-}H\alpha}$ [Hz]**	**$^3J_{H\alpha\text{-}H\beta}$ [Hz]**	**$p_{(\chi1 = -60°)}$ [%]**	**$p_{(\chi1 = 180°)}$ [%]**	**$p_{(\chi1 = 60°)}$ [%]**
***N*Me-Arg**[1]			9.4 / 4.8	82-85		15-18
Gly[2]	-3.05	8.1 / 4.2				
Asp[3]	-	9.0	proR: 10.8 proS: 3.8	4-11	74-86	10-15
***N*Me-**D-**Phe**[4]			8.5 / 7.1	0-5	95-100	
Val[5]	0.53	8.9	3.3	73	0-6	21-27

Appendix D

Resonance assignments of *N*-methylated cyclic (-a-A-A-A-A-A-) peptides

All resonances were assigned in DMSO-d6 at 300 K and at a proton resonance frequency of 500 MHz. Chemical shifts are referenced to the DMSO ^{1}H resonance at 2.52 ppm and the DMSO $^{13}C^{Me}$ resonance at 40.45 ppm.

Table D.1: Resonance assignment ***N*Me(1)**

	H^N (H^{Me})	H^α	H^β	C'	C^α	C^β	C^{Me}
1 D-Ala	(2.954)	4.794	1.260	171.9	53.57	14.97	31.20
2 Ala	8.224	4.219	1.284	172.8	48.98	18.51	
3 Ala	7.716	4.184	1.328	173.3	49.46	18.75	
4 Ala	8.293	3.876	1.262	172.6	50.99	17.21	
5 Ala	7.914	4.019	1.282	172.3	49.81	18.19	
6 Ala	7.871	4.579	1.172	172.5	46.88	18.22	

Table D.2: Resonance assignment ***N*Me(5)**

	H^N or (H^{Me})	H^α	H^β	C'	C^α	C^β	C^{Me}
1 D-Ala	8.538	4.197	1.195	173.2	49.94	17.22	
2 Ala	8.664	4.117	1.268	171.8	49.42	17.85	
3 Ala	7.398	4.433	1.239	173.2	47.22	20.45	
4 Ala	8.703	4.743	1.227	173.4	44.87	17.73	
5 Ala*	(2.578)	5.160	1.218	169.8	55.91	15.57	29.04
6 Ala	8.169	4.362	1.188	172.3	49.72	19.39	

Table D.3: Resonance assignment ***N*Me(1,2)**

	H^N or (H^{Me})	H^α	H^β	C'	C^α	C^β	C^{Me}
1 D-Ala	(3.035)	4.804	1.297	173.4	51.98	14.90	-
2 Ala	(2.897)	5.106	1.241	170.5	52.14	14.35	30.94
3 Ala	7.316	4.313	1.408	172.7	48.49	19.35	
4 Ala	8.235	3.809	1.268	173.1	52.07	17.12	
5 Ala	8.079	4.033	1.283	172.2	50.19	18.06	
6 Ala	7.320	4.674	1.202	172.8	46.90	18.68	

Table D.4: Resonance assignment ***N*Me(1,5)**

	H^N or (H^{Me})	H^α	H^β	C'	C^α	C^β	C^{Me}
1 D-Ala	(3.017)	4.834	1.284	173.0	53.13	15.87	31.19
2 Ala	8.657	4.063	1.268	171.9	49.55	18.01	
3 Ala	7.138	4.394	1.206	173.0	47.36	20.60	
4 Ala	8.751	4.692	1.211	173.4	45.32	17.74	
5 Ala	(2.583)	5.133	1.245	169.9	55.90	15.75	29.12
6 Ala	8.363	4.741	1.188	171.8	46.96	18.90	

Table D.5: Resonance assignment ***N*Me(1,6)**

	H^N or (H^{Me})	H^α	H^β	C'	C^α	C^β	C^{Me}
1 D-Ala	(2.817)	5.213	1.170	171.1	51.88	13.91	30.24
2 Ala	7.201	4.412	1.319	173.6	47.99	19.25	
3 Ala	8.419	3.829	1.259	173.2	51.81	16.82	
4 Ala	8.242	3.998	1.318	172.3	49.80	17.41	
5 Ala	7.585	4.618	1.087	172.3	47.03	17.90	
6 Ala	(3.072)	4.113	1.251	171.3	57.13	14.85	-

Table D.6: Resonance assignment ***N*Me(2,5)**

	H^N or (H^{Me})	H^α	H^β	C'	C^α	C^β	C^{Me}
1 D-Ala	8.770	4.579	1.223	174.6	45.92	16.79	
2 Ala	(2.982)	5.106	1.228	169.7	52.28	14.22	30.77
3 Ala	7.147	4.361	1.263	172.9	47.69	20.39	
4 Ala	8.728	4.759	1.233	173.5	44.85	17.89	
5 Ala	(2.572)	5.229	1.207	169.7	56.09	15.47	29.19
6 Ala	7.951	4.353	1.206	172.8	49.47	19.76	

Table D.7: Resonance assignments ***N*Me(3,5)**

***N*Me(3,5)$_{cis2\text{-}3,cis4\text{-}5}$**	H^N or (H^{Me})	H^α	H^β	C'	C^α	C^β	C^{Me}
1 D-Ala	7.631	4.346	1.162	171.0	48.78	17.47	
2 Ala	7.780	4.744	1.167	172.1	45.10	18.96	
3 Ala	(2.641)	4.712	1.446	171.8	55.80	16.10	30.11
4 Ala	8.065	4.691	1.280	172.5	47.10	17.36	
5 Ala	(2.630)	4.838	1.339	170.1	55.71	15.06	29.24
6 Ala	8.063	4.458	1.203	172.0	48.78	19.17	

***N*Me(3,5)$_{cis2\text{-}3}$**	H^N or (H^{Me})	H^α	H^β	C'	C^α	C^β	C^{Me}
1 D-Ala	7.343	4.271	1.225	172.6	49.26	20.47	
2 Ala	8.746	4.777	1.232	173.4	44.38	18.62	
3 Ala	(2.594)	5.258	1.248	169.0	56.13	15.50	29.39
4 Ala	7.716	4.605	1.217	171.3	47.10	17.90	
5 Ala	(3.127)	3.644	1.339	171.3	62.00	13.84	37.93
6 Ala	7.810	4.285	1.247	171.6	49.00	16.83	

Table D.8: Resonance assignment ***N*Me(4,5)**

	H^N or (H^{Me})	H^α	H^β	C'	C^α	C^β	C^{Me}
1 D-Ala	8.630	4.160	1.204	173.4	50.18	16.99	
2 Ala	8.689	4.160	1.276	171.8	49.19	17.86	
3 Ala	7.567	4.843	1.204	173.4	45.93	18.12	
4 Ala	(3.109)	5.231	1.306	173.7	49.36	15.98	31.19
5 Ala	(2.548)	5.095	1.226	169.6	55.88	15.49	28.65
6 Ala	8.208	4.385	1.168	172.5	49.65	19.36	

Table D.9: Resonance assignments ***N*Me(5,6)**

***N*Me(5,6)$_{cis5\text{-}6}$**	H^N or (H^{Me})	H^α	H^β	C'	C^α	C^β	C^{Me}
1 D-Ala	8.002	4.392	1.262	172.3	49.19	20.44	
2 Ala	8.195	4.179	1.273	173.0	50.55	18.49	
3 Ala	8.238	4.041	1.297	171.5	50.23	17.99	
4 Ala	7.405	4.529	1.117	171.9	46.72	17.92	
5 Ala	(2.998)	5.249	1.241	173.3	49.72	15.61	31.09
6 Ala	(2.834)	4.801	1.347	171.1	53.87	17.57	29.27

***N*Me(5,6)$_{cis4\text{-}5,cis5\text{-}6}$**	H^N or (H^{Me})	H^α	H^β	C'	C^α	C^β	C^{Me}
1 D-Ala	8.423	4.164	1.267	175.0	50.44	16.87	
2 Ala	8.967	3.952	1.293	172.8	51.01	17.42	
3 Ala	7.426	4.023	1.145	172.4	49.21	18.02	
4 Ala	7.423	4.292	1.123	170.9	46.18	18.25	
5 Ala	(2.834)	4.831	1.365	171.4	53.00	18.09	31.89
6 Ala	(2.776)	4.554	1.503	173.6	54.36	18.53	30.64

Table D.10: Resonance assignment ***N*Me(1,2,5)**

	H^N or (H^{Me})	H^α	H^β	C'	C^α	C^β	C^{Me}
1 D-Ala	(3.088)	4.919	1.326	174.5	51.05	15.00	31.65
2 Ala	(2.951)	5.088	1.217	169.6	52.00	14.33	30.87
3 Ala	7.110	4.353	1.263	172.7	47.78	20.62	
4 Ala	8.736	4.707	1.230	173.7	45.06	17.85	
5 Ala	(2.582)	5.246	1.220	169.7	56.12	15.77	29.30
6 Ala	8.121	4.748	1.235	173.0	47.36	18.93	

Table D.11: Resonance assignment ***N*Me(1,3,6)**

	H^N or (H^{Me})	H^α	H^β	C'	C^α	C^β	C^{Me}
1 D-Ala	(2.600)	5.201	1.151	170.2	52.41	13.93	29.23
2 Ala	7.004	4.878	1.191	172.9	45.14	18.38	
3 Ala	(3.196)	3.688	1.335	171.0	61.16	14.90	27.17
4 Ala	8.095	4.000	1.342	171.5	49.61	16.74	
5 Ala	7.952	4.803	1.165	171.6	45.40	17.99	
6 Ala	(3.086)	3.878	1.235	170.8	58.25	14.88	28.35

Table D.12: Resonance assignment ***N*Me(2,4,5)**

	H^N or (H^{Me})	H^α	H^β	C'	C^α	C^β	C^{Me}
1 D-Ala	8.822	4.574	1.236	174.7	45.74	16.68	
2 Ala	(2.997)	5.133	1.238	169.4	52.19	14.30	30.69
3 Ala	7.267	4.803	1.218	173.0	46.41	18.34	
4 Ala	(3.095)	5.229	1.308	173.9	49.41	16.09	31.03
5 Ala	(2.544)	5.147	1.225	169.7	56.07	15.55	28.55
6 Ala	8.037	4.38	1.194	172.9	49.51	19.86	

Table D.13: Resonance assignment ***N*Me(1,2,4,5)**

	H^N or (H^{Me})	H^α	H^β	C'	C^α	C^β	C^{Me}
1 D-Ala	(3.117)	4.914	1.339	174.8	51.12	14.88	31.69
2 Ala	(2.972)	5.121	1.220	169.5	51.80	14.18	30.71
3 Ala	7.210	4.813	1.212	173.0	46.45	18.42	
4 Ala	(3.095)	5.184	1.300	174.1	49.71	16.07	31.40
5 Ala	(2.566)	5.170	1.237	169.8	56.07	15.65	28.88
6 Ala	8.151	4.792	1.228	173.4	47.27	19.18	

Table D.14: Resonance assignments ***N*Me(1,2,5,6)**

***N*Me(1,2,5,6)$_{cis4\text{-}5}$**	H^N or (H^{Me})	H^α	H^β	C'	C^α	C^β	C^{Me}
1 D-Ala	(2.740)	5.676	1.194	171.3	47.43	15.52	29.43
2 Ala	(2.781)	5.141	1.140	170.3	52.40	13.51	30.81
3 Ala	7.229	4.107	1.262	171.5	49.41	17.31	
4 Ala	8.669	4.952	1.294	171.9	44.81	18.53	
5 Ala	(2.606)	5.552	1.313	168.2	54.85	18.11	29.24
6 Ala	(2.477)	5.274	1.140	170.1	52.40	14.79	29.44

***N*Me(1,2,5,6)$_{cis5\text{-}6}$**	H^N or (H^{Me})	H^α	H^β	C'	C^α	C^β	C^{Me}
1 D-Ala	(2.994)	5.398	1.084	170.5	49.51	15.58	30.35
2 Ala	(2.873)	5.189	1.250	170.8	52.94	14.02	29.90
3 Ala	8.205	4.053	1.312	171.3	50.27	16.39	
4 Ala	7.380	4.554	1.080	172.4	46.41	17.98	
5 Ala	(3.036)	5.307	1.285	173.4	48.61	16.52	30.61
6 Ala	(2.953)	5.473	1.342	172.2	51.14	17.29	30.85

Table D.15: Resonance assignments ***N*Me(1,4,5,6)**

***N*Me(1,4,5,6)$_{cis4\text{-}5,cis5\text{-}6}$**	H^N or (H^{Me})	H^α	H^β	C'	C^α	C^β	C^{Me}
1 D-Ala	(3.201)	4.671	1.314	171.6	53.06	18.00	31.61
2 Ala	8.742	4.085	1.267	171.9	49.59	17.41	
3 Ala	7.254	4.550	1.032	171.3	45.22	17.85	
4 Ala	(2.723)	5.734	1.160	170.1	46.24	15.46	29.31
5 Ala	(2.858)	5.421	1.390	172.3	53.30	18.31	31.85
6 Ala	(2.867)	4.761	1.448	175.5	53.01	17.38	32.16

*N*Me(1,4,5,6)$_{cis3\text{-}4}$	H^N or (H^{Me})	H^α	H^β	C'	C^α	C^β	C^{Me}
1 D-Ala	(2.734)	5.065	1.137	169.9	52.24	13.39	30.27
2 Ala	7.115	4.277	1.308	172.9	47.93	18.43	
3 Ala	8.181	4.870	1.277	173.5	46.30	18.25	
4 Ala	(2.693)	5.156	1.316	169.8	51.86	18.39	29.97
5 Ala	(2.698)	5.274	1.115	170.7	50.21	14.75	30.51
6 Ala	(2.804)	4.702	1.296	170.4	54.18	14.98	32.40

Table D.16: Resonance assignments ***N*Me(2,4,5,6)**

*N*Me(2,4,5,6)$_{cis3\text{-}4,cis4\text{-}5}$	H^N or (H^{Me})	H^α	H^β	C'	C^α	C^β	C^{Me}
1 D-Ala	6.777	4.793	1.143	172.6	45.72	18.09	
2 Ala	(2.995)	5.096	1.462	172.2	53.03	14.45	30.74
3 Ala	8.005	4.696	1.339	173.7	47.63	17.83	
4 Ala	(2.610)	5.030	1.320	169.3	52.10	18.03	29.85
5 Ala	(2.630)	5.467	1.347	170.5	54.66	17.39	29.81
6 Ala	(2.537)	5.118	1.211	169.8	52.94	13.89	29.83

*N*Me(2,4,5,6)$_{cis4\text{-}5,cis5\text{-}6}$	H^N or (H^{Me})	H^α	H^β	C'	C^α	C^β	C^{Me}
1 D-Ala	8.428	4.747	1.286	174.3	45.71	17.36	
2 Ala	(3.156)	4.970	1.293	170.7	53.27	14.46	31.28
3 Ala	7.146	4.470	1.102	171.5	46.28	17.34	
4 Ala	(2.727)	5.545	1.157	169.9	46.97	15.47	29.43
5 Ala	(2.819)	5.284	1.428	171.6	53.82	18.05	32.12
6 Ala	(2.728)	4.430	1.472	172.7	54.92	19.06	31.94

*N*Me(2,4,5,6)$_{all\text{-}trans}$	H^N or (H^{Me})	H^α	H^β	C'	C^α	C^β	C^{Me}
1 D-Ala	8.896	4.803	1.243	172.6	46.39	18.11	
2 Ala	(2.996)	4.912	1.265	170.9	53.12	15.34	31.99
3 Ala	7.800	4.676	1.214	172.2	45.93	18.20	
4 Ala	(2.868)	5.256	1.133	171.0	50.39	14.90	30.67
5 Ala	(2.808)	4.705	1.300	173.4	54.26	15.10	32.53
6 Ala	(2.514)	4.382	1.385	168.9	56.87	16.68	30.20

Comparison of ^{3}J coupling constants, temperature gradients of H^N chemical shifts, and chemical shifts of *N*Me(1,5), *N*Me(3,5)$_{cis2\text{-}3}$, *N*Me(1,2,5,6)$_{cis4\text{-}5}$, and *N*Me(1,4,5,6)$_{cis3\text{-}4}$

According to the scaffolds given in Figure 4.7, *N*Me(3,5)$_{cis(2,3)}$ and *N*Me(1,4,5,6)$_{cis(5\text{-}6)}$ possess conformations that are similar to the second template structure (bottom of Figure 4.3) but rotated along the scaffold. Table D.17 and Table D.18 provide NMR data that supports this assumption. The residue given in the top row is suggested to occupy position i+1 of the upper β-turn. All resonances were assigned in DMSO-d6 at 300 K and at a proton resonance frequency of 500 MHz. Chemical shifts are referenced to the DMSO ^{1}H resonance at 2.52 ppm and the DMSO $^{13}C^{Me}$ resonance at 40.45 ppm.

Table D.17: $^{3}J_{HN\text{-}H\alpha}$ coupling constants (in Hertz), temperature gradients of H^N chemical shifts (in ppb/K), and chemical shifts (in ppm) that support the structural similarity of ***N*Me(3,5)$_{cis(2\text{-}3)}$** with ***N*Me(1,5)** are highlighted (**bold type**).

***N*Me(1,5)**	**$^{3}J_{HN\text{-}H\alpha}$**	**dδ/dT**	**H^N or (H^{Me})**	**H^α**	**H^β**	**C'**	**C^α**	**C^β**	**C^{Me}**
1 D-Ala			(3.017)	4.834	1.284	173.0	53.13	15.87	31.19
2 Ala	**7.5**	**-5.2**	8.657	**4.063**	**1.268**	**171.9**	**49.55**	18.01	
3 Ala	8.1	**0.0**	7.138	4.394	**1.206**	**173.0**	47.36	**20.60**	
4 Ala	4.3	**-4.6**	**8.751**	**4.692**	**1.211**	**173.4**	**45.32**	**17.74**	
5 Ala			**(2.583)**	**5.133**	**1.245**	**169.9**	**55.90**	**15.75**	**29.12**
6 Ala	7.0	**-2.0**	8.363	4.741	**1.188**	**171.8**	**46.96**	**18.90**	

***N*Me(3,5)$_{cis2\text{-}3}$**	**$^{3}J_{HN\text{-}H\alpha}$**	**dδ/dT**	**H^N or (H^{Me})**	**H^α**	**H^β**	**C'**	**C^α**	**C^β**	**C^{Me}**
5 Ala			(3.127)	3.644	1.339	171.3	62.00	13.84	-
6 Ala	**8.2**	**-3.5**	7.810	**4.285**	**1.247**	**171.6**	**49.00**	16.83	
1 D-Ala	6.5-7.0	**-0.2**	7.343	4.271	**1.225**	**172.6**	49.26	**20.47**	
2 Ala	6.4	**-4.6**	**8.746**	**4.777**	**1.232**	**173.4**	**44.38**	**18.62**	
3 Ala			**(2.594)**	**5.258**	**1.248**	**169.0**	**56.13**	**15.50**	**29.39**
4 Ala	5.0	**-1.9**	7.716	4.605	**1.217**	**171.3**	**47.10**	**17.90**	

Table D.18: $^{3}J_{HN\text{-}H\alpha}$ coupling constants (in Hertz), temperature gradients of H^N chemical shifts (in ppb/K), and chemical shifts (in ppm) that support the structural similarity of ***N*Me(1,4,5,6)$_{cis(3\text{-}4)}$** with ***N*Me(1,2,5,6)$_{cis(4\text{-}5)}$** are highlighted (**bold type**).

***N*Me(1,2,5,6)$_{cis4\text{-}5}$**	**$^{3}J_{HN\text{-}H\alpha}$**	**dδ/dT**	**H^N or (H^{Me})**	**H^α**	**H^β**	**C'**	**C^α**	**C^β**	**C^{Me}**
1 D-Ala			**(2.740)**	5.676	1.194	171.3	47.43	15.52	29.43
2 Ala			**(2.781)**	**5.141**	**1.140**	**170.3**	**52.40**	**13.51**	**30.81**
3 Ala	4.8	**-3.7**	**7.229**	**4.107**	**1.262**	171.5	49.41	17.31	
4 Ala	**8.5**	**-3.6**	8.669	**4.952**	**1.294**	171.9	**44.81**	**18.53**	
5 Ala			**(2.606)**	5.552	**1.313**	168.2	54.85	18.11	29.24
6 Ala			(2.477)	**5.274**	**1.140**	170.1	52.40	**14.79**	29.44

NMe(1,4,5,6)$_{cis3\text{-}4}$	**$^{3}J_{HN\text{-}H\alpha}$**	**dδ/dT**	**H^N or (H^{Me})**	**H^α**	**H^β**	**C'**	**C^α**	**C^β**	**C^{Me}**
6 Ala			**(2.804)**	4.702	1.296	170.4	54.18	14.98	32.40
1 D-Ala			**(2.734)**	**5.065**	**1.137**	**169.9**	**52.24**	**13.39**	**30.27**
2 Ala	7.7	**-3.3**	**7.115**	**4.277**	**1.308**	172.9	47.93	**18.43**	
3 Ala	**7.4**	**-4.7 ± 1.2**	8.181	**4.870**	**1.277**	173.5	**46.30**	**18.25**	
4 Ala			**(2.693)**	5.156	**1.316**	169.8	51.86	18.39	29.97
5 Ala			(2.698)	**5.274**	**1.115**	170.7	50.21	**14.75**	30.51

Distance restraints for *N*-methylated cyclic (-a-A-A-A-A-A-) peptides

Table D.19: Distance restraints for *N*Me(1)

interproton distance		d_{low} [Å]	d_{upp} [Å]
*N*Me-D-Ala^{1} H^{Me}	*N*Me-D-Ala^{1} H$^{\alpha}$	3.23	4.35
*N*Me-D-Ala^{1} H^{Me}	Ala^{2} H	3.41	4.56
*N*Me-D-Ala^{1} H^{Me}	Ala^{5} H	4.30	5.66
*N*Me-D-Ala^{1} H^{Me}	Ala^{6} H$^{\alpha}$	2.30	3.21
*N*Me-D-Ala^{1} H^{Me}	Ala^{6} H	3.57	4.76
Ala^{2} H	*N*Me-D-Ala^{1} H$^{\alpha}$	1.96	2.39
Ala^{2} H	Ala^{2} H$^{\alpha}$	2.49	3.04
Ala^{2} H	Ala^{3} H	2.34	2.87
Ala^{2} H	Ala^{5} H	3.37	4.11
Ala^{2} H	Ala^{6} H	3.42	4.18
Ala^{3} H	*N*Me-D-Ala^{1} H$^{\alpha}$	3.10	3.79
Ala^{3} H	Ala^{2} H$^{\alpha}$	2.42	2.96
Ala^{3} H	Ala^{3} H$^{\alpha}$	2.32	2.83
Ala^{3} H$^{\beta}$	Ala^{3} H	2.66	3.65
Ala^{3} H$^{\beta}$	Ala^{4} H	2.81	3.84
Ala^{3} H$^{\beta}$	Ala^{5} H	4.14	5.46
Ala^{3} H$^{\beta}$	Ala^{6} H	3.87	5.13
Ala^{4} H	Ala^{3} H$^{\alpha}$	2.14	2.61
Ala^{4} H	Ala^{3} H	2.80	3.42
Ala^{4} H$^{\alpha}$	Ala^{4} H	2.18	2.66
Ala^{4} H$^{\beta}$	Ala^{4} H	2.66	3.65
Ala^{4} H	Ala^{5} H	2.62	3.20
Ala^{4} H$^{\alpha}$	Ala^{6} H	3.37	4.12
Ala^{5} H	Ala^{4} H$^{\alpha}$	2.22	2.72
Ala^{5} H	Ala^{5} H$^{\alpha}$	2.13	2.61
Ala^{6} H$^{\beta}$	*N*Me-D-Ala^{1} H$^{\alpha}$	3.69	4.91
Ala^{6} H$^{\beta}$	Ala^{3} H	4.21	5.55
Ala^{6} H	Ala^{5} H$^{\alpha}$	2.25	2.75
Ala^{6} H	Ala^{6} H$^{\alpha}$	2.37	2.89
Ala^{6} H	Ala^{6} H$^{\beta}$	2.87	3.90

Table D.20: Distance restraints for *N*Me(5)

interproton distance		d_{low} [Å]	d_{upp} [Å]	d_{DG} [Å]	d_{viol} [Å]
D-Ala^1 H	D-Ala^1 H$^\alpha$	2.47	3.02	3.03	0.01
D-Ala^1 H	Ala^3 H	3.63	4.44	4.38	
D-Ala^1 H	Ala^6 H$^\alpha$	1.91	2.34	2.37	0.03
D-Ala^1 H	Ala^6 H	2.87	3.51	3.07	
D-Ala^1 H$^\beta$	D-Ala^1 H	2.5	3.46	2.82	
D-Ala^1 H$^\beta$	Ala^2 H	3.49	4.66	3.24	-0.25
Ala^2 H	D-Ala^1 H$^\alpha$	1.8	2.2	2.30	0.1
Ala^2 H	Ala^2 H$^\alpha$	2.43	2.97	2.95	
Ala^2 H	Ala^3 H	2.3	2.81	2.70	
Ala^2 H$^\beta$	Ala^2 H	2.57	3.54	2.63	
Ala^2 H$^\beta$	Ala^3 H	3.78	5.01	3.89	
Ala^3 H	D-Ala^1 H$^\alpha$	2.97	3.63	3.38	
Ala^3 H	Ala^2 H$^\alpha$	2.68	3.27	3.20	
Ala^3 H	Ala^3 H$^\alpha$	2.44	2.98	2.91	
Ala^3 H$^\beta$	Ala^3 H	2.83	3.86	3.14	
Ala^3 H$^\beta$	Ala^4 H	2.58	3.55	3.15	
Ala^4 H	Ala^3 H$^\alpha$	2.04	2.5	2.49	
Ala^4 H	Ala^3 H	3.63	4.44	4.46	+0.02
Ala^4 H	Ala^4 H$^\alpha$	2.48	3.04	2.73	
Ala^4 H$^\beta$	Ala^4 H	2.67	3.66	2.55	-0.12
*N*Me-Ala^5 H$^\alpha$	Ala^4 H$^\alpha$	1.56	1.9	1.83	
*N*Me-Ala^5 H^{Me}	Ala^4 H$^\alpha$	4.02	5.31	4.18	
*N*Me-Ala^5 H^{Me}	*N*Me-Ala^5 H$^\alpha$	3.39	4.54	3.48	
*N*Me-Ala^5 H^{Me}	Ala^6 H$^\alpha$	4.36	5.73	5.48	
*N*Me-Ala^5 H^{Me}	Ala^6 H	3.24	4.36	4.01	
Ala^6 H	Ala^3 H	3	3.67	3.52	
Ala^6 H	Ala^4 H$^\alpha$	3	3.66	3.66	
Ala^6 H	*N*Me-Ala^5 H$^\alpha$	2.12	2.59	2.40	
Ala^6 H	Ala^6 H$^\beta$	3.05	4.13	3.37	
Ala^6 H	Ala^6 H$^\alpha$	2.43	2.97	2.71	

Table D.21: Distance restraints for *N*Me(1,2)

interproton distance		d_{low} [Å]	d_{upp} [Å]	d_{DG} [Å]	d_{viol} [Å]
*N*Me-D-Ala^{1} H$^{\alpha}$	*N*Me-D-Ala^{1} H^{Me}	3.04	4.11	3.32	
*N*Me-D-Ala^{1} H$^{\beta}$	*N*Me-D-Ala^{1} H^{Me}	2.92	4.37	3.64	
*N*Me-D-Ala^{1} H$^{\alpha}$	*N*Me-Ala^{2} H^{Me}	2.29	3.19	2.63	
*N*Me-D-Ala^{1} H$^{\beta}$	*N*Me-Ala^{2} H$^{\alpha}$	4.3	5.66	4.86	
*N*Me-D-Ala^{1} H$^{\beta}$	Ala^{6} H$^{\alpha}$	4.2	5.54	5.07	
*N*Me-D-Ala^{1} H^{Me}	Ala^{6} H	3.82	5.07	4.40	
*N*Me-D-Ala^{1} H^{Me}	Ala^{6} H$^{\beta}$	3.53	5.12	3.90	
*N*Me-Ala^{2} H^{Me}	*N*Me-D-Ala^{1} H$^{\beta}$	3.67	5.29	3.25	-0.42
*N*Me-Ala^{2} H$^{\alpha}$	*N*Me-Ala^{2} H^{Me}	3.46	4.62	3.40	-0.06
*N*Me-Ala^{2} H^{Me}	*N*Me-Ala^{2} H$^{\beta}$	3.01	4.47	2.94	-0.07
*N*Me-Ala^{2} H$^{\beta}$	Ala^{3} H	3.39	4.55	4.12	
*N*Me-Ala^{2} H$^{\beta}$	Ala^{3} H$^{\alpha}$	4.21	5.54	5.40	
*N*Me-Ala^{2} H^{Me}	Ala^{3} H$^{\alpha}$	4.82	6.29	5.84	
*N*Me-Ala^{2} H^{Me}	Ala^{3} H$^{\beta}$	4.11	5.81	5.11	
*N*Me-Ala^{2} H^{Me}	Ala^{6} H$^{\alpha}$	4.25	5.6	6.84	1.24
Ala^{3} H	*N*Me-D-Ala^{1} H$^{\alpha}$	3.16	3.86	3.03	-0.13
Ala^{3} H	*N*Me-Ala^{2} H$^{\alpha}$	2.45	2.99	3.04	0.05
Ala^{3} H	*N*Me-Ala^{2} H^{Me}	3.04	4.12	3.65	
Ala^{3} H$^{\beta}$	*N*Me-Ala^{2} H$^{\alpha}$	5.08	6.62	4.98	-0.1
Ala^{3} H	Ala^{3} H$^{\alpha}$	2.9	3.13	2.69	-0.21
Ala^{3} H	Ala^{3} H$^{\beta}$	2.91	3.96	3.36	
Ala^{4} H	Ala^{3} H$^{\alpha}$	2.25	2.75	2.55	
Ala^{4} H	Ala^{3} H$^{\beta}$	2.85	3.88	3.15	
Ala^{4} H	Ala^{4} H$^{\alpha}$	2.42	2.8	2.31	
Ala^{4} H	Ala^{4} H$^{\beta}$	2.78	3.8	3.15	
Ala^{4} H	Ala^{5} H	2.88	3.51	3.46	
Ala^{5} H	Ala^{4} H$^{\alpha}$	2.36	2.89	2.51	
Ala^{5} H	Ala^{5} H$^{\alpha}$	2.31	2.81	2.36	
Ala^{5} H$^{\beta}$	Ala^{5} H	3.11	4.2	3.40	
Ala^{5} H	Ala^{6} H	2.45	2.99	4.00	1.01
Ala^{6} H$^{\alpha}$	*N*Me-D-Ala^{1} H^{Me}	2.28	3.19	2.42	
Ala^{6} H	Ala^{5} H$^{\alpha}$	2.83	3.46	3.67	0.21
Ala^{6} H	Ala^{5} H$^{\beta}$	3.23	4.36	2.58	-0.65
Ala^{6} H$^{\beta}$	Ala^{5} H$^{\alpha}$	4.37	5.75	5.27	
Ala^{6} H	Ala^{6} H$^{\alpha}$	2.56	3.13	2.87	
Ala^{6} H	Ala^{6} H$^{\beta}$	3.08	4.17	3.05	-0.03

Table D.22: Distance restraints for *N*Me(1,5)

interproton distance		d_{low} [Å]	d_{upp} [Å]	d_{DG} [Å]	d_{viol} [Å]
*N*Me-D-Ala^{1} H$^{\alpha}$	*N*Me-D-Ala^{1} H^{Me}	3.26	4.42	3.29	
*N*Me-D-Ala^{1} H$^{\alpha}$	Ala^{3} H	2.98	3.65	2.78	-0.2
*N*Me-D-Ala^{1} H^{Me}	*N*Me-D-Ala^{1} H$^{\beta}$	2.75	4.25	3.70	
*N*Me-D-Ala^{1} H^{Me}	Ala^{2} H	5.17	6.75	4.77	-0.4
*N*Me-D-Ala^{1} H^{Me}	Ala^{3} H	4.72	6.21	3.73	-0.99
*N*Me-D-Ala^{1} H^{Me}	*N*Me-Ala^{5} H$^{\alpha}$	4.12	5.47	4.49	
*N*Me-D-Ala^{1} H^{Me}	Ala^{6} H	3.46	4.68	3.10	-0.36
*N*Me-D-Ala^{1} H^{Me}	Ala^{6} H$^{\beta}$	3.80	5.52	4.33	
Ala^{2} H	*N*Me-D-Ala^{1} H$^{\alpha}$	1.82	2.23	2.42	0.19
Ala^{2} H	Ala^{2} H$^{\alpha}$	2.52	3.08	2.95	
Ala^{2} H	Ala^{3} H	2.28	2.79	2.51	
Ala^{2} H$^{\beta}$	Ala^{3} H	3.47	4.68	3.99	
Ala^{2} H$^{\beta}$	Ala^{3} H$^{\alpha}$	4.05	5.39	5.11	
Ala^{3} H	Ala^{2} H$^{\alpha}$	2.69	3.29	3.06	
Ala^{3} H	Ala^{3} H$^{\alpha}$	2.46	3.01	2.88	
Ala^{3} H	Ala^{3} H$^{\beta}$	2.91	3.99	3.15	
Ala^{3} H	*N*Me-Ala^{5} H$^{\alpha}$	4.24	5.18	5.19	0.01
Ala^{4} H	Ala^{3} H	3.92	4.79	4.28	
Ala^{4} H	Ala^{3} H$^{\alpha}$	2.00	2.45	2.37	
Ala^{4} H	Ala^{4} H$^{\alpha}$	2.45	3.00	2.69	
*N*Me-Ala^{5} H$^{\alpha}$	Ala^{4} H$^{\alpha}$	1.58	1.93	1.84	
*N*Me-Ala^{5} H$^{\beta}$	Ala^{6} H	4.03	5.37	4.12	
*N*Me-Ala^{5} H^{Me}	Ala^{4} H$^{\alpha}$	4.43	5.86	4.20	-0.23
*N*Me-Ala^{5} H^{Me}	*N*Me-Ala^{5} H$^{\alpha}$	3.39	4.59	3.49	
*N*Me-Ala^{5} H^{Me}	*N*Me-Ala^{5} H$^{\beta}$	2.95	4.49	3.20	
*N*Me-Ala^{5} H^{Me}	Ala^{6} H	3.12	4.25	3.14	
*N*Me-Ala^{5} H^{Me}	Ala^{6} H$^{\alpha}$	4.37	5.78	5.31	
*N*Me-Ala^{5} H^{Me}	Ala^{6} H$^{\beta}$	3.32	4.94	4.58	
Ala^{6} H	Ala^{3} H	3.05	3.72	3.95	0.23
Ala^{6} H	Ala^{4} H$^{\alpha}$	2.85	3.48	3.57	0.09
Ala^{6} H	*N*Me-Ala^{5} H$^{\alpha}$	2.11	2.58	2.87	0.29
Ala^{6} H	Ala^{6} H$^{\alpha}$	2.47	3.02	2.87	
Ala^{6} H	Ala^{6} H$^{\beta}$	3.02	4.13	3.18	
Ala^{6} H$^{\alpha}$	*N*Me-D-Ala^{1} H^{Me}	2.31	3.26	2.55	
Ala^{6} H$^{\alpha}$	Ala^{3} H	4.14	5.06	5.70	0.64

Table D.23: Distance restraints for *N*Me(1,6)

interproton distance		d_{low} [Å]	d_{upp} [Å]	d_{DG} [Å]	d_{viol} [Å]
*N*Me-D-Ala^{1} H$^{\alpha}$	*N*Me-D-Ala^{1} H^{Me}	3.33	4.47	3.50	
*N*Me-D-Ala^{1} H^{Me}	*N*Me-D-Ala^{1} H$^{\beta}$	2.92	4.37	3.46	
*N*Me-D-Ala^{1} H^{Me}	Ala^{2} H$^{\alpha}$	4.51	5.91	4.85	
*N*Me-D-Ala^{1} H^{Me}	Ala^{3} H	5.35	6.94	6.06	
*N*Me-D-Ala^{1} H^{Me}	Ala^{4} H	5.42	7.02	6.24	
*N*Me-D-Ala^{1} H$^{\beta}$	*N*Me-Ala^{6} H$^{\alpha}$	4.64	6.07	5.16	
Ala^{2} H	*N*Me-D-Ala^{1} H$^{\alpha}$	2.29	2.81	2.28	-0.01
Ala^{2} H	*N*Me-D-Ala^{1} H$^{\beta}$	4.15	5.47	4.08	-0.07
Ala^{2} H	*N*Me-D-Ala^{1} H^{Me}	2.95	4.01	3.81	
Ala^{2} H	Ala^{2} H$^{\alpha}$	2.56	3.14	3.06	
Ala^{2} H	*N*Me-Ala^{6} H$^{\alpha}$	3.62	4.42	4.45	+0.03
Ala^{3} H	Ala^{2} H$^{\alpha}$	2.12	2.59	2.42	
Ala^{3} H	Ala^{2} H$^{\beta}$	2.68	3.68	3.23	
Ala^{3} H	Ala^{3} H$^{\alpha}$	2.26	2.76	2.70	
Ala^{3} H	Ala^{3} H$^{\beta}$	2.70	3.70	2.60	-0.1
Ala^{4} H	Ala^{3} H$^{\alpha}$	2.08	2.54	2.27	
Ala^{4} H	Ala^{3} H$^{\beta}$	2.95	4.01	3.67	
Ala^{4} H	Ala^{4} H$^{\alpha}$	2.09	2.55	2.34	
Ala^{4} H	Ala^{5} H	2.34	2.86	2.77	
Ala^{5} H	*N*Me-D-Ala^{1} H^{Me}	3.47	4.64	4.73	+0.09
Ala^{5} H$^{\beta}$	Ala^{2} H	4.27	5.62	4.16	-0.11
Ala^{5} H	Ala^{3} H$^{\alpha}$	3.73	4.55	4.01	
Ala^{5} H	Ala^{4} H$^{\alpha}$	2.67	3.27	2.93	
Ala^{5} H	Ala^{5} H$^{\alpha}$	2.52	3.08	2.64	
Ala^{5} H	Ala^{5} H$^{\beta}$	2.98	4.05	3.34	
Ala^{5} H$^{\alpha}$	*N*Me-Ala^{6} H^{Me}	2.21	3.10	2.45	
Ala^{5} H$^{\beta}$	*N*Me-Ala^{6} H$^{\alpha}$	4.91	6.40	5.26	
*N*Me-Ala^{6} H$^{\alpha}$	*N*Me-D-Ala^{1} H^{Me}	2.26	3.16	2.48	
*N*Me-Ala^{6} H$^{\beta}$	*N*Me-D-Ala^{1} H$^{\alpha}$	4.73	6.19	4.83	
*N*Me-Ala^{6} H$^{\beta}$	Ala^{2} H	4.39	5.76	5.51	
*N*Me-Ala^{6} H^{Me}	Ala^{2} H	4.87	6.36	5.45	
*N*Me-Ala^{6} H$^{\beta}$	Ala^{5} H$^{\alpha}$	4.63	6.05	4.99	
*N*Me-Ala^{6} H$^{\beta}$	Ala^{5} H	4.58	6.00	5.71	
*N*Me-Ala^{6} H^{Me}	Ala^{5} H$^{\beta}$	3.67	5.29	3.80	
*N*Me-Ala^{6} H^{Me}	Ala^{5} H	3.58	4.77	4.22	
*N*Me-Ala^{6} H$^{\alpha}$	*N*Me-Ala^{6} H^{Me}	2.39	3.32	3.05	
*N*Me-Ala^{6} H^{Me}	*N*Me-Ala^{6} H$^{\beta}$	3.05	4.53	2.84	-0.21

Table D.24: Distance restraints for *N*Me(2,5)

interproton distance		d_{low} [Å]	d_{upp} [Å]	d_{DG} [Å]	d_{viol} [Å]
D-Ala^1 H	D-Ala^1 H$^{\alpha}$	2.46	3.00	2.96	
D-Ala^1 H$^{\beta}$	D-Ala^1 H	2.57	3.54	2.70	
D-Ala^1 H$^{\alpha}$	*N*Me-Ala^2 H^{Me}	2.14	3.02	2.60	
D-Ala^1 H	Ala^3 H	4.55	5.57	4.55	
D-Ala^1 H	Ala^6 H	3.05	3.73	3.68	
D-Ala^1 H	Ala^6 H$^{\alpha}$	1.96	2.40	2.30	
*N*Me-Ala^2 H^{Me}	D-Ala^1 H	4.48	5.88	4.89	
*N*Me-Ala^2 H^{Me}	*N*Me-Ala^2 H$^{\alpha}$	3.45	4.61	3.43	-0.02
*N*Me-Ala^2 H^{Me}	Ala^3 H$^{\beta}$	3.83	5.48	5.33	
*N*Me-Ala^2 H^{Me}	Ala^6 H	4.93	6.43	5.68	
Ala^3 H	D-Ala^1 H$^{\alpha}$	3.21	3.93	3.51	
Ala^3 H	*N*Me-Ala^2 H$^{\alpha}$	2.39	2.93	2.93	
Ala^3 H	*N*Me-Ala^2 H^{Me}	2.86	3.90	3.59	
Ala^3 H	Ala^3 H$^{\alpha}$	2.45	2.99	2.92	
Ala^3 H$^{\beta}$	Ala^3 H	2.91	3.95	3.08	
Ala^3 H$^{\beta}$	Ala^4 H	2.84	3.87	3.58	
Ala^3 H$^{\beta}$	Ala^6 H	4.03	5.33	5.00	
Ala^4 H	Ala^3 H	4.27	5.21	4.27	
Ala^4 H	Ala^3 H$^{\alpha}$	2.06	2.52	2.28	
Ala^4 H	Ala^4 H$^{\alpha}$	2.55	3.11	2.61	
Ala^4 H$^{\beta}$	Ala^4 H	2.66	3.65	2.70	
Ala^4 H	Ala^6 H	3.88	4.74	4.74	
*N*Me-Ala^5 H$^{\alpha}$	Ala^4 H$^{\alpha}$	1.58	1.94	1.89	
*N*Me-Ala^5 H^{Me}	Ala^4 H$^{\alpha}$	4.13	5.45	4.05	-0.08
*N*Me-Ala^5 H^{Me}	*N*Me-Ala^5 H$^{\alpha}$	3.55	4.73	3.42	-0.13
*N*Me-Ala^5 H^{Me}	Ala^6 H	3.24	4.36	4.02	
Ala^6 H	D-Ala^1 H$^{\alpha}$	4.19	5.13	4.19	
Ala^6 H	Ala^4 H$^{\alpha}$	3.56	4.36	4.20	
Ala^6 H	*N*Me-Ala^5 H$^{\alpha}$	2.11	2.57	2.41	
Ala^6 H	Ala^6 H$^{\alpha}$	2.42	2.96	2.70	

Table D.25: Distance restraints for *N*Me(4,5)

interproton distance		d_{low} [Å]	d_{upp} [Å]	d_{DG} [Å]	d_{viol} [Å]
D-Ala^{1} H	D-Ala^{1} H$^{\alpha}$	2.44	2.99	3.01	0.01
D-Ala^{1} H$^{\beta}$	D-Ala^{1} H	2.52	3.48	2.78	
D-Ala^{1} H	Ala^{3} H	3.91	4.78	4.52	
D-Ala^{1} H	Ala^{6} H	2.93	3.58	3.38	
D-Ala^{1} H	Ala^{6} H$^{\alpha}$	1.88	2.3	2.33	0.03
Ala^{2} H$^{\beta}$	Ala^{2} H	2.58	3.55	2.59	
Ala^{2} H	Ala^{3} H	2.24	2.74	2.86	0.12
Ala^{2} H$^{\beta}$	Ala^{3} H	3.55	4.74	3.90	
Ala^{2} H$^{\beta}$	Ala^{3} H$^{\alpha}$	3.92	5.19	4.90	
Ala^{2} H	Ala^{6} H	4.32	5.28	5.44	0.16
Ala^{3} H	Ala^{3} H$^{\alpha}$	2.47	3.02	2.99	
Ala^{3} H$^{\alpha}$	*N*Me-Ala^{4} H^{Me}	2.12	2.99	2.57	
*N*Me-Ala^{4} H^{Me}	Ala^{3} H	5.11	6.64	4.87	-0.24
*N*Me-Ala^{4} H$^{\beta}$	*N*Me-Ala^{4} H^{Me}	2.68	4.08	2.81	
*N*Me-Ala^{4} H^{Me}	*N*Me-Ala^{4} H$^{\alpha}$	3.35	4.49	3.29	-0.06
*N*Me-Ala^{4} H$^{\alpha}$	*N*Me-Ala^{5} H$^{\alpha}$	1.54	1.88	1.86	
*N*Me-Ala^{4} H$^{\beta}$	*N*Me-Ala^{5} H$^{\alpha}$	3.43	4.59	3.88	
*N*Me-Ala^{5} H$^{\beta}$	*N*Me-Ala^{4} H$^{\alpha}$	3.28	4.41	3.14	-0.14
*N*Me-Ala^{5} H^{Me}	*N*Me-Ala^{4} H$^{\alpha}$	3.81	5.06	4.16	
*N*Me-Ala^{5} H^{Me}	*N*Me-Ala^{4} H$^{\beta}$	5.58	7.63	4.85	-0.73
*N*Me-Ala^{5} H^{Me}	*N*Me-Ala^{5} H$^{\alpha}$	3.32	4.45	3.45	
*N*Me-Ala^{5} H^{Me}	*N*Me-Ala^{5} H$^{\beta}$	3.02	4.49	3.39	
*N*Me-Ala^{5} H^{Me}	Ala^{6} H	3.07	4.15	3.93	
*N*Me-Ala^{5} H^{Me}	Ala^{6} H$^{\alpha}$	5.00	6.52	5.59	
*N*Me-Ala^{5} H^{Me}	Ala^{6} H$^{\beta}$	3.58	5.18	4.67	
Ala^{6} H	Ala^{3} H	2.81	3.43	3.46	0.03
Ala^{6} H$^{\alpha}$	Ala^{3} H	4.48	5.48	5.54	0.06
Ala^{6} H	*N*Me-Ala^{4} H$^{\alpha}$	2.82	3.45	3.87	0.42
Ala^{6} H	*N*Me-Ala^{5} H$^{\alpha}$	2.06	2.52	2.41	
Ala^{6} H$^{\beta}$	*N*Me-Ala^{5} H$^{\alpha}$	4.42	5.8	4.88	
Ala^{6} H	Ala^{6} H$^{\alpha}$	2.43	2.96	2.76	
Ala^{6} H$^{\beta}$	Ala^{6} H	3.05	4.13	3.31	

Table D.26: Distance restraints for *N*Me(5,6)$_{cis5\text{-}6}$

interproton distance		d_{low} [Å]	d_{upp} [Å]	d_{DG} [Å]	d_{viol} [Å]
D-Ala^1 H$^\alpha$	D-Ala^1 H	2.66	3.26	2.96	
D-Ala^1 H$^\beta$	D-Ala^1 H	3.09	4.18	2.93	-0.16
D-Ala^1 H$^\alpha$	Ala^2 H	2.07	2.53	2.51	
D-Ala^1 H$^\alpha$	Ala^4 H	3.75	4.59	3.75	
Ala^2 H$^\alpha$	D-Ala^1 H	3.89	4.76	4.73	
Ala^2 H$^\alpha$	Ala^2 H	2.51	3.07	2.99	
Ala^2 H$^\alpha$	Ala^4 H	4.01	5.36	4.36	
Ala^3 H	Ala^2 H$^\beta$	2.46	3.4	3.19	
Ala^3 H$^\alpha$	Ala^2 H	3.9	4.72	4.73	+0.01
Ala^3 H	Ala^4 H	2.75	3.36	2.75	
Ala^3 H$^\beta$	Ala^4 H	3.04	4.57	3.03	-0.01
Ala^4 H	D-Ala^1 H	3.88	4.75	4.75	
Ala^4 H	Ala^2 H	3.23	4.4	3.37	
Ala^4 H$^\alpha$	Ala^4 H	2.92	3.41	2.92	
Ala^4 H$^\beta$	Ala^4 H	3.02	4.55	3.10	
Ala^4 H$^\beta$	*N*Me-Ala^5 H$^\alpha$	4.25	5.59	4.93	
Ala^4 H$^\beta$	*N*Me-Ala^5 H^{Me}	3.14	4.65	3.08	-0.06
*N*Me-Ala^5 H$^\alpha$	D-Ala^1 H	2.58	3.16	2.59	
*N*Me-Ala^5 H^{Me}	Ala^4 H	4.07	5.37	4.77	
*N*Me-Ala^5 H^{Me}	Ala^4 H$^\alpha$	2.34	3.26	2.66	
*N*Me-Ala^5 H$^\beta$	*N*Me-Ala^5 H^{Me}	2.92	4.37	2.87	-0.05
*N*Me-Ala^5 H^{Me}	*N*Me-Ala^5 H$^\alpha$	3.52	4.7	3.33	-0.19
*N*Me-Ala^5 H$^\beta$	*N*Me-Ala^6 H^{Me}	3.71	5.34	4.70	
*N*Me-Ala^6 H$^\alpha$	D-Ala^1 H	2.04	2.5	2.37	
*N*Me-Ala^6 H$^\beta$	D-Ala^1 H	3.29	4.42	3.67	
*N*Me-Ala^6 H$^\beta$	D-Ala^1 H$^\alpha$	3.98	5.25	4.82	
*N*Me-Ala^6 H^{Me}	D-Ala^1 H	4.47	5.86	5.21	
*N*Me-Ala^6 H^{Me}	D-Ala^1 H$^\alpha$	4.52	5.93	5.65	
*N*Me-Ala^6 H$^\beta$	*N*Me-Ala^5 H$^\alpha$	3.79	5.03	3.93	
*N*Me-Ala^6 H^{Me}	*N*Me-Ala^5 H$^\alpha$	3.85	5.1	4.12	
*N*Me-Ala^6 H$^\beta$	*N*Me-Ala^6 H^{Me}	2.72	4.12	2.90	
NMe-Ala^6 H^{Me}	NMe-Ala^6 H$^\alpha$	3.54	4.72	3.41	-0.13

Table D.27: Distance restraints for *N*Me(1,2,5)

interproton distance		d_{low} [Å]	d_{upp} [Å]	d_{DG} [Å]	d_{viol} [Å]
*N*Me-D-Ala^{1} H$^{\beta}$	*N*Me-D-Ala^{1} H^{Me}	2.88	3.92	3.40	
*N*Me-D-Ala^{1} H^{Me}	*N*Me-D-Ala^{1} H$^{\alpha}$	3.47	4.64	3.45	
*N*Me-D-Ala^{1} H$^{\beta}$	*N*Me-Ala^{2} H^{Me}	3.49	4.67	3.53	
*N*Me-D-Ala^{1} H$^{\alpha}$	Ala^{3} H	3.20	3.91	3.22	
*N*Me-D-Ala^{1} H$^{\beta}$	Ala^{3} H	4.52	5.52	5.12	
*N*Me-D-Ala^{1} H^{Me}	Ala^{3} H	5.12	6.66	4.85	-0.27
*N*Me-D-Ala^{1} H^{Me}	Ala^{6} H	4.36	5.72	4.08	-0.28
*N*Me-D-Ala^{1} H^{Me}	Ala^{6} H$^{\alpha}$	2.41	3.35	2.38	-0.03
*N*Me-D-Ala^{1} H^{Me}	Ala^{6} H$^{\beta}$	3.62	4.83	4.11	
*N*Me-Ala^{2} H^{Me}	*N*Me-D-Ala^{1} H$^{\alpha}$	2.29	3.20	2.55	
*N*Me-Ala^{2} H^{Me}	*N*Me-D-Ala^{1} H$^{\beta}$	3.56	4.75	3.53	-0.03
*N*Me-Ala^{2} H^{Me}	*N*Me-Ala^{2} H$^{\alpha}$	3.53	4.72	3.50	-0.03
*N*Me-Ala^{2} H^{Me}	*N*Me-Ala^{2} H$^{\beta}$	3.08	4.17	3.27	
*N*Me-Ala^{2} H$^{\alpha}$	Ala^{3} H	2.43	2.97	2.99	0.02
*N*Me-Ala^{2} H$^{\beta}$	Ala^{3} H	4.29	5.25	4.12	-0.17
*N*Me-Ala^{2} H^{Me}	Ala^{3} H	3.05	4.13	3.02	-0.03
*N*Me-Ala^{2} H^{Me}	Ala^{3} H$^{\alpha}$	4.26	5.61	5.29	
*N*Me-Ala^{2} H^{Me}	Ala^{3} H$^{\beta}$	3.86	5.12	4.97	
*N*Me-Ala^{2} H^{Me}	Ala^{6} H	5.38	6.98	5.51	
Ala^{3} H$^{\beta}$	Ala^{3} H	3.00	3.67	2.77	-0.23
Ala^{3} H	Ala^{4} H	4.01	4.90	4.43	
Ala^{3} H$^{\alpha}$	Ala^{4} H	2.21	2.70	2.72	0.02
Ala^{3} H	Ala^{6} H	2.97	3.63	3.65	0.02
Ala^{4} H	Ala^{3} H$^{\beta}$	2.86	3.50	2.80	-0.06
Ala^{4} H	Ala^{4} H$^{\beta}$	2.63	3.22	2.60	-0.03
Ala^{4} H	Ala^{4} H$^{\alpha}$	2.38	2.92	2.91	
Ala^{4} H$^{\alpha}$	*N*Me-Ala^{5} H$^{\alpha}$	1.62	1.98	1.88	
*N*Me-Ala^{5} H^{Me}	Ala^{4} H$^{\alpha}$	4.37	5.74	4.07	-0.30
*N*Me-Ala^{5} H^{Me}	*N*Me-Ala^{5} H$^{\alpha}$	3.63	4.84	3.35	-0.28
*N*Me-Ala^{5} H^{Me}	*N*Me-Ala^{5} H$^{\beta}$	3.27	4.40	3.56	
*N*Me-Ala^{5} H$^{\alpha}$	Ala^{6} H	2.25	2.75	2.66	
*N*Me-Ala^{5} H^{Me}	Ala^{6} H	3.30	4.43	3.14	
*N*Me-Ala^{5} H^{Me}	Ala^{6} H$^{\alpha}$	4.62	6.04	5.30	
*N*Me-Ala^{5} H^{Me}	Ala^{6} H$^{\beta}$	3.75	4.98	4.86	
Ala^{6} H$^{\beta}$	*N*Me-D-Ala^{1} H^{Me}	3.38	4.53	4.11	
Ala^{6} H	Ala^{3} H$^{\beta}$	4.12	5.04	4.97	
Ala^{6} H	Ala^{6} H$^{\beta}$	3.19	3.90	3.20	
Ala^{6} H	Ala^{6} H$^{\alpha}$	2.38	2.92	2.88	

Table D.28: Distance restraints for *N*Me(2,4,5)

interproton distance		d_{low} [Å]	d_{upp} [Å]	d_{DG} [Å]	d_{viol} [Å]
D-Ala^{1} H	D-Ala^{1} H$^{\alpha}$	2.44	2.98	2.98	
D-Ala^{1} H$^{\alpha}$	*N*Me-Ala^{2} H^{Me}	2.12	3.00	2.66	
D-Ala^{1} H	Ala^{3} H	3.79	4.63	3.91	
D-Ala^{1} H	Ala^{6} H	3.14	3.84	3.66	
D-Ala^{1} H	Ala^{6} H$^{\alpha}$	1.89	2.31	2.31	
*N*Me-Ala^{2} H$^{\alpha}$	D-Ala^{1} H	3.97	4.85	5.12	0.27
*N*Me-Ala^{2} H^{Me}	D-Ala^{1} H	4.89	6.37	4.88	-0.01
*N*Me-Ala^{2} H$^{\alpha}$	*N*Me-Ala^{2} H^{Me}	3.32	4.46	3.32	
*N*Me-Ala^{2} H^{Me}	Ala^{6} H	4.87	6.36	6.03	
Ala^{3} H	D-Ala^{1} H$^{\alpha}$	3.20	3.92	3.69	
Ala^{3} H	*N*Me-Ala^{2} H$^{\alpha}$	2.29	2.8	2.91	0.11
Ala^{3} H	*N*Me-Ala^{2} H^{Me}	2.85	3.88	4.10	0.22
Ala^{3} H	Ala^{3} H$^{\beta}$	2.67	3.67	2.91	
Ala^{3} H	*N*Me-Ala^{4} H$^{\alpha}$	3.97	4.85	4.73	
Ala^{3} H$^{\beta}$	*N*Me-Ala^{4} H$^{\alpha}$	3.25	4.37	4.68	0.29
Ala^{3} H	Ala^{6} H$^{\alpha}$	4.39	5.36	4.77	
*N*Me-Ala^{4} H^{Me}	Ala^{3} H	4.65	6.08	4.84	
*N*Me-Ala^{4} H^{Me}	Ala^{3} H$^{\alpha}$	2.17	3.05	2.70	
*N*Me-Ala^{4} H^{Me}	Ala^{3} H$^{\beta}$	2.94	4.39	3.01	
*N*Me-Ala^{4} H$^{\alpha}$	*N*Me-Ala^{4} H^{Me}	3.36	4.51	3.45	
*N*Me-Ala^{4} H^{Me}	*N*Me-Ala^{4} H$^{\beta}$	2.73	4.14	3.06	
*N*Me-Ala^{4} H$^{\alpha}$	*N*Me-Ala^{5} H$^{\alpha}$	1.63	1.99	1.89	
*N*Me-Ala^{4} H^{Me}	*N*Me-Ala^{5} H$^{\alpha}$	4.61	6.04	4.14	-0.47
*N*Me-Ala^{4} H^{Me}	Ala^{6} H	4.84	6.31	4.84	
*N*Me-Ala^{5} H^{Me}	*N*Me-Ala^{4} H$^{\alpha}$	4.00	5.29	4.15	
*N*Me-Ala^{5} H^{Me}	*N*Me-Ala^{4} H$^{\beta}$	4.41	6.19	4.93	
*N*Me-Ala^{5} H$^{\alpha}$	*N*Me-Ala^{5} H^{Me}	3.38	4.54	3.42	
*N*Me-Ala^{5} H^{Me}	Ala^{6} H$^{\alpha}$	4.23	5.57	5.60	0.03
*N*Me-Ala^{5} H^{Me}	*N*Me-Ala^{6} H$^{\beta}$	3.50	5.08	4.96	
Ala^{6} H	D-Ala^{1} H$^{\alpha}$	4.20	5.13	4.11	-0.09
Ala^{6} H	Ala^{3} H	2.79	3.41	3.15	
Ala^{6} H	Ala^{3} H$^{\alpha}$	4.32	5.28	4.64	
Ala^{6} H	*N*Me-Ala^{4} H$^{\alpha}$	3.05	3.72	4.13	
Ala^{6} H	*N*Me-Ala^{5} H$^{\alpha}$	2.1	2.57	2.42	
Ala^{6} H	*N*Me-Ala^{5} H^{Me}	3.05	4.13	4.13	
Ala^{6} H	Ala^{6} H$^{\alpha}$	2.4	2.93	2.84	
Ala^{6} H$^{\beta}$	Ala^{6} H	2.82	3.85	3.22	

Table D.29: Distance restraints for *N*Me(1,2,4,5)

interproton distance		d_{low} [Å]	d_{upp} [Å]	d_{DG} [Å]	d_{viol} [Å]
*N*Me-D-Ala^{1} H^{Me}	*N*Me-D-Ala^{1} H$^{\alpha}$	3.38	4.54	3.37	-0.01
*N*Me-D-Ala^{1} H^{Me}	*N*Me-D-Ala^{1} H$^{\beta}$	2.69	4.09	3.52	
*N*Me-D-Ala^{1} H$^{\alpha}$	*N*Me-Ala^{2} H^{Me}	2.14	3.02	2.58	
*N*Me-D-Ala^{1} H^{Me}	Ala^{3} H	3.94	5.21	3.79	-0.15
*N*Me-D-Ala^{1} H^{Me}	Ala^{6} H	3.94	5.22	3.65	-0.29
*N*Me-Ala^{2} H^{Me}	*N*Me-D-Ala^{1} H$^{\beta}$	3.35	4.90	3.48	
*N*Me-Ala^{2} H^{Me}	*N*Me-Ala^{2} H$^{\alpha}$	3.30	4.44	3.47	
Ala^{3} H	*N*Me-D-Ala^{1} H$^{\alpha}$	3.06	3.74	3.14	
Ala^{3} H	*N*Me-Ala^{2} H$^{\alpha}$	2.26	2.76	2.78	0.02
Ala^{3} H	*N*Me-Ala^{2} H^{Me}	2.83	3.86	3.49	
Ala^{3} H	Ala^{3} H$^{\beta}$	2.76	3.77	3.06	
NMe-Ala^{4} H^{Me}	*N*Me-Ala^{4} H$^{\alpha}$	3.24	4.36	3.35	
NMe-Ala^{4} H^{Me}	*N*Me-Ala^{4} H$^{\beta}$	2.73	4.13	2.87	
*N*Me-Ala^{5} H^{Me}	*N*Me-Ala^{5} H$^{\beta}$	2.90	4.35	3.53	
NMe-Ala^{5} H$^{\alpha}$	*N*Me-Ala^{5} H^{Me}	3.22	4.34	3.39	
Ala^{6} H	*N*Me-D-Ala^{1} H$^{\alpha}$	3.78	4.62	3.81	
Ala^{6} H	Ala^{3} H	2.89	3.53	3.55	
Ala^{6} H	*N*Me-Ala^{5} H$^{\alpha}$	2.06	2.52	2.53	0.01
Ala^{6} H	*N*Me-Ala^{5} H^{Me}	3.02	4.09	3.51	
Ala^{6} H$^{\beta}$	Ala^{6} H	2.91	3.96	3.04	
Ala^{6} H	Ala^{6} H$^{\alpha}$	2.42	2.96	2.97	0.01

Table D.30: Distance restraints for *N*Me(1,2,5,6)$_{cis4\text{-}5}$

interproton distance		d_{low} [Å]	d_{upp} [Å]	d_{DG} [Å]	d_{viol} [Å]
*N*Me-D-Ala^1 H^{Me}	*N*Me-D-Ala^1 H$^{\beta}$	2.93	4.38	3.63	
*N*Me-D-Ala^1 H^{Me}	Ala^3 H	3.76	5.00	3.71	-0.05
*N*Me-D-Ala^1 H^{Me}	*N*Me-Ala^5 H$^{\alpha}$	3.16	4.26	3.73	
*N*Me-D-Ala^1 H^{Me}	*N*Me-Ala^6 H$^{\alpha}$	2.31	3.23	2.71	
*N*Me-Ala^2 H^{Me}	*N*Me-D-Ala^1 H$^{\alpha}$	2.28	3.19	2.61	
*N*Me-Ala^2 H$^{\alpha}$	*N*Me-Ala^2 H^{Me}	3.25	4.38	3.45	
*N*Me-Ala^2 H$^{\beta}$	*N*Me-Ala^2 H^{Me}	2.97	4.43	3.03	
*N*Me-Ala^2 H$^{\alpha}$	Ala^3 H	2.21	2.69	2.71	0.02
*N*Me-Ala^2 H$^{\beta}$	Ala^3 H	3.88	5.14	4.11	
*N*Me-Ala^2 H^{Me}	Ala^3 H	3.30	4.43	3.81	
Ala^3 H$^{\alpha}$	Ala^3 H	2.46	2.90	2.91	0.01
Ala^3 H$^{\beta}$	Ala^3 H	3.19	4.30	2.95	-0.24
Ala^3 H$^{\alpha}$	Ala^4 H	2.48	3.04	3.05	0.01
Ala^4 H$^{\alpha}$	Ala^4 H	2.90	3.20	2.98	
Ala^4 H$^{\alpha}$	*N*Me-Ala^5 H$^{\alpha}$	1.72	2.10	1.89	
*N*Me-Ala^5 H^{Me}	*N*Me-Ala^5 H$^{\alpha}$	3.38	4.54	3.40	
*N*Me-Ala^5 H^{Me}	*N*Me-Ala^5 H$^{\beta}$	3.19	4.70	3.45	
*N*Me-Ala^5 H^{Me}	*N*Me-Ala^6 H$^{\beta}$	3.70	5.32	4.70	
*N*Me-Ala^6 H^{Me}	Ala^3 H	3.08	4.17	4.24	0.07
*N*Me-Ala^6 H^{Me}	Ala^3 H$^{\beta}$	3.34	4.88	4.52	
*N*Me-Ala^6 H^{Me}	Ala^4 H	3.73	4.96	4.74	
*N*Me-Ala^6 H^{Me}	*N*Me-Ala^5 H$^{\alpha}$	2.58	3.56	2.91	
*N*Me-Ala^6 H^{Me}	*N*Me-Ala^6 H$^{\alpha}$	3.40	4.56	3.44	
*N*Me-Ala^6 H^{Me}	*N*Me-Ala^6 H$^{\beta}$	3.21	4.72	3.15	-0.06

Table D.31: Distance restraints for *N*Me(1,2,5,6)$_{cis5\text{-}6}$

interproton distance		d_{low} [Å]	d_{upp} [Å]	d_{DG} [Å]	d_{viol} [Å]
*N*Me-D-Ala^1 H$^\beta$	*N*Me-D-Ala^1 H^{Me}	3.11	4.60	3.66	
*N*Me-D-Ala^1 H^{Me}	*N*Me-D-Ala^1 H$^\alpha$	3.27	4.40	3.35	
*N*Me-D-Ala^1 H^{Me}	*N*Me-Ala^2 H$^\alpha$	3.42	4.58	4.38	
*N*Me-D-Ala^1 H^{Me}	Ala^4 H	3.83	5.08	4.01	
*N*Me-D-Ala^1 H^{Me}	*N*Me-Ala^5 H$^\alpha$	3.05	4.12	4.13	0.01
*N*Me-D-Ala^1 H^{Me}	*N*Me-Ala^6 H$^\alpha$	2.17	3.06	2.65	
*N*Me-Ala^2 H^{Me}	*N*Me-D-Ala^1 H$^\alpha$	2.21	3.10	2.32	
*N*Me-Ala^2 H$^\beta$	*N*Me-Ala^2 H^{Me}	2.85	4.29	3.40	
*N*Me-Ala^2 H^{Me}	*N*Me-Ala^2 H$^\alpha$	3.10	4.19	3.46	
*N*Me-Ala^2 H$^\alpha$	Ala^3 H	2.29	2.81	2.30	
*N*Me-Ala^2 H^{Me}	Ala^4 H	2.85	3.88	3.50	
*N*Me-Ala^2 H^{Me}	*N*Me-Ala^6 H$^\alpha$	3.30	4.43	4.64	0.21
Ala^3 H$^\alpha$	Ala^3 H	2.26	2.77	2.32	
Ala^3 H$^\beta$	Ala^3 H	2.90	3.95	3.33	
Ala^3 H$^\alpha$	Ala^4 H	2.50	3.06	2.97	
Ala^3 H$^\beta$	Ala^4 H	3.44	4.6	4.08	
Ala^4 H	Ala^3 H	2.47	3.02	2.70	
Ala^4 H$^\alpha$	Ala^4 H	2.57	3.14	2.83	
Ala^4 H$^\beta$	Ala^4 H	2.95	4.00	3.23	
Ala^4 H$^\beta$	*N*Me-Ala^5 H^{Me}	3.12	4.62	3.21	
*N*Me-Ala^5 H^{Me}	Ala^4 H$^\alpha$	2.16	3.04	2.55	
*N*Me-Ala^5 H$^\beta$	*N*Me-Ala^5 H^{Me}	2.81	4.24	2.90	
*N*Me-Ala^5 H^{Me}	*N*Me-Ala^5 H$^\alpha$	3.35	4.49	3.39	
*N*Me-Ala^6 H$^\beta$	*N*Me-D-Ala^1 H^{Me}	3.10	4.59	3.10	
*N*Me-Ala^6 H^{Me}	*N*Me-Ala^6 H$^\beta$	2.93	4.38	3.42	

Temperature dependence of chemical shifts of cyclic (-a-A-A-A-A-A-) peptides

The temperature dependence of amide proton resonances was derived from 1D ^{1}H NMR spectra that were detected at 300 K, 305 K, and 310 K at 500 MHz proton resonance frequency in DMSO-d6.

Table D. 32: Temperature dependence of ^{1}H NMR chemical shifts.

	H^N D-Ala^1	H^N Ala^2	H^N Ala^3	H^N Ala^4	H^N Ala^5	H^N Ala^6
			Δδ/ΔT [ppb/K]			
***N*Me(1)**		-5.6	-1.8	-5.5	-5.2	-3.4
***N*Me(5)**	-6.1	-5.2	-1.0	-3.4		-1.4
***N*Me(1,2)**			-1.5 - -0.1*	-4.6	-5.1	-1.5 - -0.1*
***N*Me(1,5)**		-5.2	0.0	-4.6		-2.0
***N*Me(1,6)**		0.5	-5.6	-6.6	-1.7	
***N*Me(2,5)**	-5.4		-0.8	-4.6		-2.0
***N*Me(3,5)**$_{cis2\text{-}3,cis4\text{-}5}$	-5.4	-3.0		-0.2		-0.8
***N*Me(3,5)**$_{cis2\text{-}3}$	-0.2	-4.6		-1.9		-3.5
***N*Me(4,5)**	-6.7	-5.7	-1.5			-1.3
***N*Me(5,6)**$_{cis5\text{-}6}$	-3.4	-4.2	-6.1	-2.0 - -1.5		
***N*Me(5,6)**$_{cis4\text{-}5,cis5\text{-}6}$	-4.6	-4.5	-2.0 - -1.5	-2.0 - -1.5		
***N*Me(1,2,5)**			-0.8	-4.0		-2.0
***N*Me(2,4,5)**	-4.7		-0.4			-1.6
***N*Me(1,2,4,5)**			-0.6			-1.6
***N*Me(1,2,5,6)**$_{cis4\text{-}5}$			-3.7	-3.6		
***N*Me(1,2,5,6)**$_{cis5\text{-}6}$			-2.4	-1.1		
***N*Me(1,4,5,6)**$_{cis4\text{-}5,cis5\text{-}6}$		-6.0	-1.6			
***N*Me(1,4,5,6)**$_{cis3\text{-}4}$		-3.3	-5.9 - -3.5			
***N*Me(2,4,5,6)**$_{cis3\text{-}4,cis4\text{-}5}$	-3.6		-3.8			
***N*Me(2,4,5,6)**$_{cis4\text{-}5,cis5\text{-}6}$	-5.0		-0.3			
***N*Me(2,4,5,6)**$_{all\ trans}$	-3.3		-6.3			

*degenerate $^{1}H^{N}$ chemical shifts.

Conformations of *N*Me(1) and *N*Me(1,3,6)

One set of signals was observed in NMR spectra of *N*Me(1) and *N*Me(1,3,6). In spectra of *N*Me(1), H^N chemical shifts are all clustered in the narrow range from 7.716 ppm (Ala^3) to 8.293 ppm (Ala^4) and their temperature dependency is between -5.5 ppm/K (Ala^4) and -1.8 ppm/K (Ala^3). Distance geometry (DG) calculations using 9 intraresidual, 13 sequential interresidual and 8 non-sequential interresidual ROEs yielded heterogeneous ensembles of different conformers with significant violations of upper and lower bounds. Thus, NMR data and distance geometry calculations clearly indicate that the conformation of *N*Me(1) can only be described by at least two conformations, that are interconverting fast on the timescale of NMR chemical shifts. Three non-sequential long-range ($Ala^{(i)}$ - $Ala^{(i+3)}$) ROEs; Ala^2 H^N - Ala^5 H^N, Ala^3 H^N – Ala^6 H^β, and Ala^3 H^β – Ala^6 H^N suggest close proximity of Ala^2 and Ala^5 in one conformation and of Ala^3 and and Ala^6 in another conformation. In conformations possessing two opposite β-turns, Ala^2 and Ala^5 are closely neighbored if Ala^6 (*N*Me D-Ala^1) and Ala^3 (Ala^4) occupy the i+1 (i+2) positions of these turns (Figure D.1 A), whereas Ala^3 and Ala^6 are closely neighbored if *N*Me D-Ala^1 (Ala^2) and Ala^4 (Ala^5) occupy the i+1 (i+2) positions of these turns (Figure D.1 B).

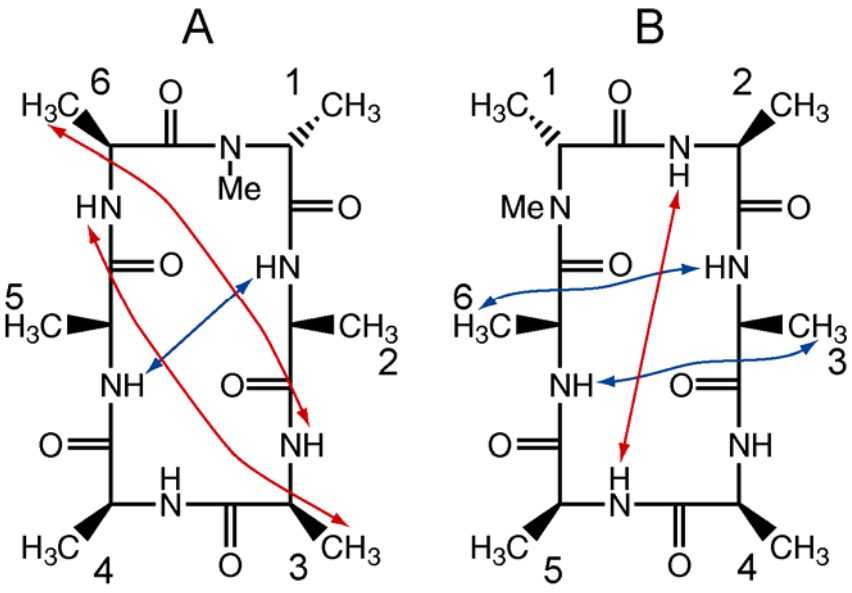

Figure D.1: Arrangement of β-turns in two structural models A and B of *N*Me(1) undergoing fast conformational exchange. Fulfilled and violated $Ala^{(i)}$ - $Ala^{(i+3)}$ long range ROEs are shown in blue, and red color, respectively.

The temperature dependencies of Ala^3 H^N (-1.8 ppb/K) and Ala^6 H^N (-3.4 ppb/K) are less pronounced than the temperature dependencies of Ala^2 H^N (-5.6 ppb/K) and

Ala^5 H^N (-5.2 ppb/K). This indicates that the amide resonances of Ala^3 and Ala^6 are more efficiently shielded from the solvent, which favors the arrangement of β-turns shown in Figure D.1 B with respect to the arrangement of β-turns shown in Figure D.1 A.

The dispersion of chemical shifts of *N*Me(1,3,6) was found to be high, (H^N: 7.004 - 8.095 ppm, H$^\alpha$: 3.688 - 5.201 ppm, H^{Me}: 2.600 - 3.196 ppm), which is often indicating a single highly preferred conformation. But in DG calculations, in which 9 intraresidual, 20 sequential interresidual and 9 non-sequential interresidual ROEs were applied, no single structure could be derived that fullfilled all restraints at once. At least two fast exchanging conformers have to be assumed, as is suggested from considering only the three Ala$^{(i)}$ - Ala$^{(i+3)}$ long range ROEs (Ala^2 H^N - Ala^5 H^N, *N*Me Ala^1 H^{Me} – Ala^4 H^N, and *N*Me Ala^1 H^{Me} – Ala^4 H$^\alpha$). In conformations possessing two opposite β-turns, Ala^2 and Ala^5 are closely neighbored if *N*Me Ala^6 (*N*Me D-Ala^1) and *N*Me Ala^3 (Ala^4) occupy the i+1 (i+2) positions of these turns (Figure D.2 A), whereas *N*Me D-Ala^1 and Ala^4 are closely neighbored if Ala^2 (*N*Me Ala^3) and Ala^5 (*N*Me Ala^6) occupy the i+1 (i+2) positions of these turns (Figure D.2 B).

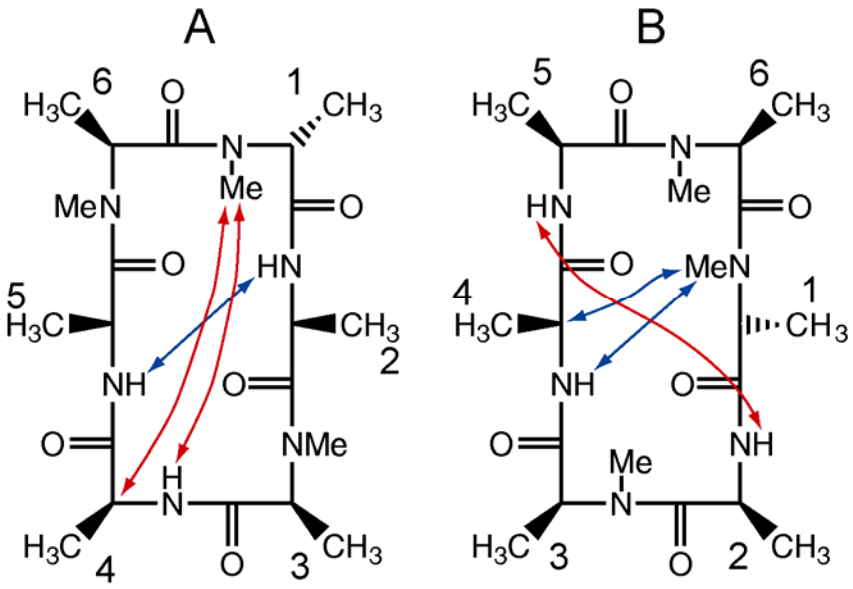

Figure D.2: Arrangement of β-turns in two structural models A and B of *N*Me(1,3,6) undergoing fast conformational exchange. Fulfilled and violated Ala$^{(i)}$ - Ala$^{(i+3)}$ long range ROEs are shown in blue, and red color, respectively.

NMR Parameters that Indicate the Similarity of Peptides Occupying the Second Template Structure

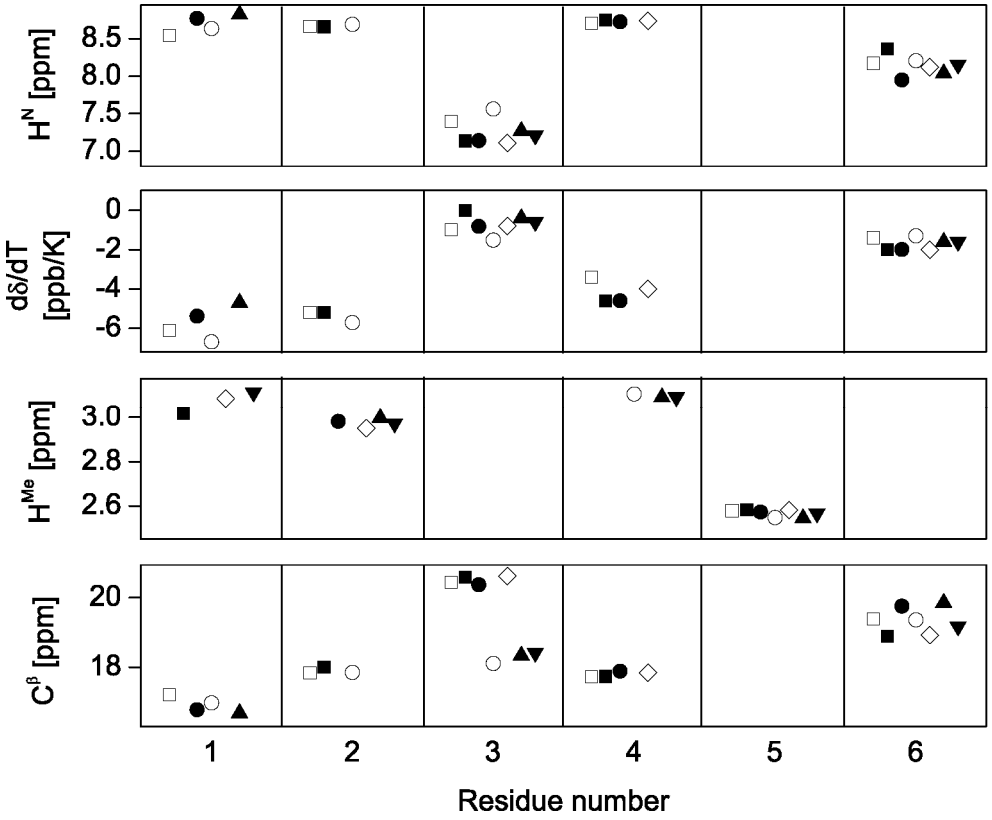

Figure D.3: H^N chemical shifts, their temperature dependence, H^{Me}, and C^β chemical shifts of the six Ala residues in *N*Me(5) (□), *N*Me(1,5) (■), *N*Me(2,5) (●), *N*Me(4,5) (○), *N*Me(1,2,5) (◊), *N*Me(2,4,5) (▲), and *N*Me(1,2,4,5) (▼). To avoid bias by other than pure conformational effects, C^β chemical shifts are only given for non-*N*-methylated residues.

Appendix E

Table E.1: Resonance assignments of the Hsp26 deletion protein $Hsp26_{30\text{-}195(\Delta 137\text{-}153)}$

	H^N	N	C'	H^α	C^α	C^β
Y32			174.76		57.55	38.93
A33	8.11	127.54	174.50		50.02	18.38
P34					62.94	31.83
P34						
R35	8.35	121.06	176.17		56.16	30.66
R36	8.30	122.16	175.76		55.99	30.75
Q37	8.38	121.85	175.55		55.69	29.40
L38	8.25	123.94	176.84		55.02	42.26
A39	8.23	124.18	177.08	4.23	52.37	19.11
N40	8.31	117.70	174.68		52.99	38.65
T41	7.97	116.46		4.50	59.76	69.64
P42					63.10	31.92
A43	8.33	124.65	177.53	4.20	52.34	19.08
K44	8.23	120.17	176.20	4.29	56.17	33.50
D45	8.33	120.97	176.71		53.95	41.27
S46	8.31	116.01	175.00	5.02	59.00	63.53
T47	8.31	114.76	175.28	4.30	62.41	69.71
G48	8.32	110.93	173.83	3.92	45.37	
K49	7.95	120.76	176.24		56.04	32.91
E50	8.47	122.09	176.40	4.23	56.64	29.82
V51	8.08	121.68	175.39	4.00	61.92	32.70
A52	8.27	127.80	176.97	4.23	52.19	19.00
R53	8.23	121.55	174.04	4.50	53.58	30.15
P54					63.04	32.02
N55	8.43	118.43	174.70		53.37	38.49
N56	8.23	118.40	174.62		53.09	38.48
Y57	7.98	120.40	175.34	4.43	58.03	38.93
A58	8.14	125.85	177.53	4.19	52.50	18.80
G59	7.66	107.42	173.46	3.79	45.14	
A60	7.96	123.13	177.31	4.24	52.41	19.21
L61	8.07	120.59	176.39		55.01	42.23
Y62	7.91	120.42	174.21	4.46	57.35	38.86
D63	8.14	124.78		4.74	51.26	41.73
P64					63.61	31.91
R65	8.31	119.63	176.22	4.13	56.55	30.30
D66	8.06	120.35	176.30		54.53	41.02
E67	8.26	121.50	176.48	4.21	56.90	30.02
T68	8.20	114.15	174.44	4.23	62.18	69.66
L69	7.97	123.55	176.81	4.26	55.11	42.21
D70	8.06	120.43	175.80		54.74	41.16
D71	8.11	119.78	175.91	4.42	54.49	41.00

	H^N	N	C'	H^α	C^α	C^β
W72	7.90	120.61	175.62	4.44	57.42	29.43
F73	7.70	120.62	174.75	4.35	57.73	39.70
D74	7.95	121.23	175.57		54.20	41.15
N75	8.06	119.01	174.70	4.51	53.52	39.16
D76	8.26	120.17	176.51	4.48	54.75	40.76
L77	8.10	122.28	177.60	4.19	55.64	41.69
S78	8.19	115.37	174.34	4.21	59.34	63.36
L79	7.78	122.12	176.28	4.14	55.14	42.41
F80	7.88	119.80	173.60		55.42	39.10
P81					63.49	31.63
S82	8.29	115.30	174.95	4.30	58.74	63.62
G83	8.28	110.45	173.66		45.20	
F84	8.04	119.78	175.74		58.05	39.50
G85	8.14	109.92	172.95		45.00	
F86	7.74	120.23	173.64	4.66	55.67	38.80
R88			176.57		58.81	31.79
S89	7.81	117.23	176.46		57.46	65.55
A91			177.01		52.17	19.18
V92	8.04	119.89	173.20		59.38	32.71
P93					63.41	32.31
V94	7.90	119.70	174.84		60.77	35.51
D95	8.56	126.74	174.50	4.96	53.27	43.52
I96	8.40	122.19	174.41	4.50	61.07	39.59
L97	9.18	129.97	174.56	4.56	54.11	42.66
D98	8.47	124.17		4.63	53.77	41.94
N101			175.39		52.82	39.52
N102	7.23	114.99	172.27	4.94	53.09	41.47
Y103	8.80	115.45	175.19	5.19	57.11	40.77
E104	9.10	124.40	173.98	5.21	54.51	32.80
L105	9.43	127.21	175.26	5.23	53.32	43.11
K106	8.86	122.40	174.91	5.00	54.84	33.48
V107	9.32	125.56	174.64		60.73	33.37
V108	8.36	129.56			63.95	31.06
V109	7.97	123.69			57.82	
P110					63.12	31.64
G111	8.47	107.36	174.75		45.85	
V112	7.30	119.58	176.51	3.89	62.58	31.70
K113	8.90	125.89	176.63	4.19	58.16	32.95
S114	7.42	111.64	173.79	4.49	56.71	65.22
K116			176.45		57.36	31.59
D117	7.42	117.45	174.49	4.51	55.10	41.44
I118	7.26	118.82	173.86	4.51	59.77	39.83
D119	9.05	127.17			53.65	43.10
I120	8.25	122.48	175.05	4.86	60.05	40.58

	H^N	N	C'	H^α	C^α	C^β
E121	8.86	125.86	173.80	4.70	54.48	34.24
Y122	8.88	123.49	174.09	5.16	56.19	40.02
H123	8.74	128.91			53.44	31.10
N125			175.70		55.82	37.20
K126	7.18	116.37	174.90		55.11	33.38
N127	7.83	119.45	172.39		53.80	37.28
Q128	7.09	112.13	174.64	5.26	53.18	32.63
I129	8.96	121.05	173.29	4.77	59.21	40.32
L130	9.11	129.03	175.56	5.03	53.95	43.77
V131	8.81	124.72	174.10	4.94	60.12	33.70
S132	8.92	120.25	171.59	4.76	56.67	65.93
G133	6.95	105.81	171.08		45.73	
E134	8.37	121.25	174.19		56.16	36.42
I135	8.23	119.63	176.20		59.85	38.37
P136					66.75	31.11
S154	7.50	106.25	173.91		58.59	63.00
G155	8.04	110.90	172.21	4.51	45.06	
K156	8.30	120.29	176.07		56.25	33.67
F157	8.48	119.01	173.34	5.16	55.98	42.80
K158	8.38	121.60	174.56		55.94	35.34
R159	9.36	125.75	173.23	4.63	53.66	33.67
V160	8.68	125.85	175.65	4.56	61.70	32.94
I161	9.38	129.75	174.70	4.27	60.73	40.59
T162	8.65	124.90	173.58		63.10	69.05
L163	8.20	127.54		4.42	52.23	40.70
D165			174.55		55.81	40.84
Y166	7.42	118.43	173.69	4.53	54.96	
P167					63.18	34.33
G168	8.62	112.47	172.84	4.16	44.28	
V169	8.01	110.92	174.41	4.83	59.30	35.15
D170	7.95	120.95	175.59		51.16	39.88
A171	7.71	124.48	178.00	3.52	53.60	18.52
D172	7.93	115.64	176.37	4.47	55.86	40.81
N173	7.09	116.24	173.32	4.96	52.84	40.09
I174	7.21	119.67	175.69	4.24	63.31	38.32
K175	8.33	128.68	174.08	4.66	54.64	35.20
A176	8.64	125.26	175.32	5.34	50.39	22.52
D177	8.70	121.05	173.34	4.87	53.45	45.47
Y178	8.77	123.83	173.54		56.87	41.81
A179	7.80	128.14	176.64	4.05	52.15	21.36
N180			174.57		53.98	37.36
G181	7.49	102.32	172.32		45.72	
V182	7.30	119.10	174.86	4.34	61.45	34.66
L183	9.34	132.31	174.37		53.20	44.32

	H^N	N	C’	H^α	C^α	C^β
T184	9.38	124.74	175.01	5.36	61.86	69.55
L185	9.56	128.37	175.49		52.83	44.03
T186	9.16	120.51	173.76	4.83	62.34	69.06
V187	9.13	127.31	172.38	4.48	58.51	33.32
P188					63.01	32.08
K189	7.61	121.29	177.40	4.48	55.81	34.61
L190	8.00	122.40	175.94	4.99	54.40	41.87
K191	8.11	121.34	174.35		53.57	32.16
P192					63.00	31.97
Q193	8.43	121.33	174.81	4.24	55.73	29.51
K194	7.89	127.56	180.89		57.60	33.50

Bibliography

[1] R. Breinbauer, I. R. Vetter, H. Waldmann, *Angew. Chem. Int. Ed.* **2002**, *41*, 2879.

[2] A. G. Murzin, S. E. Brenner, T. Hubbard, C. Chothia, *J. Mol. Biol.* **1995**, *247*, 536.

[3] C. A. Orengo, A. D. Michie, S. Jones, D. T. Jones, M. B. Swindells, J. M. Thornton, *Structure* **1997**, *5*, 1093.

[4] H. M. Berman, J. Westbrook, Z. Feng, G. Gilliland, T. N. Bhat, H. Weissig, I. N. Shindyalov, P. E. Bourne, *Nucleic Acids Res.* **2000**, *28*, 235.

[5] E. Fischer, *Ber. Deut. Chem. Ges.* **1894**, *27*, 2985.

[6] E. Fischer, *Ber. Deut. Chem. Ges.* **1894**, *27*, 3189.

[7] T. Matthews, M. Salgo, M. Greenberg, J. Chung, R. DeMasi, D. Bolognesi, *Nat. Rev. Drug Discov.* **2004**, *3*, 215.

[8] M. A. Dechantsreiter, B. Mathä, A. Jonczyk, S. L. Goodman, H. Kessler, in *Peptides 1996* (Eds.: R. Ramage, R. Epton), Mayflower Scientific, Kingswinford, **1996**, pp. 329.

[9] M. A. Dechantsreiter, E. Planker, B. Mathä, E. Lohof, G. Hölzemann, A. Jonczyk, S. L. Goodman, H. Kessler, *J. Med. Chem.* **1999**, *42*, 3033.

[10] R. M. Scarborough, M. A. Naughton, W. Teng, J. W. Rose, D. R. Phillips, L. Nannizzi, A. Arfsten, A. M. Campbell, I. F. Charo, *J. Biol. Chem.* **1993**, *268*, 1066.

[11] C. A. Lipinski, F. Lombardo, B. W. Dominy, P. J. Feeney, *Adv. Drug Deliver. Rev.* **2001**, *46*, 3.

[12] D. F. Veber, S. R. Johnson, H. Y. Cheng, B. R. Smith, K. W. Ward, K. D. Kopple, *J. Med. Chem.* **2002**, *45*, 2615.

[13] S. Lande, *J. Org. Chem.* **1962**, *27*, 4558.

[14] E. J. Ariëns, *Medicinal Chemistry: Drug Design*, Academic Press, New York, **1971**.

[15] H. Gerlach, J. A. Owtschinnikow, V. Prelog, *Helv. Chim. Acta* **1964**, *47*, 2294.

[16] H. Gerlach, G. Haas, V. Prelog, *Helv. Chim. Acta* **1966**, *49*, 603.

[17] V. Prelog, H. Gerlach, *Helv. Chim. Acta* **1964**, *47*, 2288.

[18] M. M. Shemyakin, Y. A. Ovchinnikov, V. T. Ivanov, *Angew. Chem. Int. Ed.* **1969**, *8*, 492.

[19] R. J. Simon, R. S. Kania, R. N. Zuckermann, V. D. Huebner, D. A. Jewell, S. Banville, S. Ng, L. Wang, S. Rosenberg, C. K. Marlowe, D. C. Spellmeyer, R. Y. Tan, A. D. Frankel, D. V. Santi, F. E. Cohen, P. A. Bartlett, *P. Natl. Acad. Sci. USA* **1992**, *89*, 9367.

[20] H. Kessler, *Angew. Chem. Int. Ed.* **1993**, *32*, 543.

[21] P. Vlieghe, V. Lisowski, J. Martinez, M. Khrestchatisky, *Drug Discov. Today* **2010**, *15*, 40.

[22] J. Reichert, P. Pechon, A. Tartar, M. K. Dunn, Tufts Center for the Study of Drug Development, Tufts University, Boston, MA 02111, USA, **2010**.

[23] J. Fogh, J. M. Fogh, T. Orfeo, *J. Natl. Cancer I.* **1977**, *59*, 221.

[24] A. L. Fink, *Curr. Opin. Struc. Biol.* **2005**, *15*, 35.

[25] D. F. Mierke, M. Kurz, H. Kessler, *J. Am. Chem. Soc.* **1994**, *116*, 1042.

[26] H. Kessler, C. Griesinger, J. Zarbock, H.-R. Loosli, *J. Magn. Reson.* **1984**, *57*, 331.

[27] A. Bax, M. F. Summers, *J. Am. Chem. Soc.* **1986**, *108*, 2093.

[28] M. Karplus, *J. Am. Chem. Soc.* **1963**, *85*, 2870.

[29] K. G. R. Pachler, *Spectrochim. Acta* **1963**, *19*, 2085.

[30] A. A. Bothner-By, R. L. Stephens, J. M. Lee, *J. Am. Chem. Soc.* **1984**, *106*, 811.

[31] C. Griesinger, R. R. Ernst, *J. Magn. Reson.* **1987**, *75*, 261.
[32] J. Schleucher, J. Quant, S. J. Glaser, C. Griesinger, in *Encyclopedia of Nuclear Magnetic Resonance, Vol. 8* (Eds.: D. M. Grant, R. K. Harris), Wiley, New York, **1996**, pp. 4789.
[33] J. Schleucher, J. Quant, S. J. Glaser, C. Griesinger, *J. Magn. Reson. Ser. A* **1995**, *112*, 144.
[34] J. Cavanagh, J. Keeler, *J. Magn. Reson.* **1988**, *80*, 186.
[35] C. M. Thiele, K. Petzold, J. Schleucher, *Chem.-Eur. J.* **2009**, *15*, 585.
[36] C. Griesinger, O. W. Sørensen, R. R. Ernst, *J. Magn. Reson.* **1987**, *75*, 474.
[37] N. Müller, R. R. Ernst, K. Wüthrich, *J. Am. Chem. Soc.* **1986**, *108*, 6482.
[38] L. Mueller, *J. Magn. Reson.* **1987**, *72*, 191.
[39] H. Kessler, A. Müller, H. Oschkinat, *Magn. Reson. Chem.* **1985**, *23*, 844.
[40] H. Kessler, H. Oschkinat, *Angew. Chem. Int. Ed.* **1985**, *24*, 690.
[41] H. Oschkinat, R. Freeman, *J. Magn. Reson.* **1984**, *60*, 164.
[42] M. Eberstadt, G. Gemmecker, D. F. Mierke, H. Kessler, *Angew. Chem. Int. Ed.* **1995**, *34*, 1671.
[43] L. Doedens, F. Opperer, M. Y. Cai, J. G. Beck, M. Dedek, E. Palmer, V. J. Hruby, H. Kessler, *J. Am. Chem. Soc.* **2010**, *132*, 8115.
[44] J. J. Titman, D. Neuhaus, J. Keeler, *J. Magn. Reson.* **1989**, *85*, 111.
[45] M. Kurz, P. Schmieder, H. Kessler, *Angew. Chem. Int. Ed.* **1991**, *30*, 1329.
[46] P. Schmieder, M. Kurz, H. Kessler, *J. Biomol. NMR* **1991**, *1*, 403.
[47] U. Wollborn, D. Leibfritz, *J. Magn. Reson.* **1992**, *98*, 142.
[48] D. Uhrín, G. Batta, V. J. Hruby, P. N. Barlow, K. E. Kövér, *J. Magn. Reson.* **1998**, *130*, 155.
[49] S. J. Archer, M. Ikura, D. A. Torchia, A. Bax, *J. Magn. Reson.* **1991**, *95*, 636.
[50] S. Grzesiek, M. Ikura, G. M. Clore, A. M. Gronenborn, A. Bax, *J. Magn. Reson.* **1992**, *96*, 215.
[51] G. W. Vuister, A. Bax, *J. Am. Chem. Soc.* **1993**, *115*, 7772.
[52] J. Klages, C. Neubauer, M. Coles, H. Kessler, B. Luy, *Chembiochem* **2005**, *6*, 1672.
[53] M. B. Schmid, M. Fleischmann, V. D'Elia, O. Reiser, W. Gronwald, R. M. Gschwind, *Chembiochem* **2009**, *10*, 440.
[54] M. U. Kiran, A. Sudhakar, J. Klages, G. Kummerlöwe, B. Luy, B. Jagadeesh, *J. Am. Chem. Soc.* **2009**, *131*, 15590.
[55] U. M. Reinscheid, J. Farjon, M. Radzom, P. Haberz, A. Zeeck, M. Blackledge, C. Griesinger, *Chembiochem* **2006**, *7*, 287.
[56] A. V. Klochkov, B. I. Khairutdinov, M. S. Tagirov, V. V. Klochkov, *Magn. Reson. Chem.* **2005**, *43*, 948.
[57] V. V. Klochkov, R. F. Baikeev, V. D. Skirda, A. V. Klochkov, F. R. Muhamadiev, I. Baskyr, S. Berger, *Magn. Reson. Chem.* **2009**, *47*, 57.
[58] G. Kummerlöwe, B. Luy, *Ann. R. NMR S.* **2009**, *68*, 193.
[59] L. M. Blumenthal, *Theory and Application of Distance Geometry*, Chelsea Publishing, New York, **1970**.
[60] G. M. Crippen, Havel, T. F., *Distance Geometry and Molecular Conformation*, John Wiley & Sons, New York, **1988**.
[61] T. Havel, K. Wüthrich, *B. Math. Biol.* **1984**, *46*, 673.
[62] J. P. Albrand, B. Birdsall, J. Feeney, G. C. K. Roberts, A. S. V. Burgen, *Int. J. Biol. Macromol.* **1979**, *1*, 37.
[63] C. B. Post, *Curr. Opin. Struc. Biol.* **2003**, *13*, 581.
[64] M. Mayer, B. Meyer, *Angew. Chem. Int. Ed.* **1999**, *38*, 1784.
[65] F. Marshall, M. Congreve, *Brit. J. Pharmacol.* **2010**, *159*, 986.
[66] R. Fredriksson, M. C. Lagerstrom, L. G. Lundin, H. B. Schioth, *Mol. Pharmacol.* **2003**, *63*, 1256.
[67] B. K. Kobilka, *BBA-Biomembranes* **2007**, *1768*, 794.

[68] W. C. Probst, L. A. Snyder, D. I. Schuster, J. Brosius, S. C. Sealfon, *DNA Cell Biol.* **1992**, *11*, 1.
[69] L. F. Kolakowski, *Receptor. Channel.* **1994**, *2*, 1.
[70] H. B. Schioth, M. C. Lagerstrom, *Nat. Rev. Drug Discov.* **2008**, *7*, 339.
[71] T. H. Ji, M. Grossmann, I. Ji, *J. Biol. Chem.* **1998**, *273*, 17299.
[72] T. Mirzadegan, G. Benko, S. Filipek, K. Palczewski, *Biochemistry* **2003**, *42*, 2759.
[73] E. Pebay-Peyroula, G. Rummel, J. P. Rosenbusch, E. M. Landau, *Science* **1997**, *277*, 1676.
[74] H. Luecke, B. Schobert, H.-T. Richter, J.-P. Cartailler, J. K. Lanyi, *J. Mol. Biol.* **1999**, *291*, 899.
[75] K. Palczewski, T. Kumasaka, T. Hori, C. A. Behnke, H. Motoshima, B. A. Fox, I. Le Trong, D. C. Teller, T. Okada, R. E. Stenkamp, M. Yamamoto, M. Miyano, *Science* **2000**, *289*, 739.
[76] J. Li, P. C. Edwards, M. Burghammer, C. Villa, G. F. X. Schertler, *J. Mol. Biol.* **2004**, *343*, 1409.
[77] T. Okada, M. Sugihara, A. N. Bondar, M. Elstner, P. Entel, V. Buss, *J. Mol. Biol.* **2004**, *342*, 571.
[78] J. Standfuss, G. F. Xie, P. C. Edwards, M. Burghammer, D. D. Oprian, G. F. X. Schertler, *J. Mol. Biol.* **2007**, *372*, 1179.
[79] J. H. Park, P. Scheerer, K. P. Hofmann, H. W. Choe, O. P. Ernst, *Nature* **2008**, *454*, 183.
[80] P. Scheerer, J. H. Park, P. W. Hildebrand, Y. J. Kim, N. Krauss, H. W. Choe, K. P. Hofmann, O. P. Ernst, *Nature* **2008**, *455*, 497.
[81] S. G. F. Rasmussen, H. J. Choi, D. M. Rosenbaum, T. S. Kobilka, F. S. Thian, P. C. Edwards, M. Burghammer, V. R. P. Ratnala, R. Sanishvili, R. F. Fischetti, G. F. X. Schertler, W. I. Weis, B. K. Kobilka, *Nature* **2007**, *450*, 383.
[82] V. Cherezov, D. M. Rosenbaum, M. A. Hanson, S. G. F. Rasmussen, F. S. Thian, T. S. Kobilka, H. J. Choi, P. Kuhn, W. I. Weis, B. K. Kobilka, R. C. Stevens, *Science* **2007**, *318*, 1258.
[83] D. M. Rosenbaum, V. Cherezov, M. A. Hanson, S. G. F. Rasmussen, F. S. Thian, T. S. Kobilka, H. J. Choi, X. J. Yao, W. I. Weis, R. C. Stevens, B. K. Kobilka, *Science* **2007**, *318*, 1266.
[84] M. A. Hanson, V. Cherezov, M. T. Griffith, C. B. Roth, V. P. Jaakola, E. Y. T. Chien, J. Velasquez, P. Kuhn, R. C. Stevens, *Structure* **2008**, *16*, 897.
[85] D. Wacker, G. Fenalti, M. A. Brown, V. Katritch, R. Abagyan, V. Cherezov, R. C. Stevens, *J. Am. Chem. Soc.* **2010**, *132*, 11443.
[86] S. G. F. Rasmussen, H. J. Choi, J. J. Fung, E. Pardon, P. Casarosa, P. S. Chae, B. T. DeVree, D. M. Rosenbaum, F. S. Thian, T. S. Kobilka, A. Schnapp, I. Konetzki, R. K. Sunahara, S. H. Gellman, A. Pautsch, J. Steyaert, W. I. Weis, B. K. Kobilka, *Nature* **2011**, *469*, 175.
[87] D. M. Rosenbaum, C. Zhang, J. A. Lyons, R. Holl, D. Aragao, D. H. Arlow, S. G. F. Rasmussen, H. J. Choi, B. T. DeVree, R. K. Sunahara, P. S. Chae, S. H. Gellman, R. O. Dror, D. E. Shaw, W. I. Weis, M. Caffrey, P. Gmeiner, B. K. Kobilka, *Nature* **2011**, *469*, 236.
[88] T. Warne, M. J. Serrano-Vega, J. G. Baker, R. Moukhametzianov, P. C. Edwards, R. Henderson, A. G. W. Leslie, C. G. Tate, G. F. X. Schertler, *Nature* **2008**, *454*, 486.
[89] T. Warne, R. Moukhametzianov, J. G. Baker, R. Nehme, P. C. Edwards, A. G. W. Leslie, G. F. X. Schertler, C. G. Tate, *Nature* **2011**, *469*, 241.
[90] V. P. Jaakola, M. T. Griffith, M. A. Hanson, V. Cherezov, E. Y. T. Chien, J. R. Lane, A. P. IJzerman, R. C. Stevens, *Science* **2008**, *322*, 1211.
[91] B. L. Wu, E. Y. T. Chien, C. D. Mol, G. Fenalti, W. Liu, V. Katritch, R. Abagyan, A. Brooun, P. Wells, F. C. Bi, D. J. Hamel, P. Kuhn, T. M. Handel, V. Cherezov, R. C. Stevens, *Science* **2010**, *330*, 1066.

[92] E. Y. T. Chien, W. Liu, Q. A. Zhao, V. Katritch, G. W. Han, M. A. Hanson, L. Shi, A. H. Newman, J. A. Javitch, V. Cherezov, R. C. Stevens, *Science* **2010**, *330*, 1091.
[93] M. Michino, E. Abola, C. L. Brooks, J. S. Dixon, J. Moult, R. C. Stevens, G. D. Participants, *Nat. Rev. Drug Discov.* **2009**, *8*, 455.
[94] M. I. Simon, M. P. Strathmann, N. Gautam, *Science* **1991**, *252*, 802.
[95] J. L. Benovic, R. H. Strasser, M. G. Caron, R. J. Lefkowitz, *P. Natl. Acad. Sci. USA* **1986**, *83*, 2797.
[96] H. Kühn, *Biochemistry* **1978**, *17*, 4389.
[97] J. L. Benovic, H. Kühn, I. Weyand, J. Codina, M. G. Caron, R. J. Lefkowitz, *P. Natl. Acad. Sci. USA* **1987**, *84*, 8879.
[98] O. B. Goodman, J. G. Krupnick, F. Santini, V. V. Gurevich, R. B. Penn, A. W. Gagnon, J. H. Keen, J. L. Benovic, *Nature* **1996**, *383*, 447.
[99] E. W. Sutherland, T. W. Rall, *J. Biol. Chem.* **1958**, *232*, 1077.
[100] G. B. Downes, N. Gautam, *Genomics* **1999**, *62*, 544.
[101] C. A. C. Moore, S. K. Milano, J. L. Benovic, *Annu. Rev. Physiol.* **2007**, *69*, 451.
[102] V. Boswell-Smith, D. Spina, C. P. Page, *Brit. J. Pharmacol.* **2006**, *147*, 252.
[103] R. E. Mains, B. A. Eipper, *J. Biol. Chem.* **1976**, *251*, 4115.
[104] B. A. Eipper, R. E. Mains, *J. Biol. Chem.* **1978**, *253*, 5732.
[105] M. E. Hadley, C. Haskell-Luevano, *Ann. N. Y. Acad. Sci.* **1999**, *885*, 1.
[106] The Melanocortin System. *Ann. N.Y. Acad. Sci.* **2003**, *994*, provides the proceedings of a symposium discussing the developments in this area.
[107] M. E. Hadley, *The Melanotropin Peptides, Vol. 1, 2 & 3*, CRC Press, Boca Raton, FL, **1989**.
[108] A. N. Eberle, *The Melanotropins: Chemistry, Physiology and Mechanisms of Action*, Karger, Basel, **1988**.
[109] S. K. Manna, B. B. Aggarwal, *J. Immunol.* **1998**, *161*, 2873.
[110] C. Maaser, K. Kannengiesser, C. Specht, A. Lugering, T. Brzoska, T. A. Luger, W. Domschke, T. Kucharzik, *Gut* **2006**, *55*, 1415.
[111] Y. Xia, J. E. Wikberg, *Cell Tissue Res.* **1996**, *286*, 63.
[112] D. I. Buckley, J. Ramachandran, *P. Natl. Acad. Sci. USA* **1981**, *78*, 7431.
[113] M. J. Low, *J. Endocrinol. Invest.* **2004**, *27*, 95.
[114] S. J. Li, K. Varga, P. Archer, V. J. Hruby, S. D. Sharma, R. A. Kesterson, R. D. Cone, G. Kunos, *J. Neuroscience* **1996**, *16*, 5182.
[115] I. Gantz, T. M. Fong, *Am. J. Physiol. Endocrinol. Metab.* **2003**, *284*, E468.
[116] W. Fan, B. A. Boston, R. A. Kesterson, V. J. Hruby, R. D. Cone, *Nature* **1997**, *385*, 165.
[117] I. S. Farooqi, J. M. Keogh, G. S. Yeo, E. J. Lank, T. Cheetham, S. O'Rahilly, *N. Engl. J. Med.* **2003**, *348*, 1085.
[118] R. Branson, N. Potoczna, J. G. Kral, K. U. Lentes, M. R. Hoehe, F. F. Horber, *N. Engl. J. Med.* **2003**, *348*, 1096.
[119] H. Wessells, N. Levine, M. E. Hadley, R. Dorr, V. Hruby, *Int. J. Impot. Res.* **2000**, *12 Suppl 4*, S74.
[120] H. Wessells, D. Gralnek, R. Dorr, V. J. Hruby, M. E. Hadley, N. Levine, *Urology* **2000**, *56*, 641.
[121] S. H. King, A. V. Mayorov, P. Balse-Srinivasan, V. J. Hruby, T. W. Vanderah, H. Wessells, *Curr. Top. Med. Chem.* **2007**, *7*, 1098.
[122] N. G. Seidah, S. Benjannet, J. Hamelin, A. M. Mamarbachi, A. Basak, J. Marcinkiewicz, M. Mbikay, M. Chretien, M. Marcinkiewicz, *Ann. N. Y. Acad. Sci.* **1999**, *885*, 57.
[123] K. G. Mountjoy, M. T. Mortrud, M. J. Low, R. B. Simerly, R. D. Cone, *Mol. Endocrinol.* **1994**, *8*, 1298.
[124] V. Chhajlani, *Biochem. Mol. Biol. Int.* **1996**, *38*, 73.

[125] T. A. Luger, T. Schwarz, H. Kalden, T. Scholzen, A. Schwarz, T. Brzoska, *Ann. N. Y. Acad. Sci.* **1999**, *885*, 209.
[126] J. E. Wikberg, *Eur. J. Pharmacol.* **1999**, *375*, 295.
[127] I. Gantz, T. M. Fong, *Am. J. Physiol. Endocrinol. Metab.* **2003**, *284*, E468.
[128] J. E. Siljee-Wong, *Eur. J. Pharmacol.* **2011**, *660*, 234.
[129] D. W. Roberts, R. A. Newton, K. A. Beaumont, J. H. Leonard, R. A. Sturm, *Pigm. Cell Res.* **2006**, *19*, 76.
[130] M. M. Ollmann, B. D. Wilson, Y. K. Yang, J. A. Kerns, Y. R. Chen, I. Gantz, G. S. Barsh, *Science* **1997**, *278*, 135.
[131] D. Lu, D. Willard, I. R. Patel, S. Kadwell, L. Overton, T. Kost, M. Luther, W. Chen, R. P. Woychik, W. O. Wilkison, et al., *Nature* **1994**, *371*, 799.
[132] J. J. Buggy, *Biochem. J.* **1998**, *331*, 211.
[133] W. Englaro, R. Rezzonico, M. Durandclement, D. Lallemand, J. P. Ortonne, R. Ballotti, *J. Biol. Chem.* **1995**, *270*, 24315.
[134] S. Kapas, A. Purbrick, J. P. Hinson, *Biochem. J.* **1995**, *305*, 433.
[135] I. Kojima, K. Kojima, H. Rasmussen, *J. Biol. Chem.* **1985**, *260*, 4248.
[136] Y. Konda, I. Gantz, J. Delvalle, Y. Shimoto, H. Miwa, T. Yamada, *J. Biol. Chem.* **1994**, *269*, 13162.
[137] V. J. Hruby, B. C. Wilkes, M. E. Hadley, F. Al-Obeidi, T. K. Sawyer, D. J. Staples, A. E. de Vaux, O. Dym, A. M. Castrucci, M. F. Hintz, et al., *J. Med. Chem.* **1987**, *30*, 2126.
[138] J. E. S. Wikberg, F. Mutulis, *Nat. Rev. Drug Discov.* **2008**, *7*, 307.
[139] V. J. Hruby, M. Y. Cai, J. Cain, J. Nyberg, D. Trivedi, *Eur. J. Pharmacol.* **2011**, *660*, 88.
[140] T. K. Sawyer, P. J. Sanfilippo, V. J. Hruby, M. H. Engel, C. B. Heward, J. B. Burnett, M. E. Hadley, *P. Natl. Acad. Sci. USA* **1980**, *77*, 5754.
[141] T. K. Sawyer, V. J. Hruby, P. S. Darman, M. E. Hadley, *P. Natl. Acad. Sci.-Biol.* **1982**, *79*, 1751.
[142] F. Al-Obeidi, M. E. Hadley, B. M. Pettitt, V. J. Hruby, *J. Am. Chem. Soc.* **1989**, *111*, 3413.
[143] F. Al-Obeidi, A. M. Castrucci, M. E. Hadley, V. J. Hruby, *J. Med. Chem.* **1989**, *32*, 2555.
[144] H. Kessler, *Angew. Chem. Int. Ed.* **1982**, *21*, 512.
[145] V. J. Hruby, *Life Sci.* **1982**, *31*, 189.
[146] M. E. Hadley, S. D. Sharma, V. J. Hruby, N. Levine, R. T. Dorr, *Ann. N. Y. Acad. Sci.* **1993**, *680*, 424.
[147] R. T. Dorr, R. Lines, N. Levine, C. Brooks, L. Xiang, V. J. Hruby, M. E. Hadley, *Life Sci.* **1996**, *58*, 1777.
[148] H. Wessells, K. Fuciarelli, J. Hansen, M. E. Hadley, V. J. Hruby, R. Dorr, N. Levine, *J. Urology* **1998**, *160*, 389.
[149] R. C. Rosen, L. E. Diamond, D. C. Earle, A. M. Shadiack, P. B. Molinoff, *Int. J. Impot. Res.* **2004**, *16*, 135.
[150] L. E. Diamond, D. C. Earle, R. C. Rosen, M. S. Willett, P. B. Molinoff, *Int. J. Impot. Res.* **2004**, *16*, 51.
[151] L. E. Diamond, D. C. Earle, W. D. Garcia, C. Spana, *Urology* **2005**, *65*, 755.
[152] L. E. Diamond, D. C. Earle, J. R. Heiman, R. C. Rosen, M. A. Perelman, R. Harning, *J. Sex. Med.* **2006**, *3*, 628.
[153] V. J. Hruby, D. Lu, S. D. Sharma, A. L. Castrucci, R. A. Kesterson, F. A. al-Obeidi, M. E. Hadley, R. D. Cone, *J. Med. Chem.* **1995**, *38*, 3454.
[154] I. K. Sebhat, W. J. Martin, Z. X. Ye, K. Barakat, R. T. Mosley, D. B. R. Johnston, R. Bakshi, B. Palucki, D. H. Weinberg, T. MacNeil, R. N. Kalyani, R. Tang, R. A. Stearns, R. R. Miller, C. Tamvakopoulos, A. M. Strack, E. McGowan, D. E. Cashen, J. E. Drisko, G. J. Hom, A. D. Howard, D. E. MacIntyre, L. H. T. van der Ploeg, A. A. Patchett, R. P. Nargund, *J. Med. Chem.* **2002**, *45*, 4589.

[155] B. L. Palucki, M. K. Park, R. P. Nargund, Z. X. Ye, I. K. Sebhat, P. G. Pollard, R. N. Kalyani, R. Tang, T. MacNeil, D. H. Weinberg, A. Vongs, C. I. Rosenblum, G. A. Doss, R. R. Miller, R. A. Stearns, Q. P. Peng, C. Tamvakopoulos, E. McGowan, W. J. Martin, J. M. Metzger, C. A. Shepherd, A. M. Strack, D. E. MacIntyre, L. H. T. van der Ploeg, A. A. Patchett, *Bioorg. Med. Chem. Lett.* **2005**, *15*, 171.
[156] A. A. Butler, R. A. Kesterson, K. Khong, M. J. Cullen, M. A. Pelleymounter, J. Dekoning, M. Baetscher, R. D. Cone, *Endocrinology* **2000**, *141*, 3518.
[157] A. S. Chen, D. J. Marsh, M. E. Trumbauer, E. G. Frazier, X. M. Guan, H. Yu, C. I. Rosenblum, A. Vongs, Y. Feng, L. Cao, J. M. Metzger, A. M. Strack, R. E. Camacho, T. N. Mellin, C. N. Nunes, W. Min, J. Fisher, S. Gopal-Truter, D. E. MacIntyre, H. Y. Chen, L. H. van der Ploeg, *Nat. Genet.* **2000**, *26*, 97.
[158] D. L. Marks, V. Hruby, G. Brookhart, R. D. Cone, *Peptides* **2006**, *27*, 259.
[159] S. J. Getting, M. Perretti, *Drug News Perspect.* **2000**, *13*, 19.
[160] W. Chen, M. A. Kelly, X. Opitz-Araya, R. E. Thomas, M. J. Low, R. D. Cone, *Cell* **1997**, *91*, 789.
[161] C. Morgan, R. E. Thomas, W. D. Ma, M. V. Novotny, R. D. Cone, *Chemical Senses* **2004**, *29*, 111.
[162] C. Morgan, R. E. Thomas, R. D. Cone, *Horm. Behav.* **2004**, *45*, 58.
[163] L. Z. Yan, D. Flora, P. Edwards, D. L. Smiley, P. J. Emmerson, H. M. Hsiung, R. Gadski, J. Hertel, M. L. Heiman, S. Husain, T. P. O'Brien, S. D. Kahl, L. S. Zhang, R. D. DiMarchi, J. P. Mayer, *Bioorg. Med. Chem. Lett.* **2005**, *15*, 4611.
[164] M. A. Bednarek, T. MacNeil, R. Tang, R. N. Kalyani, L. H. T. van der Ploeg, D. H. Weinberg, *Biochem. Bioph. Res. Co.* **2001**, *286*, 641.
[165] A. W. H. Cheung, L. D. Qi, V. Gore, X. J. Chu, D. Bartkovitz, G. Kurylko, J. Swistok, W. Danho, L. Chen, K. Yagaloff, *Bioorg. Med. Chem. Lett.* **2005**, *15*, 5504.
[166] L. N. Koikov, F. H. Ebetino, J. C. Hayes, D. Cross-Doersen, J. J. Knittel, *Bioorg. Med. Chem. Lett.* **2004**, *14*, 4839.
[167] P. Grieco, P. M. Balse, D. Weinberg, T. MacNeil, V. J. Hruby, *J. Med. Chem.* **2000**, *43*, 4998.
[168] A. V. Mayorov, M. Cai, K. B. Chandler, R. R. Petrov, A. R. VanScoy, Z. Yu, D. K. Tanaka, D. Trivedi, V. J. Hruby, *J. Med. Chem.* **2006**, *49*, 1946.
[169] A. V. Mayorov, M. Cai, E. S. Palmer, M. M. Dedek, J. P. Cain, A. R. Van Scoy, B. Tan, J. Vagner, D. Trivedi, V. J. Hruby, *J. Med. Chem.* **2008**, *51*, 187.
[170] S. Ballet, A. V. Mayorov, M. Y. Cai, D. Tymecka, K. B. Chandler, E. S. Palmer, K. Van Rompaey, A. Misicka, D. Tourwe, V. J. Hruby, *Bioorg. Med. Chem. Lett.* **2007**, *17*, 2492.
[171] M. A. Bednarek, T. MacNeil, R. Tang, T. M. Fong, M. A. Cabello, M. Maroto, A. Teran, *J. Med. Chem.* **2007**, *50*, 2520.
[172] M. A. Bednarek, T. MacNeil, R. Tang, T. M. Fong, M. A. Cabello, M. Maroto, A. Teran, *Chem. Biol. Drug Des.* **2007**, *69*, 350.
[173] P. Balse-Srinivasan, P. Grieco, M. Y. Cai, D. Trivedi, V. J. Hruby, *J. Med. Chem.* **2003**, *46*, 3728.
[174] A. V. Mayorov, S. Y. Han, M. Cai, M. R. Hammer, D. Trivedi, V. J. Hruby, *Chem. Biol. Drug. Des.* **2006**, *67*, 329.
[175] C. Chen, J. H. Yu, B. A. Fleck, S. R. J. Hoare, J. Saunders, A. C. Foster, *J. Med. Chem.* **2004**, *47*, 4083.
[176] J. P. Cain, A. V. Mayorov, M. Y. Cai, H. Wang, B. Tan, K. Chandler, Y. Lee, R. R. Petrov, D. Trivedi, V. J. Hruby, *Bioorg. Med. Chem. Lett.* **2006**, *16*, 5462.
[177] S. C. Miller, T. S. Scanlan, *J. Am. Chem. Soc.* **1997**, *119*, 2301.
[178] E. Biron, J. Chatterjee, H. Kessler, *J. Pept. Sci.* **2006**, *12*, 213.

[179] H. Kessler, C. Griesinger, J. Lautz, A. Müller, W. F. van Gunsteren, H. J. C. Berendsen, *J. Am. Chem. Soc.* **1988**, *110*, 3393.
[180] M. Heller, M. Sukopp, N. Tsomaia, M. John, D. F. Mierke, B. Reif, H. Kessler, *J. Am. Chem. Soc.* **2006**, *128*, 13806.
[181] B. W. Matthews, *Macromolecules* **1972**, *5*, 818.
[182] C. M. Venkatachalam, *Biopolymers* **1968**, *6*, 1425.
[183] W. Vale, P. Brazeau, G. Grant, A. Nussey, R. Burgus, J. Rivier, N. Ling, R. Guillemin, *CR Acad. Sci. D Nat.* **1972**, *275*, 2913.
[184] V. D. Corleto, S. Nasoni, E. Panzuto, S. Cassetta, G. Delle Fave, *Digest. Liver Dis.* **2004**, *36*, 8.
[185] D. Hoyer, G. I. Bell, M. Berelowitz, J. Epelbaum, W. Feniuk, P. P. A. Humphrey, A. M. Ocarroll, Y. C. Patel, A. Schonbrunn, J. E. Taylor, T. Reisine, *Trends Pharmacol. Sci.* **1995**, *16*, 86.
[186] T. Reisine, G. I. Bell, *Endocr. Rev.* **1995**, *16*, 427.
[187] A. V. Schally, *Cancer Res.* **1988**, *48*, 6977.
[188] C. Scarpignato, I. Pelosini, *Chemotherapy* **2001**, *47*, 1.
[189] M. N. Pollak, A. V. Schally, *Proc. Soc. Exp. Biol. Med.* **1998**, *217*, 143.
[190] C. Bousquet, E. Puente, L. Buscail, N. Vaysse, C. Susini, *Chemotherapy* **2001**, *47*, 30.
[191] K. Oberg, *Neuroendocrinology* **2004**, *80 Suppl 1*, 57.
[192] M. Blaker, M. Schmitz, A. Gocht, S. Burghardt, M. Schulz, D. C. Broring, A. Pace, H. Greten, A. de Weerth, *J. Hepatol.* **2004**, *41*, 112.
[193] O. Ovadia, S. Greenberg, B. Laufer, C. Gilon, A. Hoffman, H. Kessler, *Expert Opi. Drug Dis.* **2010**, *5*, 655.
[194] E. Biron, J. Chatterjee, O. Ovadia, D. Langenegger, J. Brueggen, D. Hoyer, H. A. Schmid, R. Jelinek, C. Gilon, A. Hoffman, H. Kessler, *Angew. Chem., Int. Ed.* **2008**, *47*, 2595.
[195] P. Brazeau, W. Vale, J. Rivier, R. Guillemin, *Biochem. Biophys. Res. Co.* **1974**, *60*, 1202.
[196] J. Rivier, P. Brazeau, W. Vale, R. Guillemin, *J. Med. Chem.* **1975**, *18*, 123.
[197] R. Chandrasekaran, A. V. Lakshminarayanan, U. V. Pandya, G. N. Ramachandran, *Biochim. Biophys. Acta* **1973**, *303*, 14.
[198] J. Rivier, M. Brown, W. Vale, *Biochem. Biophys. Res. Co.* **1975**, *65*, 746.
[199] D. F. Veber, F. W. Holly, R. F. Nutt, S. J. Bergstrand, S. F. Brady, R. Hirschmann, M. S. Glitzer, R. Saperstein, *Nature* **1979**, *280*, 512.
[200] D. F. Veber, F. W. Holly, W. J. Paleveda, R. F. Nutt, S. J. Bergstrand, M. Torchiana, M. S. Glitzer, R. Saperstein, R. Hirschmann, *P. Natl. Acad. Sci. USA* **1978**, *75*, 2636.
[201] D. F. Veber, R. M. Freidlinger, D. S. Perlow, W. J. Paleveda, Jr., F. W. Holly, R. G. Strachan, R. F. Nutt, B. H. Arison, C. Homnick, W. C. Randall, M. S. Glitzer, R. Saperstein, R. Hirschmann, *Nature* **1981**, *292*, 55.
[202] S. P. Rohrer, E. T. Birzin, R. T. Mosley, S. C. Berk, S. M. Hutchins, D. M. Shen, Y. S. Xiong, E. C. Hayes, R. M. Parmar, F. Foor, S. W. Mitra, S. J. Degrado, M. Shu, J. M. Klopp, S. J. Cai, A. Blake, W. W. S. Chan, A. Pasternak, L. H. Yang, A. A. Patchett, R. G. Smith, K. T. Chapman, J. M. Schaeffer, *Science* **1998**, *282*, 737.
[203] A. Pasternak, Y. P. Pan, D. Marino, P. E. Sanderson, R. Mosley, S. P. Rohrer, E. T. Birzin, S. E. W. Huskey, T. Jacks, K. D. Schleim, K. Cheng, J. M. Schaeffer, A. A. Patchett, L. H. Yang, *Bioorg. Med. Chem. Lett.* **1999**, *9*, 491.
[204] S. E. Wolkenberg, C. J. Thut, *Curr. Opin. Drug Di. De.* **2008**, *11*, 446.
[205] W. Bauer, U. Briner, W. Doepfner, R. Haller, R. Huguenin, P. Marbach, T. J. Petcher, J. Pless, *Life Sci.* **1982**, *31*, 1133.
[206] S. W. Lamberts, A. J. van der Lely, W. W. de Herder, L. J. Hofland, *N. Engl. J. Med.* **1996**, *334*, 246.

[207] Y. Toledano, L. Rot, Y. Greenman, S. Orlovsky, Y. Pauker, D. Olchovsky, A. Eliash, O. Bardicef, O. Makhoul, G. Tsvetov, M. Gershinsky, O. Cohen-Ouaqnine, R. Ness-Abramof, Z. Adnan, J. Ilany, H. Guttmann, M. Sapir, C. Benbassat, I. Shimon, *Pituitary* **2009**, *12*, 285.
[208] R. Z. Cai, B. Szoke, R. Lu, D. Fu, T. W. Redding, A. V. Schally, *P. Natl. Acad. Sci. USA* **1986**, *83*, 1896.
[209] G. Weckbecker, I. Lewis, R. Albert, H. A. Schmid, D. Hoyer, C. Bruns, *Nat. Rev. Drug Discov.* **2003**, *2*, 999.
[210] E. P. Krenning, D. J. Kwekkeboom, W. H. Bakker, W. A. P. Breeman, P. P. M. Kooij, H. Y. Oei, M. Vanhagen, P. T. E. Postema, M. Dejong, J. C. Reubi, T. J. Visser, A. E. M. Reijs, L. J. Hofland, J. W. Koper, S. W. J. Lamberts, *Eur. J. Nucl. Med.* **1993**, *20*, 716.
[211] L. K. Kvols, E. A. Woltering, *Anti-Cancer Drug.* **2006**, *17*, 601.
[212] C. Susini, L. Buscail, *Ann. Oncol.* **2006**, *17*, 1733.
[213] H. Kessler, M. Bernd, H. Kogler, J. Zarbock, O. W. Sørensen, G. Bodenhausen, R. R. Ernst, *J. Am. Chem. Soc.* **1983**, *105*, 6944.
[214] C. R. R. Grace, L. Durrer, S. C. Koerber, J. Erchegyi, J. C. Reubi, J. E. Rivier, R. Riek, *J. Med. Chem.* **2005**, *48*, 523.
[215] C. R. R. Grace, J. Erchegyi, S. C. Koerber, J. C. Reubi, J. Rivier, R. Riek, *J. Med. Chem.* **2006**, *49*, 4487.
[216] C. R. R. Grace, J. Erchegyi, J. C. Reubi, J. E. Rivier, R. Riek, *Biopolymers* **2008**, *89*, 1077.
[217] C. R. R. Grace, S. C. Koerber, J. Erchegyi, J. C. Reubi, J. Rivier, R. Riek, *J. Med. Chem.* **2003**, *46*, 5606.
[218] J. Szolcsányi, E. Pintér, Z. Helyes, G. Oroszi, J. Nemeth, *Brit. J. Pharmacol.* **1998**, *125*, 916.
[219] J. Szolcsányi, Z. Helyes, G. Oroszi, J. Nemeth, E. Pintér, *Brit. J. Pharmacol.* **1998**, *123*, 936.
[220] D. F. Veber, R. Saperstein, R. F. Nutt, R. M. Freidinger, S. F. Brady, P. Curley, D. S. Perlow, W. J. Paleveda, C. D. Colton, A. G. Zacchei, D. J. Tocco, D. R. Hoff, R. L. Vandlen, J. E. Gerich, L. Hall, L. Mandarino, E. H. Cordes, P. S. Anderson, R. Hirschmann, *Life Sci.* **1984**, *34*, 1371.
[221] J. Chatterjee, B. Laufer, J. G. Beck, Z. Helyes, E. Pintér, J. Szolcsányi, A. Horvath, J. Mandl, J. C. Reubi, G. Keri, H. Kessler, *ACS Med. Chem. Lett.* **2011**, *2*, 509.
[222] H. Kessler, C. Griesinger, K. Wagner, *J. Am. Chem. Soc.* **1987**, *109*, 6927.
[223] B. H. Arison, R. Hirschmann, D. F. Veber, *Bioorg. Chem.* **1978**, *7*, 447.
[224] C. Mas-Moruno, F. Rechenmacher, H. Kessler, *Anti-Cancer Agent. ME* **2010**, *10*, 753.
[225] G. Tabatabai, M. Weller, B. Nabors, M. Picard, D. Reardon, T. Mikkelsen, C. Ruegg, R. Stupp, *Target. Oncol.* **2010**, *5*, 175.
[226] R. O. Hynes, *Cell* **2002**, *110*, 673.
[227] D. Cox, M. Brennan, N. Moran, *Nat. Rev. Drug Discov.* **2010**, *9*, 804.
[228] T. Arndt, U. Arndt, U. Reuning, H. Kessler, in *Cancer Therapy: Molecular Targets in Tumor-Host Interactions* (Ed.: G. F. Weber), Horizon Bioscience, **2005**, pp. 93.
[229] C. J. Avraamides, B. Garmy-Susini, J. A. Varner, *Nat. Rev. Cancer* **2008**, *8*, 604.
[230] J. S. Desgrosellier, D. A. Cheresh, *Nat. Rev. Cancer* **2010**, *10*, 9.
[231] E. Ruoslahti, M. D. Pierschbacher, *Science* **1987**, *238*, 491.
[232] E. F. Plow, T. K. Haas, L. Zhang, J. Loftus, J. W. Smith, *J. Biol. Chem.* **2000**, *275*, 21785.
[233] R. Haubner, D. Finsinger, H. Kessler, *Angew. Chem. Int. Ed.* **1997**, *36*, 1374.
[234] A. Meyer, J. Auernheimer, A. Modlinger, H. Kessler, *Curr. Pharm. Des.* **2006**, *12*, 2723.

[235] M. Friedlander, P. C. Brooks, R. W. Shaffer, C. M. Kincaid, J. A. Varner, D. A. Cheresh, *Science* **1995**, *270*, 1500.
[236] N. Skuli, S. Monferran, C. Delmas, G. Favre, J. Bonnet, C. Toulas, E. C. J. Moyal, *Cancer Res.* **2009**, *69*, 3308.
[237] B. L. Bader, H. Rayburn, D. Crowley, R. O. Hynes, *Cell* **1998**, *95*, 507.
[238] L. E. Reynolds, L. Wyder, J. C. Lively, D. Taverna, S. D. Robinson, X. Huang, D. Sheppard, R. O. Hynes, K. M. Hodivala-Dilke, *Nat. Med.* **2002**, *8*, 27.
[239] P. Carmeliet, *Nat. Med.* **2002**, *8*, 14.
[240] R. O. Hynes, *Nat. Med.* **2002**, *8*, 918.
[241] D. A. Cheresh, D. G. Stupack, *Nat. Med.* **2002**, *8*, 193.
[242] S. Kim, K. Bell, S. A. Mousa, J. A. Varner, *Am. J. Pathol.* **2000**, *156*, 1345.
[243] N. J. Boudreau, J. A. Varner, *J. Biol. Chem.* **2004**, *279*, 4862.
[244] A. R. Reynolds, I. R. Hart, A. R. Watson, J. C. Welti, R. G. Silva, S. D. Robinson, G. Da Violante, M. Gourlaouen, M. Salih, M. C. Jones, D. T. Jones, G. Saunders, V. Kostourou, F. Perron-Sierra, J. C. Norman, G. C. Tucker, K. M. Hodivala-Dilke, *Nat. Med.* **2009**, *15*, 392.
[245] M. Weller, D. Reardon, B. Nabors, R. Stupp, *Nat. Med.* **2009**, *15*, 726.
[246] R. Stupp, C. Ruegg, *J. Clin. Oncol.* **2007**, *25*, 1637.
[247] J. Chatterjee, C. Gilon, A. Hoffman, H. Kessler, *Acc. Chem. Res.* **2008**, *41*, 1331.
[248] P. P. Bose, U. Chatterjee, C. Nerelius, T. Govender, T. Norstrom, A. Gogoll, A. Sandegren, E. Gothelid, J. Johansson, P. I. Arvidsson, *J. Med. Chem.* **2009**, *52*, 8002.
[249] K. S. Harris, J. L. Casey, A. M. Coley, J. A. Karas, J. K. Sabo, Y. Y. Tan, O. Dolezal, R. S. Norton, A. B. Hughes, D. Scanlon, M. Foley, *J. Biol. Chem.* **2009**, *284*, 9361.
[250] H. C. Qu, P. Magotti, D. Ricklin, E. L. Wu, I. Kourtzelis, Y. Q. Wu, Y. N. Kaznessis, J. D. Lambris, *Mol. Immunol.* **2011**, *48*, 481.
[251] A. C. Bach, C. J. Eyermann, J. D. Gross, M. J. Bower, R. L. Harlow, P. C. Weber, W. F. Degrado, *J. Am. Chem. Soc.* **1994**, *116*, 3207.
[252] A. C. Bach, J. R. Espina, S. A. Jackson, P. F. W. Stouten, J. L. Duke, S. A. Mousa, W. F. DeGrado, *J. Am. Chem. Soc.* **1996**, *118*, 293.
[253] J. Chatterjee, O. Ovadia, G. Zahn, L. Marinelli, A. Hoffman, C. Gilon, H. Kessler, *J. Med. Chem.* **2007**, *50*, 5878.
[254] J. P. Xiong, T. Stehle, R. Zhang, A. Joachimiak, M. Frech, S. L. Goodman, M. A. Arnaout, *Science* **2002**, *296*, 151.
[255] R. Haubner, R. Gratias, B. Diefenbach, S. L. Goodman, A. Jonczyk, H. Kessler, *J. Am. Chem. Soc.* **1996**, *118*, 7461.
[256] J. Chatterjee, D. Mierke, H. Kessler, *J. Am. Chem. Soc.* **2006**, *128*, 15164.
[257] J. Chatterjee, D. F. Mierke, H. Kessler, *Chem.-Eur. J.* **2008**, *14*, 1508.
[258] B. Laufer, A. O. Frank, J. Chatterjee, T. Neubauer, C. Mas-Moruno, G. Kummerlowe, H. Kessler, *Chem.-Eur. J.* **2010**, *16*, 5385.
[259] M. Pfaff, K. Tangemann, B. Muller, M. Gurrath, G. Muller, H. Kessler, R. Timpl, J. Engel, *J. Biol. Chem.* **1994**, *269*, 20233.
[260] G. Müller, M. Gurrath, H. Kessler, *J. Comput. Aided Mol. Des.* **1994**, *8*, 709.
[261] M. Q. Zhang, B. Wilkinson, *Curr. Opin. Biotechnol.* **2007**, *18*, 478.
[262] T. Wieland, H. Faulstich, *CRC Crit. Rev. Biochem.* **1978**, *5*, 185.
[263] J. F. Tjia, I. R. Webber, D. J. Back, *Br. J. Clin. Pharmacol.* **1991**, *31*, 344.
[264] J. C. Kolars, W. M. Awni, R. M. Merion, P. B. Watkins, *Lancet* **1991**, *338*, 1488.
[265] S. S. Cathapermal, M. L. Foegh, C. S. Rau, P. W. Ramwell, *Drug. Metab. Dispos.* **1991**, *19*, 735.
[266] A. M. Dahlem, A. S. Hassan, S. P. Swanson, W. W. Carmichael, V. R. Beasley, *Pharmacol. Toxicol.* **1989**, *64*, 177.

[267] S. Hess, Y. Linde, O. Ovadia, E. Safrai, D. E. Shalev, A. Swed, E. Halbfinger, T. Lapidot, I. Winkler, Y. Gabinet, A. Faier, D. Yarden, Z. Xiang, F. P. Portitlo, C. Haskell-Luevano, C. Gilon, A. Hoffman, *J. Med. Chem.* **2008**, *51*, 1026.
[268] T. R. White, C. M. Renzelman, A. C. Rand, T. Rezai, C. M. McEwen, V. M. Gelev, R. A. Turner, R. G. Linington, S. S. F. Leung, A. S. Kalgutkar, J. N. Bauman, Y. Z. Zhang, S. Liras, D. A. Price, A. M. Mathiowetz, M. P. Jacobson, R. S. Lokey, *Nat. Chem. Biol.* **2011**, *7*, 810.
[269] A. Fjellestad-Paulsen, P. Höglund, S. Lundin, O. Paulsen, *Clin. Endocrinol.* **1993**, *38*, 177.
[270] S. Lundin, H. Vilhardt, *Acta Endocrinol. (Copenh.)* **1986**, *112*, 457.
[271] P. P. Bose, U. Chatterjee, I. Hubatsch, P. Artursson, T. Govender, H. G. Kruger, M. Bergh, J. Johansson, P. I. Arvidsson, *Bioorgan. Med. Chem.* **2010**, *18*, 5896.
[272] G. Fricker, J. Drewe, *J. Pept. Sci.* **1996**, *2*, 195.
[273] O. Ovadia, S. Greenberg, J. Chatterjee, B. Laufer, F. Opperer, H. Kessler, C. Gilon, A. Hoffman, *Mol. Pharm.* **2011**, *8*, 479.
[274] H.-R. Loosli, H. Kessler, H. Oschkinat, H.-P. Weber, T. J. Petcher, A. Widmer, *Helv. Chim. Acta* **1985**, *68*, 682.
[275] M. J. Gething, J. Sambrook, *Nature* **1992**, *355*, 33.
[276] J. Buchner, *FASEB J.* **1996**, *10*, 10.
[277] F. U. Hartl, *Nature* **1996**, *381*, 571.
[278] M. Beissinger, J. Buchner, *Biol Chem* **1998**, *379*, 245.
[279] M. Litt, P. Kramer, D. M. LaMorticella, W. Murphey, E. W. Lovrien, R. G. Weleber, *Hum. Mol. Genet.* **1998**, *7*, 471.
[280] G. C. Fan, X. Ren, J. Qian, Q. Yuan, P. Nicolaou, Y. Wang, W. K. Jones, G. Chu, E. G. Kranias, *Circulation* **2005**, *111*, 1792.
[281] M. M. Wilhelmus, W. C. Boelens, I. Otte-Holler, B. Kamps, R. M. de Waal, M. M. Verbeek, *Brain Res.* **2006**, *1089*, 67.
[282] M. F. Tsai, C. C. Wang, G. C. Chang, C. Y. Chen, H. Y. Chen, C. L. Cheng, Y. P. Yang, C. Y. Wu, F. Y. Shih, C. C. Liu, H. P. Lin, Y. S. Jou, S. C. Lin, C. W. Lin, W. J. Chen, W. K. Chan, J. J. Chen, P. C. Yang, *J. Natl. Cancer Inst.* **2006**, *98*, 825.
[283] M. F. Roelofs, W. C. Boelens, L. A. Joosten, S. Abdollahi-Roodsaz, J. Geurts, L. U. Wunderink, B. W. Schreurs, W. B. van den Berg, T. R. Radstake, *J. Immunol.* **2006**, *176*, 7021.
[284] O. V. Evgrafov, I. Mersiyanova, J. Irobi, L. Van Den Bosch, I. Dierick, C. L. Leung, O. Schagina, N. Verpoorten, K. Van Impe, V. Fedotov, E. Dadali, M. Auer-Grumbach, C. Windpassinger, K. Wagner, Z. Mitrovic, D. Hilton-Jones, K. Talbot, J. J. Martin, N. Vasserman, S. Tverskaya, A. Polyakov, R. K. Liem, J. Gettemans, W. Robberecht, P. De Jonghe, V. Timmerman, *Nat. Genet.* **2004**, *36*, 602.
[285] J. M. Fontaine, X. Sun, A. D. Hoppe, S. Simon, P. Vicart, M. J. Welsh, R. Benndorf, *FASEB J.* **2006**, *20*, 2158.
[286] S. Ackerley, P. A. James, A. Kalli, S. French, K. E. Davies, K. Talbot, *Hum. Mol. Genet.* **2006**, *15*, 347.
[287] P. Vicart, A. Caron, P. Guicheney, Z. Li, M. C. Prevost, A. Faure, D. Chateau, F. Chapon, F. Tome, J. M. Dupret, D. Paulin, M. Fardeau, *Nat. Genet.* **1998**, *20*, 92.
[288] M. Haslbeck, T. Franzmann, D. Weinfurtner, J. Buchner, *Nat. Struct. Mol. Biol.* **2005**, *12*, 842.
[289] T. M. Franzmann, P. Menhorn, S. Walter, J. Buchner, *Mol. Cell* **2008**, *29*, 207.
[290] T. M. Franzmann, M. Wuhr, K. Richter, S. Walter, J. Buchner, *J. Mol. Biol.* **2005**, *350*, 1083.
[291] K. Pervushin, R. Riek, G. Wider, K. Wüthrich, *P. Natl. Acad. Sci. USA* **1997**, *94*, 12366.

[292] K. K. Kim, R. Kim, S. H. Kim, *Nature* **1998**, *394*, 595.
[293] R. L. van Montfort, E. Basha, K. L. Friedrich, C. Slingsby, E. Vierling, *Nat. Struct. Biol.* **2001**, *8*, 1025.
[294] E. Hilario, E. C. Teixeira, G. A. Pedroso, M. C. Bertolini, F. J. Medrano, *Acta Crystallogr. F* **2006**, *62*, 446.
[295] K. Miki, K. Takeda, T. Hayashi, T. Abe, Y. Hirano, Y. Hanazono, M. Yohda, *J. Struct. Biol.* **2011**, *174*, 92.
[296] J. Söding, A. Biegert, A. N. Lupas, *Nucleic Acids Res.* **2005**, *33*, W244.
[297] J. Söding, *Bioinformatics* **2005**, *21*, 951.
[298] M. Ikura, L. E. Kay, A. Bax, *Biochemistry* **1990**, *29*, 4659.
[299] L. E. Kay, M. Ikura, R. Tschudin, A. Bax, *J. Magn. Reson.* **1990**, *89*, 496.
[300] T. E. Skinner, T. O. Reiss, B. Luy, N. Khaneja, S. J. Glaser, *J. Magn. Reson.* **2003**, *163*, 8.
[301] T. E. Skinner, T. O. Reiss, B. Luy, N. Khaneja, S. J. Glaser, *J. Magn. Reson.* **2004**, *167*, 68.
[302] K. Kobzar, T. E. Skinner, N. Khaneja, S. J. Glaser, B. Luy, *J. Magn. Reson.* **2004**, *170*, 236.
[303] B. Luy, K. Kobzar, T. E. Skinner, N. Khaneja, S. J. Glaser, *J. Magn. Reson.* **2005**, *176*, 179.
[304] L. Verdier, P. Sakhaii, M. Zweckstetter, C. Griesinger, *J. Magn. Reson.* **2003**, *163*, 353.
[305] K. Kobzar, B. Luy, *J. Magn. Reson.* **2007**, *186*, 131.
[306] M. Piotto, V. Saudek, V. Sklenár, *J. Biomol. NMR* **1992**, *2*, 661.
[307] A. Kumar, G. Wagner, R. R. Ernst, K. Wüthrich, *J. Am. Chem. Soc.* **1981**, *103*, 3654.
[308] T. F. Havel, *Prog. Biophys. Mol. Biol.* **1991**, *56*, 43.
[309] D. F. Mierke, A. Geyer, H. Kessler, *Int. J. Pept. Protein Res.* **1994**, *44*, 325.
[310] E. Lindahl, B. Hess, D. van der Spoel, *J. Mol. Model.* **2001**, *7*, 306.
[311] D. van der Spoel, E. Lindahl, B. Hess, G. Groenhof, A. E. Mark, H. J. C. Berendsen, *J. Comput. Chem.* **2005**, *26*, 1701.
[312] D. van der Spoel, E. Lindahl, B. Hess, A. R. van Buuren, P. J. Apol, P. J. Meulenhoff, D. P. Tieleman, A. L. T. M. Sijbers, K. A. Feenstra, R. van Drunen, H. J. C. Berendsen, *Gromacs User Manual version 4.0*, **2005**.
[313] W. Humphrey, A. Dalke, K. Schulten, *J. Mol. Graph.* **1996**, *14*, 33.
[314] SYBYL 8.0, Tripos International, 1699 South Hanley Rd., St. Louis, Missouri, 63144, USA
[315] W. F. van Gunsteren, S. R. Billeter, A. A. Eising, P. H. Hünenberger, P. Krüger, A. E. Mark, W. R. P. Scott, I. G. Tironi, *Biomolecular simulation: the GROMOS96 manual and user guide, 1st ed.*, Hochschulverlag AG an der ETH Zürich, Zürich, **1996**.
[316] S. Miyamoto, P. A. Kollman, *J. Comput. Chem.* **1992**, *13*, 952.
[317] J. P. Ryckaert, G. Ciccotti, H. J. C. Berendsen, *J. Comput. Phys.* **1977**, *23*, 327.
[318] H. J. C. Berendsen, J. P. M. Postma, W. F. van Gunsteren, A. Dinola, J. R. Haak, *J. Chem. Phys.* **1984**, *81*, 3684.
[319] K. B. Mullis, F. A. Faloona, *Method. Enzymol.* **1987**, *155*, 335.
[320] R. K. Saiki, S. Scharf, F. Faloona, K. B. Mullis, G. T. Horn, H. A. Erlich, N. Arnheim, *Science* **1985**, *230*, 1350.
[321] J. Grodberg, J. J. Dunn, *J. Bacteriol.* **1988**, *170*, 1245.
[322] M. Sattler, J. Schleucher, C. Griesinger, *Prog. Nucl. Mag. Res. Sp.* **1999**, *34*, 93.
[323] B. K. John, D. Plant, R. E. Hurd, *J. Magn. Reson. Ser. A* **1992**, *101*, 113.
[324] M. Leutner, R. M. Gschwind, J. Liermann, C. Schwarz, G. Gemmecker, H. Kessler, *J. Biomol. NMR* **1998**, *11*, 31.
[325] Y. Shen, F. Delaglio, G. Cornilescu, A. Bax, *J. Biomol. NMR* **2009**, *44*, 213.